

www.zte.com.cn/magazine/English

ISSN 1673-5188
CODEN ZCTOAK

ZTE COMMUNICATIONS

March 2012, Vol.10 No.1

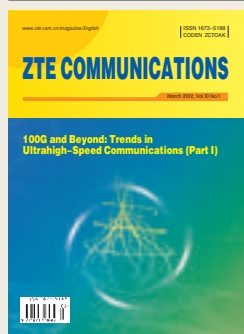
100G and Beyond: Trends in Ultrahigh-Speed Communications (Part I)

ISSN 1673-5188



C O N T E N T S

[Http://www.zte.com.cn/magazine/English](http://www.zte.com.cn/magazine/English)
Email: magazine@zte.com.cn



EDITORIAL BOARD

Cheng-Zhong Xu
Wayne State University (USA)

Houlin Zhao
International Telecommunication
Union (ITU)

Ke-Li Wu
The Chinese University of Hong
Kong (China)

Shiduan Cheng
Beijing University of Posts and
Telecommunications (China)

Wen Gao
Peking University (China)

Zhengkun Mi
Nanjing University of Posts and
Telecommunications (China)

Special Topic

100G and Beyond: Trends in Ultrahigh-Speed Communications (Part I)

01 Guest Editorial

by Gee-Kung Chang, Jianjun Yu, and Xiang Wang

03 High Spectral Efficiency 400G Transmission

by Xiang Zhou

10 Greater than 200 Gb/s Transmission Using Direct-Detection Optical OFDM Superchannel

*by Wei-Ren Peng, Itsuro Morita, Hidenori Takahashi,
and Takehiro Tsuritani*

18 Spatial Mode-Division Multiplexing for High-Speed Optical Coherent Detection Systems

*by William Shieh, An Li, Abdullah Al Amin, Xi Chen, Simin Chen,
and Guanjun Gao*

23 Exploiting the Faster-Than-Nyquist Concept in Wavelength-Division Multiplexing Systems Using Duobinary Shaping

*by Jianqiang Li, Ekawit Tipsuwannakul, Magnus Karlsson, and
Peter A. Andrekson*

30 Super-Receiver Design for Superchannel Coherent Optical Systems

*by Cheng Liu, Jie Pan, Thomas Detwiler, Andrew Stark, Yu-Ting
Hsueh, Gee-Kung Chang, and Stephen E. Ralph*

34 Design of a Silicon-Based High-Speed Plasmonic Modulator

by Mu Xu, Jiayang Wu, Tao Wang, and Yikai Su

40 The Key Technology in Optical OFDM-PON

by Xiangjun Xin

45 Compensating for Nonlinear Effects in Coherent-Detection

Optical Transmission Systems

by Fan Zhang

50 1 Tb/s Nyquist-WDM PM-RZ-QPSK Superchannel

Transmission over 1000 km SMF-28 with MAP Equalization

by Ze Dong, Jianjun Yu, and Hung-Chang Chien

Research Papers

54 Hardware Architecture of Polyphase Filter Banks Performing
Embedded Resampling for Software-Defined Radio Front-Ends

*by Mehmood Awan, Yannick Le Moullec, Peter Koch, and Fred
Harris*

63 A Histogram-Based Static Error Correction Technique for Flash
ADCs: Implementation

*by J Jacob Wikner, Armin Jalili, Sayed Masoud Sayedi, and
Rasoul Dehghani*

Departments

02 Introduction to ZTE Communications

22 Ad Index

ZTE COMMUNICATIONS

Vol. 10 No.1 (Issue 33)

Quarterly

First Issue Published in 2003

Supervised by:

Anhui Science and Technology Department

Sponsored by:

ZTE Corporation and Anhui Science
and Technology Information
Research Institute

Staff Members:

Editor-in-chief: Xie Daxiong

Deputy Editor-in-chief: Deng Xin

Executive Deputy

Editor-in-chief: Huang Xinming

Editor in Charge: Zhu Li

Editors: Paul Sleswick, Yang Qinyi, Xu Ye,
Lu Dan

Producer: Yu Gang

Circulation Executive: Wang Pingping

Assistant: Wang Kun

Editorial Correspondence:

Add: 12/F Kaixuan Building,

329 Jinzhai Road,

HeFei 230061, P. R. China

Tel: +86-551-5533356

Fax: +86-551-5850139

Email: magazine@zte.com.cn

Published and Circulated (Home and Abroad) by:

Editorial Office of

ZTE COMMUNICATIONS

Printed by:

Hefei Zhongjian Color Printing Company

Publication Date:

March 25, 2012

Publication Licenses:

ISSN 1673-5188

CN 34-1294/TN

Advertising License:

皖合工商广字 0058 号

Annual Subscription Rate:

USD\$50

Responsibility for content rests
on authors of signed articles and
not on the editorial board of
ZTE COMMUNICATIONS or its sponsors.
All rights reserved.

100G and Beyond: Trends in Ultrahigh-Speed Communications (Part I)

Gee-Kung Chang



Jianjun Yu



Xiang Wang



Fiber optics underpins the communication infrastructure of today's information society. Rapid progress in advanced modulation formats, high-gain coding, optical amplification, coherent detection with digital signal processing, and new types of transmission fibers have significantly affected optical communications. Increasing transmission capacity and bit rate per channel is the trend for optical transmission systems and networks. Commercial transmission capacity has increased more than one hundred thousand times since the first optical transmission system was deployed in the 1980s. Spectral efficiency of a single channel has increased from 0.025 b/s/Hz to 2 b/s/Hz. Bit rate per channel for commercial products has increased from 155 Mb/s to more than 100 Gb/s. Larger capacity is driven by the proliferation of broadband FTTH access networks, broadband wireless communications, and high-speed data communication systems in data centers and high performance computing. High bit rate per channel simplifies the management of complex optical networks. Although 100G is just the beginning of the commercial manufacturing and deployment stage, major optical networking research groups have been focusing on standards and technologies beyond 100G. The challenge of generating 400 Gb/s and 1 Tb/s per channel and transmitting at these speeds is one of the hottest topics in recent conferences on optical communications. Many forward-looking solutions have been proposed, and experiments have been carried out to achieve these high bit rates.

Globally, many research groups have been developing novel enabling technologies for meeting the requirements of high capacity and high bit rate operation using spectrally efficient multiplexing and modulation formats. These advanced techniques include single-carrier polarization multiplexing QPSK (which is currently used in 100G

commercial products), multicarrier optical orthogonal frequency division multiplexing, multicore or multimode spatial multiplexing, and coherent detection based on digital signal processing. For high-speed optical signal transmission, a traditional transponder with direct modulation and detection has a simple, low-cost architecture. However, the transmission distance at high bit rate is limited by the rigid requirements of high optical signal-to-noise ratio, polarization mode dispersion, and optical/electrical filtering effects. Coherent detection based on digital signal processing is becoming the trend for optical signal receivers because it can lift these limitations. The change from direct detection to coherent detection is revolutionary. Receiver architecture, transmission fiber and distance, and network management will be completely reshaped from previous direct-detection systems.

This special issue includes comprehensive reviews and original technical contributions that cover the rapid advances and broad scope of technologies in optical fiber communications. The invited papers of Part I of this issue come from service providers, telecommunication equipment manufacturers, and top universities and research institutes. After peer review, eleven papers were selected for this special issue. We hope it serves as a timely and high-quality networking forum for scientists and engineers.

The first two papers come from service providers. In the first paper, "High Spectral Efficiency 400G Transmission," Dr. Xiang Zhou from AT&T labs gives an overview of the generation and transmission of 450 Gb/s wavelength-division multiplexed channels over the standard 50 GHz ITU-T grid at a net spectral efficiency of 8.4 b/s/Hz. In the second paper, "Direct-Detection Optical OFDM Superchannel for Transmitting at Greater Than 200 Gb/s," Dr. Peng Wei Ren et al. from KDD&I propose and experimentally demonstrate a direct-detection optical

orthogonal-frequency-division-multiplexing (OFDM) superchannel and optical multiband receiving method to support a data rate higher than 200 Gb/s and to support longer distance for direct-detection systems.

Papers 3–9 come from universities that are renowned for research on optical transmission. In the third paper, “Spatial Mode Division Multiplexing for High-Speed Optical Coherent Detection Systems,” Professor William Shieh from the University of Melbourne proposes using spatial mode division multiplexing to increase transmission capacity. In the fourth paper, “Exploiting the Faster-Than-Nyquist Concept in Wavelength-Division Multiplexing Systems by Duobinary Shaping,” Dr. Jianqiang Li from Chalmers University of Technology presents a novel algorithm at the coherent receiver that is based on digital signal processing and is designed to tolerate strong filtering effects. In the fifth paper, “Super Receiver Design for Superchannel-Coherent Optical Systems,” Dr. Cheng Liu from Georgia Institute of Technology presents a novel super-receiver architecture for Nyquist-WDM superchannel coherent systems. This receiver detects and demodulates multiple WDM channels simultaneously and performs better than conventional coherent receivers in Nyquist-WDM systems. In the sixth paper, “Design of Silicon-Based High-Speed Plasmonic Modulator,” Professor Yikai Su from Shanghai Jiao Tong University proposes a silicon-based high-speed plasmonic modulator. This modulator is based on a double-layer structure with a 16 μm long metal-dielectric-metal plasmonic waveguide at the upper layer and two silicon single-mode waveguides at the bottom layer. In the seventh paper, “Key Technology in Optical OFDM-PON,” Professor Xiangjun Xin from Beijing University of Posts and Telecommunications proposes a novel optical access network based on OFDM. In the eighth paper, “Compensation of Nonlinear Effects in Coherent Detection Optical Transmission Systems,” Professor Fan Zhang from Beijing University reviews two kinds of nonlinear compensation methods: digital backward

propagation, and nonlinear electrical equalizer based on the time-domain Volterra series. The last paper comes from a telecommunication equipment manufacturer. In “Performance Assessment of 1 Tb/s Nyquist-WDM PM-RZ-QPSK Superchannel Transmission over 1000 km SMF-28 with MAP Equalization,” Dr. Ze Dong from ZTE (USA) evaluates the transmission performance of a 1 Tb/s (10×112 Gb/s) Nyquist-WDM PM-RZ-QPSK superchannel over a widely deployed SMF-28 fiber with and without MAP equalization.

We thank all authors for their valuable contributions and all reviewers for their timely and constructive feedback on submitted papers. We hope the contents of this issue are informative and useful for all readers.

Biographies

Gee-Kung Chang received his PhD degree in physics from the University of California, Riverside. He worked for 23 years at Telcordia Technologies (formerly Bell Systems-Bell Labs, and then Bellcore), where he held research and management positions, including director and chief scientist of optical internet research, director of optical networking systems and testbed, and director of optical system integration and network interoperability. Prior to joining Georgia Institute of Technology, he was vice president and chief technology strategist at OpNext Inc., an offshoot of Hitachi Telecom. Dr. Chang is currently the Byers endowed chair professor of optical networking at the School of Electrical and Computer Engineering, Georgia Institute of Technology. He is an eminent scholar of the Georgia Research Alliance. He is also co-director of the 100G Optical Networking Center at Georgia Tech. He holds 56 U.S. patents and has co-authored more than 360 peer-reviewed journal and conference papers. He was made a Telcordia Fellow in 1999 for pioneering work in the optical networking project, MONET, and NGI. He was made a fellow of the Photonic Society of Chinese-Americans in 2000. He is a fellow of the IEEE Photonics Society and a fellow of the Optical Society of America, recognized for his contributions to DWDM optical networking and label switching technologies. He has served at many IEEE LEOS and OSA conferences. He has been the lead guest editor for three special issues of the Journal of Lightwave Technology, which is sponsored by IEEE LEOS and OSA.

Jianjun Yu (yu.jianjun@zte.com.cn) received his PhD degree in electrical engineering from Beijing University of Posts and Telecommunications in 1999. From June 1999 to January 2001, he was an assistant research professor at the Research Center COM, Technical University of Denmark. From February 2001 to December 2002, he was a member of the technical staff at Lucent Technologies and Agere Systems, Murray Hill, NJ. He joined Georgia Institute of Technology in January 2003 as a research faculty member and director of the Optical Network Laboratory. From November 2005 to February 2010, he was a senior member of technical staff at NEC Laboratories America, Princeton, NJ. Currently, he works for ZTE Corporation as the chief scientist on high-speed optical transmission and director of optics labs in North America. He is also a chair professor at Fudan University and adjunct professor and PhD supervisor at the Georgia Institute of Technology, Beijing University of Posts and Telecommunications, and Hunan University. He has authored more than 100 papers for prestigious journals and conferences. Dr. Yu holds 8 U.S. patents with 30 others pending. He is a fellow of the Optical Society of America. He is editor-in-chief of Recent Patents on Engineering and an associate editor for the Journal of Lightwave Technology and Journal of Optical Communications and Networking. Dr. Yu was a technical committee member at IEEE LEOS from 2005 to 2007 and a technical committee member of OFC from 2009 to 2011.

Xiang Wang received his BSc degree in computer science from Nanjing University in 1991, and MSc degree in electronic engineering from Southeast University in 1997. He joined ZTE Corporation in 1997 and has led the planning, designing, R&D and product managing of programmable switches, wired network products, softswitch products, and service software products. Several products he and his team had developed won multiple national awards. He has rich experience and deep understanding of development of the communications industry. He is now a vice president of ZTE Corporation, taking charge of overall technical strategies, R&D, and platform and architecture designing of wired products.

Introduction to ZTE Communications

ZTE Communications is a quarterly peer-reviewed technical magazine ISSN (1673-5188) and CODEN (ZCTOAK). It is edited, published and distributed by ZTE Corporation. The magazine focuses on hot topics and cutting edge technologies in the telecom industry. It has been listed in the Ulrich's Periodicals Directory, Index of Copernicus (IC), and Cambridge Scientific Abstracts (CSA). *ZTE Communications* is distributed to telecom operators, science and technology research institutes, and colleges and universities in more than 140 countries.

High Spectral Efficiency 400G Transmission

Xiang Zhou

(AT&T Labs—Research, Middletown, NJ 07748, USA)

Abstract

This paper gives an overview of the generation and transmission of 450 Gb/s wavelength-division multiplexed (WDM) channels over the standard 50 GHz ITU-T grid at a net spectral efficiency (SE) of 8.4 b/s/Hz. The use of nearly ideal Nyquist pulse shaping, spectrally-efficient high-order modulation format, distributed Raman amplification, distributed compensation of ROADM filtering effects, coherent equalization, and high-coding gain forward error correction (FEC) code may enable future 400G systems to operate over the standard 50 GHz grid optical network.

Keywords

spectral efficiency; optical; modulation format; coherent

1 Introduction

Optical transport costs have traditionally been lowered by increasing per-channel data rates and spectral efficiency (SE). With 100 Gb/s wavelength-division multiplexed (WDM) technology being made commercially available in 2010, research is now being conducted on per-channel bit rates beyond 100 Gb/s that have spectral efficiencies greater than 2 b/s/Hz. It is likely that 400 Gb/s will be the next-generation transport standard [1]. From an historical point of view, increasing the transport interface rate in proportion to SE has minimized the cost per bit transmitted. In line with this trend, SE of 8 b/s/Hz might be needed for future 400 Gb/s systems (Fig. 1). Such SE enables future 400 Gb/s systems to operate over existing optical networks with 50 GHz WDM channel spacing; therefore, it is very attractive from a carrier's perspective.

Because of several limitations, transmitting 400 Gb/s per-channel signals on the 50 GHz WDM grid is very challenging. First, according to Shannon theory, 11.76 dB signal-to-noise ratio (SNR) is required for an 8 b/s/Hz 400 Gb/s system, and this is higher than in current 2 b/s/Hz 100 Gb/s systems (without taking fiber nonlinearity into consideration). Second, fiber nonlinearity limits the allowable launch power and, consequently, the achievable signal SNR. Furthermore, a higher-SE modulation format is less tolerant of fiber nonlinearity because of the reduced Euclidean distance. Third, non-ideal passband shapes from optical network components, such as the widely used reconfigurable

add/drop multiplexer (ROADM), cause significant channel narrowing. Finally, a high-SE modulation format is less tolerant of laser phase noise, which may introduce extra penalty.

Spectrally efficient, high-order coherent modulation formats, coherent detection, transmitter- and receiver-side digital signal processing (DSP), distributed Raman amplification, high-coding-gain forward error correction (FEC) code, and new low-loss, low-nonlinearity fibers have all been considered as enabling technologies for next generation high-speed transport systems. These technologies are currently being explored by the research community. Single-channel bit rates beyond 100 Gb/s have been demonstrated using single-carrier high-order coherent modulation formats (up to 448 Gb/s) [2] and multicarrier-based high-order coherent modulation formats (up to 448 Gb/s [3],[4] and 1.2 Tb/s [5]). For WDM transmission, the following have been demonstrated using polarization-division-multiplexed (PDM)-16 QAM, digital coherent detection, distributed Raman amplification, and new ultralarge-area fiber (ULAF): 50 GHz-spaced, 10×224 Gb/s over 12×100 km with SE of 4 b/s/Hz [6]; 70 GHz-spaced, 10×456 Gb/s over 8×100 km with SE of 6.1 b/s/Hz [7]; and 100 GHz-spaced, 3×485 Gb/s over 48×100 km with SE of 4 b/s/Hz [8].

Recently, 400G transmission over the standard 50 GHz WDM grid has been demonstrated using PDM-32 QAM [9]–[11]. In [10], 8×450 Gb/s WDM signals transmitted over 400 km of ULAF fiber and passing through one 50 GHz grid wavelength-selective switch (WSS)-based ROADM was

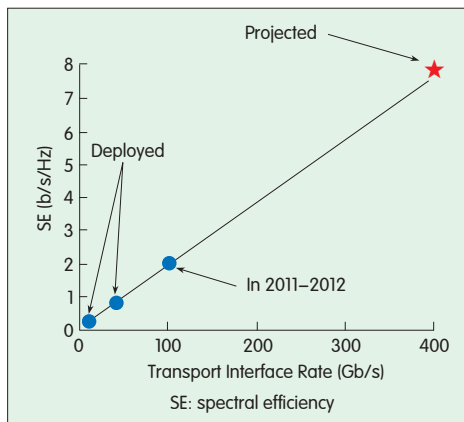


Figure 1. Projected demand for SE for the next-generation transport standard.

demonstrated with net SE of 8 b/s/Hz. This was the first demonstration of a 400G WDM system over the standard 50 GHz grid optical network. In [11], the transmission reach was extended to 800 km by introducing a broadband optical spectral-shaping technique to compensate for ROADMs filtering effects. This is the longest transmission distance beyond 4 b/s/Hz that has been demonstrated for WDM SE. Key enabling technologies and experimental results are reviewed in the following sections.

In section 2, the 450 Gb/s PDM-Nyquist-32 QAM transmitter is described. In section 3, the coherent receiver and DSP algorithms are presented. In section 4, two WDM transmission experiments and back-to-back are presented. In section 5, a summary is given.

2 450 Gb/s PDM-Nyquist 32-QAM Transmitter

To overcome limited digital-to-analog converter (DAC) bandwidth, a frequency-locked five-subcarrier generation method is used to create the 450 Gb/s per-channel signal [10], [11]. Fig. 2 shows the demonstrated 450 Gb/s PDM-Nyquist-32 QAM transmitter. The output from a continuous-wave (CW) laser with line width of approximately 100 kHz is split by a 3 dB optical coupler (OC). One output is sent to a Mach-Zehnder modulator (MZM-1) driven by a 9.2 GHz clock in order to generate two 18.4 GHz-spaced subcarriers per channel (the two first-order signal components) that are offset from the original wavelengths by ± 9.2 GHz. After an erbium-doped fiber amplifier (EDFA) and a 12.5/25 GHz interleaver filter (ILF), the original wavelengths and second-order harmonics are suppressed by more than 40 dB relative to the first-order components (Fig. 2a). The signal is then equally split between two outputs of a

polarization beam splitter (PBS) prepared by a polarization controller (PC). The two subcarriers on one PBS output are sent to an IQ modulator (IQ MOD1), driven by a pre-equalized 9 Gbaud Nyquist 32-QAM signal with $2^{15} - 1$ pseudorandom pattern length. The Nyquist pulse shaping has roll-off factor of 0.01, and the digital Nyquist filter has a tap length of 64. Fig. 3 shows the Nyquist filter impulse response used in this experiment and the resulting eye diagram of the generated 32-QAM baseband signal in one quadrature. Frequency-domain based pre-equalization [12] is used to compensate for the band-limiting effects of the DACs, which have 3 dB bandwidths less than 5 GHz at 10 bit resolution and a 24 GSa/s sample rate. Fig. 4 shows the relative amplitude spectra of the generated 9 Gbaud Nyquist 32-QAM baseband electrical drive signals (after DACs) with and without pre-equalization. The filtering effects caused by the DACs are compensated for using frequency-domain-based digital pre-equalization.

A second Mach-Zehnder modulator (MZM-2) driven by a 9.2 GHz clock is placed at the second PBS output to generate first-order signal components at 0 GHz and 18.4 GHz offsets from the original wavelength. After MZM-2, the signals pass through two 25/50 GHz interleavers to suppress the 0 GHz signal components and the unwanted harmonics (Fig. 2b). The second ILF re-inserts the original CW signal (from the second 3 dB OC output), resulting in three 18.4 GHz-spaced subcarriers from the original wavelength. These three subcarriers pass through an IQ modulator (IQ MOD2) that is driven by a second pre-equalized 9 Gbaud Nyquist 32-QAM signal with $2^{15} - 1$ pseudorandom pattern length and originating from a second DAC. Then, the sets of two and three 45 Gb/s subcarriers are passively combined and polarization multiplexed with 20 ns relative delay. This results in a 450 Gb/s signal that occupies a spectral width of 45.8 GHz, sufficiently confined to be placed on the 50 GHz

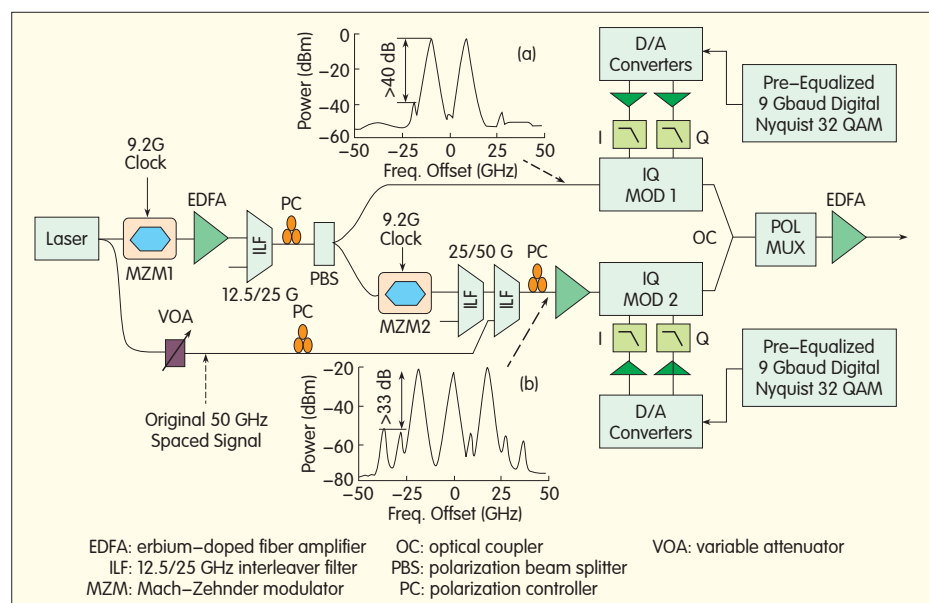
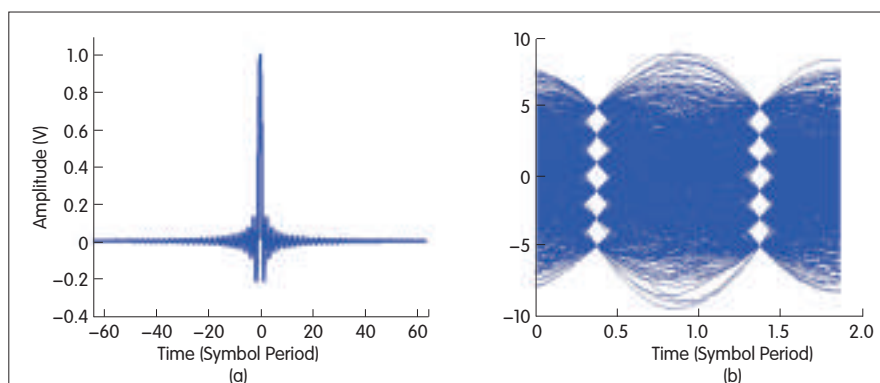
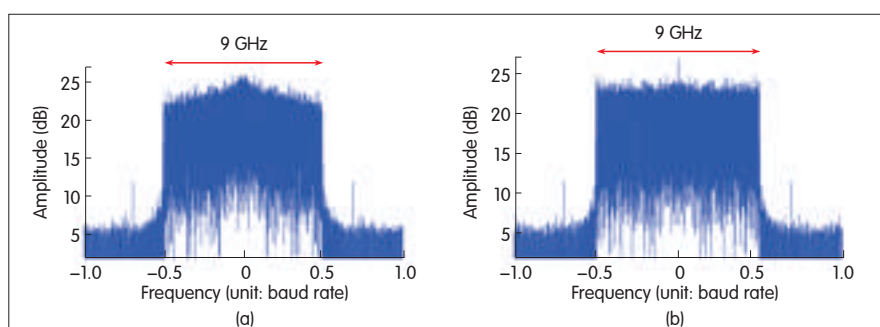


Figure 2. 450 Gb/s PDM-Nyquist 32-QAM transmitter.



▲ Figure 3. (a) Interpolated impulse response of the Nyquist filter and (b) the resulting eye diagram of the generated baseband 32-QAM signal.



▲ Figure 4. Measured relative amplitude spectra of 9 Gbaud Nyquist 32 QAM baseband electrical drive signals (after DAC) (a) without pre-equalization and (b) with pre-equalization.

ITU grid (Fig. 5).

3 Coherent Receiver Hardware and Algorithm

A DSP-enabled coherent receiver is used to detect and demodulate the received PDM-Nyquist-32 QAM signal. The polarization- and phase-diverse coherent receiver front-end consists of a polarization-diverse 90-degree hybrid, a tunable external cavity laser (ECL) with approximately 100 kHz line width that serves as the local oscillator (LO), and four balanced photodetectors. An optical tunable filter (OTF) with approximately 50 GHz -3 dB bandwidth is used to select the desired channel for detection. The subcarriers are selected by tuning the LO to within 200 MHz of their center frequencies. A four-channel real-time sampling scope with 50 GSa/s sample rate and 16 GHz analog bandwidth performs sampling and digitization (ADC), followed by post-transmission DSP of the captured data on a desktop computer.

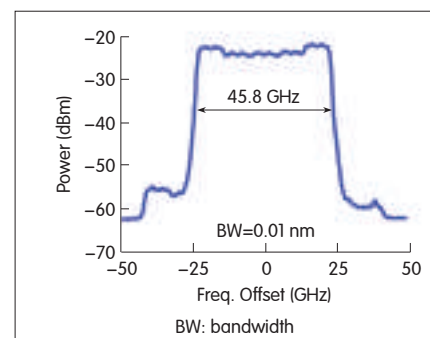
Fig. 6 shows the flow chart for the offline receiver DSP. After digitally compensating for sampling skews and hybrid phase errors in the front-end, and after anti-aliasing filtering, the 50 GSa/s signal is down-sampled to a rate double the symbol rate. Then, the bulk chromatic dispersion (CD) is compensated for using a fixed T/2-spaced finite impulse response (FIR) filter with 72 complex-value taps. In a

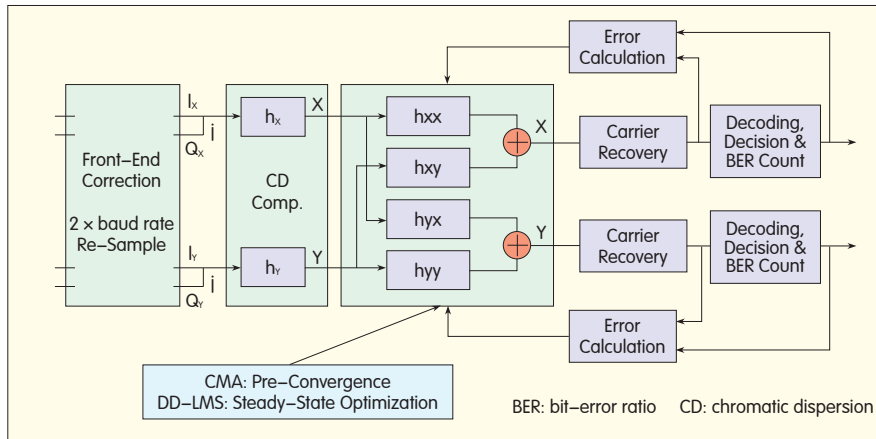
practical system, frequency-domain-based equalization is more efficient than time-domain-based equalization. Next, polarization recovery and residual CD compensation are simultaneously performed with four complex-valued, 51-tap, T/2-spaced adaptive FIR filters, optimized using a two-stage equalization strategy. The classic constant-modulus algorithm is used in the first stage for pre-convergence, and then a decision-directed least-mean-square algorithm is used for steady-state optimization.

The carrier frequency and phase are recovered after the initial equalization. The frequency offset between the LO and signal is estimated by using a constellation-assisted two-stage blind frequency search method [12]. The frequency offset is scanned at a step size of 10 MHz and 1 MHz, and the optimal frequency offset is the one that gives the minimum mean-square error. For each trial frequency, the carrier phase is recovered on a best-effort basis using a newly proposed hybrid blind-phase search (BPS) and maximum likelihood (ML) phase-estimation method [13]. Decisions made after phase estimation are then used as reference

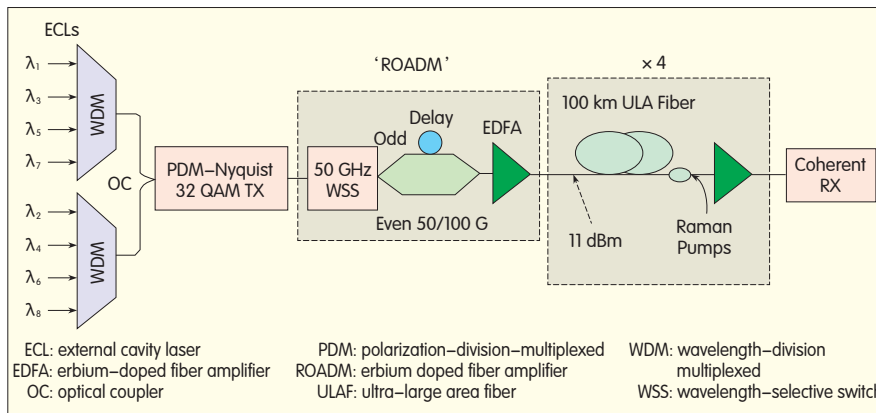
signals for mean-square error calculation. This frequency recovery method is applicable for any modulation format and only uses tens of symbols (96 are used in the experiments in section 3) to reliably recover the carrier frequency. The carrier phase is estimated using a two-stage method; that is, the carrier phase recovered from the previous symbol is used as an initial test-phase angle. The signal decided on after the initial test-phase angle is then used as a reference for a more accurate ML-based phase recovery using a feed-forward configuration [13]. For the first block of data, the initial phase angle is obtained using BPS [14]. To reduce the probability of cycle-slipping (no differential coding/encoding is used in the experiments in section 3), sliding-window-based symbol-by-symbol phase estimation is used. To calculate the bit-error ratio (BER), errors are counted for more than

Figure 5. ► Measured optical spectrum of the generated 450 Gb/s PDM-Nyquist 32-QAM signal consisting of five subcarriers.





▲ Figure 6. Post-transmission offline DSP flow chart.



▲ Figure 7. Experiment setup for 8 × 450 Gb/s over 400 km transmission.

1.2 × 10⁶ bits of information.

4 WDM Experiments

Two 450 Gb/s per-channel WDM transmission experiments using PDM-Nyquist-32 QAM were performed [10], [11]. In the first experiment, no optical pulse shaping was used to compensate for the filtering effects caused by the 50 GHz grid ROADMs. In the second experiment, a liquid-crystal-on-silicon (LCoS)-based flexible-bandwidth WSS was used as a broadband optical pulse shaper to mitigate the ROADMs filtering effects.

4.1 8 × 450 Gb/s over 400 km Without Optical Shaping

Fig. 7 shows the experiment setup for WDM transmission of 8×450 Gb/s PDM-Nyquist-32 QAM signals over 400 km. The eight 450 Gb/s C-band channels are based on odd (192.30–192.60 THz) and even (192.35–192.65 THz) sets of multiplexed, 100 GHz-spaced ECLs. These ECLs are combined using a 3 dB OC and are modulated in the 450 Gb/s PDM-Nyquist-32 QAM transmitter (Fig. 1). The measured optical spectrum of a single 450 Gb/s 32-QAM channel is shown in Fig. 5, and the eight-channel WDM spectrum prior to transmission is shown in Fig. 8.

Fig. 9 shows the back-to-back BER for a single subcarrier operating at 9 Gbauds, a single 450 Gb/s channel comprising five subcarriers, and one of the center channels of the 8×450 Gb/s WDM 50 GHz-spaced channels. The optical signal noise ratio (OSNR) for the single subcarrier in Fig. 9 is a scaled result obtained by multiplying the actual OSNR of the single subcarrier signal by five. No ROADMs filtering was used in these back-to-back measurements. Fig. 9 also shows the recovered Nyquist-32 QAM constellation diagram at an OSNR of 38.9 dB for a single 450 Gb/s channel. For comparison, a theoretical curve is included in Fig. 9. There is an approximately 6 dB implementation penalty at 2 × 10⁻³ BER. Because digital Nyquist pulse shaping is used, the OSNR penalty at 2 × 10⁻³ BER from interchannel WDM crosstalk is very small, even without narrow optical filtering. This is because the 450 Gb/s signal is well confined within a 45.8 GHz bandwidth. The OSNR penalty from intersubcarrier crosstalk is less than 1 dB. A portion of the intersubcarrier crosstalk originates from the out-of-band aliased spectral components from the electrical drive signals.

For WDM transmission, the eight 450 Gb/s signals pass through a 1×850 GHz-spaced WSS based on liquid-crystal technology in order to emulate the filtering by a ROADMs.

Odd and even channels are sent to separate WSS output ports for maximum filtering, and a relative delay of 175 symbols decorrelates the odd and even channels before they are recombined using a 3 dB OC. Filtering from the WSS passband is significant because the -3 dB bandwidth is 42.2 GHz, and the -6 dB bandwidth is 46.6 GHz (Fig. 10). The transmission line after the ROADMs consists of four 100 km spans of ULA fiber with, at 1550 nm, average Aeff of 135 μm², average attenuation of 0.179 dB/km, and average dispersion of 20.2 ps/nm/km. The span inputs are spliced to standard single-mode fiber jumpers, and a 1450/1550 nm WDM coupler is included for the counter-propagating Raman pumps at the span outputs. The span losses are 19.2, 19.6,

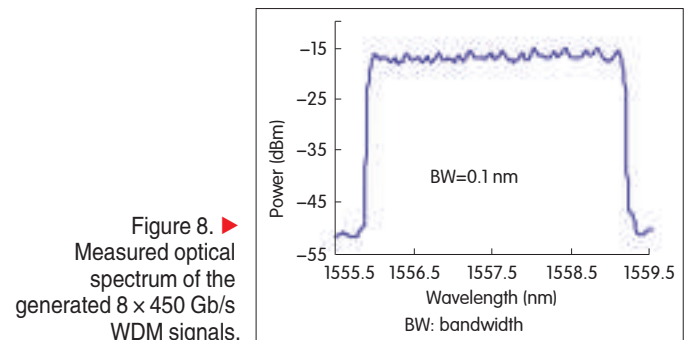
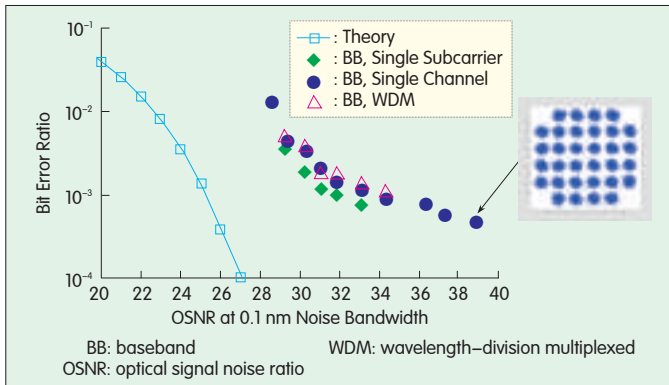
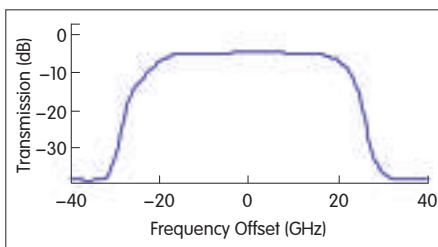


Figure 8. ► Measured optical spectrum of the generated 8 × 450 Gb/s WDM signals.



▲ Figure 9. Measured back-to-back performance under three different conditions.



◀ Figure 10. Power transmission of the 50 GHz-grid WSS used to emulate the ROADM.

19.2, and 18.9 dB. Hybrid Raman-EDFAs are used, with an on/off Raman gain of 11 dB per span from approximately 1450 nm pumps. Because of the gain-flattened EDFAs and the narrow total bandwidth (approximately 3 nm) of the eight 450 Gb/s channels, after 400 km the spectrum is flat to within 1 dB for a large range of span input powers.

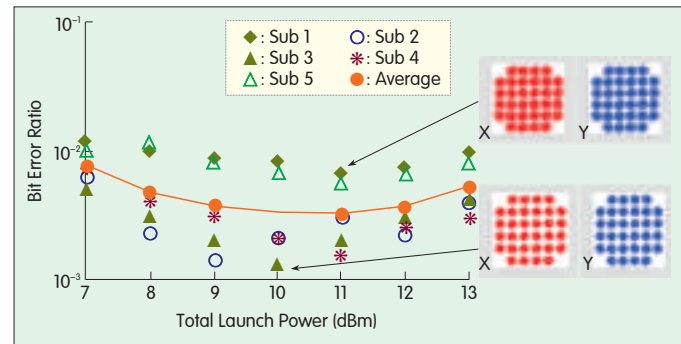
Fig. 11 and Fig. 12 show the results of the 8×450 Gb/s transmission experiment. The BERs of the five subcarriers of the center channel at 192.50 THz are measured because the total launch power to the spans is varied. From the average BER of the five subcarriers, the optimum launch power per span is 11 dBm, an average of 2 dBm per 450 Gb/s channel and -5 dBm per subcarrier (Fig. 11). At this launch power, the OSNR is 34 dB per 0.1 nm after the 400 km transmission. It is assumed that digital signals from all five subcarriers coexist on one silicon chip, and the FEC is encoded on a per-channel basis, not on a per-subcarrier basis. Thus, the net BER of the 450 Gb/s channel is the average BER of the subcarriers [15]. Fig. 12 shows the performance of each of the eight 450 Gb/s DWDM channels at the optimum 11 dBm total launch power. The average BER of the five subcarriers of all eight channels is better than 3.8×10^{-3} , which is lower than the 4.5×10^{-3} BER threshold for a 7% continuously interleaved BCH code. The inset in Fig. 12 shows the optical spectrum after 400 km, and spectral filtering by the WSS is evident.

4.2 5×450 Gb/s over 800 km with Optical Shaping

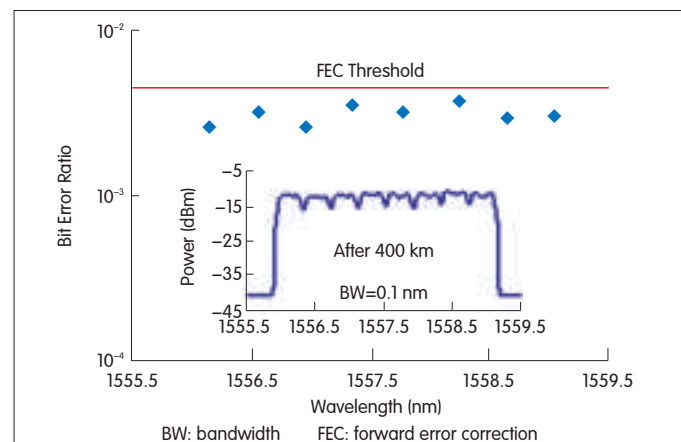
Fig. 13 shows the experiment setup for WDM transmission of 5×450 Gb/s PDM-Nyquist-32 QAM over 800 km. An LCoS-based dynamic, broadband optical spectral shaper with 1 GHz resolution is followed by a booster EDFA and is inserted before the 50 GHz grid ROADM. The optical spectral

shaper pre-compensates for the ROADM filtering. Pre-compensation results in enhanced interchannel WDM crosstalk because of the limited channel isolation of the 50 GHz WSS. Therefore, a 50/100G interleaver is used inside the ROADM emulator to combine the odd and even channels and further suppress interchannel WDM crosstalk. The recirculating loop contains the same four 100 km spans of ULA fiber with 11 dB on/off Raman gain, as previously described for the 400 km experiment. After two circulations (800 km), the spectrum of the five 450 Gb/s channels was flat to within 1 dB for span input powers ranging from 6 to 12 dBm. The optimal total launch power at the span inputs was 9 dBm.

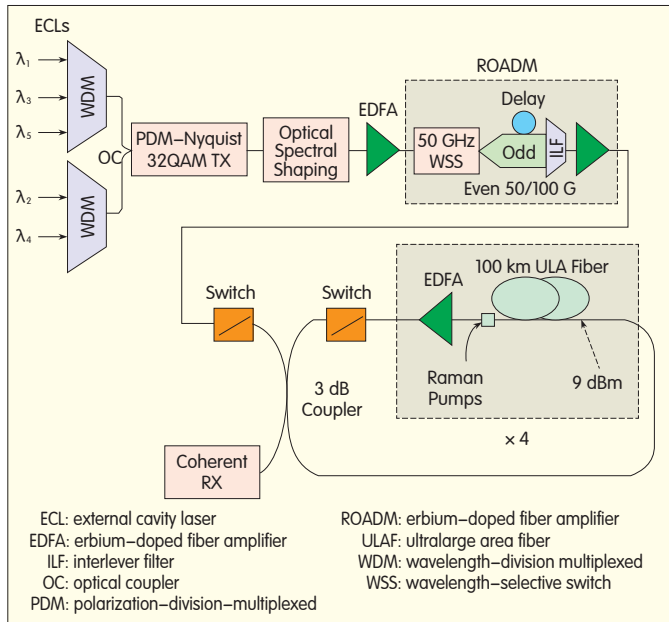
The optical spectra of a single 450 Gb/s 32-QAM channel before and after the 50 GHz ROADM are shown in Fig. 14(a) and (b), respectively. The thin lines show the spectra without optical spectral shaping. When the signal without optical spectral shaping passes through the 50 GHz ROADM, a significant amount of filtering occurs. The power loss due to filtering can be largely precompensated for by using broadband optical spectral shaping, shown by the thick lines in Fig. 14(a) and (b). The optical spectra of the five 450 Gb/s



▲ Figure 11. BER for the five subcarriers of the center DWDM channel at 192.50 THz after 4×100 km transmission for a range of total launch powers into the fiber spans.



▲ Figure 12. Average BER of the five subcarriers of all eight channels after 400 km transmission with optimum launch power. The inset shows the optical spectrum after 400 km.



▲ Figure 13. Setup for 8 × 450 Gb/s transmission over 800 km.

DWDM signals that have been spectrally shaped prior to and after the ROADM are shown in Fig. 14(c). The filtering effects of all five channels have been largely precompensated for.

Fig. 15 shows the measured OSNR sensitivity for the 450 Gb/s PDM-Nyquist-32 QAM signal for a single channel without ROADM optical filtering (the back-to-back case with no optical shaping), with ROADM filtering and optical spectral shaping, and with ROADM filtering but without optical shaping. For comparison, a theoretical OSNR sensitivity curve is also shown in Fig. 15. Compared with the previous experiment, back-to-back sensitivity is improved by about 2 dB at 2×10^{-3} BER. This improvement is achieved mainly by improving bias optimization for the two IQ modulators. With ROADM filtering, optical spectral shaping improves OSNR sensitivity by more than 2 dB at 2×10^{-3} BER.

Fig. 16 shows the optical spectrum after 800 km transmission. The measured OSNR is 31 dB per 0.1 nm. Fig. 17 shows the measured BER of all five WDM channels at the optimal total launch power of 9 dBm (2 dBm per channel). The inset in Fig. 17 shows the measured BER for the center channel located at 192.5 THz as the total launch power into the spans is varied. The BER of all five channels is better than 3.8×10^{-3} , and the worst subcarrier BER is 4.3×10^{-3} , both of which are lower than the 4.5×10^{-3} BER threshold for a 7% continuously interleaved BCH code [16].

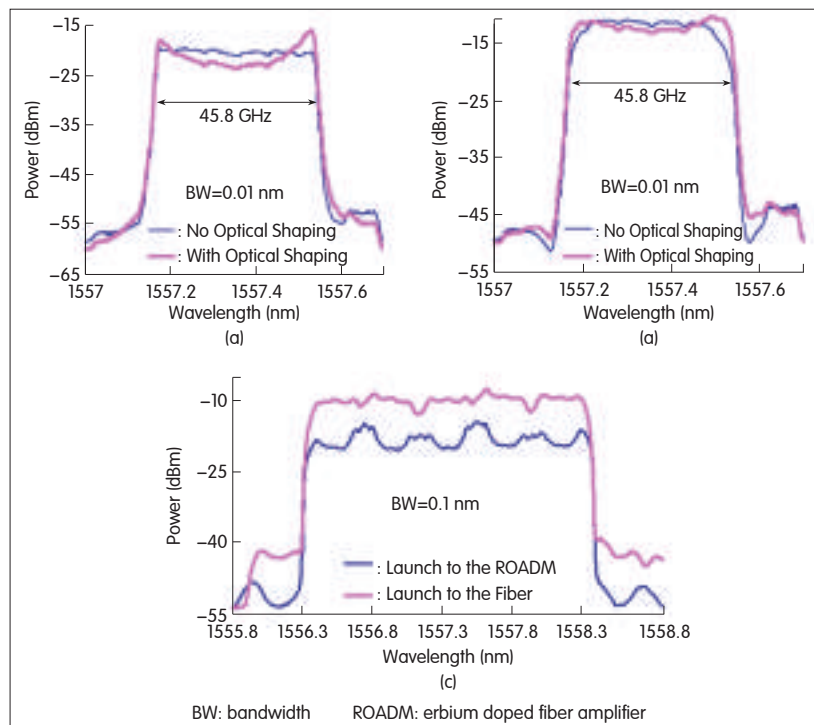
5 Conclusion

This paper describes two high-SE 8.4 b/s/Hz 400G transmission experiments. These experiments

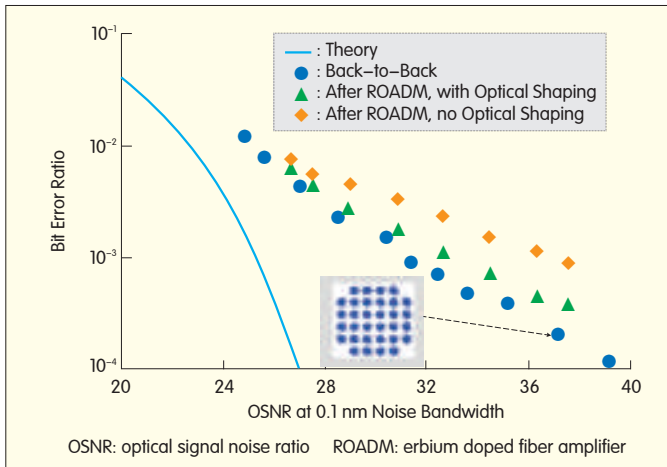
show for the first time that 400 Gb/s per channel WDM signals can be transmitted up to 800 Km (eight 100 km spans) over the conventional 50 GHz ITU-T grid and passing through one 50 GHz grid ROADM. These results are achieved by using a spectrally efficient high-order modulation format, that is, Nyquist-shaped PDM-32 QAM, as well as pre- and post-transmission digital equalization. Low-nonlinearity fiber and low-noise Raman amplification can also be used to address the reduced nonlinear and noise tolerance of the high-order modulation format.

To overcome the bandwidth limitation of the available DACs, a frequency-locked five-subcarrier generation method with high sideband suppression is used to create the 450 Gb/s PDM-Nyquist-32 QAM signals. By using five frequency-locked subcarriers and near ideal Nyquist pulse shaping, the 450 Gb/s spectrum has a signal spectral width of about 45.8 GHz, well within the 50 GHz channel spacing. Using multiple subcarriers (with Nyquist pulse shaping) within each channel allows all-optical subwavelength grooming, which may be useful for future 400 Gb/s and ultrahigh-speed systems.

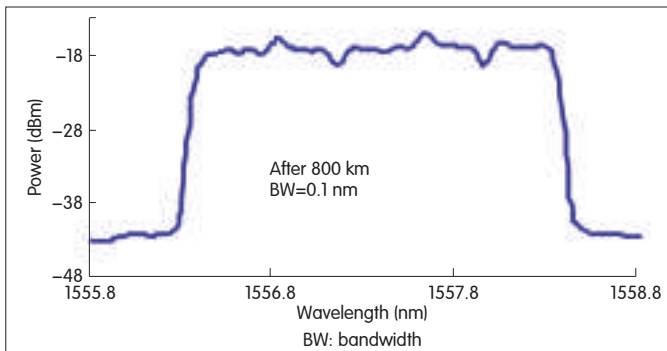
Another key enabling technology is LcoS-based broadband optical spectral shaping. This spectral-shaping technique can be used to mitigate the narrow ROADM filtering effects. An optical spectral shaper could be designed within each ROADM to compensate for ROADM filtering effects in a distributed manner. Distributed ROADM filtering compensation has some advantages over transmitter-side pre-equalization or receiver-side post-equalization



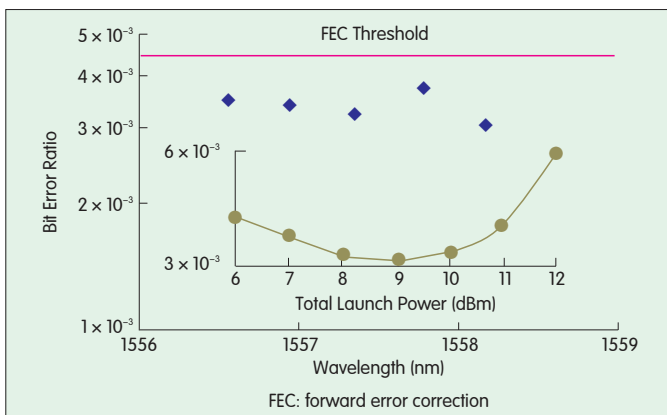
▲ Figure 14. (a) Optical spectra for a single channel with and without optical spectral shaping; (b) before and after the ROADM, and (c) the spectra of the five DWDM signals with optical spectral shaping before and after the ROADM (launch to the fiber).



▲ Figure 15. OSNR sensitivity for the generated 450 Gb/s signal.



▲ Figure 16. Measured optical spectrum after 800 km transmission.



▲ Figure 17. Measured BER of the five 450 Gb/s DWDM channels after 800 km transmission. The inset shows measured BER for the center DWDM channel versus total launch power for all five 450 Gb/s channels.

because, unlike transmitter-side pre-equalization, distributed compensation does not require more launch power into the fiber. Therefore, it does not increase fiber nonlinearity. Distributed compensation also does not increase noise components, unlike receiver-side post-equalization. A drawback of distributed compensation is the need for extra optical amplification to compensate for the loss caused by the

optical spectral shaper.

References

- [1] M. Camera, B. E. Olsson, and G. Bruno, "Beyond 100 Gbit/s: System implications towards 400G and 1T," in *Proc. ECOC 2010 Symp. Toward 1 Tb/s*, Torino, Italy, paper Th10G1.
- [2] P. J. Winzer, A. H. Gnauck, S. Chandrasekhar, S. Draving, J. Evangelista, and B. Zhu, "Generation and 1,200-km transmission of 448 Gb/s ETDM 56-Gbaud PDM 16QAM using a single I/Q modulator," in *Proc. ECOC 2010 Symp. Toward 1 Tb/s*, Torino, Italy, paper PDP 2.2.
- [3] J. Yu, X. Zhou, M. F. Huang, D. Qian, P. N. Ji, "400 Gb/s (4 × 100 Gb/s) orthogonal PDM-RZ-QPSK DWDM Signal Transmission over 1040 km SMF-28," *Optics Express*, vol. 17, no. 20, pp. 17928–17933, 2009.
- [4] X. Liu, S. Chandrasekhar, B. Zhu, A. H. Gnauck, and D. W. Peckham, "Transmission of a 448 Gb/s reduced-guard-interval CO-OFDM signal with a 60 GHz optical bandwidth over 2000 km of ULAF and five 80 GHz Grid ROADMs," in *Proc. OFC/NFOEC 2010*, San Diego, CA, paper PDP C2.
- [5] S. Chandrasekhar, X. Liu, B. Zhu, and D. W. Peckham, "Transmission of a 1.2 Tb/s 24-carrier no-guard-interval coherent OFDM superchannel over 7200 km of ultra-large-area fiber," in *Proc. ECOC 2009*, Vienna, Austria, paper PDP 2.6.
- [6] A. H. Gnauck, P. J. Winzer, S. Chandrasekhar, X. Liu, B. Zhu, and D. W. Peckham, "10 × 224 Gb/s WDM transmission of 28 Gbaud PDM 16QAM on a 50 GHz grid over 1,200 km of fiber," in *Proc. OFC/NFOEC 2010*, San Diego, CA, paper PDP B8.
- [7] Y.-K. Huang, E. Ip, M.-F. Huang, B. Zhu, P. N. Ji, Y. Shao, D. W. Peckham, R. Lingle, Jr., Y. Aono, T. Tajima, and T. Wang, "10 × 456 Gb/s DP-16QAM Transmission over 8 × 100 km of ULAF using Coherent Detection with a 30 GHz Analog-to-Digital Converter," in *Proc. OEC 2010*, Sapporo, Japan, paper PDP 3.
- [8] X. Liu, S. Chandrasekhar, P. J. Winzer, B. Zhu, D. W. Peckham, S. Draving, J. Evangelista, N. Hoffman, C. J. Young, Y. H. Kwon, and E. S. Nam, "3 × 485-Gb/s WDM Transmission over 4800 km of ULAF and 12 × 100-GHz WSSs Using CO-OFDM and Single Coherent Detection with 80-GS/s ADCs" in *Proc. OFC/NFOEC 2011*, Los Angeles, CA, paper JThA37.
- [9] H. Takahashi, K. Takeshima, I. Morita, and H. Tanaka, "400 Gbit/s Optical OFDM Transmission over 80 km in 50 GHz Frequency Grid," in *Proc. ECOC 2010*, Torino, Italy, paper Tu.3.C.1.
- [10] X. Zhou, L. E. Nelson, P. Magill, R. Issac, B. Zhu, D. W. Peckham, P. Borel, and K. Carlson, "8 × 450 Gb/s, 50 GHz-spaced, PDM-32QAM transmission over 400 km and one 50 GHz grid ROADMs," in *Proc. OFC/NFOEC 2011*, Los Angeles, CA, paper PDP B3.
- [11] X. Zhou, L. E. Nelson, P. Magill, R. Issac, B. Zhu, D. W. Peckham, P. Borel, and K. Carlson, "800 km transmission of 5 × 450-Gb/s PDM-32QAM on the 50 GHz grid using electrical and optical spectral shaping," in *Proc. ECOC 2011*, Geneva, Switzerland, paper We.8.B.2.
- [12] X. Zhou, J. Yu, M. F. Huang, Y. Shao, T. Wang, L. Nelson, P. D. Magill, M. Birk, P. I. Borel, D. W. Peckham and R. Lingle, "64 Tb/s, 8 b/s/Hz, PDM-36QAM transmission over 320 km using both pre- and post-transmission digital signal processing," *J. Lightwave Technol.*, vol. 29, no. 4, pp. 571–577, Feb. 2011.
- [13] X. Zhou, "An improved feed-forward carrier recovery algorithm for coherent receiver with M-QAM modulation format," *IEEE Photonics Technol. Lett.*, vol. 22, no. 14, pp. 1051–1053, 2010.
- [14] T. Pfau, S. Hoffmann, and R. Noé, "Hardware-efficient coherent digital receiver concept with feed-forward carrier recovery for M-QAM constellations," *J. Lightwave Technol.*, vol. 27, no. 8, pp. 989–999, Apr. 2009.
- [15] M. Tomizawa and Y. Yamabayashi, "Parallel FEC code in high-speed optical transmission systems," *Electronics Lett.*, vol. 35, no. 16, pp. 1367–1368, 1999.
- [16] F. Chang, K. Onohara and T. Mizuoichi, "Forward error correction for 100G Transport Networks," *IEEE Commun. Mag.*, vol. 48, no. 3, pp. 48–55, 2010.

Manuscript received: November 29, 2011

Biography

Xiang Zhou received his PhD degree in electrical engineering from Beijing University of Posts and Telecommunications in 1999. From 1999 to 2001, he was a research fellow at Nanyang Technological University, Singapore. He conducted research on optical CDMA and wideband Raman amplification. Since October 2001, he has been a senior member of the technical staff at AT&T Labs-Research, working on aspects of long-haul optical transmission and photonic networking technologies. His areas of interest include Raman amplification, polarization-related impairments, optical power transient control, advanced modulation formats, and DSP at 100 Gb/s and beyond. He has authored or co-authored more than 100 peer-reviewed journals and conference publications. He holds 28 patents in the US and is the associate editor of *Optics Express*. He is member of the OSA and a senior member of IEEE.

Greater than 200 Gb/s Transmission Using Direct-Detection Optical OFDM Superchannel

Wei-Ren Peng, Itsuro Morita, Hidenori Takahashi, and Takehiro Tsuritani

(KDDI R&D Laboratories Inc., Fujimino-shi, Saitama 356-8502, Japan)

Abstract

In this paper, we propose direct-detection optical orthogonal frequency division multiplexing superchannel (DDO-OFDM-S) and optical multiband receiving method (OMBR) to support a greater than 200 Gb/s data rate and longer distance for direct-detection systems. For the new OMBR, we discuss the optimum carrier-to-sideband power ratio (CSPR) in the cases of back-to-back and post transmission. We derive the analytical form for CSPR and theoretically verify it. A low overhead training method for estimating I/Q imbalance is also introduced in order to improve performance and maintain high system throughput. The experiment results show that these proposals enable an unprecedented data rate of 214 Gb/s (190 Gb/s without overhead) per wavelength over an unprecedented distance of 720 km SSMF in greater than 100 Gb/s DDO-OFDM systems.

Keywords

orthogonal frequency division multiplexing (OFDM); direct detection; multiband transmission

1 Introduction

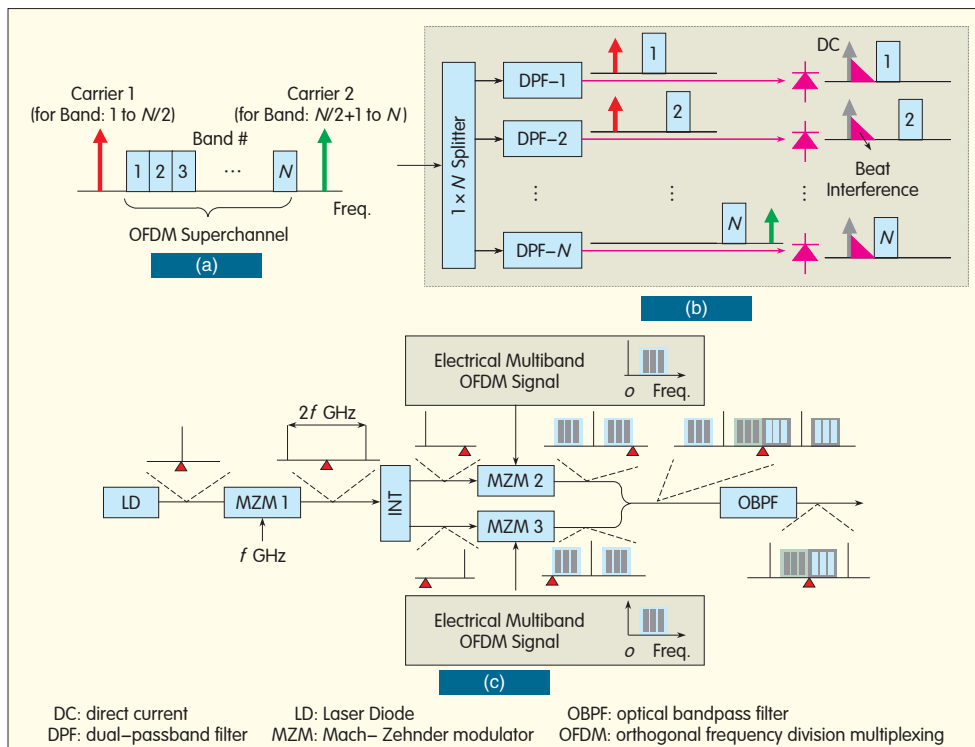
For years, papers have been written on direct-detection transmission because it uses a very simple receiver that usually only requires photodiodes for detection [1], [2]. Most research on direct-detection has been focused only on the dispersion-managed links, and not until recently has electronic equalization has been introduced into optical communications to compensate for chromatic dispersion (CD) [3]. Electronic equalization has ushered in a new era of dispersion-unmanaged links that do not require dispersion map design and offer a lower-nonlinear transmission medium [4]. Joint direct-detection receiving and dispersion-unmanaged links is an interesting topic related to implementation cost.

To incorporate direct-detection in a dispersion-unmanaged link, single-carrier transmission with pre-equalization [3] and multicarrier transmission with post-equalization [5] have been proposed. The pre-equalization in [3] could work very well to counter CD; however, when used in dynamic routing networks, it requires the link information (the exact information of the accumulated CD) beforehand via complex signaling methods [6], [7]. The proposal in [5], commonly referred to as direct-detection

optical orthogonal frequency division multiplexing (DDO-OFDM), automatically estimates and compensates for CD at the receiver, without any link information. Therefore, DDO-OFDM could easily support both point-to-point and dynamic routing networks. DDO-OFDM should be repositioned because of its transparency to different kinds of network architectures.

Even with these advantages, conventional DDO-OFDM has limited transmission performance that might restrict its application only to short-reach networks [8], [9]. Among the many reported DDO-OFDM systems, a self-coherent OFDM [10] system extends both the capacity and reach of conventional DDO-OFDM and significantly increases the receiver's complexity, which diminishes the inherent benefits of using direct detection. Therefore, a laudable goal for a DDO-OFDM system is to improve transmission with simple solutions while keeping the cost of direct detection low.

In this paper, we propose DDO-OFDM superchannel (DDO-OFDM-S) with a simple optical multiband receiving (OMBR) [11], [12] method. DDO-OFDM-S has dual carriers at both sides to reduce receiver bandwidth, and OMBR detects the signal band-by-band to relax the sampling rate of the receiver and to reduce the frequency gap between carriers and superchannel for high spectral usage. In this paper, an optimum carrier-to-sideband power ratio (CSPR)



▲ Figure 1. (a) Direct-detection optical OFDM superchannel (DDO-OFDM-S), (b) optical multiband receiving (OMBR), and (c) a possible transmitter solution to implement the proposed DD-O-OFDM-S with single laser source.

is discussed for back-to-back and post transmission, and its analytical form is theoretically derived and verified. We also describe a low-overhead I/Q imbalance estimation approach that can be used to adaptively compensate for I/Q imbalances while maintaining the system's high capacity. In greater than 100 Gb/s DDO-OFDM systems, the proposed DDO-OFDM-S enables an unprecedented 214 Gb/s data rate per wavelength over 720 km standard single-mode fiber (SSMF) with EDAF-only amplification.

In section 2, the working principles of DDO-OFDM-S and OMBR are given, and a solution for generating DDO-OFDM-S with only one wavelength is proposed. In section 3, a CSPR for the new OMBR is suggested that is optimized for minimum required optical signal-to-noise ratio (OSNR) in back-to-back transmission (conventional definition) and better signal performance after transmission. An analytical form of optimum CSPR in back-to-back transmission is also derived. In section 4, we describe the setup for our 16-QAM, 214 Gb/s DDO-OFDM-S transmission experiment. In section 5, we propose a low-overhead I/Q imbalance training method and introduce a zero-overhead phase noise compensator. In section 6, numerical results for CSPR and experiment results for transmissions are presented. Section 7 concludes the paper.

2 Principle of Operation

The proposed DDO-OFDM-S can be better understood

from its spectrum (Fig. 1a). The spectrum consists of one OFDM superchannel at the center and two optical carriers, inserted at both sides, with a frequency gap, N_g , from the superchannel. In this paper, the superchannel and carriers are assumed to be aligned in the same polarization, and only this polarization is used for transmission. The use of dual-polarization transmission, that is, polarization division multiplexing (PDM), would be a powerful means of doubling the channel capacity; however, in this paper, we conduct a preliminary investigation into single-polarization transmission. The superchannel itself comprises closely spaced OFDM bands [13], denoted 1, 2, 3, ..., N in Fig. 1(a). The surrounding two carriers, 1 and 2 in Fig. 1(b), demodulate the half that is lower-frequency bands and the other half that is upper-frequency bands. Carrier 1 is responsible for bands 1 to $N/2$, and carrier 2 is responsible for bands $N/2+1$ to N . When N is an

odd number, that is, when odd-numbered OFDM bands are transmitted, the central band should have similar spectral distances from both carriers so that it can be demodulated by either of them.

To demodulate a DDO-OFDM-S, we use the proposed OMBR at the receiver to process the signal in a band-by-band manner, as shown in Fig. 1(b). An optical coupler splits the received signal into N parallel paths, each of which consists of one dual-passband filter (DPF) that has its two passbands targeting the desired OFDM band and one of the carriers. Therefore, in the m th path in Fig. 1b (top), only the m th OFDM band, and carrier p (where $p = 1$ if $m \leq N/2$ or $p = 2$ if $m > N/2$) reach the photodiode for detection. After the photodiode, the converted electrical current in each path contains the desired passband signal and unwanted (signal-signal) beat interference near the direct current (DC) frequency. After down-conversion, the desired baseband signal in each path is lowpass filtered, digitally-sampled, and processed with a regular OFDM equalizer. In this way, all the bands in the superchannel can be demodulated with a bank of cheaper low-bandwidth receivers.

Compared with a conventional DDO-OFDM signal [14], our DDO-OFDM-S has unique characteristics: It uses dual carriers, and the width of the frequency gap is smaller. Dual carriers are used to reduce the bandwidth of the receivers. If only carrier 1 were used with the superchannel, the carrier would have to cover all the transmitted bands from 1 to N at the receivers. This means the photodiode in N th branch

would need to have an ultrahigh bandwidth to cover the frequency between carrier 1 and band N . Therefore, the dual-carrier arrangement, in which each carrier takes care of 50% of the bands in the superchannel, can relax the high-bandwidth requirement of the receiver by a factor of two. The smaller gap width is created by optical pre-filtering before detection. In conventional systems, the required gap width has to be at least equal to the sideband bandwidth, and this leads to poor spectral efficiency. With OMBR, the DPF only allows one desired band and the carrier to be detected, so the required gap width can be reduced to a size similar to that of a single band. The gap width does not need to be the same as that of the whole superchannel, and this improves spectral efficiency.

The proposed DDO-OFDM-S and OMBR has the following advantages:

- better spectral efficiency because of the reduced gap width
- relaxed bandwidth requirement for receivers because of the dual-carrier arrangement and band-by-band demodulation
- simple receiver architecture because only one filter is used for each band

However, an issue to be considered is how to generate the DDO-OFDM-S. There might be a number of options, including multiple lasers, to generate the DDO-OFDM-S. Fig. 1(c) shows the transmitter architecture of a possible solution that uses only one laser. The output from the laser is first split into two tones by an intensity modulator. These tones are later coupled into the upper and lower branches using one wavelength interleaver. The two tones are individually modulated with electrical multiband OFDM signals [15] using two intensity modulators that are biased slightly away from the null. This processing results in a double-sideband OFDM signal with a carrier on each branch. An optical coupler combines the signals from the two branches (that form the DDO-OFDM-S) with two residual sidebands from the carriers (Fig. 1c, insets). A following optical bandpass filter (OBPF) with appropriate bandwidth removes the residual sidebands. Finally, the output signal of the filter has a central superchannel surrounded by two optical carriers, which is the proposed DDO-OFDM-S.

3 Carrier to Sideband Power Ratio

In this section, we focus on CSPR for DDO-OFDM-S. CSPR is the power of both carriers over the power of the superchannel, that is, $\text{CSPR} = 2P_c/(NP_s)$, where P_c is the power of each carrier and P_s is the power of each signal band. Typically, there is an optimum CSPR, denoted CSPR_{MRO} . The CSPR_{MRO} demands the minimum required OSNR at a target bit error rate (BER), usually $\text{BER} = 1\text{e-}3$. This optimum CSPR has been theoretically and experimentally proven to be approximately 0 dB for conventional DDO-OFDM systems [14], [16]. However, CSPR_{MRO} itself is a function of the optical filters [17], [18], and thus its value is subject to change when a different receiving technique, such as the proposed OMBR,

is used. In the following, we derive the analytical form of CSPR_{MRO} specifically for our DDO-OFDM-S signal and OMBR.

A higher electrical signal-to-noise ratio (ESNR) usually leads to a lower BER; there is a one-to-one relationship between BER and ESNR. Therefore, the minimum required OSNR for a target BER becomes the minimum required OSNR for a target ESNR. Before CSPR_{MRO} can be derived, the relationship between ESNR and OSNR has to be determined. We assume the DDO-OFDM-S contains an N -band superchannel at the center with two carriers at both sides and that both the passbands of the DPF have a brick-wall shape and have the same bandwidths, B_o . These bandwidths should be equal to or slightly greater than the bandwidth of one OFDM band, B_s . The received ESNR for each desired band can be expressed as a function of OSNR:

$$\text{ESNR} = \frac{P_c P_s}{(P_c + P_s)N_o B_o + (N_o B_o)^2} \approx \frac{\text{CSPR}}{(N \times \text{CSPR} + 2)(\text{CSPR} + 1)} \times \frac{B_N}{B_o} \times \text{OSNR} \quad (1)$$

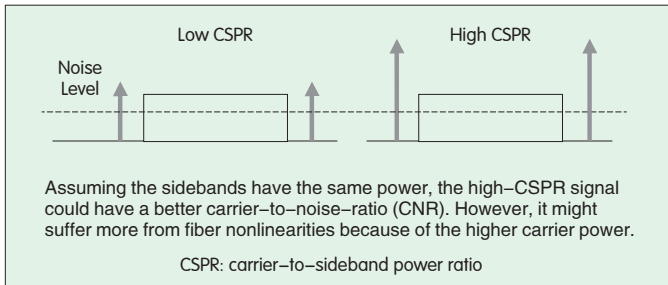
where $\text{OSNR} = (2P_c + NP_s) / (N_o B_o)$, N_o is the noise spectral density, and B_N is the noise bandwidth. With Cauchy-Schwarz's inequality, the upper-bound of the ESNR and the lower bound of the OSNR can be obtained from (1):

$$\text{ESNR} \leq \frac{(\sqrt{2} + \sqrt{N})^2}{\text{CSPR}} \times \frac{B_N}{B_o} \times \text{OSNR} \quad (2)$$

$$\text{OSNR} \geq \frac{\text{CSPR}}{(\sqrt{2} + \sqrt{N})^2} \times \frac{B_o}{B_N} \times \text{ESNR} \quad (3)$$

Therefore, the minimum OSNR given an ESNR (or a target BER) can be achieved with $\text{CSPR}_{\text{MRO}} = \sqrt{2/N}$, which implies that CSPR_{MRO} is proportional to the inverse of the square root of the band number. For instance, considering a nine-band DDO-OFDM-S, CSPR_{MRO} should be $\sqrt{2/9} \approx 0.47 \approx -3$ dB. In section 6, we verify this theory.

We have derived the CSPR optimized according to minimum required OSNR in back-to-back transmission where only linear noise is considered. Because a lower required OSNR typically offers a larger noise margin and longer transmission distance, CSPR_{MRO} is defined in terms of longer distance. However, for DDO-OFDM systems, we propose a new transmission strategy that uses a higher CSPR, other than CSPR_{MRO} , to achieve a longer distance even though it may not meet the minimum required OSNR constraint. This idea comes from a CO-OFDM system where the carrier is offered by the local oscillator (LO) that has a high carrier-to-noise ratio (CNR). This concept is shown in Fig. 2 for two cases — lower CSPR (CSPR_L) and even higher CSPR (CSPR_H) — where sideband powers are assumed to be equal. If both signals are transmitted over the same link with the same amount of accumulated ASE noise, the signal with CSPR_H has a higher CNR than the signal with CSPR_L (Fig. 2). However, the benefit of high CNR comes at the price of larger fiber nonlinearities caused by the use of higher carrier power (under the same sideband power constraint). Therefore, the



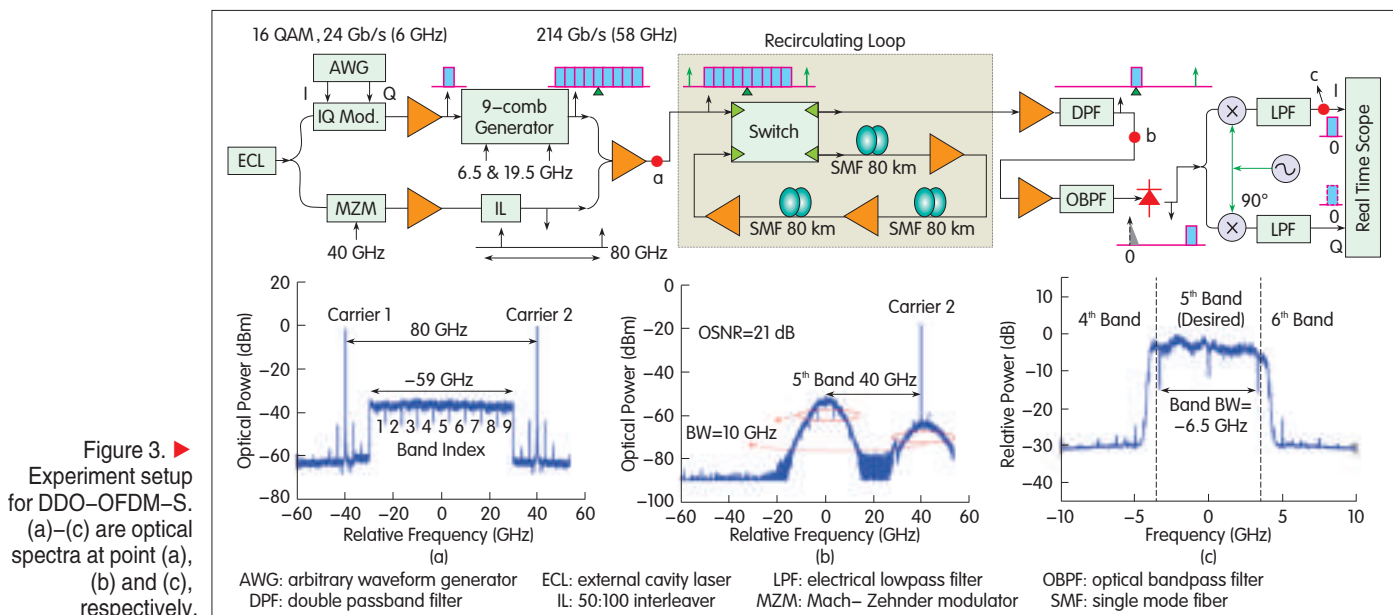
▲ Figure 2. Spectra of low-CSPR and high-CSPR DDO-OFDM-S.

optimum CSPR should trade off the better CNR for lower fiber nonlinearities, which may not be equal to CSPR_{MRO} . In section 6, we show that the optimum CSPR, defined in terms of longer distance, is greater than CSPR_{MRO} when both the linear noise and fiber nonlinearities are taken into account.

4 Experiment Setup

Fig. 3 shows the experiment setup for the 214 Gb/s DDO-OFDM-S system. A 100 kHz line width external cavity laser (ECL) operated at approximately 192.76 THz is the transmitter light source, and this is followed by a 1×2 optical splitter that equally couples the laser output into the upper and lower branches. In the upper branch, the light is first modulated along with the electrical OFDM signal via an optical in-phase/quadrature (I/Q) modulator. The OFDM waveform is generated offline with MATLAB and comprises continuous frames, each of which contains two training symbols and 150 data symbols. In each OFDM symbol, binary data is randomly generated, mapped to 16-QAM format, and modulated onto 152 data subcarriers, which are later zero-padded to a fast Fourier transform (FFT) size of 256. A pilot is not used in order to minimize overhead. After inverse FFT (IFFT), a length of ten-point cyclic prefix (CP) is attached

to each OFDM symbol, creating a total of 266 points per symbol. This OFDM waveform is then loaded into an arbitrary waveform generator (AWG) that has its real and imaginary outputs driving the optical I/Q modulator with a 10 GSa/s sampling rate. Hence, the raw data rate of the output signal is 23.75 Gb/s and occupies a bandwidth of approximately 6 GHz. The output of the I/Q modulator is sent to a nine-comb generator, which cascades two intensity modulators driven by 6.5 GHz and 19.5 GHz sine wave signals in order to emulate a nine-band superchannel [6]. The output superchannel occupies a bandwidth of approximately 58 GHz (with band spacing of 6.5 GHz) and has an aggregate data rate of 214 Gb/s. After removing the training, CP, and 7% FEC overhead, the net data rate is 190 Gb/s. An optical coupler follows to combine this superchannel with the signal from the lower branch. In the lower branch, the light is first modulated with a 40 GHz electrical sine wave signal with one intensity modulator biased at the null. This results in two strong carriers spaced at 80 GHz as well as one residual carrier at the laser frequency. A 50:100 GHz wavelength interleaver (IL) is used to suppress this residual carrier, leaving only the two 80 GHz-spaced carriers. The two 80 GHz-spaced carriers are then combined with the 58 GHz superchannel, forming the DDO-OFDM-S spectrum, as shown in Fig. 3 insets (a), (b) and (c). The frequency gap between the carrier and the superchannel is approximately 11 GHz at both sides. The spectral distance between carriers (80 GHz here) can be further reduced at the expense of sacrificing the edge bands because of beat interference. In the experiments, this 80 GHz spacing is appropriate for balancing spectrum usage and receiving performance. At the transmitter output, the DDO-OFDM-S is sent to a re-circulating fiber loop that comprises three EDFAs and three spools of 80 km SSMF. After 720 km transmission, the signal is fed to the optical multiband receiver. At the receiver, the signal is pre-amplified with an EDFA and then passed through a DPF that has two



10 GHz passbands targeting one of the carriers and the desired signal band. Because of the power loss of DPF, an EDFA and an 80 GHz optical bandpass filter (OBPF) raise the signal power before the signal enters the photodiode. In this experiment, the first to fifth bands are demodulated with the left carrier (carrier 1), and the sixth to ninth bands are demodulated with the right carrier (carrier 2). After the photodiode, the desired band is down-converted to its baseband via an electrical I/Q demodulator. This I/Q demodulator comprises one splitter, one synthesizer, one power amplifier, two mixers, and two electrical low-pass filters (3 dB bandwidth = 3.7 GHz). The I/Q output signals are recorded by a real-time scope operated at 20 GSa/s. Synchronization, cyclic prefix removal, channel estimation, and equalization are performed offline using MATLAB. The BER is evaluated with an error-counting method, and for each BER analysis, 2 million sampling points are considered.

Fig. 3(a) shows the optical spectra of the transmitter output (resolution = 20 MHz); Fig. 3(b) shows the DPF output (targeting the 5th band); and Fig. 3(c) shows the digital spectrum of the 5th band after the real-time scope (where the band index is defined in Fig. 3a). In Fig. 3(c), the power ripples on top of the signal come from the power reflection, at the RF ports, of the mixers in the I/Q demodulator. These ripples are a function of frequency and introduce some OSNR penalty to the system, that is, implementation penalty.

Here, we highlight several points about the experiment setup. First, at the transmitter, the length of the optical paths between the sideband and carrier branches should be controlled so that they are as similar as possible. A significant difference in length would lead to strong phase incoherency between the carrier and sideband, and this would cause dramatic phase noise after the photodiode. In this experiment, we not only equalized the optical lengths of the carrier and sideband paths, but we also used a zero-overhead phase noise compensator at the receiver (section 5). Second, 6.5 GHz and 19.5 GHz frequencies for the 9-comb generator are phase-locked in order to maintain the orthogonality and reduce linear crosstalk between the adjacent bands [13]. However, because of the sufficiently large band spacing, the performance is hardly degraded, even if we remove the phase locking between the synthesizers. Third, to obtain a broadband bandwidth, we assemble the I/Q demodulator with discrete components rather than use an integrated I/Q mixer, which would introduce I/Q imbalances into the signal. This would mean I/Q imbalance estimation and compensation would be critically necessary in our system. In section 5, we introduce a low-overhead I/Q imbalance estimation approach that uses only two training symbols, that is, the same symbols for channel estimation.

5 Low-Overhead Signal Processing Methods

To compensate for I/Q imbalance and phase noise, we propose a low-overhead training method to estimate I/Q imbalance and introduce a zero-overhead decision-directed

phase noise compensator (DD-PNC) [19].

5.1 I/Q Imbalance Training Method

For each frame, the proposed method uses only two consecutive training symbols (the same as those for channel estimation). The first symbol is randomly generated, and the second symbol simply copies the first one and inverts the signs of the data symbols on negative subcarriers. The two consecutive training symbols are denoted $[a_k, b_{-k}]$ and $[a_k, -b_{-k}]$, where a_k and b_{-k} are the data symbols on k th and $-k$ th subcarriers, respectively, and k is a positive integer ranging from 1 to $N_d/2$, with N_d being the data subcarrier number. At the receiver, the received training symbols disrupted by I/Q imbalances are denoted $[p_k, q_{-k}]$ and $[r_k, l_{-k}]$ for the first and second training symbols, respectively. Then, the input and output symbols can be expressed in 2×2 mutually coupled matrixes [20]:

$$\begin{bmatrix} p_k \\ q_{-k} \end{bmatrix} = \begin{bmatrix} H_{11} & H_{12} \\ H_{21} & H_{22} \end{bmatrix} \begin{bmatrix} a_k \\ b_{-k} \end{bmatrix} \quad (4)$$

and

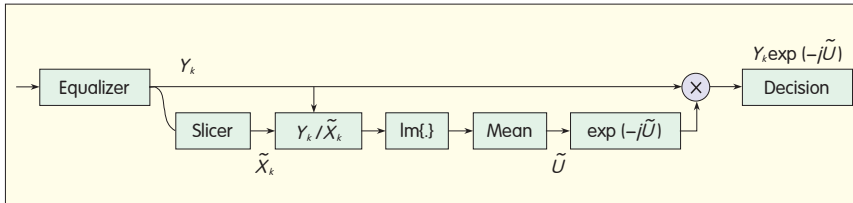
$$\begin{bmatrix} r_k \\ l_{-k} \end{bmatrix} = \begin{bmatrix} H_{11} & H_{12} \\ H_{21} & H_{22} \end{bmatrix} \begin{bmatrix} a_k \\ -b_{-k} \end{bmatrix} \quad (5)$$

The four elements in the 2×2 channel matrix \mathbf{H} (H_{ij} , which should contain both the channel response and I/Q imbalances) can be easily derived with $H_{11} = (p_k + r_k)/(2a_k)$, $H_{12} = (p_k - r_k)/(2b_{-k})$, $H_{21} = (q_{-k} + l_{-k})/(2a_k)$, and $H_{22} = (q_{-k} - l_{-k})/(2b_{-k})$, for which the estimation accuracy can be further improved using the intrachannel frequency-domain average method [15].

After obtaining the four elements, the inverse matrix of \mathbf{H} can be derived for subsequent equalization. Because this technique uses the same training symbols (two per frame) for both channel and I/Q imbalance estimation, the training overhead is relatively lower than that in [20].

This data-aided adaptive approach is simple, has low overhead, and is a better way to estimate and compensate for I/Q imbalance. In the offline I/Q estimation proposal in [21], the I/Q imbalance in each individual receiver needs to be customized; however, using this new approach, the I/Q imbalances of each individual receiver can be handled adaptively using only two training symbols (which can be the same ones for channel estimation). In particular, the adaptive method is suitable for lab experiments where I/Q imbalances vary over time because of the replacement of any component or the slow bias drift of the optical modulators.

Here we briefly discuss the computational complexity of this I/Q imbalance estimation method. At the training stage, to obtain the channel matrix for all subcarriers, $2N_d$ complex multiplications are needed for each OFDM symbol, and the matrix inversions for equalization need an additional $3N_d$ multiplications. Therefore, at the training stage, $5N_d$ multiplications are needed, which is $4N_d$ more multiplications than in regular channel estimation. At the equalization stage, two subcarriers are jointly equalized via a 2×2 matrix so that the number of multiplications for each OFD symbol is $2N_d$,



▲ Figure 4. Zero-overhead decision-directed phase noise compensator (DD-PNC).

which is N_d more multiplications than in regular channel equalization (using a one-tap equalizer).

5.2 Phase Noise Compensation Method

DD-PNC uses all tentative decisions of the OFDM symbol being processed to estimate its common phase error (CPE). The CPE is later used for de-rotating the phase of the OFDM symbol [19]. If noise and I/Q imbalance are ignored, the received data symbol on the k th subcarrier can be simply written as $Y_k = UX_k$, where X_k and Y_k are the transmitted and equalized symbols (with no channel effect) on k th subcarrier, respectively, and U is the CPE, which is assumed to be independent of the subcarrier index k . Assuming CPE is not significant and the tentative decisions are statistically reliable, U can be estimated with $U \approx (1/N_d) \text{Im}\{\sum_{k=1}^{N_d} Y_k / X_k\}$, where x_k is the tentative decision of the equalized symbol, Y_k , N_d is the number of data subcarriers, and $\text{Im}\{x\}$ takes the real part of x . The output for final decision will be $Y_k \exp(-jU)$, and in this output, CPE should have been greatly mitigated. Fig. 4 [19] shows the corresponding processing. A more detailed discussion on, for example, computational complexity, can be found in [19].

The signal processing sequence is: 1) synchronization, 2) CP removal and FFT, 3) joint channel and I/Q imbalance estimation using proposed training symbols, 4) estimation enhancement using intra-symbol frequency domain averaging method [22], 5) joint channel and I/Q imbalance equalization with the inverse channel matrix, and 6) CPE mitigation using DD-PNC.

6 Results and Discussions

6.1 Numerical Results for Optimum CSPP Transmission

The detailed system parameters in the simulations are almost the same as those in the experiment setup in section 4, except for CSPP, which is herein treated as a variable in order to determine its effect on system performance. The transmission link comprises nine spans of 80 km SSMF (720 km in total). The fiber loss, dispersion, and dispersion slope are 0.2 dB/km, 16 ps/(nm.km), and 0.02 ps/(nm².km), respectively. The effective area is 80 μm^2 , and the nonlinearity coefficient is 1.3 ($\text{W}^{-1}\text{km}^{-1}$). The EDFA's noise figure is set to 6 dB, and the EDFA's gain is set to 16 dB, which fully compensates for the fiber loss of each span. Each passband profile of DPF has a second-order Gaussian shape and a 3 dB bandwidth of 10 GHz. The signal quality is expressed as Q^2 , obtained from the BER in (6):

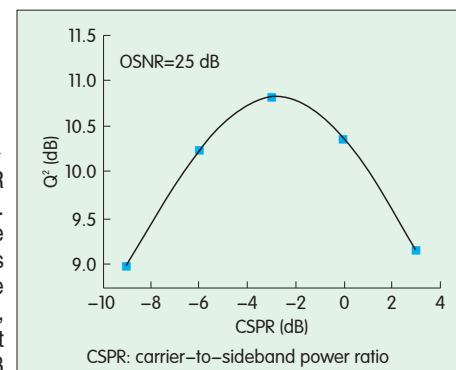
$$Q^2[\text{dB}] = 20 \times \log_{10}(\sqrt{2} \text{erfcinv}\{2 \times \text{BER}\}), \quad (6)$$

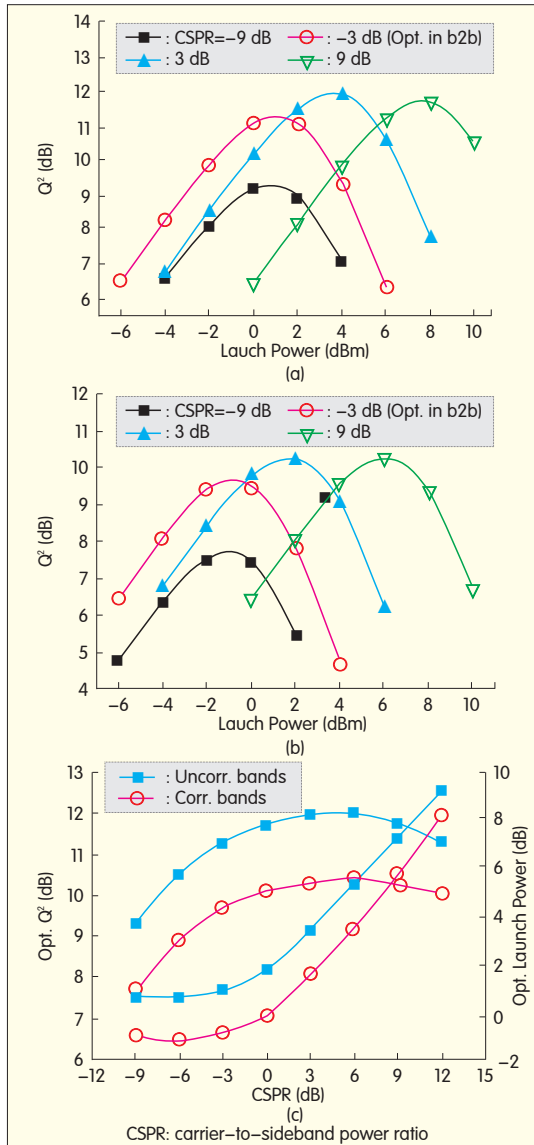
where $\text{erfcinv}\{x\}$ gives the inverse complementary error function value of x , and BER is derived with the direct-error counting method. OSNR is defined with 0.1 nm noise bandwidth.

Fig. 5 shows the Q^2 factor versus CSPP in back-to-back transmission in which OSNR = 25 dB. The optimum CSPP in back-to-back transmission is approximately -3 dB, which conforms to our theoretical prediction that $\text{CSPP}_{\text{MRO}} = \sqrt{2/9} \approx -3$ dB and verifies our analytical analysis in section 3. This result differs from the previously derived optimum CSPP of 0 dB [12], [14] because of the OMBR receiving method used in our system. However, this new CSPP_{MRO} is obtained in back-to-back transmission without nonlinear distortions being taken into account. Therefore, it is necessary to study the CSPP_{MRO} again after transmission.

In Fig. 6(a) and (b), we show Q^2 as a function of launch power with different CSPPs. In Fig. 6(a), the data sets for each band are mutually independent, that is, uncorrelated at the transmitter; however, in Fig. 6(b), the data sets for all the bands are the same, that is, strongly correlated at the transmitter. The correlated data sets might lead to strong nonlinear phase noise at the beginning of the link [13], which is exactly the case in our experiment. Therefore, the case with correlated data sets has to be compared with the case with uncorrelated data sets. Because the curves in Fig. 6(a) and (b) are similar with respect to CSPPs, we simply focus on the results shown in Fig. 6(a). With a lower CSPP, for example, -9 dB, the optimum launch power is similar to that of $\text{CSPP}_{\text{MRO}} = -3$ dB, and the optimum Q^2 has approximately 2 dB degradation relative to that of CSPP_{MRO} . With a higher CSPP, for example, 3 dB, the optimum launch power increases by approximately 3 dB. The raised power comes mostly from the carriers. More importantly, there is an approximately 0.7 dB improvement over CSPP_{MRO} by using 3 dB CSPP. This implies that with 3 dB CSPP, the improved CNR can bring more benefits than the negative four-wave mixing (FWM) terms caused by the high power of the carriers. A further increase in CSPP to 9 dB would result in a slight sacrifice of signal quality but drastically enhance optimum launch power. Fig. 6(c) shows the optimum Q^2 factors and

Figure 5. Q^2 factor vs. CSPP with OSNR = 25 dB. Except for CSPP, the simulation parameters are all similar to those of the 16-QAM, 214 Gb/s experiment in section 3.

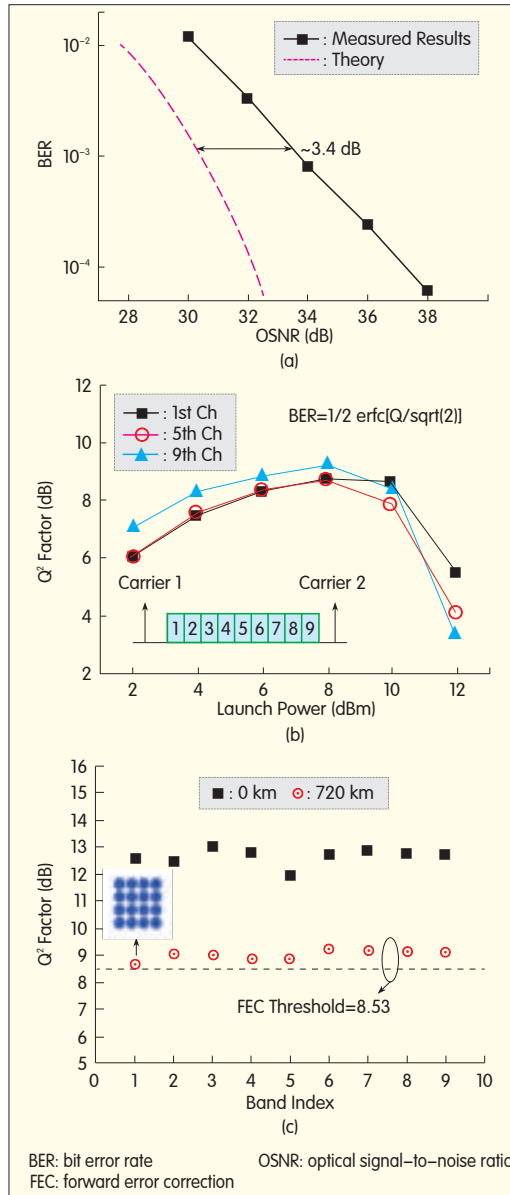




▲ Figure 6. (a) Q^2 factor vs. launch power after 9×80 km SSMF with CFSR = -9, -3, 3, and 9 dB when nine data bands are mutually independent (uncorrelated). (b) Same as (a); however, data bands are equal at the transmitter (highly-correlated), and (c) Optimum Q^2 factor and optimum launch power vs. CFSR with uncorrelated and correlated data bands.

launch power as a function of CFSR (with 3 dB resolution). These functions can be used to determine the optimum CFSR (after transmission). Again, in Fig. 6(c), the curves for uncorrelated and correlated data sets are shown for comparison. From Fig. 6(c), we can draw the following conclusions:

- The optimum CFSRs after transmission are similar for both cases and are approximately 3 dB to 6 dB, which is higher than the CFSR_{MRO} of -3 dB in back-to-back transmission. This means that higher carrier power, that is, higher CFSR, is encouraged in order to overcome linear noise



▲ Figure 7. Experimental demonstration for 16-QAM, 214 Gb/s DDO-OFDM-S: (a) OSNR tolerance, with 0 km SSMF, (b) Q^2 vs. launch power with 720 km SSMF, and (c) Q^2 vs. band index with 720 km SSMF.

back-to-back only.

6.2 Experiment Results for DDO-OFDM-S Transmission

The band index is defined in the inset of Fig. 3(b). OSNR is measured with 1.6 nm (200 GHz) resolution that covers the whole signal's bandwidth and is later scaled to the presented value with 0.1 nm resolution. Q^2 factors (in decibels) are derived from the BER in (6).

Fig. 7 shows the experiment results for 16-QAM, 214 Gb/s DDO-OFDM-S. To achieve longer distance, we use the new high-CFSR strategy in section 3. In this experiment, we use approximately 10 dB CFSR (optimum after 720 km

and nonlinear distortions.

- At the optimum CFSRs, the uncorrelated bands give approximately the uncorrelated bands outperform the correlated bands by approximately 1.7 dB, which suggests that the distance achieved in our experiment could be further extended if uncorrelated data bands were used.

- Even though higher CFSR might lead to better performance, the corresponding optimum launch power is relatively high. In a WDM system, a suitable CFSR should be determined, taking into consideration both the channel number and the maximum output power of fiber amplifiers.

6.1.1 Discussion

The CFSR that demands the minimum required OSNR, which can be derived easily in back-to-back, has long been considered the optimum value for DDO-OFDM systems. However, we have shown that even greater CFSR, with higher optimum launch power, can further improve the signal quality after transmission. The optimum CFSR should be the value that promises better signal quality after transmission rather than in

transmission) to achieve a higher CNR after transmission. Fig. 7(a) shows the OSNR tolerance in back-to-back. The dashed line is the theoretical limit and is shown for comparison. The required OSNR for a BER of $1e-3$ is approximately 33.8 dB due to the use of 10 dB CSPR. Compared with the theoretical limit, the implementation penalty is approximately 3.4 dB. This implementation penalty can be attributed to imperfections in the components, power ripples (see section 4), residual phase noise, and linear crosstalk between bands. With 10 dB CSPR, the required OSNR for the superchannel alone could be approximately 23.4 dB. This OSNR is similar to that for a coherent system [23], where the required OSNR at BER = $1e-3$ is approximately 23.4 dB with 224 Gb/s and would become approximately 23.2 dB after scaled to 214 Gb/s. The signal quality in our DDO-OFDM-S system is almost dominated by the sideband because of the high applied CSPR.

Fig. 7(b) shows the measured Q^2 as a function of the fiber launch power after 720 km transmission. The presented curves correspond to the first, fifth, and ninth bands, respectively. The optimum power is approximately 8 dBm, which provides the best performance under the limitations of ASE and nonlinear distortion. If we consider the high CSPR of approximately 10 dB, the launch power for the superchannel alone is only about -2.4 dBm.

Fig. 7(c) shows measured Q^2 as a function of the band index in back-to-back and after 720 km SSMF. The optimum launch power of 8 dBm is applied. In back-to-back, the fifth band shows the worst performance ($Q^2 \approx 12$ dB) caused by insufficient bandwidth of the receiver's components; the other bands have Q^2 factors greater than 12 dB. After transmission, the worst performance occurs on the first band, which still yields a Q^2 higher than the 7% FEC threshold of 8.53 dB [24], and the Q^2 factor variation between the different bands is reduced because it is the noise and nonlinear distortion, not the receiver's bandwidth, that dominate performance.

6.2.1 Discussion

Using our proposals, in the 16-QAM experiment, we generated and demodulated the record capacity per wavelength (214 Gb/s) for DDO-OFDM systems. We also achieved a record distance of 720 km SSMF for greater than 100 Gb/s DDO-OFDM systems. Because of the strong nonlinear phase noise at the beginning of the link, a longer distance might be possible by using uncorrelated data bands, for example, approximately 2 dB Q^2 difference, as shown in Fig. 6(c). To reach 720 km transmission, we used a high CSPR of approximately 10 dB, that is, high carrier power, to provide better CNR after transmission. Such a high carrier power would induce strong FWM terms at both sides out of the carriers, which in our experiment, could be removed through moderate optical filtering. In a WDM system, these FWM terms would possibly overlap with the adjacent channels and become in-band nonlinear noise that results in some penalty. Therefore, in WDM systems, CSPR should be carefully controlled and optimized so that strong FWM terms are not involved. Another simple way to avoid FWM is to use

polarization interleaving for WDM neighboring channels. However, this would eliminate the possibility of using PDM.

7 Conclusion

We have proposed DDO-OFDM-S and OMBR, a high-capacity long-reach solution for DDO-OFDM systems. We have discussed optimum CSPR in back-to-back and after transmission and found that a higher carrier power is needed to improve performance after transmission. We have also derived the analytical form of back-to-back CSPR and verified its correctness using numerical simulations. To maintain the system's high throughput, we have proposed a low-overhead I/Q imbalance estimation method. Our experiment shows that in greater than 1 Gb/s DDO-OFDM systems, the proposed DDO-OFDM-S enables unprecedented capacity of 214 Gb/s per wavelength over an unprecedented distance of 720 km SSMF.

References

- [1] P. J. Winzer, G. Raybon, S. Haoyu, A. Adamiecki, S. Corteselli, A. H. Gnauck, D. A. Fishman, C. R. Doerr, S. Chandrasekhar, L. L. Buhl, T. J. Xia, G. Wellbrock, W. Lee, B. Basch, T. Kawanishi, K. Higuma, and Y. Painchaud, "100 Gbit/s DQPSK transmission: from laboratory experiments to field trials," *IEEE J. Lightwav. Technol.*, vol. 26, no. 20, pp. 3388–3402, Oct. 2008.
- [2] M. Daikoku, I. Morita, H. Taga, H. Tanaka, T. Kawanishi, T. Sakamoto, T. Miyazaki, T. Fujita, "100-Gbit/s DQPSK transmission experiment without OTDM for 100G Ethernet transport," *IEEE J. Lightwav. Technol.*, vol. 25, no. 1, pp. 139–145, Jan. 2007.
- [3] R. I. Killey, P. M. Watts, M. Glick, and P. Bayvel, "Electronic dispersion compensation by signal pre-distortion," in *Optical Fiber Commun. Conf. (OFC '06)*, Anaheim, CA, Paper OWB3.
- [4] S. L. Jansen, I. Morita, K. Forzesh, S. Randel, D. van den Borne, H. Tankak, "Optical OFDM, a hype or is it for real?" *Proc. European Conf. Optical Commun. (ECOC '08)*, Brussels, Paper Mo3E3.
- [5] A. J. Lowery, L. Du, and J. Armstrong, "Orthogonal frequency division multiplexing for adaptive dispersion compensation in long haul WDM systems," *Proc. Optical Fiber Commun. Conf. (OFC '06)*, Anaheim, CA, paper PDP39, 2006.
- [6] S. Seno, E. Horiuchi, T. Sugihara, T. Uesugi, T. Ichikawa, Y. Baba, and T. Mizuochoi, "A GMPLS-based path establishment experiment with tunable dispersion compensation over in-field fibers," *Proc. European Conf. Optical Commun. (ECOC 2010)*, Turin, Italy, paper Tu.4.B.3.
- [7] M. Yagi, S. Tanaka, S. Satomi, S. Ryu, K. Okamura, M. Aoyagi and S. Asano, "Field trial of GMPLS triple plane integration for 40 Gbit/s dynamically reconfigurable wavelength path network," *Electron. Lett.*, vol. 41, pp. 492–494, Apr. 2005.
- [8] A. Amin, H. Takahashi, I. Morita, and H. Tanaka, "100-Gbps direct-detection OFDM transmission on independent polarization tributaries," *IEEE Photon. Technol. Lett.*, vol. 22, no. 7, pp. 468–470, 2010.
- [9] D. Qian, N. Cvijetic, J. Hu, and T. Wang, "108 Gbit/s OFDMA-PON with polarization multiplexing and direct detection," *IEEE J. Lightwave Technol.*, vol. 28, no. 4, pp. 484–493, Feb. 2010.
- [10] B. J. C. Schmidt, Z. Zan, L. B. Du and A. J. Lowery, "120 Gbit/s over 500-km using single-band polarization-multiplexed self-coherent optical OFDM," *IEEE J. Lightwav. Technol.*, vol. 28, no. 4, pp. 328–335, Feb. 2010.
- [11] W.-R. Peng, H. Takahashi, I. Morita, and H. Tanaka, "Transmission of a 214-Gbit/s single-polarization direct-detection optical OFDM superchannel over 720-km standard single mode fiber with EDFA-only amplification," *Proc. Optical Fiber Commun. Conf. (ECOC 2010)*, Torino, Italy, Paper PDP 2.5.
- [12] W.-R. Peng, H. Takahashi, I. Morita, and H. Tanaka, "117-Gbit/s optical OFDM super-channel transmission over 1200-km SSMF using direct detection and EDFA-only amplification," presented at *Optical Fiber Commun. Conf. (OFC 2011)*, Los Angeles, CA, Paper OThX1.
- [13] Q. Yang, Y. Tang, Y. Ma, W. Shieh, "Experimental demonstration and numerical simulation of 107-Gbit/s high spectral efficiency coherent optical OFDM," *J. Lightwav. Technol.*, vol. 27, no. 3, pp. 168–176, Feb. 2009.
- [14] A. J. Lowery, L. B. Du, and J. Armstrong, "Performance of optical OFDM in ultra-long haul WDM lightwave systems," *J. Lightwav. Technol.*, vol. 25, no. 1, pp. 131–138, Jan. 2007.
- [15] S. L. Jansen, I. Morita, and H. Tanaka, "10 × 121.9 Gbit/s PDM-OFDM transmission with 2-b/s/Hz spectral efficiency over 1,000 km of SSMF," *Proc. Optical Fiber Commun. Conf. (OFC 2008)*, San Diego, CA, paper PDP2, 2008.

➔To P. 29

Spatial Mode-Division Multiplexing for High-Speed Optical Coherent Detection Systems

William Shieh¹, An Li¹, Abdullah Al Amin¹, Xi Chen¹, Simin Chen¹, and Guanjun Gao^{1,2}

(1. Department of Electrical and Electronic Engineering, The University of Melbourne, 3010 Parkville, VIC, Australia;

2. State Key Laboratory of Information Photonics and Optical Communications (Beijing), Beijing University of Posts and Telecommunications, 100876, China)

Abstract

Spatial mode-division multiplexing is emerging as a potential solution to further increasing optical fiber capacity and spectral efficiency. We report a dual-mode, dual-polarization transmission method based on mode-selective excitation and detection over a two-mode fiber. In particular, we present 107 Gbit/s coherent optical OFDM (CO-OFDM) transmission over a 4.5 km two-mode fiber using LP_{01} and LP_{11} modes in which mode separation is performed optically.

Keywords

coherent communications; few-mode fiber; mode converter; fiber optic components

1 Introduction

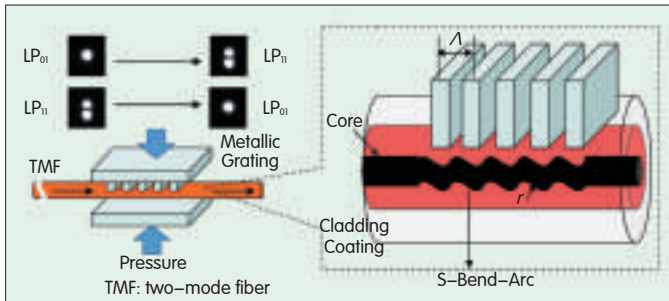
The fast advance of high-speed optical transport systems has spurred the use of dense wavelength division multiplexing (DWDM), polarization multiplexing, coherent detection, and multilevel modulation schemes in optical fiber transmission. However, higher required optical signal-to-noise ratio (OSNR) causes higher transmission power per channel, and this may give rise to impairments caused by fiber nonlinearity [1], [2]. Recently, there has been increasing interest in few-mode fiber (FMF) as the next-generation fiber for achieving capacity beyond that of standard single-mode fiber (SSMF) [3]–[7]. One of the advantages of FMF, for example, two-mode fiber (TMF), is that spacial modes are multiplexed, and this doubles or triples fiber capacity without exponentially increasing SNR (as is the case with SSMF fiber) [4]–[7]. By adding another degree of freedom (here, the spatial modes with respect to the wavelength, polarization, and higher-order modulation), the information data coding can also be made more efficient [8]. Compared with previous approaches based on conventional multimode fiber (MMF) [9]–[12], FMF has better mode selectivity and can more easily manage mode impairments. Recently, a number of groups have mode-division multiplexed (MDM) LP_{01} and LP_{11} modes [4], [5], two degenerate LP_{11} modes ($LP_{11a} + LP_{11b}$) [6], and even all three modes ($LP_{01} + LP_{11a} + LP_{11b}$) [7] over FMFs or TMFs. The

advance to FMF transmission requires new research on topics ranging from device to system level, including TMF design, TMF-compatible component design, and TMF transmission. In mode-multiplexed transmission systems, mode-selective components are critical. All the mode-selective devices proposed in [4] and [5] fall into two main categories: free-space based and fiber based. The former uses phase masks that are based on liquid crystal on silicon (LCoS) spatial light modulator (SLM) [6] or specially fabricated glass plate [7]. Free-space components are often bulky whereas a fiber-based one is compact and can be easily integrated. The coupler proposed in [13] could be a promising solution for future MDM systems even though fabrication of the coupler involves sophisticated fiber etching, fusion, and tapering. A simple, tunable mechanical pressure-induced long-period fiber grating (LPFG) is an efficient mode converter [14]. An LPFG mode converter has been applied in a 2×10 Gb/s non-return-to-zero (NRZ) MDM system [5] and a 107 Gb/s mode-multiplexed OFDM transmission system [4]. We propose 107 Gbit/s coherent optical OFDM (CO-OFDM) transmission over a 4.5 km TMF using LP_{01} and LP_{11} modes in which mode separation is performed optically.

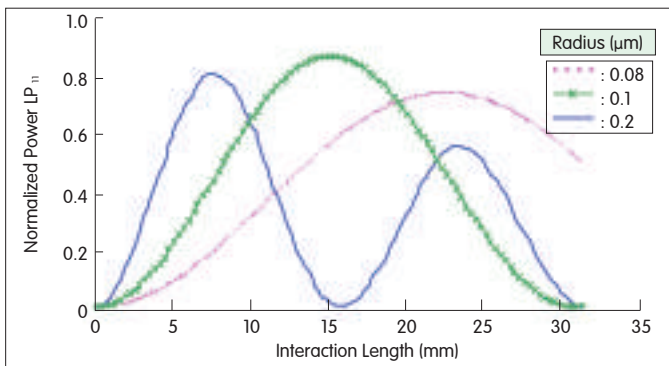
2 Mode-Selective Component Design

2.1 LPFG-Based Mode Converter

The main purpose of the mode converter is to convert



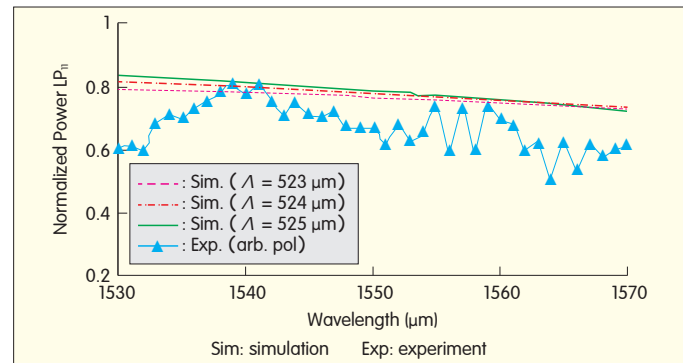
▲ Figure 1. Schematic of an LPFG-based LP_{01}/LP_{11} mode converter. The groove pitch, Λ , and pressure can be optimized for a certain wavelength or conversion ratio. The deformation of the fiber core is assumed to be an s-bend shape with radius r .



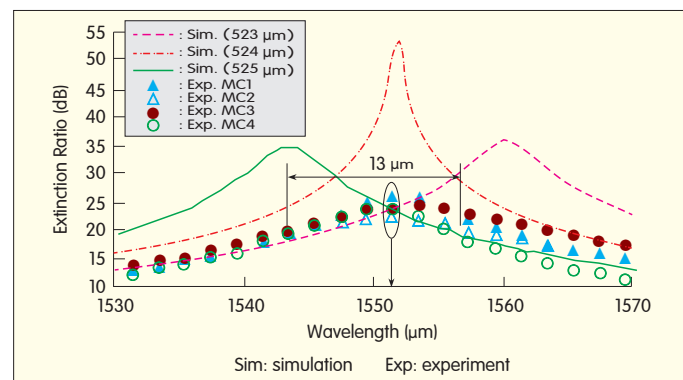
▲ Figure 2. Normalized power of LP_{11} versus effective coupling length for an LPFG-based mode converter with grating pitch $\Lambda = 524 \mu\text{m}$ at wavelength $\lambda = 1550 \text{ nm}$. The three curves correspond to core deformation radii of 0.08, 0.1 and $0.2 \mu\text{m}$.

optical signals from LP_{01} to LP_{11} and vice versa. There are various methods for performing this conversion on an FMF or TMF. These include microbending [14], periodic mechanical pressure [15], and refractive index modulation induced by lasers [16]. Resonant coupling occurs when the grating pitch, Λ , equals the beating length, given by $L_B = 2\pi/(\beta_{01} - \beta_{11})$, where β_{01} and β_{11} are the propagation constants of LP_{01} and LP_{11} [17]. Fig. 1 shows the physical design of the mode converter. The TMF we use is a 4.5 km germanium-doped step-index fiber with a core diameter of $11.9 \mu\text{m}$ and nominal refractive index step, Δn , of 5.4×10^{-3} . The LP_{11} mode cutoff wavelength is 2323 nm , and the loss is 0.26 dB/km . The modal group delay is 3.0 ns/km , and the mode beat length, L_B , is approximately $524 \mu\text{m}$. The large differential group delay (DGD) results in very small modal mixing in our TMF because of the large mismatch of modal effective indices [18]. To simplify our analysis, we only consider the deformation effect in a mode converter. The simulation is based on the beam propagation method [19], and the core deformation is assumed to have an s-bend shape (Fig. 1). The coupling efficiency depends on the coupling length, and core deformations are defined for s-bend arc radii of 0.08, 0.1, and $0.2 \mu\text{m}$ (Fig. 2). The optimum coupling length is inversely proportional to the core deformation radius r , and for a $0.2 \mu\text{m}$ deformation, the optimum coupling length is 8.1 mm , which

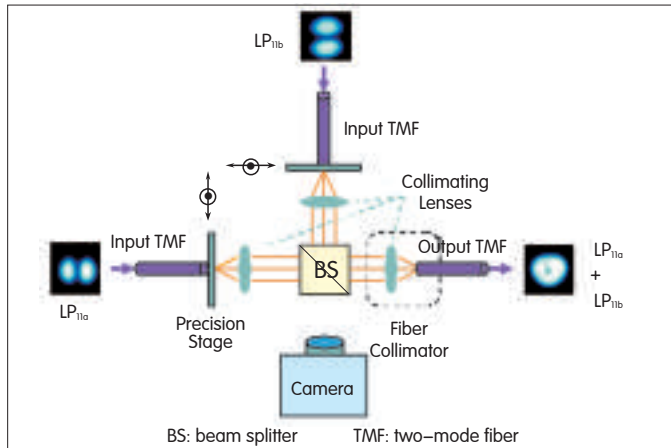
means our mode converter is very compact. Fig. 3 shows the wavelength dependence of coupling efficiency at a coupling length of 8.1 mm (approximately 15.5 ridges) and core deformation of $0.2 \mu\text{m}$. Fig. 4 shows the extinction ratio (ER) versus wavelength using the same coupling length and core deformation. The ER is the power ratio between LP_{11} and LP_{01} after mode conversion. Theoretically, the ER can be very high, around 1550 nm , and remain above 20 dB for a wavelength range of more than 10 nm . In light of the simulation result, we fabricated four metal gratings with 20 evenly spaced grooves on one polished surface. The groove pitch is given by $\Lambda_0 = 510 \pm 5 \mu\text{m}$. To fabricate the four mode converters, first we place a 0.9 mm jacketed TMF onto an aluminum slab with tape. The TMF and grating are then mounted between a three-axis stage and L-shaped steel. The angle between grating and fiber, and the applied pressure can be controlled by the stage and position of the fiber. The angle between the grating and fiber determines the effective pitch, given by $\Lambda = \Lambda_0/\sin\theta$, where Λ_0 is the original pitch of the grating, and θ is the angle. After appropriate adjustment of the stage and position of the fiber, the maximum coupling ratio and ER for all mode converters occurs at around 1550 nm . From the measured and simulated ERs shown in Fig. 4, the ER can be maintained beyond 20 dB for a 13 nm wavelength range. The best ERs are $26.8, 22.8, 24.6$, and 24.3 dB and occur at 1551 nm for mode converters



▲ Figure 3. Normalized power of LP_{11} versus wavelength for an LPFGG-based mode converter with core deformation radius of $0.2 \mu\text{m}$.



▲ Figure 4. Extinction ratio versus wavelength for an LPFG-based MC with core deformation radius of $0.2 \mu\text{m}$.



▲ Figure 5. Schematic of a free-space mode combiner. The precision stages have freedom of two axes, x and y . The light propagation axis is denoted Z . The beams are collimated before entering the BS to minimize divergence and distortion.

one to four.

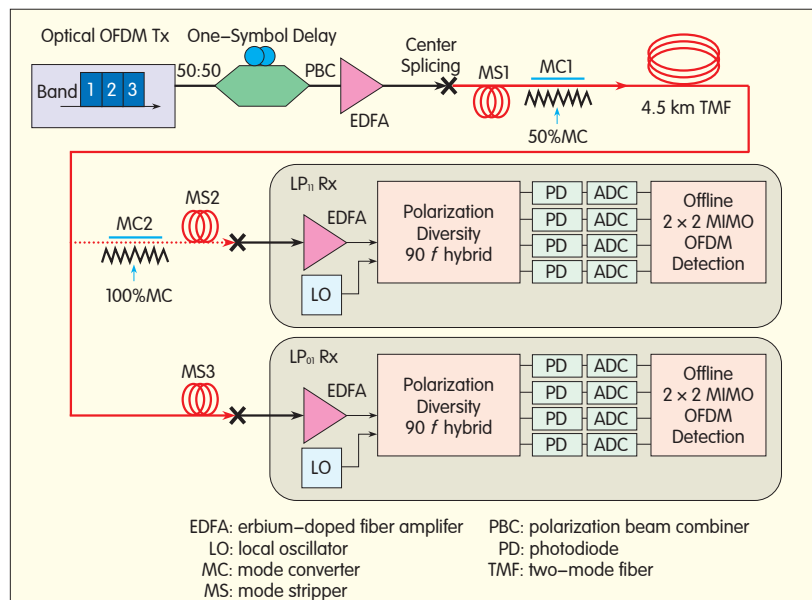
2.2 Free-Space Mode Combiner/Splitter

The mode combiner/splitter comprises two double-axis precision stages, one beamsplitter (BS), and three collimating lenses (Fig. 5). The signal is polarization multiplexed and mode converted before entering the mode combiner. The two input TMFs that carry either LP_{11a} or LP_{11b} generated by the mode converters are connected with the two input ports of the mode combiner, whose position can be manually aligned by the precision stages. The output port of the mode combiner is fixed using a fiber collimator and connected with the 4.5 km transmission fiber. The input signal is first collimated to a spot size with 2 mm diameter by one of the movable collimating lenses with numerical aperture (NA) of 0.25 and effective focal length f of 11.0 mm. The collimated beam is subsequently passed through the BS in either transmission or reflection direction and is finally focused onto the core of the output fiber by another lens inside the packaged collimator. The BS is polarization insensitive with less than 5% difference in transmission for s-polarization and p-polarization at 1550 nm. The input and output of the TMFs are connectorized before being mounted onto the stage with an FC-type adapter. The connectors are specially designed with an adjustable key so that the fiber can be axially rotated. By adjusting the key of the connectors, the orientation of the two LP_{11} modes can be changed so that the modes are orthogonal (90 degrees to each other). An infrared camera is placed in the unused path of the BS to monitor the orientation and orthogonality of the two LP_{11} modes (Fig. 5). The loss in the reflection path of the BS is approximately 3.5 dB, and the loss in the transmission path of the BS is approximately 4.5 dB. The loss in the focusing system caused by misalignment and Fresnel

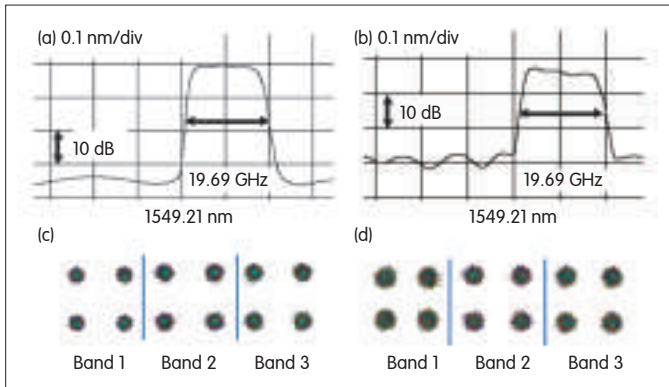
reflection is approximately 1 dB. The 1 dB power difference between the two paths is balanced using an SMF attenuator before mode conversion. It is also possible to upgrade to a 3×1 mode combiner by introducing another precision stage and collimating lens as well as another BS, which we introduce in the triple-mode ($LP_{01} + LP_{11a} + LP_{11b}$) transmission experiment. The mode splitter has the same structure as the combiner except that it is operated in opposite direction.

3 LP_{01}/LP_{11} Transmission Setup and Results

Fig. 6 shows the 107 Gbit/s LP_{01}/LP_{11} dual-mode coherent OFDM transmission setup 0. Four transmitters corresponding to LP_{01} and LP_{11} (both modes have two polarizations, x and y) are implemented as follows: First, the OFDM signal is generated offline with MATLAB. The fast Fourier transform (FFT) size is 64, with the middle 40 subcarriers filled. The Cyclic prefix (CP) is set to 1/8 of the observation window. The OFDM waveform consists of 500 symbols, and an initial 20 symbols with alternative polarization launch are used as training symbol (TS) for channel estimation. After FFT, the real and imaginary components of the time-domain signal are uploaded onto a Tektronix arbitrary waveform generator (AWG). Then, three tones spaced at 6.563 GHz are generated by an external cavity laser operating at 1549.3 nm wavelength and an intensity modulator (IM) driven by a synthesizer. The optical OFDM signal is then modulated on each tone by using the AWG to drive a nested Mach-Zehnder modulator. The orthogonally multiplexed triple-band OFDM signal is divided and recombined on orthogonal polarizations with one symbol delay to emulate polarization multiplexing. The sampling rate of the AWG is 10 GSa/s and as a consequence, the OFDM



▲ Figure 6 Experiment setup for 107 Gb/s dual-mode dual polarization transmission over 4.5 km TMF fiber. The center-spliced controlled couplings between LP_{01} modes of SMF and TMF are marked \times .



▲ Figure 7. (a) Optical spectrum and (c) constellations of LP_{01} after 4.5 km transmission in three bands. (b) Optical spectrum and (d) constellations for LP_{11} after 4.5 km transmission in three bands.

symbol length is 7.2 ns. The raw data rate is 150 Gb/s, and the net data rate after overheads (7% FEC, 4% TS, 12.5% CP, and five discarded subcarriers around the DC) is 107 Gb/s. Constant optical power of around 5.5 dBm is launched into the SMF before the MC1 for TMF transmission. A mode stripper (MS) is used after center splicing to strip off the unwanted LP_{11} , ensuring pure LP_{01} is launched into the TMF. The MS is realized by tightly bending the bare TMF over 7 mm posts of about 20 rounds that provide a rejection ratio of greater than 30 dB against LP_{11} [4]. The first mode combiner has a nominal 50:50 conversion ratio on LP_{01}/LP_{11} , with both modes carrying the previously described polarization multiplexed signal. We estimate that after the 4.5 km TMF, the delay between LP_{01} and LP_{11} is 13.5 ns. This delay is nearly double the OFDM symbol length. Therefore, the two modes are completely decorrelated after 4.5 km TMF transmission, and the signal can be independently received on LP_{01} or LP_{11} . At the receiver, the two modes are detected individually. For LP_{01} , a mode stripper (MS2) is used to strip off LP_{11} , and the remaining LP_{01} is coupled into the SMF. The signal is subsequently detected by a coherent optical receiver. For LP_{11} , a second mode converter (MC2) with nominal 100% conversion ratio is used to convert LP_{11} into LP_{01} . Any residual LP_{11} not converted to LP_{01} and any LP_{01} converted to LP_{11} is stripped off by a subsequent MS. The converted LP_{11} (now LP_{01}) is coupled into the SMF and is subsequently fed into the coherent optical receiver.

The received signal is converted from the optical to electrical domain and sampled by a 50 GSa/s digital oscilloscope. The received signal is processed using a 2×2 MIMO CO-OFDM program. The digital signal processing consists of five steps: 1) timing synchronization, 2) frequency offset compensation, 3) channel estimation and phase estimation, 4) subcarrier mapping and constellation recovery, 5) BER and Q computation. With this setup, the received power of LP_{01} is -0.5 dBm and that of LP_{11} is -5.3 dBm. Therefore, the end-to-end loss is 6 dB for LP_{01} and 10.8 dB for LP_{11} . The higher loss for LP_{11} can be attributed to the excessive loss in MSs (0.2–0.4 dB) and loss in the MCs (approximately 0.4 dB in MC1 and approximately 1.5 dB in

MC2). Also, there is random coupling between the degenerate LP_{11} modes inside the 4.5 km TMF, whereas only one of the two orientations can be launched or detected because of the asymmetry of our mode converter. Fig. 7(a) shows the high-resolution (0.01 nm) optical spectrum of a signal received from LP_{01} , and Fig. 7(b) shows the high-resolution optical spectrum of a signal received from LP_{11} . Good constellations in all three bands and for both modes are shown in Fig. 7(c) and (d). We could not detect any errors in the 100,590 bits of any of the 12 possible combinations of signal states (three bands, two polarizations, and two modes). Overall Q factors for all bands, polarizations, and modes are shown in Table 1. The 2 dB relative difference in average Q between LP_{01} and LP_{11} can be attributed to the increased crosstalk in LP_{11} . The ER of the mode converter becomes non-ideal under random perturbation between two LP_{11} spatial modes. The results demonstrate the feasibility of using TMF for dual-mode and dual-polarization transmission in order to increase fiber capacity and/or SE. In this experiment, we assume negligible mode coupling between LP_{01} and LP_{11} because of the high modal mismatch and relatively short distance. This negligible coupling has been tested in [18]. The modes are detected individually without the need for MIMO processing, and this reduces complexity. The main limiting factors for a TMF-based transmission system are 1) mode converter ER and MS rejection ratio; 2) dependence of mode converters and free-space components on polarization and mode, which causes mode-dependant loss, polarization-dependant loss, and crosstalk discrepancy in ER; and 3) the intrinsic loss of the fiber because a TMF amplifier is not readily available. For long-haul transmission, MIMO processing is necessary because there is significant accumulation of mode coupling.

4 Conclusion

We have presented a dual-mode, dual-polarization transmission method on a TMF using a grating-based LP_{01}/LP_{11} mode converter for mode-selective detection. Spectrally efficient transmission over a 4.5 km TMF at 107 Gb/s using CO-OFDM is achieved using a QPSK subcarrier. Spatial mode division multiplexing may be a solution to increasing optical fiber capacity beyond that of SSF.

▼ Table 1. Measured Q factor (dB) for a 107 Gb/s, triple-band CO-OFDM dual-mode, dual-polarization transmission on 4.5 km TMF

LP_{01}	Band 1	Band 2	Band 3	Average
Pol-x	19.5	18.4	18.1	18.7
Pol-y	18.5	18.3	17.9	18.3
Average	19.0	18.4	18.0	18.5
LP_{11}	Band 1	Band 2	Band 3	Average
Pol-x	15.2	18.6	16.2	16.9
Pol-y	14.7	17.0	16.5	16.2
Average	15.0	17.8	16.4	16.5

Spatial Mode-Division Multiplexing for High-Speed Optical Coherent Detection Systems

William Shieh, An Li, Abdullah Al Amin, Xi Chen, Simin Chen, and Guanjun Gao

References

- [1] R. Essiambre, G. Kramer, G.J. Foschini, and P.J. Winzer, "Optical fiber and information theory," in *Proc. 44th Annual Conf. Inf. Sci. Syst. (CISS' 10)*, Princeton, NJ, pp. 1–5.
- [2] W. Shieh and X. Chen, "Information spectral efficiency and launch power density limits due to fiber nonlinearity for coherent optical OFDM systems," *IEEE Photon. J.*, vol. 3, no. 2, pp. 158–173, Mar. 2011.
- [3] W. Shieh, "High spectral efficiency coherent optical OFDM for 1 Tb/s Ethernet transport," in *Proc. Optical Fiber Commun. Conf. (OFC/NFOEC 2009)*, San Diego, CA, pp. 1–3.
- [4] A. Li, A. Al Amin, X. Chen, and W. Shieh. (Apr. 2011). Transmission of 107 Gb/s mode and polarization multiplexed CO-OFDM signal over a two-mode fiber. *Optics Express* [Online]. vol. 19, no. 9, pp. 8808–8814. Available: <http://www.opticsinfobase.org/oe/abstract.cfm?URI=oe-19-9-8808>
- [5] N. Hanzawa, K. Saitoh, T. Sakamoto, T. Matsui, S. Tomita, and M. Koshiba, "Demonstration of mode-division multiplexing transmission over 10 km two-mode fiber with mode coupler," in *Proc. Optical Fiber Commun. Conf. (OFC/NFOEC 2011)*, Los Angeles, CA, paper OWA4.
- [6] M. Salsi, C. Koebele, D. Sperti, P. Tran, P. Brindel, H. Mardoyan, S. Bigo, A. Boutin, F. Verluise, P. Sillard, M. Bigot-Astruc, L. Provost, F. Cerou, and G. Charlet. (Aug 2011). Transmission at 2 × 100 Gb/s, over Two Modes of 40 km-long Prototype Few-Mode Fiber, using LCOS based Mode Multiplexer and Demultiplexer. *Optics Express* [Online] vol. 19, no. 17, pp. 16593–16600. Available: <http://www.opticsinfobase.org/abstract.cfm?URI=oe-19-17-16593>
- [7] R. Ryf, S. Randel, A. Gnauck, C. Bolle, R. Essiambre, P. Winzer, D. Peckham, A. McCurdy, and R. Lingle, "Space-division multiplexing over 10 km of three-mode fiber using coherent 6 × 6 MIMO processing," in *Proc. Optical Fiber Commun. Conf. (OFC/NFOEC 2011)*, Los Angeles, CA, paper PDPB10.
- [8] I.B. Djordjevic, M. Arabaci, L. Xu, and T. Wang. (Mar. 2011) Spatial-domain-based multidimensional modulation for multi-Tb/s serial optical transmission. *Optics Express* [Online]. vol. 19, no. 7, pp. 6845–6857. Available: <http://www.opticsinfobase.org/oe/abstract.cfm?URI=oe-19-7-6845>
- [9] S. Berdague, P. Facq, "Mode division multiplexing in optical fibers," *Applied Optics*, vol. 21, no. 11, pp. 1950–1955, 1982.
- [10] S. H. Murshid, A. Chakravarty, and R. Biswas, "Simultaneous Transmission of Two Channels Operating at the Same Wavelength in Standard Multimode Fibers," in *Proc. Conf. Quantum Electronics and Laser Science (CLEO/QELS '08)*, San Jose, CA, paper JWA107.
- [11] B. C. Thomsen, "MIMO enabled 40 Gb/s transmission using mode division multiplexing in multimode fiber," in *Proc. Optical Fiber Commun. Conf. (OFC/NFOEC 2010)*, San Diego, CA, paper OTHM6.
- [12] B. Franz, D. Suikat, R. Dschler, F. Buchali, and H. Buelow, "High speed OFDM data transmission over 5 km GI-multimode fiber using spatial multiplexing with 2 × 4 MIMO processing," in *Proc. 36th European Conf. Optical Commun. (ECOC 2010)*, Torino, Italy, paper Tu3.C.4.
- [13] Kwang Yong Song; In Kag Hwang; Seok Hyun Yun; Byoung Yoon Kim, "High performance fused-type mode-selective coupler using elliptical core two-mode fiber at 1550 nm," *IEEE Photonics Tech. Lett.*, vol. 14, no. 4, pp. 501–503, Apr. 2002.
- [14] I. Hwang, S. Yun, and B. Kim. (Sep. 1999) Long-period fiber gratings based on periodic microbends. *Optics Letters* [Online] vol. 24, no. 18, pp. 1263–1265. Available: http://fiber.kaist.ac.kr/kj_pap/Long-period%20fiber%20gratings%20based%20on%20periodic%20microbends.pdf
- [15] S. Savin, M. Dignonnet, G.S. Kino, H. J. Shaw, "Tunable mechanically induced long-period fiber gratings," *Optics Letters*, vol. 25, no. 10, pp. 710–712, 2000.
- [16] D. Davis, T.K. Gaylor, E.N. Glytsis, S.G. Kosinski, S.C. Mettler, A.M. Vengsarkar, "Long-period fibre grating fabrication with focused CO₂ laser pulses," *Electronics Lett.*, vol. 34, no. 3, pp. 302–303, Feb. 1998.
- [17] Yariv, A. "Coupled-mode theory for guided-wave optics," *IEEE J. Quantum Electron.*, vol. 9, no. 9, pp. 919–933, 1973.
- [18] F. Yaman, N. Bai, Y. Huang, M. Huang, B. Zhu, T. Wang, and G. Li. (Sep. 2010) 10 × 112 Gb/s PDM-QPSK transmission over 5032 km in few-mode fibers. *Optics Express* [Online]. vol. 18, no. 20, pp. 21342–21349. Available: <http://www.opticsinfobase.org/oe/abstract.cfm?URI=oe-18-20-21342>
- [19] J. VanRoey, J. van derDonk, and P. Lagasse, "Beam-propagation method:

analysis and assessment," *J. Opt. Soc. America*, vol. 71, pp. 803–810, 1981.

Manuscript received: January 6, 2012

Biographies

William Shieh (shieh@unimelb.edu.au) received his MS degree in electrical engineering communications from the University of Southern California, Los Angeles, in 1994. He received his PhD degree in physics from the same university in 1996. Since 2004, he has worked in the Department of Electrical and Electronic Engineering, University of Melbourne, Australia. His research interests include OFDM techniques in wireless and optical communications, coherent optical communication systems, and optical packet switching. He has published more than 110 journal and conference papers and submitted 14 U.S. patents (nine issued) for polarization controller, wavelength stabilization in WDM systems, and Raman amplifier-based systems and subsystems. Dr. Shieh is a fellow of the Optical Society of America (OSA).

An Li (a.li2@pgrad.unimelb.edu.au) received his BE degree in optical information science and technology from Huazhong University of Science and Technology, Wuhan, China, in 2003. He received his ME degree in physical electronics from the same university in 2006. From 2006 to 2007 he worked at Fiberxon Inc. (Source Photonics) on G(E)PON optical transceivers. He is currently working toward his PhD degree in the department of electrical and electronic engineering, University of Melbourne, Australia. His research interests include signal processing, wavelet analysis, few-mode fiber transmission, and optical OFDM system design.

Abdullah Al Amin (aalam@unimelb.edu.au) received his BE, ME and PhD degrees in electronic engineering from the University of Tokyo in 1999, 2001, and 2005. From 2005 to 2007, he was a postdoctoral research fellow at the Research Center for Advanced Science and Technology, University of Tokyo. He was responsible for developing an optical router prototype as part of NEDO-funded Photonic Network Project. From 2007 to 2009, he worked at KDDI R&D Laboratories, Saitama, Japan, where he conducted research on high-speed optical transmission using advanced modulation formats. He joined the University of Melbourne as a research fellow in 2010. His research focus is coherent optical OFDM and few-mode fiber based transmission systems.

Xi Chen (xi.chen@ee.unimelb.edu.au) was born in Hunan, China. She received the B.E. degree in communication engineering in 2008, from National University of Defense Technology, Changsha, China. She is currently a Ph.D candidate in electrical and electronic engineering at the University of Melbourne, Melbourne, Australia. Her current research interests include optical OFDM systems, fiber nonlinear effects, and few-mode fiber (FMF) based communication systems.

Simin Chen (simin.chen@unimelb.edu.au) received his BS and MS degrees in electrical and electronic engineering from Sichuan University, China. He is working toward his PhD degree in the Department of Electrical and Electronic Engineering at the University of Melbourne, Australia. From 2006 to 2007 he worked at Fiberxon Inc. on optical transceivers and FPGA. His research interests are signal processing and coherent optical communication systems with a focus on the real-time implementation of coherent optical OFDM transmitter and receiver.

Guanjun Gao (gaog@unimelb.edu.au) received his BE degree in communication engineering from Beijing University of Posts and Telecommunications (BUPT) in 2006. He is currently a PhD candidate at BUPT and a visiting student at the University of Melbourne, Australia. His research interests include optical OFDM systems, few-mode fiber (FMF) communication systems, and cross-layer design of optical networks.

AD Index

Back Cover:
ZTE Corporation



Exploiting the Faster-Than-Nyquist Concept in Wavelength-Division Multiplexing Systems Using Duobinary Shaping

Jianqiang Li, Ekawit Tipsuwannakul, Magnus Karlsson, and Peter A. Andrekson

(Photonics Laboratory, Dept. of Microtechnology and Nanoscience, Chalmers University of Technology, SE-412 96, Göteborg, Sweden)

Abstract

This paper begins with Nyquist wavelength-division multiplexing (WDM) and then introduces faster-than-Nyquist. In faster-than-Nyquist, a certain amount of inter-symbol interference (ISI) is accepted, which violates the fundamental principle of Nyquist WDM. This results in much-relaxed transceiver bandwidth and simpler spectral design. However, in faster-than-Nyquist, implementation complexity is shifted from the transmitter side to the receiver side. Therefore, successful application of faster-than-Nyquist depends on innovation in the receiver structure. In this paper, we discuss the guidelines for implementing suboptimum, low-complexity receivers based on faster-than-Nyquist. We suggest that duobinary shaping is a good technique for trading off achievable spectral efficiency, detection performance, and implementation complexity and might be preferable to Nyquist WDM. Experiments are conducted to verify robustness of the proposed technique.

Keywords

coherent detection; digital signal processing; optical fiber communications; spectral-efficiency; wavelength division multiplexing

1 Introduction

Ever-increasing demand for bandwidth has driven optical communication systems to higher and higher capacities. There is a strong motivation to enhance spectral efficiency in order to upscale total capacity and reduce cost per bit. These goals have inspired intensive research and many laboratory experiments [1]–[19]. Spectral efficiency can be enhanced with high-level modulation formats, but this comes at the cost of high complexity and lower power efficiency [2]–[4]. If the modulation format is already specified, two research directions, based on spectral multiplexing, can be taken to achieve high spectral efficiency. One area of research is orthogonal frequency-division multiplexing (OFDM), which uses orthogonality to allow for spectral overlapping [5]–[10]. The other area of research is innovations on conventional wavelength-division multiplexing (WDM). Compared to approaches based on OFDM, approaches based on WDM relax the analog bandwidth and sampling-speed requirements of the digital-to-analog

converters (DACs) and analog-to-digital converters (ADCs) in transceivers [11]. Moreover, the absence of temporal and spectral overheads, that is, guard intervals, training sequences, or pilot tones, means the approaches based on WDM are more efficient and less complex. In this paper, we discuss several new concepts for improving spectral efficiency in WDM systems, and we propose solution in which spectral efficiency, performance, and complexity are traded off to achieve a reasonable compromise.

2 Nyquist WDM and Faster-Than-Nyquist

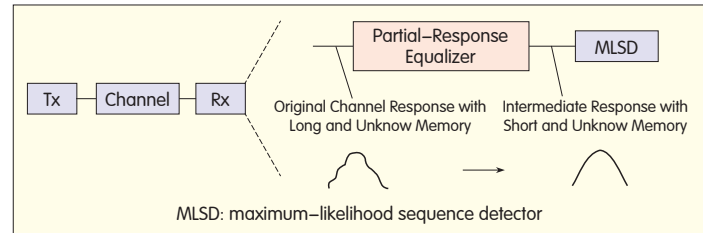
In WDM systems, an individual channel can be viewed as band-limited with a cut-off bandwidth equal to the channel spacing. In this way, improving spectral efficiency means increasing the symbol rate for a given channel spacing or reducing the channel spacing for a given symbol rate. One recently-studied concept is Nyquist WDM, in which the Nyquist limit is approached by using Nyquist filtering or shaping [11]–[15]. In Nyquist WDM, the spectrum of one WDM channel is optically or electrically tailored to fit into the

near-symbol-rate channel spacing. Ideally, inter-symbol interference (ISI) is absent. However, filtering or spectral shaping often requires special treatment so that this Nyquist ISI-free criterion is met. It is also difficult to approach the Nyquist limit in practice; the channel spacing has to be slightly larger than the symbol rate because of inter-channel linear crosstalk [12]–[15]. Nyquist WDM assumes that the overall channel has no ISI or a small amount of linear ISI (excluding chromatic dispersion and polarization-mode dispersion, which are all-pass effects). Thus, optimum performance can be approached by combining a linear equalizer and a hard-decision-based detector, which is widely used in conventional WDM systems with coherent detection. In Nyquist WDM, the lower bound of the channel spacing is the symbol rate because the Nyquist ISI-free criterion dictates that the symbol rate cannot exceed the Nyquist rate of $2W$ over an ISI-free band-limited channel with single-sided cut-off bandwidth W [16].

To exceed the Nyquist limit, faster-than-Nyquist has been proposed [16]–[19]. The fundamental idea behind this new concept is to increase the symbol rate above Nyquist rate by accepting a certain amount of ISI left to the detectors. The optimum detectors are those based on maximum a-posteriori probability (MAP) and maximum-likelihood (ML) criteria, not hard-decision criteria. Relaxing the ISI-free criterion greatly reduces bandwidth requirements on the transceiver and eases the difficulty of Nyquist filtering or shaping in practice. These benefits encourage the application of faster-than-Nyquist in realistic WDM systems. Our intention is to use faster-than-Nyquist without forcing the symbol rate beyond the Nyquist rate (even though it can be done). Although faster-than-Nyquist is relatively new in optical communications, it has already been leveraged in the systems described in [20]–[25]. In these systems, ISI was introduced by commercial electrical or optical analog filters (without any specific designs), and some ISI was left to the final MAP or ML detectors. A problem with an optimal MAP or ML receiver is that computations and storage grow exponentially with channel memory [26]. The channel memory induced by ISI in constrained-bandwidth systems (such as those in [20]–[22]) often spans a large number of symbols, and this results in unacceptably complex detectors. Moreover, the ISI pattern in these systems is unknown and unconditioned, and additional channel estimators are needed. Therefore, the success of faster-than-Nyquist depends on innovations that address all these problems.

3 A Practical Suboptimal Receiver

In [27], a finite impulse response (FIR) equalizer is used to shape the channel response into an intermediate truncated channel response with a short memory. The FIR equalizer then feeds the equalized output to a simplified maximum-likelihood sequence detector (MLSD) (Fig. 1). This equalizer is a partial-response equalizer because its shaping goal is one channel with a specified truncated ISI pattern. By using a partial-response equalizer, the overall memory or

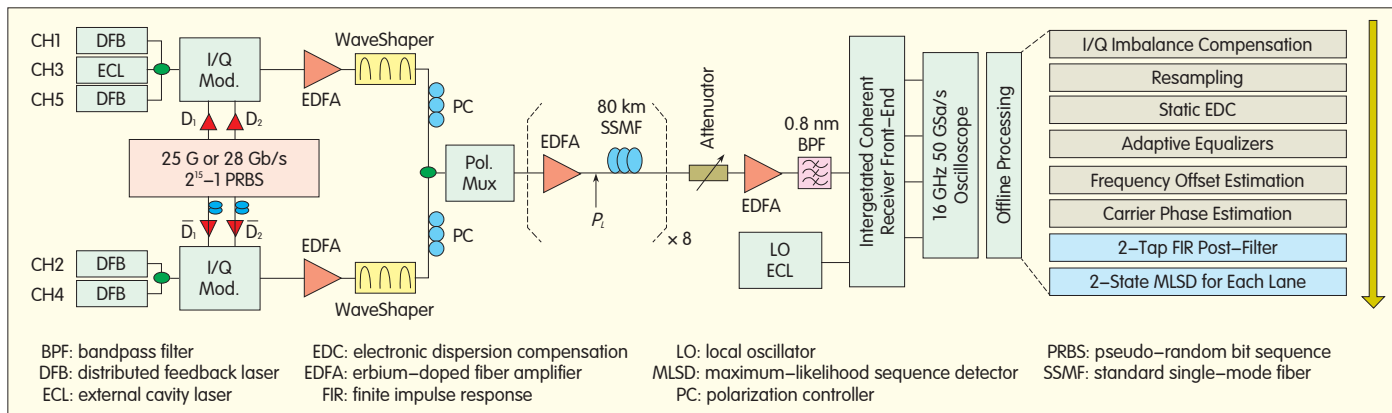


▲ Figure 1. The typical system structure suggested in [27].

accounted-for ISI can be arbitrarily shared between the partial-response equalizer and the MLSD. This allows a trade-off between complexity and performance, and the solution has been the basis of numerous receiver structures [28]–[30]. In these receivers, the least-mean-square (LMS) algorithm is commonly used so that the equalizer is adaptive. The adaptive equalizer can operate in a decision-directed [28], [29] or decision-feedback manner [30]. Regardless of which structure is used, the performance advantage of the MLSD is retained by carefully selecting the intermediate truncated channel so that the amplitude response is similar to that of the original channel. The reason for this guideline is that the shaping process by the partial-response equalizer would alter the spectral characteristic and power of the noise, which would ultimately influence the effective signal-to-noise ratio (SNR) and MLSD performance.

Linear equalizers in fiber-optic systems are essential and have been widely applied [31]. Adaptive equalizers can conveniently perform polarization demultiplexing and compensate for almost all static and time-varying linear impairments. In optical coherent receivers, adaptive equalizers using constant modulus algorithm (CMA) and decision-directed LMS (DD-LMS) algorithm are used to mitigate ISI in the channel. However, noise may be strong if ISI is strong [26]. The shaping goal of an adaptive equalizer is an ISI-free channel, and an adaptive equalizer cannot be used for partial-response shaping. Moreover, it might also be inadvisable to modify the equalizer in an optical coherent receiver referring to [28]–[30] because this would not only complicate the equalizer itself but also significantly change the carrier recovery algorithms. For example, the equalizer structure proposed in [22] is similar to that in [29] for optical coherent receivers whereas the frequency offset was assumed to be known and had to be compensated for before the equalizer. Therefore, it is desirable to innovate on receiver structures without altering the existing mature coherent receiver algorithms.

Another concern is how to determine the intermediate channel response in spectrally-efficient optical WDM systems by using the previously mentioned guideline. For general time-varying channels, an algorithm has been developed to adaptively optimize the intermediate channel response by minimizing the mean-square error [28]. In real optical networks, the memory or ISI in one channel (excluding the ISI induced by dispersion) is commonly introduced by bandwidth-limiting components such as the optical modulators, WDM components, reconfigurable optical



▲ Figure 2. Experiment setup and offline DSP flow for a five-channel PM-QPSK WDM system.

add-drop multiplexers (ROADMs), analog electrical/microwave driving circuits, and photodetectors. The amplitude responses of these components are relatively constant. Although a cascade of multiple ROADMs causes accumulated narrowband filtering, the rough shape of the overall channel response is maintained. Therefore, adaptations such as those in [28] are not imperative in optical communication systems where the channel is quasi-static. This means that the desired intermediate channel response can be determined in back-to-back (B2B) and can be kept fixed in the real optical network where the setup and hardware are specified. This reduces implementation complexity, but performance is compromised when the channel response changes slightly.

4 Duobinary Shaping

Partial-response maximum-likelihood (PRML) technology is widely applied in magnetic recording systems. A magnetic recording channel can be shaped into a partial-response channel because the memory in the read-out signals from magnetic media is inherently similar to a certain partial-response class [32], [33]. This leads us to consider whether the channel in a spectrally efficient WDM system can be shaped into a partial-response channel with a short memory. Recently, we showed that the channel amplitude response in the presence of regular electrical or optical filters has a similar shape to the well-known duobinary response [23]–[25]. More importantly, a novel receiver structure has been proposed for duobinary shaping or equalization prior to the MLSD. A simple duobinary digital post-filter is introduced after the conventional adaptive linear equalizers and carrier recovery modules. In this way, the existing digital signal processing (DSP) algorithms in the conventional digital coherent receivers were all preserved. The short one-symbol memory of the duobinary response considerably simplifies the MLSD. The proposed duobinary shaping scheme is robust to narrowband optical filtering, and the requirements on the transceiver hardware are greatly relaxed. An ideal duobinary response has a double-sided cut-off bandwidth that is the same as the symbol rate. According to the shaping guideline

previously mentioned, the proposed duobinary shaping scheme applies to WDM systems with a channel spacing approximately equal to the symbol rate (maybe slightly higher or lower). The symbol rate can be pushed beyond the Nyquist limit through more aggressive filtering and searching other intermediate channel responses with longer memory. However, this might disable the convergence of the conventional adaptive equalizers because noise would (possibly) be infinitely augmented. Although this problem could be solved by modifying the whole DSP structure and associated algorithms, we suggest that duobinary shaping provides a good trade-off between spectral-efficiency, detection performance, and DSP complexity.

5 Experiment with the Proposed Duobinary Shaping Technique in a PM-QPSK WDM System

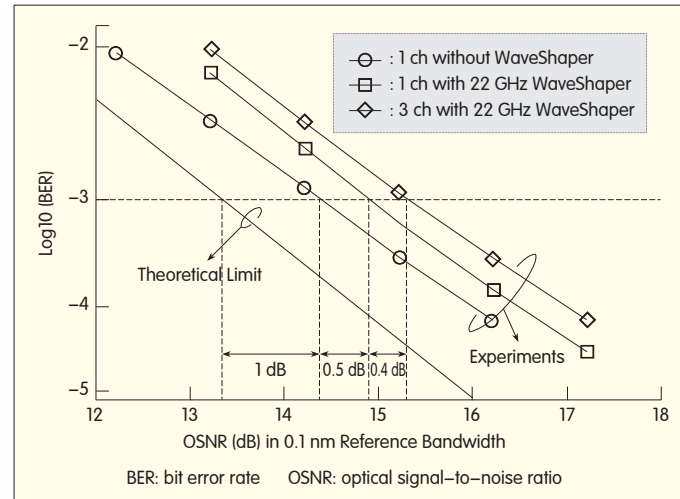
To determine the benefits and robustness of the proposed duobinary shaping technique, we carried out experiments using 25 GHz spaced, 100 Gb/s polarization-multiplexed QPSK (PM-QPSK) WDM with up to five channels.

Fig. 2 shows the experiment setup and DSP flow. One external-cavity laser (ECL) and four distributed-feedback (DFB) lasers provide up to five 25 GHz-spaced continuous-wave (CW) optical carriers. An ECL with approximately 100 kHz linewidth serves for the central channel that we are investigating. Four decorrelated 25 Gb/s or 28 Gb/s pseudo-random bit sequence (PRBS) signals all have a codeword length of $2^{15}-1$. These PRBS signals are generated from a quad-channel pulse pattern generator (PPG). The decorrelation between channel D_1 and D_2 is 214 bits, and the decorrelation between D_1 and \bar{D}_1 is 54 bits. These paired PRBS data streams drive two I/Q modulators with full swings to produce optical QPSK signals. The odd and even channels are further decorrelated by a differential delay of approximately 180 symbols. Prior to being combined by a 3 dB optical coupler, the odd and even channels are spectrally shaped and filtered by two commercial WaveShapers, both programmed with fourth-order super-Gaussian profiles for each WDM channel. Spectral

shaping and filtering allows the PM-QPSK signals to be accommodated on a 25 GHz grid with acceptable linear crosstalk. The two WaveShapers and 3 dB coupler act as an optical interleaver with the ability to tune the optical-filtering bandwidth. This tunability allows us to determine the tolerance of the proposed duobinary shaping scheme to the optical-filtering bandwidth. Spectral shaping can also be done by electrical filters such as those in [23] and [24]. Here, we take an optical approach to spectral shaping because WDM components are used in practice to combine WDM channels. Then, the entire WDM signal is polarization-multiplexed with a differential delay of approximately 180 symbols between the two polarizations. The fiber link was built up in a straight line using eight 80 km standard single-mode fiber (SSMF) spans with erbium-doped fiber amplifiers (EDFAs) only. The optical power, PL, launched into the SSMF spool in each span was the same. At the receiver, the WDM signal was pre-amplified and then filtered by a 0.8 nm optical bandpass filter (BPF) to suppress wideband noise. Intradyne detection of the central channel was implemented using a commercial integrated-coherent receiver in a conventional polarization- and phase-diverse configuration. Finally, the four detected tributaries were captured, each with 3×10^6 samples, by a 50 GSa/s digital sampling oscilloscope with 16 GHz analog bandwidth for offline processing.

The conventional DSP blocks for a PM-QPSK coherent receiver are preserved without modification, which is a tenet of the proposed DSP structure. The proposed structure allows DSP reconfiguration because all the DSP blocks work in a feed-forward fashion, and the additional post-filter and MLSD can be easily switched to hard decision. After I/Q imbalance is compensated for using the Gram-Schmidt algorithm [31], electronic dispersion compensation (EDC) based on static time-domain equalization is performed to compensate for all the accumulated dispersion. The sample streams are then resampled to two samples per symbol. A blind adaptive equalizer with four 15-tap $T/2$ -spaced butterfly FIR filters adapted using the classic CMA follows. Carrier recovery is then performed, which includes frequency offset estimation based on fast Fourier transform (FFT) [34] and carrier phase estimation based on the fourth-power Viterbi-Viterbi algorithm [31]. After these conventional DSP blocks, the digital post-filter performs duobinary shaping and the MLSD performs suboptimum detection on each signal quadrature of each polarization, that is, each electrical lane in a practical PM-QPSK transponder. (Fig. 2, highlighted boxes). On each signal quadrature in each polarization, the signal can be considered to have a 2-ary pulse-amplitude modulation (PAM) format. Therefore, the MLSD based on Viterbi algorithm only has two states for each quadrature of each polarization. Differential coding is used for all cases to overcome cycle slipping and phase ambiguity.

We first investigated performance at different symbol rates. Fig. 3 shows B2B performance at a 25 Gbaud symbol rate, which is equal to the channel spacing. First, the performance of a single-channel PM-QPSK signal was measured by

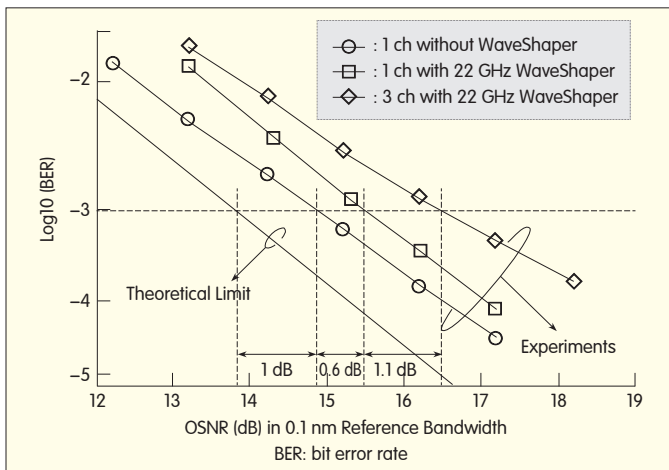


▲ Figure 3. BER as a function of OSNR in B2B at 25 Gbaud.

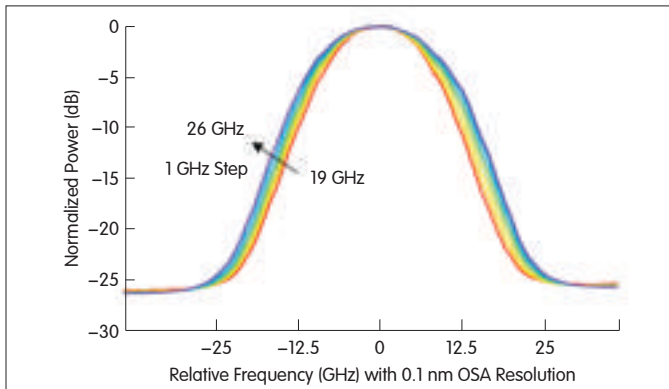
configuring the WaveShaper in all-pass mode. The post-filter and MLSD were turned off in the DSP because there was no strong ISI. Compared with the theoretical limit and taking into account the differential coding, there is approximately 1 dB typical optical SNR (OSNR) penalty at a bit error rate (BER) of 10^{-3} . Second, aggressive spectral shaping was performed on the single-channel PM-QPSK signal by configuring the WaveShaper with a 22 GHz 3 dB bandwidth. The post-filter and MLSD were activated to perform duobinary shaping and suboptimum detection. By virtue of the post-filter and MLSD, a single-channel PM-QPSK signal only suffers approximately 0.5 dB required OSNR penalty. Third, we turned on the two channels that were closest to each other in order to determine the effect of inter-channel linear crosstalk. Another 0.4 dB required OSNR penalty appears (Fig. 3). There is less than 1 dB OSNR penalty in WDM systems with a channel spacing equal to symbol rate. Next, we pushed the symbol rate to 28 Gbaud while maintaining the 25 GHz channel spacing. The symbol rate was faster than Nyquist, and the raw spectral efficiency was above 4 b/s/Hz. Fig. 4 shows B2B BER as a function of OSNR at 28 Gbaud. There is only 0.6 dB implementation penalty for single channel, similar to the penalty at 25 Gbaud. However, the penalty is larger when there is linear crosstalk due to the boosted symbol rate. This implies that the proposed duobinary shaping technique works well, and performance loss is mainly due to interchannel linear crosstalk not the technique itself. The BER of 10^{-3} cannot be reached in the three-channel setup if the proposed technique is disabled at 25 Gbaud or 28 Gbaud. In sum, we have shown that there is an implementation penalty of approximately 0.9 dB at 25 Gbaud and an implementation penalty of approximately 1.7 dB at 28 Gbaud on a 25 GHz WDM grid. By comparison, the systems in [13], [15], and [20] had greater than 2 dB OSNR penalty at B2B. To the best of our knowledge, the implementation penalties described in this paper are the smallest for PM-QPSK WDM systems with such high spectral efficiency. This small implementation penalty is achieved by only using one-symbol memory in the MLSD.

Exploiting the Faster-Than-Nyquist Concept in Wavelength-Division Multiplexing Systems Using Duobinary Shaping

Jianqiang Li, Ekawit Tipsuwannakul, Magnus Karlsson, and Peter A. Andrekson



▲ Figure 4. BER as a function of OSNR in B2B at 28 Gbaud.

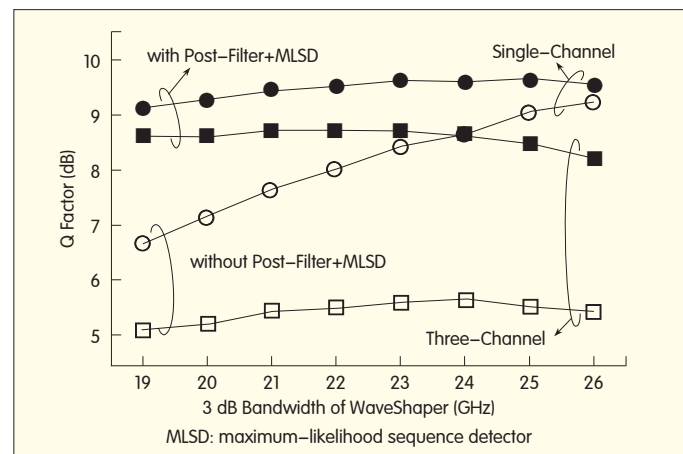


▲ Figure 5. Optical spectra of a single-channel 28 Gbaud PM-QPSK signal after spectral shaping with different 3 dB bandwidths of the WaveShaper.

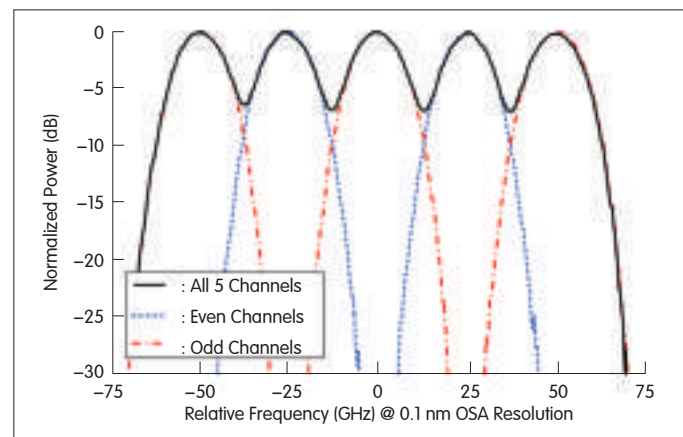
To determine the robustness of the proposed scheme, the optical filtering bandwidth was swept from 19 GHz to 26 GHz by reconfiguring the WaveShapers. The symbol rate was set to 28 Gbaud. This bandwidth sweep altered the original channel response and changed the deviation of the channel response to the ideal duobinary response. Fig. 5 shows the optical spectra of a single-channel 28 Gbaud PM-QPSK signal after spectral shaping with different 3 dB bandwidths. Fig. 6 shows the experiment results for single-channel and triple-channel setups, given a fixed per-channel OSNR of 15.2 dB. There are several important observations from Fig. 6. The function marked with solid dots shows that stronger spectral shaping is possible despite a slightly larger penalty. Furthermore, a system in which the proposed technique is used is tolerant to the spectral-shaping bandwidth. The function marked with solid squares shows there is an optimal bandwidth (22 GHz) for the triple-channel setup. This means a tradeoff has been made between inter-channel crosstalk and intra-channel shaping or filtering. If the post-filter and MLSD were turned off, the triple-channel setup would have a much larger penalty compared with the single-channel setup. Therefore, increasing linear crosstalk plays a dominant role in

increasing in-band noise enhancement.

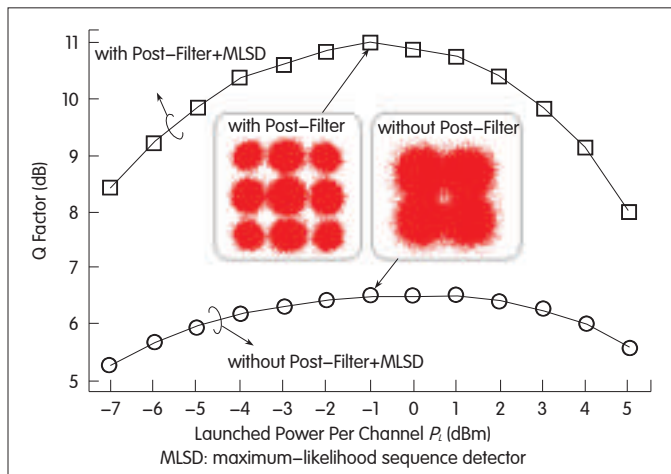
Finally, 25 GHz-spaced 5×112 Gb/s PM-QPSK signals were transmitted over 640 km SSMF using the setup shown in Fig. 2. The WaveShapers were programmed with a 22 GHz fourth-order super-Gaussian profile for each WDM channel. Fig. 7 shows the transmitted WDM optical spectra. Channel isolation greater than 30 dB is achieved on a 25 GHz grid, and the interchannel linear crosstalk occurs on the spectral edge of each channel. Limited equipment availability meant that 640 km SSMF transmissions with EDFAs could only be implemented in a straight line, leaving an OSNR margin. Therefore, we adjusted the attenuator before the Rx pre-amplifier (Fig. 2) to obtain a reasonable OSNR range in which we would have a sufficient error count. Fig. 8 shows the Q-factor of the central channel as a function of the launched power after 640 km SSMF transmission. The insets in Fig. 8 show that the enhanced in-band noise and linear crosstalk are suppressed, and the constellation evolves to a nine-point constellation after duobinary shaping. With the post-filter and MLSD, the optimal launch power is -1 dBm. The case without post-filter and MLSD has a higher optimal optical launch power and less sensitivity to the launch power because



▲ Figure 6. Tolerance to spectral shaping bandwidth of the WaveShapers.



▲ Figure 7. Transmitted optical spectra in experiments on 25 GHz-spaced five-channel 112 Gb/s PM-QPSK WDM.



▲ Figure 8. 640 km SSMF transmission performance versus launch power per channel.

performance is mainly penalized by increased in-band noise and interchannel linear crosstalk. In this case, more nonlinearity is required to further penalize the signal.

6 Conclusion

Applying the faster-than-Nyquist concept in spectrally-efficient WDM systems has been discussed. The fundamental idea behind faster-than-Nyquist is to increase spectral efficiency by accepting ISI. In light of this idea, we have proposed a novel receiver structure based on duobinary shaping in order to achieve a balanced trade-off between spectral efficiency, detection performance, and implementation complexity in optical WDM systems. Experiments were carried out in 25 GHz-spaced 100 Gb/s PM-QPSK WDM system with small implementation penalty and promising robustness. The proposed scheme can be expanded to higher-level modulation formats, for example, 16-ary quadrature amplitude modulation (QAM) for higher spectral efficiency [25].

References

- [1] P. J. Winzer, "Beyond 100G ethernet," *IEEE Commun. Mag.*, vol. 48, no. 7, pp. 26–30, 2010.
- [2] A. H. Gnauck, P. J. Winzer, S. Chandrasekhar, X. Liu, B. Zhu, and D. W. Peckham, "Spectrally efficient long-haul WDM transmission using 224-Gb/s polarization-multiplexed 16-QAM," *J. Lightw. Technol.*, vol. 29, no. 4, pp. 373–377, 2011.
- [3] J. Yu, X. Zhou, Y. K. Huang, S. Gupta, M. F. Huang, T. Wang, and P. Magill, "112.8-Gb/s PM-RZ-64QAM optical signal generation and transmission on a 12.5 GHz WDM grid," in *Proc. OFC2010*, Mar. 2010, Paper OThM1.
- [4] X. Zhou, J. Yu, M.-F. Huang, Y. Shao, T. Wang, L. Nelson, P. Magill, M. Birk, P. I. Borel, D. W. Peckham, R. Lingle, Jr., and B. Zhu, "64-Tb/s, 8 b/s/Hz, PDM-36QAM transmission over 320 km using both pre- and post-transmission digital signal processing," *J. Lightw. Technol.*, vol. 29, no. 4, pp. 571–577, Feb. 2011.
- [5] W. Shieh, "OFDM for flexible high-speed optical networks," *J. Lightw. Technol.*, vol. 29, no. 10, pp. 1560–1577, May. 2011.
- [6] A. Sano, E. Yamada, H. Masuda, E. Yamazaki, T. Kobayashi, E. Yoshida, Y. Miyamoto, R. Kudo, K. Ishihara, and Y. Takatori, "No-guard-interval coherent optical OFDM for 100-Gb/s long-haul WDM transmission," *J. Lightw. Technol.*, vol. 27, no. 16, pp. 3705–3713, Aug. 2009.
- [7] X. Liu, S. Chandrasekhar, B. Zhu, P. J. Winzer, A. H. Gnauck, and D. W. Peckham, "448-Gb/s reduced-guard-interval CO-OFDM transmission over 2000 km of ultra-large-area fiber and five 80-GHz-grid ROADMs," *J. Lightw. Technol.*, vol. 29, no. 4, pp. 483–490, Feb. 2011.
- [8] J. Zhang, N. Chi, J. Yu, Y. Shao, J. Zhu, B. Huang, L. Tao, "Generation of coherent and frequency-lock multi-carriers using cascaded phase modulators and recirculating frequency shifter for Tb/s optical communication," *Opt. Express*, vol. 19, no. 14, pp. 12891–12902, 2011.
- [9] J. Yu, Z. Dong, X. Xiao, Y. Xia, S. Shi, C. Ge, W. Zhou, N. Chi and Y. Shao, "Generation of 112 coherent multi-carriers and transmission of 10 Tb/s (112x100Gb/s) single optical OFDM superchannel over 640 km SMF," in *Proc. OFC2011*, Mar. 2011, Paper PDPA6.
- [10] J. Yu, Z. Dong, J. Zhang, X. Xiao, H.-C. Chien, and N. Chi, "Generation of coherent and frequency-locked multi-carriers using cascaded phase modulators for 10Tb/s optical transmission," *J. Lightw. Technol.* vol. 30, no. 4, pp. 458–465, Feb. 2012.
- [11] G. Bosco, A. Carena, V. Curri, P. Poggiolini, and F. Forghieri, "Performance limits of Nyquist-WDM and CO-OFDM in high-speed PM-QPSK systems," *IEEE Photon. Technol. Lett.*, vol. 22, no. 15, pp. 1129–1131, Aug. 2010.
- [12] X. Zhou, L. Nelson, P. Magill, R. Isaac, B. Zhu, D. W. Peckham, P. Borel, and K. Carlson, "8x450-Gb/s, 50-GHz-Spaced, PDM-32QAM transmission over 400km and one 50-GHz-Grid ROADMs," in *Proc. OFC2011*, Mar. 2011, Paper PDPB3.
- [13] K. Igarashi, Y. Mori, K. Katoh, and K. Kikuchi, "Bit-error rate performance of Nyquist wavelength-division multiplexed quadrature phase-shift keying optical signals," in *Proc. OFC2011*, Mar. 2011, Paper OMR6.
- [14] R. Cigliutti, E. Torrenco, G. Bosco, N. P. Caponio, A. Carena, V. Curri, P. Poggiolini, Y. Yamamoto, T. Sasaki, and F. Forghieri, "Transmission of 9x138Gb/s prefiltered PM-8QAM signals over 4000 km of pure silica-core fiber," *J. Lightw. Technol.*, vol. 29, no. 15, pp. 2310–2318, Aug. 2011.
- [15] G. Gavioli, E. Torrenco, G. Bosco, A. Carena, V. Curri, V. Miot, P. Poggiolini, M. Belmonte, F. Forghieri, C. Muzio, S. Picciaccia, A. Brincioti, A. La Porta, C. Lezzi, S. Savory, S. Abrate, "Investigation of the impact of ultra-narrow carrier spacing on the transmission of a 10-carrier 1Tb/s superchannel," in *Proc. OFC2010*, San Diego, CA, Mar. 2010, Paper OThD3.
- [16] H. J. Landau, "Sampling, data transmission, and the Nyquist rate," *Proc. IEEE*, vol. 55, pp. 1701–1706, Oct. 1967.
- [17] J. E. Mazo, "Faster-than-Nyquist signaling," *Bell System Tech. J.*, vol. 54, no. 8, pp. 1451–1462, Oct. 1975.
- [18] A. D. Liveris and C. N. Georgiades, "Exploiting faster-than-Nyquist signaling," *IEEE Trans. Commun.*, vol. 51, no. 9, pp. 1502–1511, Sep. 2003.
- [19] G. Colavolpe, "Faster-than-Nyquist and beyond: how to improve spectral efficiency by accepting interference," in *Proc. ECOC 2011*, Sep. 2011, Paper Mo.1.B.
- [20] J.-X. Cai, Y. Cai, C. R. Davidson, D. G. Foursa, A. J. Lucero, O. V. Sinkin, W. W. Patterson, A. N. Pilipetskii, G. Mohs, and N. S. Bergano, "Transmission of 96x100-Gb/s bandwidth-constrained PDM-RZ-QPSK channels with 300% spectral efficiency over 10610 km and 400% spectral efficiency over 4370 km," *J. Lightw. Technol.*, vol. 29, no. 4, pp. 491–498, Feb. 2011.
- [21] J.-X. Cai, Y. Cai, C. R. Davidson, A. Lucero, H. Zhang, D. G. Foursa, O. V. Sinkin, W. W. Patterson, A. Pilipetskii, G. Mohs, and N. S. Bergano, "20 Tbit/s capacity transmission over 6,860 km," in *Proc. OFC2011*, Mar. 2011, Paper PDPB4.
- [22] K. Horikoshi, T. Kobayashi, S. Yamanaka, E. Yamazaki, A. Sano, E. Yoshida, and Y. Miyamoto, "Spectrum-narrowing tolerant 171-Gbit/s PDM-16QAM transmission over 1,200 km using maximum likelihood sequence estimation," in *Proc. ECOC 2011*, Sep. 2011, Paper We.10.P1.73.
- [23] J. Li, Z. Tao, H. Zhang, W. Yan, T. Hoshida, J. C. Rasmussen, "Enhanced digital coherent receiver for high spectral-efficiency dual-polarization quadrature duobinary systems," presented in *ECOC 2010*, Turin, Italy, Sep. 2010, Paper Th.10.A.3.
- [24] J. Li, Z. Tao, H. Zhang, W. Yan, T. Hoshida, J. C. Rasmussen, "Spectrally efficient quadrature duobinary coherent systems with symbol-rate digital signal processing," *J. Lightw. Technol.*, vol. 29, no. 8, pp. 1098–1104, Apr. 2011.
- [25] J. Li, E. Tipsuwannakul, T. Eriksson, M. Karlsson, and P. A. Andrekson, "Approaching Nyquist limit in wavelength-division multiplexing systems by low-complexity duobinary shaping and detection," to be published in *J. Lightw. Technol.*
- [26] J. G. Proakis, *Digital Communications*, Fourth Edition, New York: McGraw-Hill, 2001.
- [27] G. D. Forney, Jr., "Maximum likelihood sequence estimation of digital sequences in the presence of intersymbol interference," *IEEE Trans. Info. Theory*, vol. IT-18, no. 3, pp. 363–378, May 1972.
- [28] D. D. Falconer and F. R. Magee, Jr., "Adaptive channel memory truncation for maximum-likelihood sequence estimation," *Bell System Tech. J.*, vol. 52, no. 9, pp. 1541–1562, Nov. 1973.
- [29] S. Qureshi and E. Newhall, "An adaptive receiver for data transmission over time-dispersive channels," *IEEE Trans. Inform Theory*, vol. IT-19, pp. 448–457, July 1973.
- [30] W. U. Lee and F. S. Hill Jr., "A maximum likelihood sequence estimator with decision feedback equalization," *IEEE Tram. Commun.*, vol. COM-25, pp. 971–980, Sept. 1977.
- [31] S. J. Savory, "Digital coherent optical receivers: algorithms and subsystems," *IEEE J. Sel. Top. Quantum Electron.*, vol. 16, no. 5, pp. 1164–1179, Sep./Oct.

Exploiting the Faster-Than-Nyquist Concept in Wavelength-Division Multiplexing Systems Using Duobinary Shaping

Jianqiang Li, Ekawit Tipsuwannakul, Magnus Karlsson, and Peter A. Andrekson

2010.

- [32] H. Kobayashi and D. T. Tang, "Application of partial-response channel coding to magnetic recording systems," *IBM J. R&D.*, vol. 14, no. 4, pp. 368–75, Jul. 1970.
- [33] H. Kobayashi, "Partial-response coding, maximum-likelihood decoding: capitalizing on the analogy between communication and recording," *IEEE Commun. Mag.*, vol. 47, no. 3, pp. 14–17, Mar. 2009.
- [34] M. Selmi, Y. Jaouen, P. Ciblat, "Accurate digital frequency offset estimator for coherent PolMux QAM transmission systems," in *Proc. ECOC 2009*, Sep. 2009, Paper P3.08

Manuscript received: November 15, 2011

Biographies

Jianqiang Li (jqlee@gmail.com) received his BE and PhD degrees from Beijing University of Posts and Telecommunications in 2005 and 2009. In July 2009, he joined Fujitsu R&D Center, Beijing, where he researched digital coherent receivers for high-speed optical communication systems. Since June 2011, he has been a postdoctoral researcher at the photonics laboratory, Chalmers University of Technology, Gothenburg, Sweden. His research experience and interests include high-speed and high-spectral-efficiency optical communication systems, and microwave photonics. He has authored and co-authored one book in Chinese and over 50 journal and conference papers on optical transmission systems and microwave photonics. He is a member of IEEE.

Ekawit Tipsuwannakul (ekawit@chalmers.se) received his BSc degree from Chulalongkorn University, Bangkok, in 2004. He received his MSc degree from the Royal Institute of Technology (KTH), Stockholm, in 2008. He is currently working toward his PhD degree at Chalmers University of Technology, Göteborg, Sweden. From 2004 to 2006, he was a test engineer at the Optical Transmitter/Receiver Manufacturing Group, Fabrinet Co. Ltd, Bangkok. In 2006, he joined Svedice/Northlight AB, Stockholm, and spent two years designing systems for high-speed optical transmitter/receiver characterizations. His research at Chalmers is in the area of high-speed optical transmission systems using multilevel modulation formats and all-optical signal processing.

Magnus Karlsson (magnus.karlsson@chalmers.se) received his PhD in 1994, and since 2003, has been a professor of photonics at Chalmers University of Technology, Sweden. His research interests are linear and nonlinear fiber transmission effects and multilevel modulation in optical communication systems. He has authored or co-authored around 200 scientific journal and conference papers, served as guest editor for the *Journal of Lightwave Technology*, and is currently associate editor of *Optics Express*. He has served in the technical program committee for the Optical Fiber Communication Conference (OFC), and is currently active in the TPCs for the Asia Communications and Photonics Conference (ACP) and the European Conference on Optical Communications (ECOC). He is a fellow of the Optical Society of America.

Peter Andrekson (peter.andrekson@chalmers.se) received his PhD from Chalmers University of Technology, Sweden, in 1988. After three years with AT&T Bell Laboratories, he returned to Chalmers University of Technology where he is now a full professor in the Department of Microtechnology and Nanoscience. From 200 to 2003, he was director of research at Cenix Inc. in Allentown, PA. From 2003 to 2004, he worked with the newly established Center for Optical Technologies at Lehigh University, Bethlehem, PA. His research interests optical amplifiers, nonlinear pulse propagation, all-optical functionalities, and very high capacity transmission. He is co-founder of the optical test and measurement company, Picosolve Inc., which is now part of EXFO (he is director of EXFO Sweden AB). Andrekson is a fellow of the Optical Society of America and a fellow of the IEEE. He is the author of about three hundred fifty scientific publications and conference papers on optical communications, among which eighty were invited papers at leading international conferences and journals, including two tutorials at the Optical Fiber Communication Conference (OFC) in 2004 and 2011. He is an elected member of the Board of Governors for the IEEE Photonics Society and has served on several technical program committees, including those for OFC and ECOC. He is an international project and candidate evaluator, and has twice served as an expert for the evaluation of the Nobel Prize in Physics. From 2003–2007, he was an associate editor for *IEEE Photonics Technology Letter*. In 1993 he was awarded a prize from the Swedish government research committee for outstanding work performed by young scientists. In 2000, he was awarded the Telenor Nordic research award for his contribution to optical technologies.

From P. 17

- [16] W.-R. Peng, X. Wu, V. R. Arbab, K.-M. Feng, B. Shamee, L. C. Christen, J.-Y. Yang, A. E. Willner, and S. Chi, "Theoretical and experimental investigations of direct-detected RF-tone assisted optical OFDM systems," *J. Lightwav. Technol.*, vol. 27, no. 10, pp. 1332–1339, May 2009.
- [17] A. J. Lowery, "Amplified spontaneous noise limit of optical OFDM lightwave systems," *Opt. Express*, vol. 16, no. 2, pp. 860–865, Jan. 2008.
- [18] W.-R. Peng, K.-M. Feng, A. Willner, "Ultimate sensitivity for optically pre-amplified direct-detected OFDM systems using spectrally-matched optical filters," *IEEE Photon. Technol. Lett.*, vol. 21, no. 23, pp. 1764–1766, Dec. 2009.
- [19] K. Nikitopoulos and A. Polydoros, "Phase-impairment effects and compensation algorithms for OFDM systems," *IEEE Trans. Comm.*, vol. 52, no. 12, pp. 698–707, Dec. 2004.
- [20] W.-R. Peng, B. Zhang, X. Wu, K.-M. Feng, A. E. Willner, S. Chi, "Compensation for IQ imbalances and bias deviation of the Mach-Zehnder modulators in direct-detected optical OFDM systems," *IEEE Photon. Technol. Lett.*, vol. 21, no. 2, pp. 103–105, Jan. 2009.
- [21] A. Amin, S. L. Jansen, H. Takahashi, I. Morita, and H. Tanaka, "A hybrid IQ imbalance compensation method for optical OFDM transmission," *Opt. Express*, vol. 18, no. 5, pp. 4859–4866, 2010.
- [22] X. Liu and F. Buchali, "Intra-symbol frequency-domain averaging based channel estimation for coherent optical OFDM," *Opt. Express*, vol. 16, no. 26, pp. 21944–21957, 2008.
- [23] A. H. Gnauck, P. J. Winzer, S. Chandrasekhar, X. Liu, B. Zhu, and D. W. Beckham, "Spectrally efficient long-haul WDM transmission using 224-Gbit/s polarization-multiplexed 16-QAM," *IEEE J. Lightwav. Technol.*, vol. 29, no. 4, pp. 373–377, 2011.
- [24] ITU-T Recommendation G.975.1, Appendix I.9, 2004.

Manuscript received: November 30, 2011

Biographies

Wei-Ren Peng (pe-weiren@kddilabs.jp) received his BSEE degree from National Taiwan University in 2001 and his MS and PhD degrees in electro-optical engineering from National Chiao Tung University, Taiwan, in 2003 and 2008. In 2007, he was a visiting researcher at the Optical Communications Laboratory at the University of Southern California. There he conducted experiments on optical orthogonal frequency division multiplexing (O-OFDM) under the supervision of professor Alan Willner. In 2009, he was a postdoctoral fellow at National Chiao Tung University, Taiwan, and focused on analyzing the performance of optical OFDM transmission. He joined KDDI R&D Laboratories Inc. in Feb. 2010 and worked as an associate researcher. Dr. Peng has authored or coauthored more than 80 papers in prestigious journals. He is a peer reviewer for the IEEE and OSA. His research interests include digital impairment compensation for single-carrier and multicarrier transmission.

Itsuro Morita (M'08) (morita@kddilabs.jp) received his BE, ME, and PhD degrees in electronic engineering from the Tokyo Institute of Technology 1990, 1992, and 2005. He joined Kokusai Denshin Denwa (KDD) Company Ltd. (now KDDI Corporation), Tokyo, in 1992 and has worked in the research and development laboratories there since 1994. He has conducted research on long-distance and high-speed optical communication systems. In 1998, he was on leave at Stanford University, CA.

Hidenori Takahashi (M'08) (takahashi@kddilabs.jp) received his BE and ME degrees in electronic engineering from Tohoku University, Japan, in 1998 and 2000. He became a member of KDD R&D Laboratories Inc. (now KDDI R&D Laboratories Inc.) in 2000. From 2006 to 2007, he was a visiting researcher and a fellow of Advanced Study Program (ASP) of Massachusetts Institute of Technology. He is involved in the research and development of silica-based planar waveguide devices, especially the tunable chromatic dispersion compensator. He also researches optical coherent OFDM transmission technologies. Dr. Takahashi is a member of the Institute of Electronics, Information, and Communication Engineers of Japan (IEICE). He received the best paper award of the 7th International Conference on the Optical Internet (COIN '08).

Takehiro Tsuritani (tsuri@kddilabs.jp) received his ME and PhD degrees in electronics engineering from Tohoku University, Miyagi, Japan, in 1997 and 2006. He joined Kokusai Denshin Denwa (KDD) Company, Limited (now KDDI Corporation), Tokyo, Japan, in 1997. Since 1998, he has been working at KDDI R&D Laboratories Inc., conducting research on long-haul wavelength-division multiplexing (WDM) transmission systems and designing and modeling photonic networks.

Super-Receiver Design for Superchannel Coherent Optical Systems

Cheng Liu, Jie Pan, Thomas Detwiler, Andrew Stark, Yu-Ting Hsueh, Gee-Kung Chang, and Stephen E. Ralph

(School of Electrical and Computer Engineering, Georgia Institute of Technology, Atlanta, GA 30332, USA)

Abstract

In this paper, we propose a novel super-receiver architecture for Nyquist-wavelength-division-multiplexing (WDM) superchannel optical coherent systems. As opposed to a conventional coherent receiver, where each subchannel is demodulated independently, the proposed super-receiver jointly detects and demodulates multiple subchannels simultaneously. By taking advantage of information from side channels that use joint DSP to cancel interchannel interference (ICI), the proposed super-receiver performs much better than a conventional receiver. This architecture also has the potential to compensate for cross-channel impairments caused by linear and nonlinear effects. We examine the proposed architecture through experiment and simulation. OSNR is improved by more than 5 dB after 1280 km fiber transmission with narrow channel spacing.

Keywords

superchannel; joint DSP; ICI; coherent receiver

1 Introduction

Superchannel transmission of 1 Tb/s and beyond has recently been proposed as an alternative to electrical OFDM for satisfying the bandwidth requirements of future optical networks. Nyquist wavelength-division multiplexing (WDM) [1]–[4] and coherent optical OFDM (CO-OFDM) [5] are the main technologies used to achieve ultrahigh spectral efficiency in superchannel optical coherent systems. In Nyquist WDM optical coherent systems, conventional WDM carriers are packed tightly for near-baud-rate or baud-rate spacing. In such systems, interchannel interference (ICI) significantly degrades system performance. The conventional way to mitigate ICI in a Nyquist WDM system is to apply strong electrical or optical filtering to each channel and use a digital signal processor (DSP) to cancel the induced ISI [6]. However, there is still strong ISI when the channel spacing is tight near the baud rate. Therefore, we propose a novel coherent receiver architecture called super-receiver for Nyquist WDM systems. The super-receiver detects and demodulates multiple channels simultaneously. Taking advantage of information from side channels that use joint DSP to cancel ICI, the super-receiver performs much better

than a conventional receiver, which processes each channel individually. Because all the side-channel information is available, other cross-channel impairments, such as nonlinear cross-phase modulation (XPM), cross-polarization modulation (XPoIM), and four wave mixing (FWM), can be compensated for. We propose using the super-receiver to jointly estimate carrier phase from the side channel information in carrier-locked Nyquist systems. In this paper, we introduce the super-receiver architecture and describe the joint DSP algorithms that compensate for linear ICI. We assess the algorithms using experimental and simulated data. There is more than 5 dB optical signal-to-noise ratio (OSNR) gain at $\text{BER} = 10^{-3}$ when the channel spacing is at baud rate.

2 Principle and Design

Fig. 1 shows the proposed super-receiver architecture. In Nyquist WDM systems, tightly spaced optical carriers are modulated by independent data and packed together by an optical multiplexer (where ICI is incurred). After optical fiber transmission and optical demultiplexing, each channel is separated and sent to its corresponding coherent receiver for O/E conversion and digital sampling. The local oscillators (LOs) for coherent receivers are generated in the same way

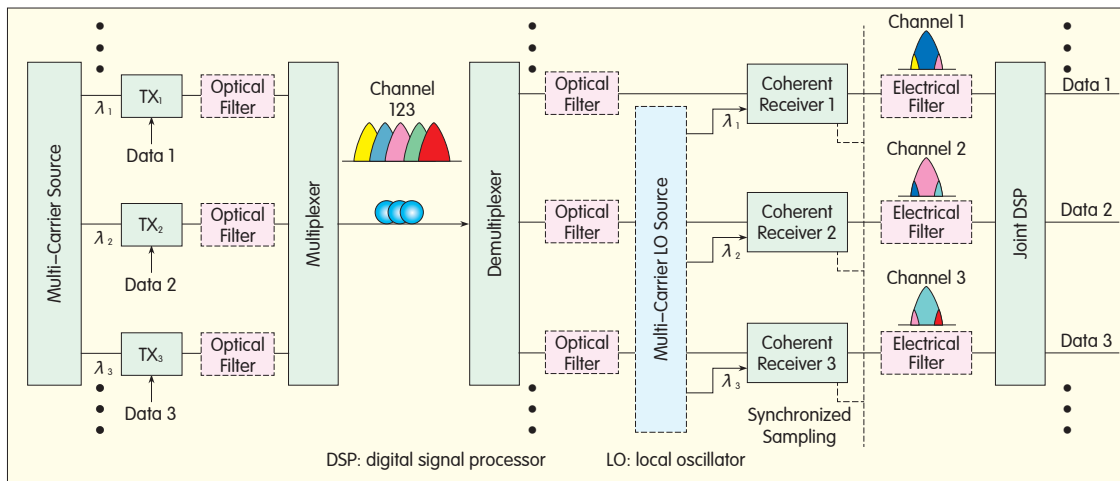


Figure 1. Proposed super-receiver architecture.

as at the transmitter side. The synchronized information across the channels is captured for future joint signal processing. For this reason, the optical path and electrical path of each demultiplexed channel need to be equal in length, and digital sampling must be synchronized across the channels. However, these requirements can be relaxed in a joint DSP block if time-domain memory size is increased (Fig. 2). In a joint DSP block, information is available from multiple channels, and this enables joint signal processing to compensate for both linear and nonlinear impairments between channels. This also enables joint carrier phase recovery in carrier-locked Nyquist WDM systems.

3 Joint DSP Based on Adaptive LMS Algorithm for Cancelling Linear ICI

Fig. 2 shows the proposed joint DSP for cancelling linear

ICI. Three channels are considered, and ICI equalization for the center channel (channel two) is shown. After the three-channel signal is sampled with synchronized ADCs, each channel undergoes conventional DSP, that is, chromatic dispersion compensation, polarization demultiplexing, timing recovery, and carrier phase estimation. After timing recovery and carrier phase recovery, an adaptive ICI equalizer based on adaptive least mean square (LMS) algorithm is used across all three channels for both X and Y polarizations. For each polarization, side channels (channels one and three) are shifted in the frequency domain by the amount of channel spacing. By shifting the side channels into the original spectral location, the overlapped spectra are aligned for subsequent ICI equalizer. After then the signals from the three channels are fed into the ICI filter, where the filter coefficients W_{12} , W_{22} , and W_{32} are jointly and adaptively updated according to the slicing error. Each filter coefficient W_{ij} represents the

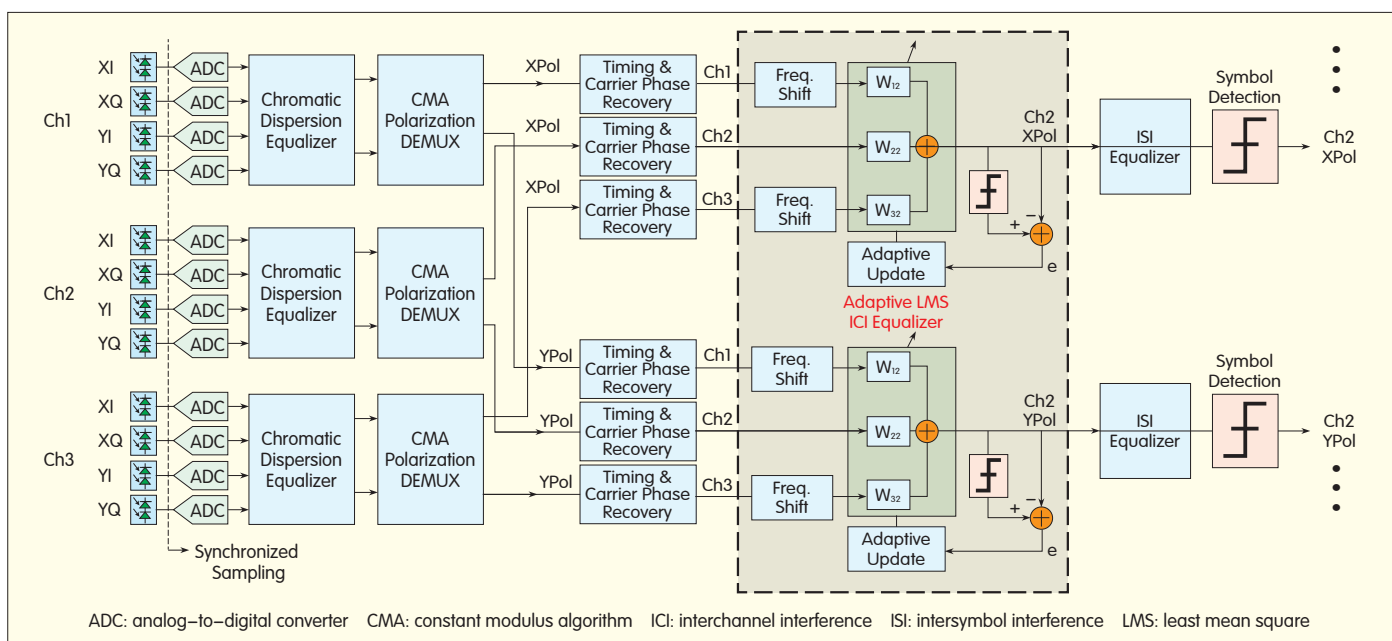
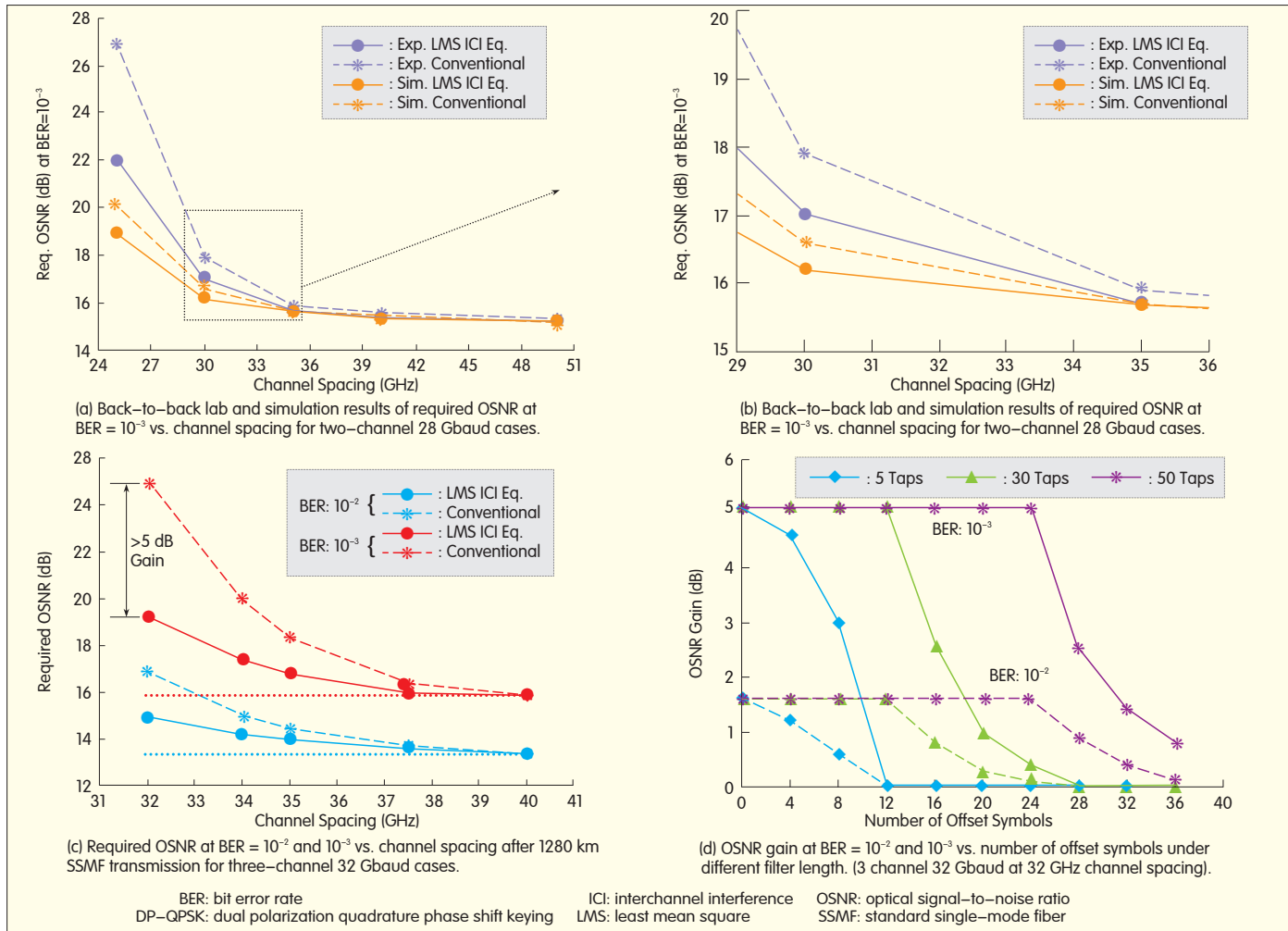


Figure 2. Joint DSP based on adaptive LMS algorithm for cancelling linear ICI.



▲ Figure 3. Comparison of proposed joint LMS ICI equalizer with conventional method.

weighted crosstalk from channel i to channel j . For each W_{ij} , there are a few taps in time domain so that timing offset between channels, caused by imperfect synchronized sampling or path mismatch, can be compensated for. After the ICI equalizer, ISI equalizers are used for each polarization to compensate for the residual ISI induced by optical or electrical filtering in the link. Conventional DSP in Nyquist WDM systems uses an ISI equalizer to compensate for the penalty introduced by strong filtering. However, a joint ICI equalizer relaxes the narrow filter bandwidth and adaptively cancels a significant part of the linear crosstalk. Channel one and three are processed in the same way using information from neighboring channels.

4 Experiment and Simulation Results

We conducted a proof-of-concept experiment on the super-receiver architecture and joint ICI algorithm and compared the results with those using simulated data. Two independent lasers each carrying 28 Gbaud dual-polarization quadrature phase-shift keying (DP-QPSK)

data were MUXed together without optical filters. At the receiver side, the signals were split into two paths and were received by two coherent receivers with synchronized 40 GSa/s Agilent sampling oscilloscopes. The electrical filters at the sampling head were 16 GHz. Fig. 3(a) and (b) shows the OSNR required to reach a BER of 10^{-3} at different channel spacings. The results are shown for experimental and simulated data. When channel spacing decreases, absolute performance degrades in all cases. However, with a joint ICI equalizer, performance degradation is reduced. For this simple two-channel case, there is a 2 dB required OSNR penalty at 30 GHz channel spacing when conventional ISI equalization is used. Joint ICI equalization reduces this penalty by 1 dB.

To give a more complete picture of the proposed system with three-channel conditions, we simulated a 3×32 Gbaud (128 Gb/s) DP-QPSK Nyquist WDM optical coherent system by using RSOF OptSim. The bandwidths of optical filters at optical multiplexing were set to 43.75 GHz in order to shape the signal spectrum. After optical multiplexing, the three channel signals were transmitted through 16 spans of 80 km

SSMF with launch power of 0 dBm per channel. The digital sampling rate was 80 GSa/s per channel, and the bandwidth of the electrical filters at the sampling head were 22 GHz. Fig. 3(c) shows the performance of joint ICI equalization versus that of conventional ICI equalization. We compared the required OSNR for $\text{BER} = 10^{-3}$ and $\text{BER} = 10^{-2}$ at different channel spacings after 1280 km standard single-mode fiber (SSMF) transmission. At $\text{BER} = 10^{-3}$ and channel spacing of 32 GHz (baud rate), the required OSNR using the conventional algorithm was more than 5 dB higher than that using the LMS algorithm in joint ICI equalization. After fiber transmission, the relative OSNR gain was maintained, and absolute performance degraded with longer transmission distance because of increased nonlinearity. Fig. 3(d) shows the timing offset between channels when different filter lengths are used. The ICI equalizer operates with two samples per symbol, so a filter length of five taps spans 2.5 symbols. As long as the number of offset symbols is within the filter memory range, the ICI equalizer is effective. By increasing the filter tap length, the equalizer is more tolerant of timing offset.

5 Conclusion

A novel coherent receiver architecture has been proposed for Nyquist-WDM super-channel systems. A joint DSP algorithm for linear ICI cancellation has been developed and verified using the proposed super-receiver architecture. When the channel spacing is at baud rate, the required OSNR using conventional ICI equalization is more than 5 dB higher than that using joint ICI equalization. As a result, the proposed super-receiver architecture can greatly enhance coherent receiver performance in Nyquist-WDM super-channel systems with high spectral efficiency.

Acknowledgement

This work was supported by the Georgia Tech 100G Consortium.

References

- [1] J. Yu, X. Zhou, M.-F. Huang, D. Qian, P. N. Ji, T. Wang, and P. Magill, "400Gb/s ($4 \times 100\text{Gb/s}$) orthogonal PDM-RZ-QPSK DWDM signal transmission over 1040km SMF-28," *Opt. Express*, vol. 17, Issue 20, pp. 17928–17933, 2009.
- [2] Z. Dong, J. Yu, H.-C. Chien, N. Chi, L. Chen, and G.-K. Chang, "Ultra-dense WDM-PON delivering carrier-centralized Nyquist-WDM uplink with digital coherent detection," *Opt. Express*, vol. 19, Issue 12, pp. 11100–11105, 2011.
- [3] E. Torrenço, R. Cigliutti, G. Bosco, G. Gavioli, A. Alaimo, A. Carena, V. Curri, F. Forghieri, S. Piciaccia, M. Belmonte, A. Brinciotti, A. La Porta, S. Abrate, and P. Poggolini, "Transoceanic PM-QPSK terabit superchannel transmission experiments at baud-rate subcarrier spacing," *36th European Conf. and Exhibition on Optical Commun.*, Torino, Sept. 2010.
- [4] Y. Cai, J. X. Cai, C. R. Davidson, D. Foursa, A. Lucero, O. Sinkin, A. Pilipetskii, G. Mohs, and N. S. Bergano, "High spectral efficiency long-haul transmission with pre-filtering and maximum a posteriori probability detection," *36th European Conf. and Exhibition on Optical Commun.*, Torino, Sept. 2010.
- [5] X. Liu, S. Chandrasekhar, B. Zhu, P. J. Winzer, A. H. Gnauck, and D. W. Peckham, "Transmission of a 448-Gb/s reduced-guard-interval CO-OFDM signal with a 60-GHz optical bandwidth over 2000 km of ULAF and five 80-GHz-grid ROADMs," *2010 Conf. on Optical Fiber Commun., collocated National Fiber Optic Engineers Conf.*, San Diego, CA, Mar. 2010.
- [6] Y. Cai, J. X. Cai, C. R. Davidson, D. Foursa, A. Lucero, O. Sinkin, A. Pilipetskii, G. Mohs, and N. S. Bergano, "Achieving high spectral efficiency in long-haul transmission with pre-filtering and multi-symbol detection," *2010 Asia Commun. and Photonics Conf. and Exhibition*, Shanghai, Dec. 2010, pp. 349–350.

Manuscript received: December 19, 2011

Biographies

Cheng Liu (lch_lian@gatech.edu) received his BS degree in electronics engineering from Peking University in 2008. He is currently pursuing a PhD degree in electrical engineering at Georgia Institute of Technology, Atlanta. He is a member of the Georgia Tech 100G Consortium—an industry and academic research alliance of Verizon, ADVA Optical Networking, Ciena, OFS, and others. In 2010, he was a research intern at the digital communication group of Mitsubishi Electric Research Laboratories in Boston, MA. His research interests include ultrahigh-speed coherent optical transmission systems, radio-over-fiber systems, and wavelength-division multiplexing passive optical networks (WDM PONs). He has authored and co-authored more than 20 peer-reviewed journal papers and international conference proceedings.

Jie Pan (jpan@gatech.edu) received her BS degree in electrical engineering from Nanjing University of Information Science and Technology in 2006. She received MS degrees in electrical engineering and chemical engineering from Miami University, OH. She is currently pursuing a PhD degree in electrical and computer engineering at Georgia Institute of Technology, Atlanta. She is a member of the Georgia Tech 100G Consortium. Her research interests include DSP for superchannel coherent optical systems.

Thomas Detwiler (tom.detwiler@gmail.com) received his BSEE degree (honors) and MSEE degree from the University of Illinois, Urbana-Champaign, in 2000 and 2003. He received his PhD degree at Georgia Institute of Technology, Atlanta, 2011. In 2000, he worked on point-to-multipoint wireless access at WavTrace, which was later acquired by Harris Microwave Communications Division. At Harris Microwave, Thomas was a digital design engineer for point-to-point software-defined microwave radio. In 2006, he joined the FPGA technology development group at Adtran. From 2008 to 2011 he was a member of the Georgia Tech 100G Consortium researching modulation formats and demodulation techniques for coherent optical links.

Andrew Stark (andy.stark@gmail.com) graduated magna cum laude with a BS in electrical engineering from the University of Texas, Dallas, in 2008. He spent a summer at the Los Alamos National Laboratory as part of the Applied Engineering and Technology division. He is currently pursuing his PhD degree in electrical engineering at Georgia Institute of Technology, Atlanta. He is a member of the Georgia Tech 100G Consortium.

Yu-Ting Hsueh (yhsueh3@gatech.edu) received her BS degree in electrical engineering from National Tsing Hua University, Taiwan, in 2003. He received his MS degree in electro-optical engineering from National Chiao Tung University, Taiwan, in 2005. She is currently working toward her PhD degree in electrical and computer engineering at Georgia Institute of Technology, Atlanta. In 2010, she was a research intern in the Optical Networking and Mobile Communications group at NEC Laboratories America. She has authored and co-authored more than 40 peer-reviewed journal papers and international conference proceedings. She is one of the recipients of the 2010 PSC Bor-Wei Chen Memorial Scholarship and IEEE Photonics Society 2011 Graduate Student Fellowship.

Gee-Kung Chang (geekung.chang@ece.gatech.edu) received his BSc degree in physics from the National Tsinghua University, Taiwan. He received his MSc and PhD degrees in physics from the University of California, Riverside. He worked for 23 years at Bell Systems: Bell Labs, Bellcore, and Telcordia Technologies. There, he held various research and management positions, including director and chief scientist of optical Internet research, director of the optical networking systems and testbed, and director of the optical system integration and network interoperability. Prior to joining Georgia Institute of Technology, he was vice president and chief technology strategist for OpNext Inc., an offshoot of Hitachi Telecom. He is currently the Byers Endowed Chair Professor in Optical Networking in the School of Electrical and Computer Engineering, Georgia Institute of Technology. He is also the co-director of the 100G Optical Networking Center at Georgia Tech.

Stephen E. Ralph (stephen.ralph@ece.gatech.edu) is a professor in the School of Electrical and Computer Engineering at Georgia Institute of Technology. He received his BEE degree (honors) from Georgia Institute of Technology and PhD in electrical engineering from Cornell University. Prior to working at Georgia Tech., Dr. Ralph held a postdoctoral position AT&T Bell Laboratories and was a visiting scientist at the Optical Sciences Laboratory at the IBM T. J. Watson Research Center. In 1992, he joined the Physics Department at Emory University. In 1998, he joined Georgia Tech and is founder and director of the new 100 Gbit/s Optical Networking Consortium.

Design of a Silicon-Based High-Speed Plasmonic Modulator

Mu Xu, Jiayang Wu, Tao Wang, and Yikai Su

(State Key Laboratory of Advanced Optical Communication Systems and Networks, Shanghai Jiaotong University, Shanghai 200240, P.R.China)

Abstract

In this paper, we propose a silicon-based high-speed plasmonic modulator. The modulator has a double-layer structure with a 16 μm long metal-dielectric-metal plasmonic waveguide at the upper layer and two silicon single-mode waveguides at the bottom layer. The upper-layer plasmonic waveguide acts as a phase shifter and has a dielectric slot that is 30 nm wide. Two taper structures that have gradually varied widths are introduced at the bottom layer to convert the photonic mode into plasmonic-slot mode with improved coupling efficiency. For a modulator with two 1 μm -long mode couplers, simulation shows that there is an insertion loss of less than 11 dB and a half-wave voltage of 3.65 V. The modulation bandwidth of the proposed modulator can be more than 100 GHz without the carrier effect being a limiting factor in silicon. The fabrication process is also discussed, and the proposed design is shown to be feasible with a hybrid of CMOS and polymer technology.

Keywords

plasmonic phase modulator; gradually varied taper; high speed

1 Introduction

A modulator is a critically important device in optical communication systems and short-reach electro-optical interconnects. Modulation speed continues to improve and is now well above 100 GHz, which rivals the processing speed of state-of-the-art CMOS electronic devices. The silicon optical modulators described in this paper are capable of having a modulation bandwidth of more than 40 GHz [1], depending on whether carrier accumulation [2], carrier injection [3], or carrier depletion [4] is used.

To enable carrier accumulation in silicon, a metal-oxide semiconductor (MOS) structure is preferred. In such a structure, the metal acts as the electrode, and the oxide acts as the barrier. When voltage is applied, free carriers accumulate at the interface between the oxide and the semiconductor. In 2004, A. Liu et al. fabricated the first silicon-based carrier accumulation modulator [2]. Although the device only had 1 GHz bandwidth, it paved the way for future silicon modulators.

Carrier injection can be achieved by using a forward-biased silicon P-I-N diode, and depletion can be achieved by using a reverse-biased silicon P-N diode. In 2007, Q. Xu et al. fabricated a silicon-ring-based carrier-injection modulator with a bandwidth of more than 12.5 GHz [3]. In 2008, S. J. Spector et al. increased the

bandwidth of a silicon-based carrier-injection modulator to more than 26 GHz, even reaching up to 40 GHz [1]. In 2010, Po Dong et al. used silicon carrier-depletion modulators integrated on 0.25 μm long silicon-on-insulator (SOI) waveguides with $V_{\pi}L$ of 1.4 V-cm to show that low energy consumption in a silicon modulator is feasible [4].

One of the limitations of silicon is two-photon absorption (TPA), which makes it hard to further increase modulation bandwidth [5]. To overcome this limitation, a silicon-organic hybrid (SOH) approach has been suggested. By combining silicon waveguides with highly nonlinear electro-optical (EO) organic materials or high-absorption multilayer III-V Quantum well materials, the modulation speed can be increased to more than 30 GHz [6],[7]. In 2011, L. Alloatti et al. developed an SOH-platform-based electro-optic modulator that operated at 42.7 Gb/s and had a $V_{\pi}L$ of about 9 V-mm [6].

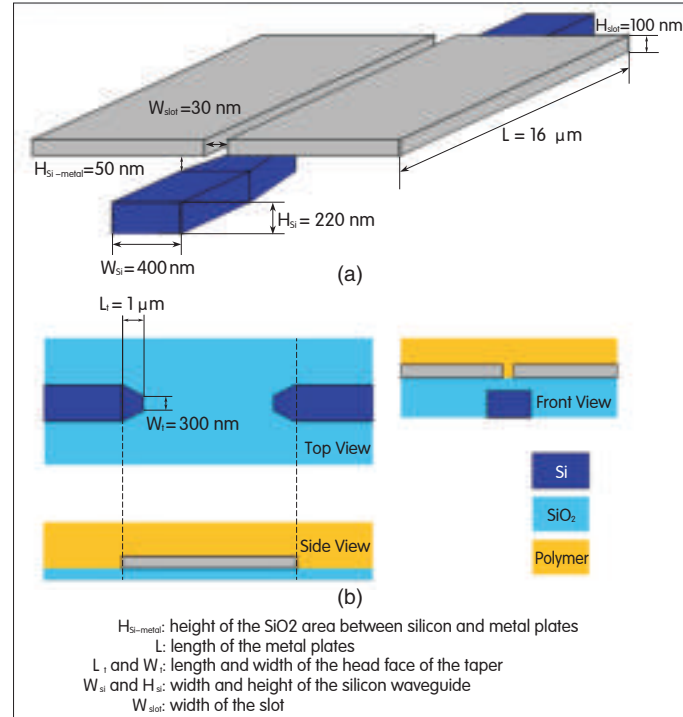
Although the response speed of $\chi^{(2)}$ nonlinearity in organic material can be at least 165 GHz [8], the speed of the practical modulator is still limited because of the weak confinement, which causes a considerable proportion of light to leak into the transparent silicon electrodes. Recent progress in plasmonic silicon photonics has greatly improved confinement in the waveguides, and this is promising for the design of future ultracompact photonic devices. However, although confinement is improved, optical loss increases because of Ohmic loss in the metal and scattering at the grain

boundaries [9]. These prevent plasmonic devices from many long-range and large-scale applications. Several silicon-based modulators with plasmonic waveguides have been theoretically described [10], [11]. In 2011, S. Zhu et al. fabricated a metal insulator silicon-based plasmonic modulator [12]. The modulator was 4 μm long and included two couplers. Although they are compact, the schemes in [10]–[12] have large loss and low modulation efficiency.

2 Device Structure and Mode Confinement

The structure of the phase modulator comprises two layers. The bottom layer comprises two unconnected silicon waveguides coated with silicon oxide for converting between photonic mode and plasmonic mode (Fig. 1). The waveguides have cross-sections of $400 \times 220 \text{ nm}^2$. The upper layer mainly comprises two parallel symmetric metal plates made from, for example, silver, and coated with an EO polymer to form an MDM structure. The polymer fills a 30 nm wide gap. The metal plates are 16 μm long and 100 nm wide and extend to both sides in order to enable electrodes to contact. The overlap between the bottom silicon waveguides and the upper metal plates ranges in length from 1 to 1.5 μm and is mainly determined by the coupling length between the different modes supported by silicon and MDM waveguides. Two gradually varied tapers are introduced at the overlapping area of the silicon waveguides in order to enhance coupling efficiency. The proposed width of the taper's end face is 400 nm, and the proposed width of the taper's head face is 300 nm.

The phase modulator uses the Pockels effect of a nonlinear polymer to produce refractive index variation and phase shift. With an appropriate synthesis and poling process, there is great potential for the nonlinear EO to have a high EO coefficient [13], large dynamic refractive index range [14], and greater resistance relative to other material fabrication processes [15]. However, in most EO-polymer-based SOH modulators, the confinement capability of the dielectric waveguides is limited, and modulation efficiency is greatly reduced by the mode energy leaking from the polymer area into the silicon waveguides. Nevertheless, plasmonic waveguides such as conductor-gap dielectric (CGD) and MDM may be a promising solution to improving mode confinement of the polymer area and increasing the refractive index tuning efficiency. Fig. 2 shows the contrast between the electric field intensity profiles of the MDM-slot waveguide and the silicon-slot waveguide that is coated with a polymer with refractive index of 1.63. The height of the plasmonic-slot waveguide is 100 nm, and the width of the slot is 30 nm. The height of the silicon-slot waveguide is 220 nm, and the width of the slot is 30 nm. Using the finite-difference time-domain (FDTD) method, we calculate the electric field energy within the slot regions defined by the white dotted lines in Fig. 2. In the plasmonic-slot waveguide in Fig. 2(a), 69.335% of the electric-field energy is confined within the slot. In the silicon-slot waveguide, shown in Fig. 2(b), 27.956% of the electric field energy is confined within the slot because of



▲ Figure 1. Structure of the silicon-based plasmonic phase modulator: (a) overall perspective of the phase modulator without coating materials, (b) top view of the bottom layer, side and front view of the phase modulator.

considerable leakage of the mode into the silicon slab. With a larger proportion of the light accumulated in the slot region, modulation can be improved by a factor of two.

3 Key Technologies for a High-Speed Plasmonic Phase Modulator

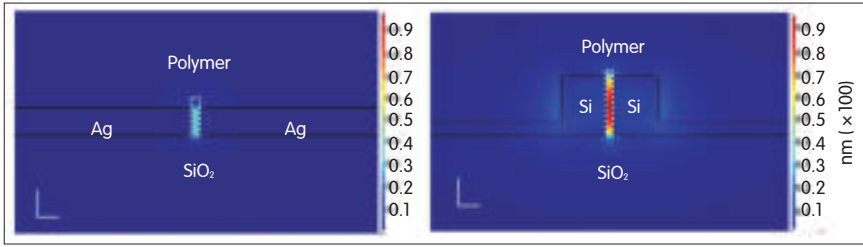
3.1 Phase Modulation and High-Speed Characteristic

After efficient poling [16], the EO polymer has a high EO coefficient of 100–200 pm/V. The proposed device uses AJLS103 EO polymer cross-linked with polymethyl methacrylate (PMMA) [15] with a refractive index, n_e , of approximately 1.63 and an EO coefficient, γ_{33} , of approximately 150 pm/V at 1550 nm wavelength. Nonlinear EO polymers typically have a very high resistivity of more than $10^{11} \Omega \cdot \text{cm}$ [17], so the two parallel metal plates comprising the slot are electrically isolated and can be used as the modulator electrodes. Then, the refractive index variance of the polymer under applied voltage can be expressed as

$$\Delta n = \frac{1}{2} n_e^3 \gamma_{33} \frac{V}{d} \quad (1)$$

where V is the applied voltage and d is the slot width. The phase shift induced by the refractive index variance can be expressed as

$$\Delta \phi = \frac{2\pi}{\lambda} \Delta n L \quad (2)$$



▲ Figure 2. Electric field-intensity mode profiles of (a) plasmonic-slot waveguide and (b) silicon-slot waveguide. The intersecting lines (bottom left) indicate a scale of 100 nm.

where l is the effective modulation length and Γ is the proportion of the electric field energy inside the polymer slot. Phase modulation can be plotted against voltage for $l = 14 \mu\text{m}$, $d = 30 \text{ nm}$, and $\Gamma = 70\%$, and the half-wave voltage $V_\pi = 3.652 \text{ V}$ can be read from the curve at phase shift π (Fig. 3). In (1), the maximum refractive index variance is 0.0392, and this is achievable using the proposed high-nonlinear EO polymer [14], [18]. The loss in the plasmonic MDM-slot waveguide is $0.38 \text{ dB}/\mu\text{m}$ and is calculated using FDTD simulation. The loss in the phase shifter is $0.38 \times l$, where $l = 5.32 \text{ dB}$. The half-wave voltage-length product can be as small as $0.0051 \text{ cm} \cdot \text{V}$ with $V_\pi = 3.652 \text{ V}$. A phase-shifter loss of 5.32 dB is tolerable. The intersection of the red dotted lines in Fig. 3 is the value of the half-wave voltage that leads to a π phase shift.

One of the attractive features of the plasmonic phase modulator is its potential for high modulation speed because it is compact and has strong optical confinement in the slot. In the proposed design, the polymer can be treated as an insulator. Fig. 4 shows the schematic of the plasmonic-slot waveguide. The two parallel metal plates with sandwiched EO polymer form a capacitor. The anode and cathode are fabricated over the extended silver plates to enable electrical signal input. From $C = \epsilon_0 \epsilon_r A/d$, the capacity is nearly on the order of several fF. The permittivity of the vacuum is ϵ_0 ; the dielectric constant of 2.657 is ϵ_r , the lateral area of the metal plates is A ; and the thickness of the metal plates is d . The modulation bandwidth, f_{max} , is proportional to $1/RC$, where R is the external loading resistance ($R = 50 \Omega$ in plasmonic modulator designs) [19]. The modulation bandwidth can be on the order of terahertz, which exceeds the processing bandwidth of state-of-the-art electronic CMOS devices. In plasmonic modulators, the metal parts can be used as electrodes to conduct signal voltage directly to the active material. This is unlike silicon photonic modulators, which rely on free carriers in the semiconductor to transport electrical signals. Thus, the time τ needed for the free-carrier transport process can be significantly reduced, and this greatly increases the response speed of the model shown in Fig. 4.

3.2 Photonic to Plasmonic Mode Conversion

Because of the internal loss mechanism of metal towards light at the wavelength of 1550 nm , plasmonic slot waveguides have larger optical loss compared with silicon waveguides, and this prevents plasma waves from being

used in far-reach and large-scale applications [20]. Couplers used for converting photonic and plasmonic modes rely on silicon waveguides as the optical transmission medium and are very important. We propose a gradually varied taper for conversion in the plasmonic phase modulator. The taper overlaps underneath the plasmonic-slot waveguide with longitude of about $1 \mu\text{m}$. The width of the taper's end face is 400 nm , and the width of the taper's head face is 300 nm .

To achieve high coupling efficiency between the photonic and plasmonic modes, correctly configuring the overlap between the upper plasmonic waveguide and bottom silicon waveguides is critical. Here, we analyze the cross-section in the overlapping area with the upper and bottom waveguides in Fig. 5. There is an efficient coupling process in the two-layer parallel waveguides structure [21]; thus, from coupling mode theory, we can assume that even modes and odd modes appear coincidentally within the proposed double-layer distribution [22]. The coupling between the photonic and plasmonic modes can be modeled as a process of the modes' propagation and interference. The coupling length, l_c , is given by

$$l_c = \frac{\pi}{|\beta_e - \beta_o|} \quad (3)$$

where β_e and β_o are the corresponding optical propagation constants of the even modes and odd modes, respectively. The maximum optical power coupled from one waveguide to

Figure 3. Phase modulation versus applied voltage.

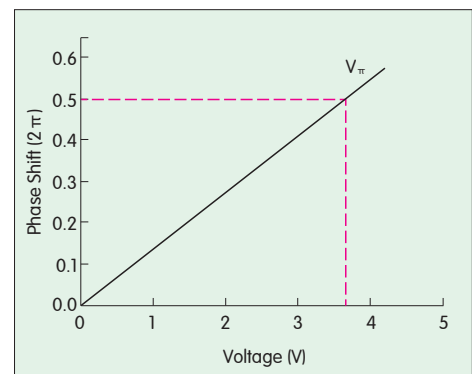
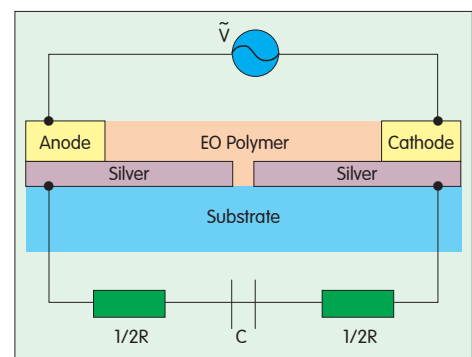
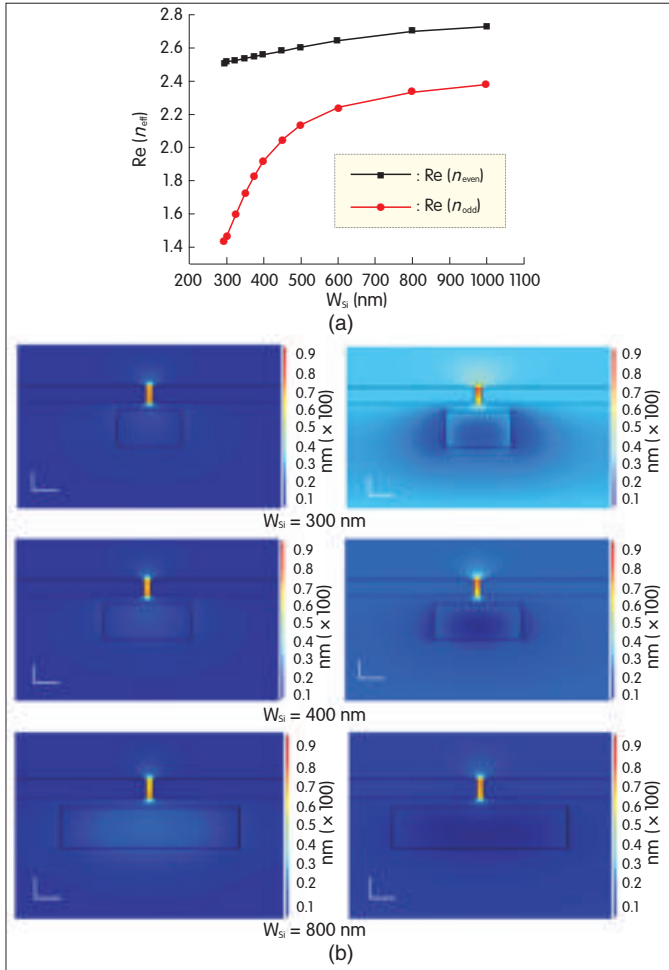


Figure 4. The electrical characteristic model of the proposed phase modulator.





▲ Figure 5. (a) Effective refractive index of even and odd modes versus W_{si} in the proposed double-layer waveguide profile, (b) E_x component intensity of the even (left) and odd (right) TE modes at W_{si} of 300 nm, 400 nm, and 800 nm.

the other is modeled in [21] and given by

$$\rho_{\text{max}} \propto \frac{\exp(-2x \arctan(x^{-1}))}{1+x^2} \quad (4)$$

where $x = 2l_c/\pi l_p$, and l_p is the average attenuation length of the lossy waveguides. From (4), given the loss coefficient of the waveguides, higher maximum transferring optical power can be achieved with shorter coupling. Fig. 5(a) shows the contrast between the effective refractive index of the even and odd modes in the profile of the proposed double-layer waveguides. Fig. 5(b) shows the electric field intensities, E_x , of the two modes at silicon waveguide widths of 300 nm, 400 nm, and 800 nm. The horizontals in the 90° angles (bottom left) are a scale of 100 nm, and the verticals are a scale of 100 nm. These electric field intensities are obtained using FDTD. Both even and odd modes are transverse electric (TE) modes and are dominant inside the plasmonic-slot waveguide. As the width of the silicon waveguide becomes narrower, the difference between the effective refractive index of the two modes becomes larger,

leading to a shorter coupling length (Fig. 6). Thus, from (4), a larger fraction of power coupling from one waveguide to another is also achieved. Reducing the width of the silicon waveguide can improve coupling efficiency. However, if the dimensions of the silicon waveguide are too small, the magnetic field is less confined within the core and a larger proportion of Poynting vector leaks into the cladding. Thus, the mode of the optical field is cut off. In waveguide optics, such a process can be quantified as a normalized propagation constant [23]:

$$B = \frac{n_{\text{eff}} - n_{\text{clad}}}{n_{\text{core}} - n_{\text{clad}}} \quad (5)$$

where n_{eff} is the effective refractive index of the optical mode, and n_{clad} and n_{core} are the refractive indexes of the cladding and core area within the waveguides. If $B \leq 0$, the effective refractive index of the particular mode is less than that of the cladding, and the mode is cut off [23]. The B curve for the proposed waveguides at the overlapping area is plotted in Fig. 7. When the width of the silicon waveguide is less than 295 nm, the normalized propagation constant of the TE odd mode is less than zero, and the mode is cut off. Therefore, the proposed couplers use two tapers with widths that gradually vary from 400 nm at the end face to 300 nm at the head face. These tapers reduce the coupling length to the greatest possible extent, and the TE odd mode is not cut off.

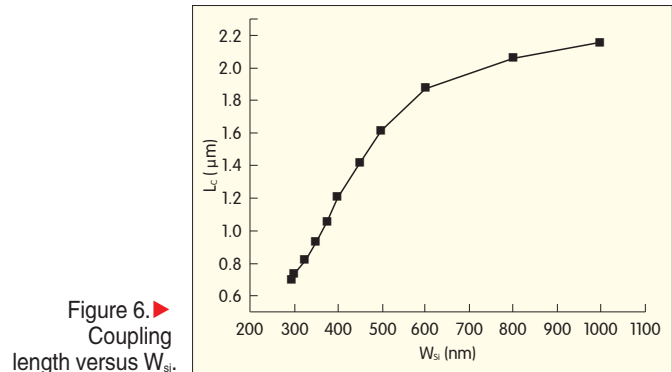
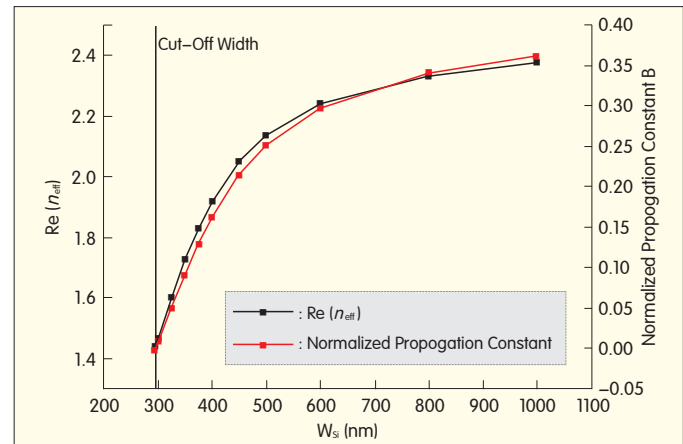
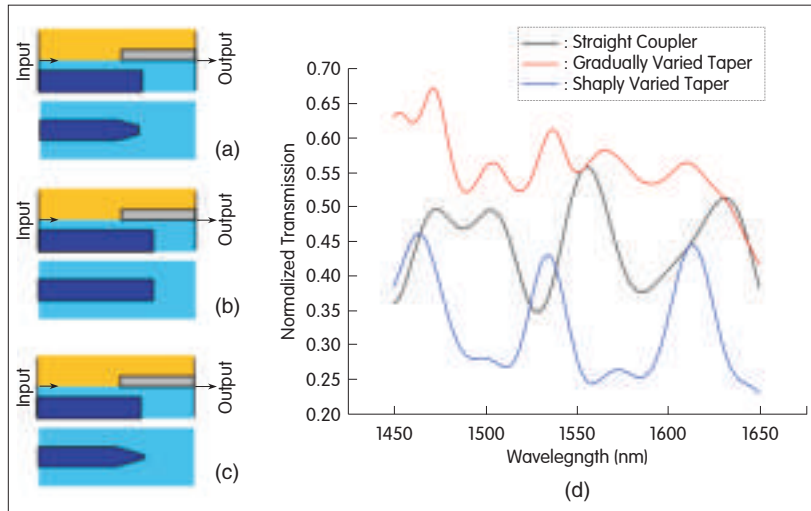


Figure 6. Coupling length versus W_{si} .



▲ Figure 7. Effective refractive index and normalized propagation constant of photonic mode versus W_{si} .



▲ Figure 8. Coupling efficiency for (a) the proposed taper with a width that gradually changes from 400 nm to 300 nm, (b) straight waveguide without taper, and (c) taper with a width that changes sharply from 400 nm to 80 nm. d) Output transmission for the three coupling structures.

Three-dimensional simulations of coupling efficiency are performed using FDTD (Fig. 8). Three coupling structures are introduced: 1) the proposed taper with a width that gradually changes from 400 nm to 300 nm (Fig. 8a), 2) a straight waveguide without taper (Fig. 8b), and 3) a taper structure with a width that changes sharply from 400 nm to 80 nm (Fig. 8c). The overlapping longitudinals of the first and second coupling structures are tuned nearly to their matched coupling lengths of 1 μm and 1.3 μm , respectively. The third structure has the same overlapping longitude as the first structure. The light fields are coupled into the plasmonic-slot waveguides and propagate for the same distance (1.5 μm) inside the slot. Their transmission curves are measured at the output port and plotted in Fig. 8(d). The resonated peaks on the curves in Fig. 8(d) are caused by the Fabry-Perot effect, which occurs because of the reflection of the end faces. Fig. 8 (a) to (d) shows that the gradually varied taper has better coupling efficiency because it has the largest transmission coefficient at 1450 nm to 1650 nm wavelength. The coupler comprising a straight waveguide has a weaker transmission coefficient because of the longer coupling length, and this leads to a lower maximum fraction of power coupling into the plasmonic-slot waveguide. The coupler with sharply varied taper has the lowest coupling efficiency, which is possibly due to the mode being cut off when the width is below 295 nm. These results show that a gradually varied taper improves mode conversion efficiency by using a short coupling length. The steady-state input and output electric field-intensity distributions of the couplers with gradually varied tapers are shown in Fig. 9(a) to (d). These distributions are calculated using the FDTD method for a wavelength of 1550 nm. The electric-field energy first transfers from the silicon waveguide to the plasmonic-slot waveguide (Fig. 9a and b). Then it is coupled into the silicon waveguide again (Fig. 9c and d), which confirms the feasibility and reliability of

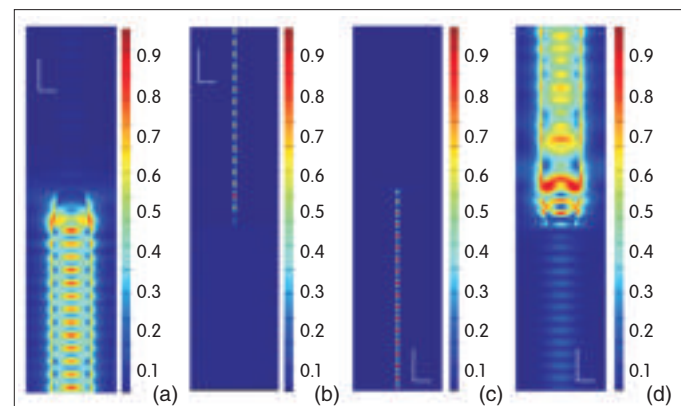
the couplers for the proposed phase modulator.

4 Fabrication Feasibility

A feasible fabrication process is described in [24]–[26]. First, 100 nm of silicon oxide is deposited on the SOI wafer. The silicon is 240 nm thick, and the buried oxide is 3 μm thick in order to act as hard mask. The pattern is transferred using photoresist and electron-beam lithography. Then, the oxide is etched using reactive ion etching (RIE). After stripping the resist, an inductively coupled plasma (ICP) etcher is used to etch the silicon. The silicon waveguides are 400 nm wide and 220 nm high, and the tapers vary from 400 nm to 300 nm in width. The device is cladded with 50 nm oxide using spin-on-glass. Second, the device window for metal evaporation is opened by a focused ion beam (FIB) on a bilayer photoresist structure over the oxide coating. Then, a 100 nm thick silver film is deposited by electron-beam evaporation. Silver is preferred because it does not oxidize easily and has a relatively small plasmonic loss at a wavelength of 1550 nm. After that, lift-off is performed in acetone to obtain the final metal-slot waveguide. Third, the EO polymer cladding is prepared using AJLS103 cross-linked with a PMMA host, and the refractive index of the polymer is approximately 1.63 at 1550 nm. A spin-coating technique needs to be used, and to achieve a high EO coefficient inside the slot, the polymer should be properly poled before the device is operated. This poling requires a large field intensity (greater than 100 V/ μm) to be applied to the two parallel metal plates as an anode and cathode.

5 Conclusion

In this paper, we have proposed a silicon-based



▲ Figure 9. Steady state electric field intensity distributions of (a) the input silicon waveguide, (b) the plasmonic-slot waveguide that overlaps above the input silicon waveguide, (c) the plasmonic-slot waveguide that overlaps above the output silicon waveguides, and (d) the output silicon waveguide. The horizontal in the 90° angle in (a)–(d) are a scale of 200 nm, and the verticals are a scale of 1 μm .

high-speed plasmonic phase modulator. The modulator is based on a double-layer vertical distributed structure. The bottom layer comprises two silicon waveguides, which are 400 nm wide and 220 nm high, together with tapers that vary from 400 nm to 300 nm in width and are 1 μ m long. A 16 μ m long MDM plasmonic-slot waveguide is laid on the top layer, which overlaps the lower silicon waveguides by about 1 μ m at each side. The slot is filled with a high second-order nonlinear polymer with χ_{33} of 150 pm/V at 1550 nm wavelength. The Pockels effect of the polymer is applied for EO modulation. Because of the strong confinement of the metal slot and ultrafast response speed of the Pockels effect, the modulation speed can reach hundreds of gigahertz. By introducing a compact, gradually varied taper structure, conversion from photonic modes to plasmonic modes is highly efficient. The feasibility of manufacturing the proposed device has also been discussed. A silicon-based high-speed plasmonic phase modulator is promising for future ultrahigh-speed optical communication networks or silicon interconnects between CMOS chips.

Acknowledgement

This work was supported in part by National Natural Science Foundation of China (61077052/61125504), and Science and Technology Commission of Shanghai Municipality (11530700400).

References

- [1] S. J. Spector, M. W. Geis, G.-R. Zhou, M. E. Grein, F. Gan, M. A. Popovic, J. U. Yoon, D. M. Lennon, E. P. Ippen, F. Z. Kärtner, and T. M. Lyszczarz, "CMOS-Compatible Dual-Output Silicon Modulator for Analog Signal Processing," *Optics Express*, vol. 16, no. 15, pp. 11027–11031, 2008.
- [2] A. Liu, R. Jones et al. "A High-Speed Silicon Optical Modulator Based on a Metal-Oxide-Semiconductor Capacitor," *Nature*, vol. 427, pp. 615–618, Feb. 2004.
- [3] Q. Xu, B. Schmidt et al., "12.5 Gb/s Carrier-Injection-Based Silicon Micro-Ring Silicon Modulators," *Optics Express*, vol. 15, no. 2, pp. 430–436, 2007.
- [4] N. Feng, S. Liao et al. "High Speed Carrier-Depletion Modulators with 1.4V-cm V π L Integrated on 0.25 μ m Silicon-on-Insulator Waveguides," *Optics Express*, vol. 18, no. 8, pp. 7994–7999, 2010.
- [5] L. Yin, G. P. Agrawal, "Impact of Two-Photon Absorption on Self-Phase Modulation in Silicon Waveguides," *Opt. Lett.*, vol. 32, no. 14, pp. 2031–2033, 2007.
- [6] L. Alloati, D. Korn, R. Palmer et al. "42.7 Gb/s Electro-Optic Modulator in Silicon Technology," *Optics Express*, vol. 19, no. 12, pp. 11841–11851, 2011.
- [7] Y. Tang, Hui-Wen Chen, S. Jain, J. D. Peters, U. Westergren, J. E. Bowers, "50 Gb/s Hybrid Silicon Traveling-Wave Electroabsorption Modulator," *Optics Express*, vol. 19, no. 7, pp. 5811–5816, 2011.
- [8] B. Bartosz, H. Yu-Chueh et al. "Electrooptic Polymer Ring Resonator Modulation up to 165 GHz," *IEEE J. Selected Topics in Quantum Elect.*, vol. 13, no. 1, pp. 104–110, 2007.
- [9] J. A. Dionne, L. A. Sweatlock, H. A. Atwater et al. "Plasmon Slot Waveguides: Towards Chip-Scale Propagation with Subwavelength-Scale Localization," *Phys. Rev. B*, vol. 73, no. 3, Jan. 2006. [Online]. Available: <http://prb.aps.org/abstract/PRB/v73/i3/e035407>.
- [10] J. A. Dionne, L. A. Sweatlock, M. T. Sheldon et al. "Silicon-Based Plasmonics for On-Chip Photonics," *IEEE J. Selected Topics in Quantum Elect.*, vol. 16, no. 1, pp. 295–306, 2010.
- [11] Shiyang Zhu, G. Q. Lo, D. L. Kwong, "Theoretical Investigation of Silicon MOS-Type Plasmonic Slot Waveguide Based MZI Modulators," *Opt. Express*, vol. 18, no. 26, pp. 27802–27819, 2010.
- [12] Shiyang Zhu, G. Q. Lo, D. L. Kwong, "Electro-Absorption Modulation in Horizontal Metal Insulator Silicon Insulator Metal Nanoplasmonic Slot Waveguides," *Appl. Phys. Lett.*, vol. 99, no. 15, pp. 151114–151114–3, Oct. 2011.
- [13] J. Luo, X.-H. Zhou, A. K.-Y. Jen, "Rational Molecular Design and Supramolecular Assembly of Highly Efficient Organic Electro-Optic Materials," *J. Mater. Chem.*, vol. 19, no. 40, pp. 7410–7424, 2009.
- [14] T. Yovcheva, T. Babeva, K. Nikolova, G. Mekishev, "Refractive Index of Corona-Treated Polypropylene Films," *J. Opt. A: Pure Appl. Opt.*, vol. 10, no. 5, Apr. 2008.
- [15] Haishan Sun, A. Pyajit, Jingdong Luo, Zhengwei Shi, S. Hau, A. K.-Y. Jen, L. R. Dalton, A. Chen, "All-Dielectric Electrooptic Sensor Based on a Polymer Microresonator Coupled Side-Polished Optical Fiber," *IEEE Sensors J*, vol. 7, no. 4, pp. 515–524, Apr. 2007.
- [16] Su Huang, Tae-Dong Kim, Jingdong Luo et al., "Highly efficient electro-optic polymers through improved poling using a thin TiO₂-modified transparent electrode," *Appl. Phys. Lett.*, vol. 96, no. 24, pp. 243311, Jun. 2010.
- [17] Xiaomeng Sun, Linjie Zhou, Xinwan Li, Zehua Hong, and Jianping Chen, "Design and analysis of a phase modulator based on a metal-polymer-silicon hybrid plasmonic waveguide," *Appl. Opt.*, vol. 50, no. 20, pp. 3428–3434, Jul. 2011.
- [18] Y. Enami, J. Hong, C. Zhang, J. Luo, A. K. Jen, "Optical Transmission Stability of Hybrid Sol-Gel Silica/Electrooptic Polymer Waveguide Modulators," *IEEE Photonics Tech. Lett.*, vol. 23, no. 20, pp. 1508–1510, Oct. 2011.
- [19] Wenshan Cai, J. S. White, M. L. Brongersma, "Compact, High-Speed and Power-Efficient Electrooptic Plasmonic Modulators," *Nano Letters*, vol. 9, no. 12, pp. 4403–4411, 2009.
- [20] S. A. Maier, *Plasmonics: Fundamentals and Applications*. New York: Springer, pp. 21–34, 2010.
- [21] G. Roelkens, O. Raz, W. M. J. Green, S. Assefa et al., "Towards a Low-Power Nanophotonic Semiconductor Amplifier Heterogeneously Integrated with SOI Waveguides," *7th IEEE Int. Conf. Group IV Photonics*, Hong Kong, Sep. 2010, pp. 16–18.
- [22] G. Veronis and Shanhui Fan, "Crosstalk Between Three-Dimensional Plasmonic Slot Waveguides," *Opt. Express*, vol. 16, no. 3, pp. 2129–2140, 2008.
- [23] A. W. Snyder, J. D. Love. *Optical Waveguide Theory*. New York: Chapman and Hall, 1983.
- [24] Biswajeet Guha, B. Bernardo, C. Kyotoku, M. Lipson, "CMOS-Compatible Athermal Silicon Microring Resonators," *Opt. Express*, vol. 18, no. 4, pp. 3487–3493, 2010.
- [25] Jie Tian, Shuqing Yu, Wei Yan, Min Qiu, "Broadband High-Efficiency Surface-Plasmon-Polariton Coupler with Silicon-Metal Interface," *Appl. Phys. Lett.* vol. 95, pp. 013504, Jul. 2009.
- [26] R. Ding, T. Baehr-Jones, Y. Liu, R. Bojko, J. Witzens, S. Huang, J. Luo, S. Benight, P. Sullivan, J.-M. Fedeli, M. Fournier, L. Dalton, A. Jen, and M. Hochberg, "Demonstration of a Low V π L Modulator with GHz Bandwidth Based on Electro-Optic Polymer-Clad Silicon Slot Waveguides," *Opt. Express*, vol. 18, pp. 15618–15623, 2010.

Manuscript received: November 30, 2011

Biographies

Mu Xu (xumu@sjtu.edu.cn) is master's candidate at the State Key Laboratory of Advanced Optical Communication Systems and Networks, Shanghai Jiaotong University. He received his BS degree from the Department of Sophisticated Instruments and Optoelectronics Engineering, Tianjin University, in 2010. His research interests include silicon photonics and plasmonic photonics.

Jiayang Wu (jiayangwu@sjtu.edu.cn) is a PhD candidate at the State Key Laboratory of Advanced Optical Communication Systems and Networks, Shanghai Jiaotong University. He received his BS degree in communication engineering from Xidian University in 2010. His research interests include silicon photonics and micro-fabrication technology of photonic devices.

Tao Wang (wangtao2007@sjtu.edu.cn) is PhD candidate at the State Key Laboratory of Advanced Optical Communication Systems and Networks, Shanghai Jiaotong University. He received his BS degree in electronic engineering from the Department of Electronic Engineering, Shandong University, in 2004. He received his MS degree from the Chinese Academy of Sciences in 2007. His research interests include optical signal processing, silicon photonics, and micro-fabrication technology in photonic devices.

Yikai Su (yikaisu@sjtu.edu.cn) received his BS degree from Hefei University of Technology, China, in 1991. He received his MS degree from Beijing University of Aeronautics and Astronautics (BUAA) in 1994 and his PhD degree in electronic engineering from Northwestern University, IL, in 2001. He worked for Bell Laboratories at Crawford Hill for three years before joining Shanghai Jiao Tong University, Shanghai, as a full professor in 2004. His research interests include optical signal processing in nano-photonic devices, ultra-fast signal transmission, and display optics. He has authored approximately 200 publications in international journals and conferences. He holds five US patents and has more than 20 US or Chinese patents pending.

The Key Technology in Optical OFDM-PON

Xiangjun Xin

(Beijing University of Posts and Telecommunications, Beijing 100876, P.R.China)

Abstract

In this paper, a novel optical access network based on orthogonal frequency division multiplexing (OFDM) is proposed. An OFDM-based passive optical network (PON) uses multicarriers to carry different information that is transmitted to different optical network units (ONUs). In this paper, system performance is analyzed for OFDM-PON with different linewidths of the lightwave source, different optical signal-to-noise ratio (OSNR), different access distances, and different modulated formats. Colorlessness in the OFDM-PON is also analyzed. Finally, a 40 Gb/s baseband OFDM-PON with two carriers and achieve error-free performance over 25 km fiber transmission is proposed.

Keywords

optical OFDM; passive optical network (PON); colorless upstream

1 Introduction

Passive optical networks (PONs) have high capacity; they are low cost; and they are easy to maintain in the access part of the optical communication network. Currently, drafting of standards for 40 Gb/s symmetric PON is underway. A number of PON architectures have been proposed to provide high bandwidth. Time-division multiplexing PON (TDM-PON) uses different time slots to carry different information transmitted to different users; wavelength-division multiplexing PON (WDM-PON) uses different wavelengths to transmit to different users; and orthogonal frequency-division PON (OFDM-PON) uses different subcarriers to transmit to different users [1]–[6].

Various research teams have proposed schemes for these PON architectures [6]–[18]. There are many issues with TDM-PON, including the high cost of the high-speed burst receiver and difficulty in timing location. WDM-PON has large access capacity and a huge number of users, but allocating resources is difficult. OFDM-PON has many advantages, including dispersion tolerance, good compatibility, dynamic bandwidth allocation, and a variety of services to the whole transparent processing. The speed of the downlink transmission single-wavelength access network has been improved by many companies. With polarization reuse and direct detection, OFDMA-PON is capable of 108 Gb/s downstream transmission over a single wavelength [19]. This constitutes a class-B light distribution network. This paper describes the system design of OFDMA-PON and gives its

experiment results under different conditions.

2 Structure of OFDM-PON

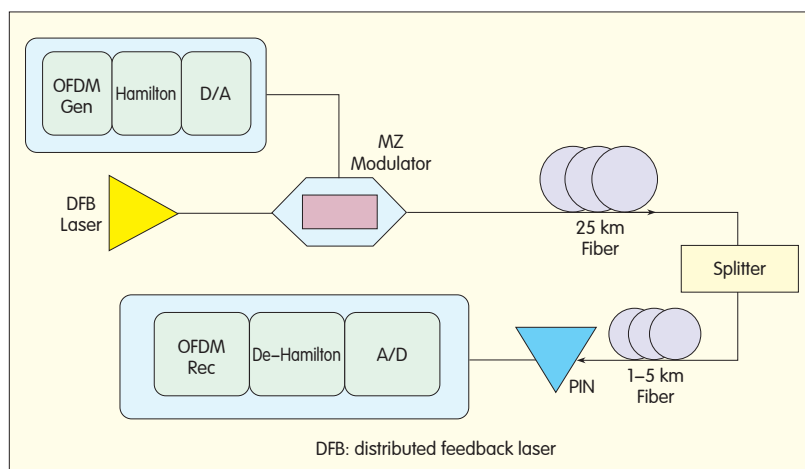
OFDM-PON structures include baseband OFDM-PON, RF-multiplexing OFDM-PON, wavelength-division multiplexing OFDM-PON (WDM-OFDM-PON), and all-optical OFDM-PON. Baseband OFDM-PON has a simple structure and is cheap to implement, which allows for a low-cost optical access network. However, there is too much pressure on ADC and DAC [20], [21]. In the following sections, we discuss the key technologies in OFDM-PON.

2.1 System Setup

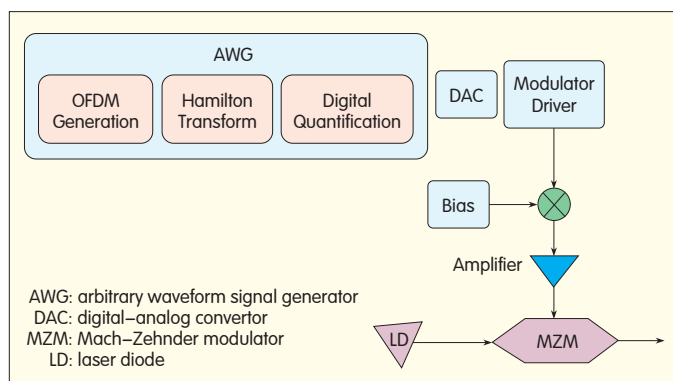
Fig. 1 shows the experimental OFDM-PON structure. It can be divided into three parts: optical line terminal (OLT), optical division network (ODN), and optical network unit (ONU).

2.2 OLT Setup in OFDM-PON

The physical-layer structure in Fig. 2 includes OFDM digital processing, Hamilton transform, digital quantification, mathematical model transform (D/A), modulator driver, offset add, and optical modulator. The OFDM access signal is generated by DSP through MATLAB and is fed into the arbitrary waveform signal generator (AWG), which produces the OFDM electrical waveform. The Hamilton transform generates corresponding conjugated OFDM information in the frequency domain. This ensures the output OFDM signal is a real signal, which means the optical OFDM signal can be directly modulated by the MZM. The OFDM signal from the



▲ Figure 1. OFDM-PON structure.



▲ Figure 2. OLT structure in OFDM-PON.

AWG is driven by a modulator driver to ensure enough drive voltage for the MZM. The amplifier requires flat frequency gain and high linearity. Because of the high peak-to-average power ratio (PAPR) of the optical OFDM, the amplifier requires the MZM to be placed in a highly linear work region.

2.3 ONU Setup in OFDM-PON

The ONU scheme in optical OFDM-PON (Fig. 3) includes the photoelectric detector (PD), separate DC device, module converter, Hamilton inverse transform module, OFDM demodulation module, and BER calculation module. A direct-detection scheme is used to simplify ONU structure and reduce cost. PD converts the optical OFDM signal into an electrical signal and has low noise, high linearity, and high sensitivity for optical OFDM signal detection. Both the PIN-PD and APD can be used for detection. The Hamilton transform converts the real OFDM signal into an I/Q OFDM signal. After Hamilton transform, the OFDM signal is demodulated through DSP processing, and it is fed into the BER testing (BERT) unit to determine the system's performance.

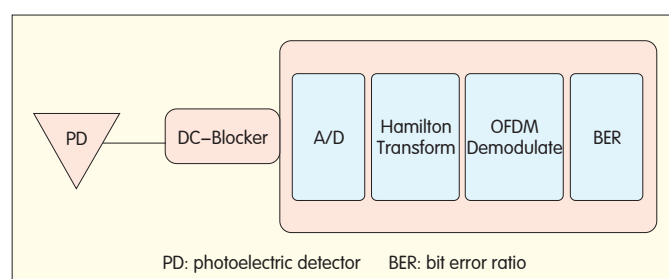
3 OFDM-PON System Performance

In this experiment, 4-QAM and 16-QAM modulations are

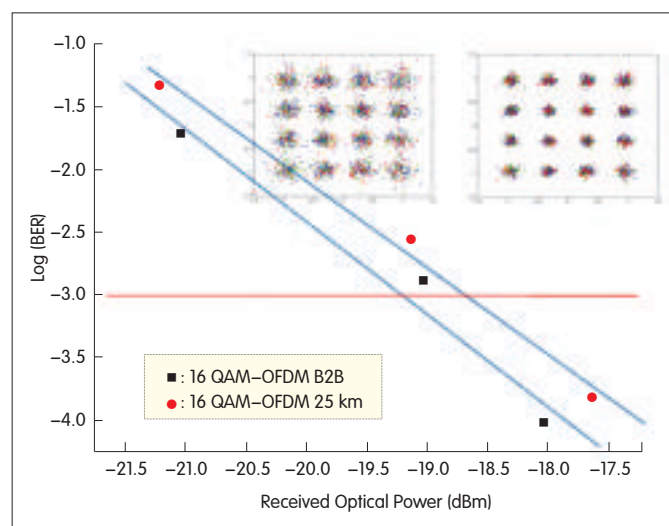
used. By adding an attenuator at the receiver, the BER of system against received optical power for different modulation formats can be measured. In this experiment, the launched optical power at the OLT is about 1 dBm. Fig. 4 shows BER functions for the 16-QAM OFDM signal with and without transmission. After transmission, the power penalty for the 16-QAM OFDM signal is about 0.5 dB. Fig. 4 (inset) shows the constellations before and after transmission. Fig. 5 shows BER functions for the 4-QAM OFDM signal with and without transmission. The power penalty for the 4-QAM OFDM signal is about 0.2 dB, which is negligible. Fig. 5 (inset) shows the constellations before and after transmission. The receive sensitivity of 4-QAM OFDM is about 3 dB better than that of 16-QAM OFDM. This experiment result conforms to the theory.

3.1 Different Modulation Formats and Noise

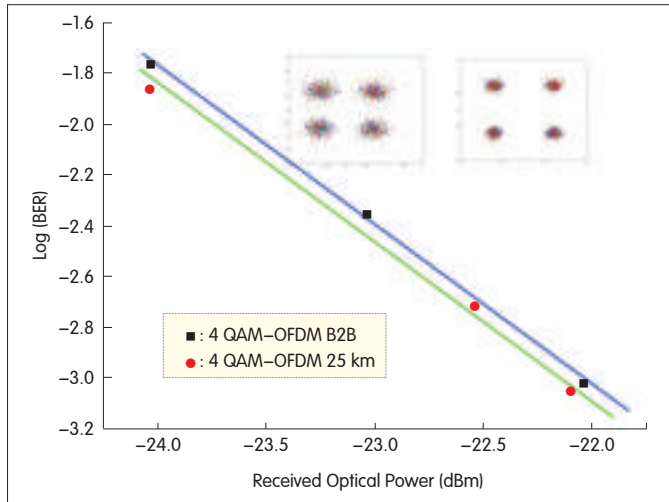
To determine the OSNR tolerance, we first analyze the performance of three types of m-QAM-mapped OFDM signal: 4-QAM, 8-QAM, and 16-QAM. The OSNR requirements of the three kinds of signal are shown in Fig. 6. The OFDM signal with higher-order constellation mapping



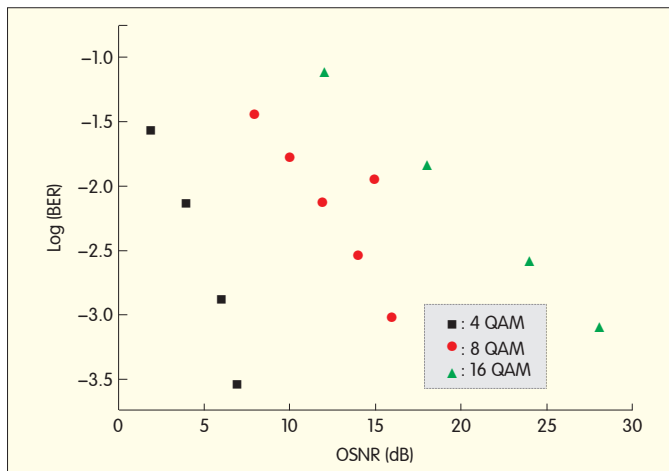
▲ Figure 3. ONU structure in OFDM PON.



▲ Figure 4. BER functions for a 16-QAM OFDM signal with and without transmission. Inset: constellations before (l) and after (r) transmission.



▲ Figure 5. BER functions for a 4-QAM OFDM signal with and without transmission. Inset: constellations before (l) and after (r) transmission.



▲ Figure 6. The OSNR effect on an OFDM signal with different constellation mapping.

has lower OSNR tolerance.

3.2 OFDM-PON Performance with Different Launch Power

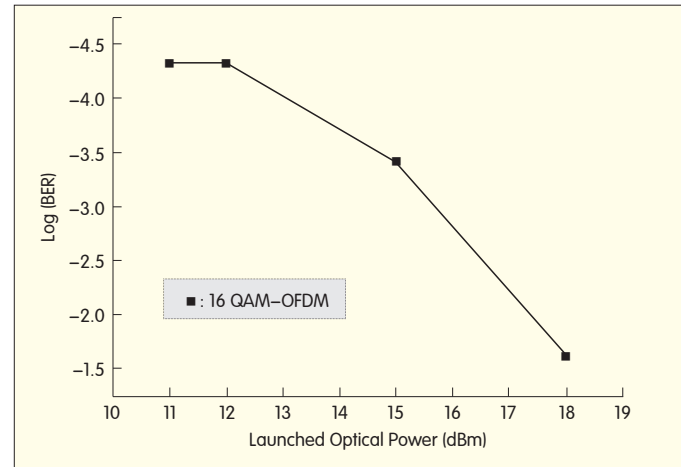
We use 16-QAM OFDM to show optical OFDM-PON performance with different launch powers (Fig. 7). When the launched optical power is more than 12.5 dBm, the performance of the optical OFDM signal begins to deteriorate, mainly because of fiber nonlinearity.

3.3 Different Laser Linewidths and System Performance

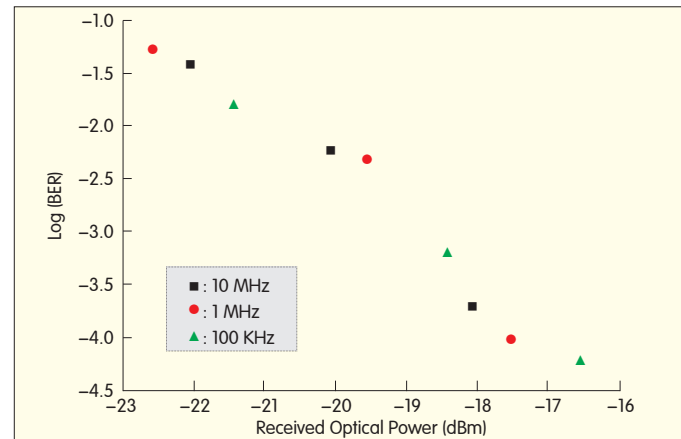
Here, system performance for laser linewidths of 1 MHz, 10 MHz, and 100 kHz is analyzed. Fig. 8 shows system performance for different linewidths. With a baseband OFDM modulation/direct-detection scheme, the laser linewidth has little effect on system performance.

3.4 Different Access Distances and System Performance

Fig. 9 shows system performance for different access



▲ Figure 7. OFDM-PON performance for different launch powers.



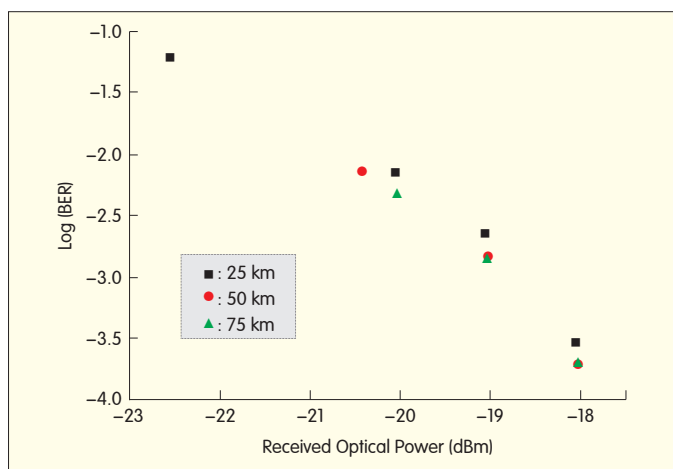
▲ Figure 8. System performance for different laser linewidths.

distances. In this experiment, the launched optical power is set to 0 dBm. For access distances within 75 km, the transmission distance has little effect on the performance of the optical OFDM signal. When the transmission distance becomes longer, the performance deteriorates slightly.

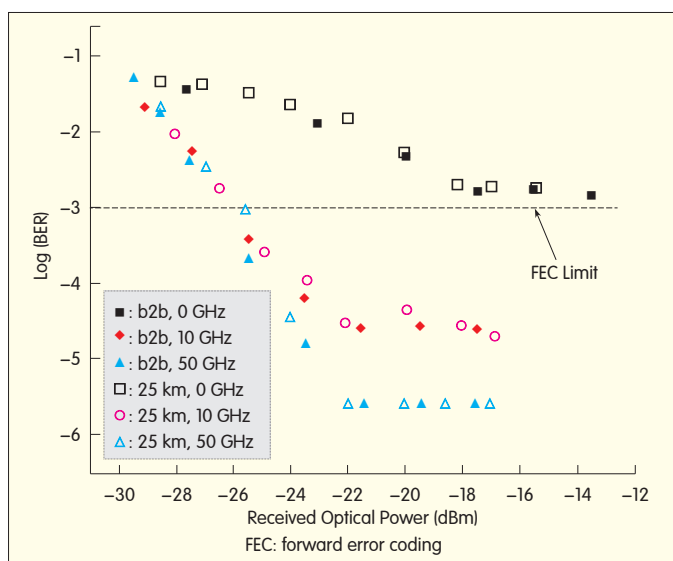
4 OFDM-PON Performance and Beating Noise

4.1 Different Wavelength Intervals and System Performance

Realization of a colorless upstream link is a hot topic in optical OFDM-PON. In this experiment, the performance of upstream signals in optical OFDM-PON is analyzed. We demonstrate three ONUs and use three tunable lasers as the light sources. Uplink signals perform differently by adjusting the wavelength interval. Fig. 10 shows the performance for different wavelength intervals before and after transmission. When the wavelength interval is greater than 10 GHz, system performance is almost the same, but the error floors are different. The receive sensitivities when $\text{BER} = 10^{-3}$ are both about -25.5 dBm. When the laser wavelength interval is



▲ Figure 9. System performance for different access distances.



▲ Figure 10. System performance for different wavelength intervals.

0 GHz; that is, when the wavelengths are the same, the upstream signal has BER greater than 10^{-3} and cannot be recovered using FEC.

4.2 Colorless OFDM-PON with the Same Lightwave Source

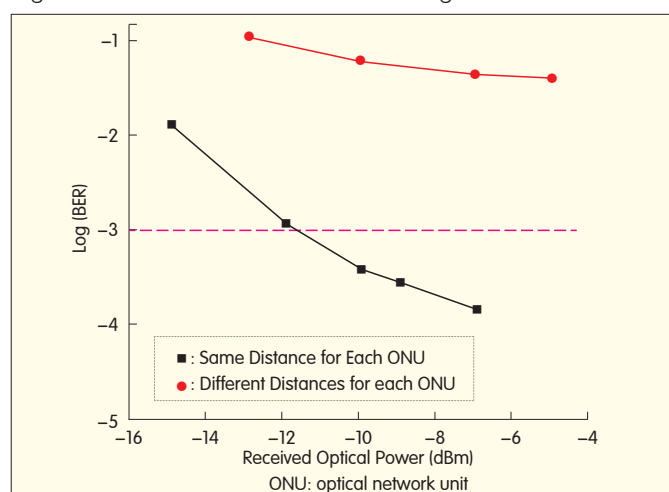
To realize a colorless upstream link, a blank downstream carrier for the whole ONU is used. This downstream carrier can be used as optical carrier for the upstream signal. In this experiment, the ONU uses a reflective optical modulator to add the upstream signal to the blank carrier. The blank carrier is highly coherent, which eliminates the optical beating interference (OBI) noise at the OLT. The distance between the ODN and ONU is different, and Fig. 11 shows the system performance for these different distances. When the distance is almost the same for each ONU, the system performs well, and the receive sensitivity at $\text{BER} = 10^{-3}$ is about 11.8 dBm. When the distance is different, performance deteriorates significantly mainly because the blank optical carriers for the

ONUs experience a different link environment, and the phase noise reduces coherency.

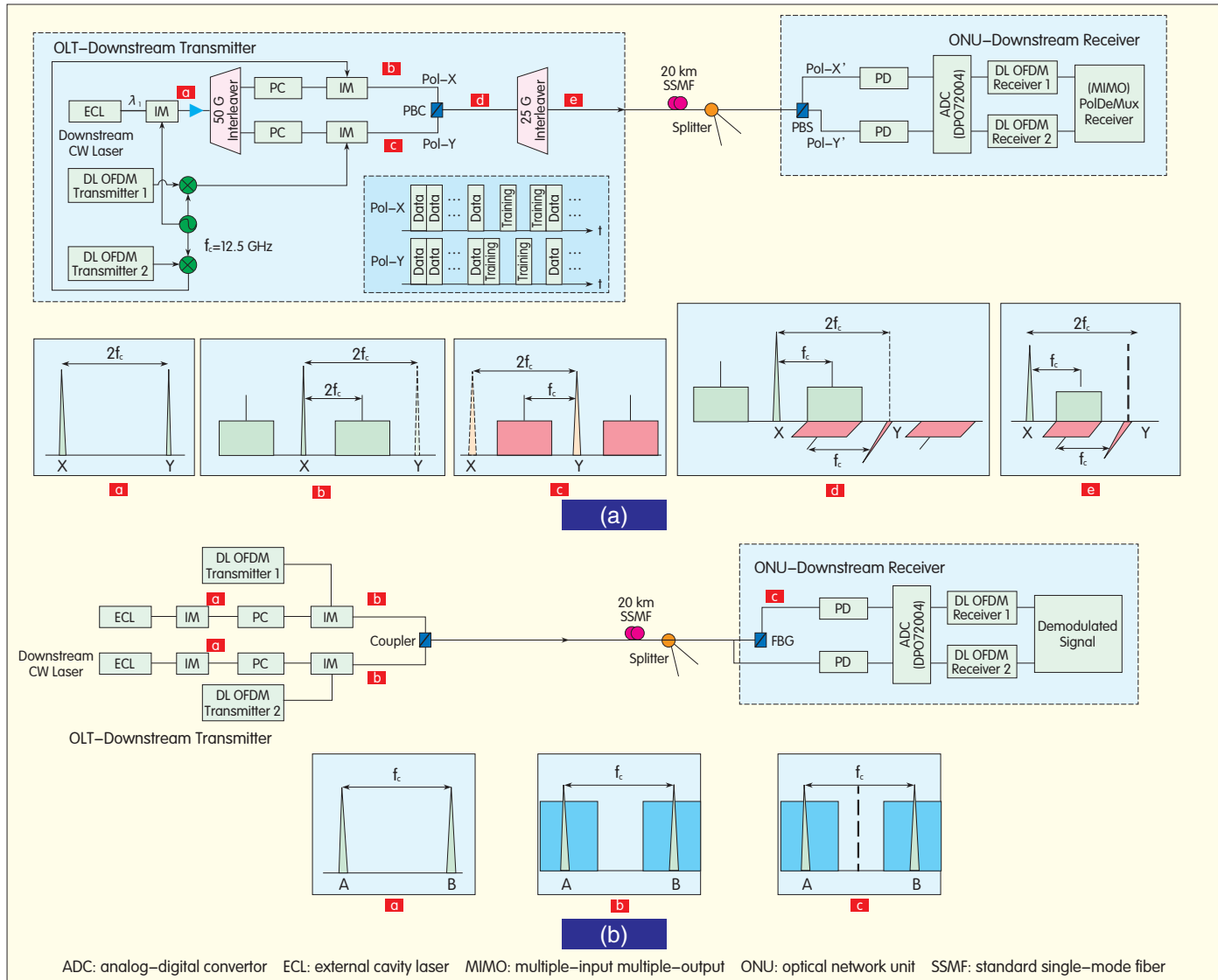
5 Experiment Setup and Performance of 40 Gb/s OFDM-PON

OFDM-PON has been widely proposed as one of candidates for next-generation 40 Gb/s optical access networks. In this paper, we adopt a two-carrier scheme to realize the 40 Gb/s OFDM-PON, and the experiment setup is shown in Fig. 12(b). Two distributed feedback lasers with 60 GHz frequency space are the light sources, and a 20 Gb/s 16-QAM OFDM downstream signal is carried on each wavelength, so the total transmission speed is 40 Gb/s. This scheme makes full use of the large wavelength resources in PON to achieve 100 GHz within the 40 Gb/s OFDM access network. Compared with NEC Corporation's proposed scheme [14],[22], which uses polarization and RF multiplexing (Fig. 12a), the proposed scheme simplifies the network structure, and reduces costs associated with OLTs and ONUs. Especially at the ONU, the proposed scheme avoids the need for a complicated MIMO algorithm. It also avoids the need for many polarization components and local radio frequency, and this is the essence of colorless access. In the scheme proposed by NEC Corporation, the signal needs to be loaded to a different local radio frequency. Strictly speaking, this is also a kind of colorless scheme. The upstream scheme still uses double-wavelengths lasers and existing 10G PON for 20 Gb/s upstream transmission. This is because achieving a colorless OFDM signal is difficult. If OFDM and TDM is used in this way, timing is still a problem.

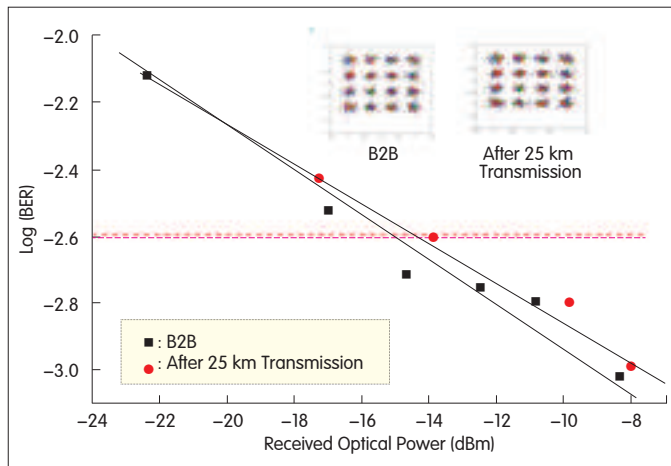
Fig. 13 shows the performance of a downstream 40 Gb/s optical OFDM access signal. The received optical power is about -14 dBm when $\text{BER} = 10^{-2.6}$, but the received signal can be recovered with the help of enhanced forward error coding (EFEC). Because the launch power of the system is about 3 dBm, the OFDM-PON can support 25 km access and 16 users, which means it is a class-B optical access network. Fig. 13 shows the constellations of the signal before and after



▲ Figure 11. System performance for same laser source.



▲ Figure 12. a) Scheme proposed by NEC Corporation, and b) two-carrier scheme proposed in this paper.



▲ Figure 13. Downstream performance of 40 Gb/s OFDM access signal.

25 km transmission.

6 Conclusion

In this paper, OFDM-PON is introduced and optical OFDM signal performance analyzed. Through experimentation, system performance is determined for different parameters. OFDM-PON is tolerant to linewidths of the lightwave source, and the system is influenced by the OSNR and mapping style. A two-carrier 40 Gb/s OFDM-PON was also proposed, and 25 km SMF was successfully transmitted.

References

- [1] N. U. Kim, H.-S. Lim, M. Kang, "Fair Bandwidth Allocation Using Effective Multicast Traffic Share in TDM-PONs," *IEEE J. Lightwave Technol.*, vol. 26, no. 7, pp. 756-767, 2008.
- [2] J. H. Moon, K. M. Choi, and C. H. Lee, "Overlay of Broadcasting Signal in a WDM-PON," in *Proc. Opt. Fiber Commun. Conf. (OFC '06)*, Anaheim, CA, 2006.

➔To P. 53

Compensating for Nonlinear Effects in Coherent-Detection Optical Transmission Systems

Fan Zhang

(State Key Laboratory of Advanced Optical Communication Systems & Networks, Peking University, Beijing 100871, P.R.China)

Abstract

Fiber nonlinearity is one of the most important limiters of capacity in coherent optical communications. In this paper, we review two nonlinear compensation methods: digital backward propagation (BP) and nonlinear electrical equalizer (NLEE) based on the time-domain Volterra series. These compensation algorithms are implemented in a single-channel 50 Gb/s coherent optical single-carrier frequency-division multiplexed (CO-SCFDM) system transmitting over 10×80 km of standard single-mode fiber (SSMF).

Keywords

coherent optical communication; fiber nonlinearity; digital signal processing

1 Introduction

The demands of high-capacity optical transmission systems have led to the rapid development of coherent optical systems. A coherent receiver with optical hybrid allows the electrical field in the two fiber polarizations to be recovered. High spectral efficiency can thus be implemented using advanced modulation-format encoding information in all the available degrees of freedom. Digital signal processing (DSP) simplifies coherent detection and gives it greater flexibility and hardware transparency as well as the potential to adaptively compensate for channel impairments in the electrical domain [1], [2]. In coherent optical communications, linear impairments, such as fiber chromatic dispersion (CD) and polarization mode dispersion (PMD) (all orders), can be compensated for in principle. Fiber capacity is limited by nonlinearity and amplified spontaneous emission (ASE) in optical amplifiers. ASE is white noise and cannot be eliminated. The maximum transfer rate for a given noise level is called the Shannon limit. Fiber nonlinearity is caused by the optical Kerr effect during signal propagation, and evolution of the optical pulse is governed by the nonlinear Schrödinger equation (NLSE). Therefore, nonlinear distortions are determinate and can be partially compensated for by DSP in the coherent receiver.

Backward propagation (BP) is proposed as a universal method of inverting nonlinear systems. In direct-detection

systems, electrical predistortion (EPD) can be used to equalize intrachannel nonlinearities by modeling channel inversion for nonlinear effects and predistorting transmitted waveform accordingly [3], [4]. Digital BP is incorporated into coherent optical receivers by using a split-step Fourier (SSF) method [5]–[7] based on a hybrid time and frequency-domain approach. BP can also be implemented using a split-step finite-impulse response filter (SS-FIR) [8] that operates entirely in the time domain. Coherent detection is usually combined with polarization-division multiplexing (PDM) to increase spectral efficiency. Fiber nonlinearity in PDM coherent systems can be compensated for by BP in the Manakov frame [9], [10], which takes the average effect of fast polarization rotations into account.

BP is an iterative numerical method. Because it is non-recursive, a nonlinear electrical equalizer based on the time-domain Volterra series has been proposed for coherent optical systems [11]. If a sufficient number of delay taps are used, the accuracy of BP is comparable to that of an SSF method with one step per span.

Coherent optical orthogonal frequency-division multiplexing (CO-OFDM) has intrinsic advantages, such as flexibility in dividing spectrum, high spectral efficiency (SE), and outstanding tolerance of CD and PMD [12]. Nonlinearity compensation has previously been performed in CO-OFDM systems using back propagation [10]–[13] and the Volterra series [14], [15].

Although CO-OFDM has some impressive advantages, its

main drawback is the high peak-to-average power ratio (PAPR), which can cause severe nonlinear impairments and inefficient power consumption [16]–[18]. Recently, coherent optical single-carrier frequency-division multiplexing (CO-SCFDM), also called discrete Fourier transform-spread OFDM (DFT-spread OFDM), has been proposed [19], [20]. This modified form of OFDM that has been used in the uplink single-carrier frequency-division multiple access (SCFDMA) scheme for LTE [21]. SCFDM has similar throughput and overall complexity as OFDM, but it is more tolerant of nonlinear impairments and has lower PAPR [20], [21].

2 Backward Propagation with Split-Step Fourier Method

2.1 Backward Propagation in the Scalar Nonlinear Schrödinger Equation

Signal propagation in fiber can be described by the scalar nonlinear Schrödinger equation (or NLSE)[22]:

$$\frac{\partial A}{\partial z} = -\frac{\alpha}{2} A + \frac{i\beta_2}{2} \frac{\partial^2 A}{\partial t^2} + i\gamma |A|^2 A \quad (1)$$

where A is the electrical field. The parameters α , β_2 and γ are the attenuation, CD coefficients, and nonlinear parameter of the fiber, respectively. Separate linear and nonlinear components results in

$$\frac{\partial A}{\partial z} = (\hat{D} + \hat{N})A \quad (2)$$

Where \hat{D} is the linear operator, given by

$$\hat{D} = -\frac{\alpha}{2} + \frac{i\beta_2}{2} \frac{\partial^2}{\partial t^2} \quad (3)$$

and \hat{N} is the nonlinear operator, given by

$$\hat{N} = i\gamma |A|^2 \quad (4)$$

Because the analytical solution of the nonlinear Schrödinger equation is difficult to obtain, a symmetric SSF solution is used. In the absence of noise, exact information about the transmitted signal can be obtained at the receiver by solving the BP equation. BP is modeled by numerically solving the nonlinear Schrödinger equation with negative link parameters and using the symmetric split-step Fourier method [7]–[23]. In each step, the optical field, $A(z, t)$, evolves according to

$$\begin{aligned} A(Z+\Delta h, t) &\approx \exp\left(\frac{\Delta h}{2} \hat{D}^{-1}\right) \exp\left(\int_z^{Z+\Delta h} \hat{N}^{-1}(z') dz'\right) \exp\left(\frac{\Delta h}{2} \hat{D}^{-1}\right) A(z, t) \\ &\approx \exp\left(\frac{\Delta h}{2} \hat{D}^{-1}\right) \exp(\Delta h \hat{N}^{-1}) \exp\left(\frac{\Delta h}{2} \hat{D}^{-1}\right) A(z, t) \end{aligned} \quad (5)$$

where \hat{D}^{-1} is the inverse linear operator, \hat{N}^{-1} is the inverse nonlinear operator, and Δh is the step size.

2.2 Manakov Equation

Coherent optical systems usually use PDM signals to increase spectral efficiency. The electrical field of the optical signal is $A = [A_x \ A_y]^T$, where A_x and A_y are the orthogonal

polarization components of the electrical field. In a birefringence-free fiber, fiber can be described by the vectorial form of the NLSE [22]:

$$\begin{aligned} \frac{\partial A_x}{\partial z} &= -\frac{\alpha}{2} A_x + \frac{i\beta_2}{2} \frac{\partial^2 A_x}{\partial t^2} + i\gamma (|A_x|^2 + \frac{2}{3} |A_y|^2) A_x + \frac{i\gamma}{3} A_x^* A_y^2 \\ \frac{\partial A_y}{\partial z} &= -\frac{\alpha}{2} A_y + \frac{i\beta_2}{2} \frac{\partial^2 A_y}{\partial t^2} + i\gamma (|A_y|^2 + \frac{2}{3} |A_x|^2) A_y + \frac{i\gamma}{3} A_y^* A_x^2 \end{aligned} \quad (6)$$

In (6), the nonlinear interaction between the two polarizations is described. The fiber randomly scatters the polarization of the electrical field during transmission. The polarization scattering length is much shorter than the nonlinear length, which is typically tens of kilometers. In channels where the nonlinear length is much greater than the length of the random polarization rotations, the Manakov equation can be derived by averaging (6) of the nonlinear operator over fast polarization changes on the Poincaré sphere [24]:

$$\begin{aligned} \frac{\partial A_x}{\partial z} &= -\frac{\alpha}{2} A_x + \frac{i\beta_2}{2} \frac{\partial^2 A_x}{\partial t^2} + \frac{8i\gamma}{3} (|A_x|^2 + |A_y|^2) A_x \\ \frac{\partial A_y}{\partial z} &= -\frac{\alpha}{2} A_y + \frac{i\beta_2}{2} \frac{\partial^2 A_y}{\partial t^2} + \frac{8i\gamma}{3} (|A_y|^2 + |A_x|^2) A_y \end{aligned} \quad (7)$$

$$\text{The nonlinear operator is } \hat{N} = \frac{8i\gamma}{9} (|A_x|^2 + |A_y|^2) \begin{bmatrix} 1 & 0 \\ 0 & 1 \end{bmatrix} \quad (8)$$

If the electrical fields of the two polarizations are obtained at the receiver side, the original signal can be approximately recovered by solving the Manakov equation with the inverse fiber link parameters and using the SSF method.

3 Nonlinear Electrical Equalizer Based on Volterra Series

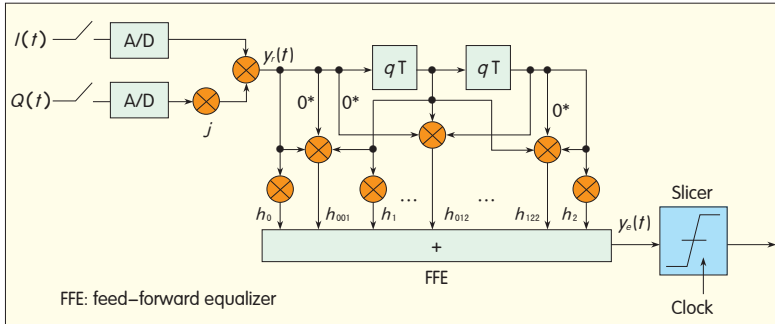
3.1 Nonlinear Electrical Equalizer for Scalar Nonlinear Schrödinger Equation

The nonlinear electrical equalizer (NLEE) derives from the theory of Volterra-series expansion [25], which is a powerful tool for analyzing nonlinear systems. The theory states that a time-invariant nonlinear system can be modeled as an infinite sum of multidimensional convolution integrals of increasing order. According to the theory, the received optical field, $y_r(t)$, is related to the modulated signal, $y_r(t)$, by

$$\begin{aligned} y_r(t) &= \int_0^\infty H_1(\tau_1) y(t-\tau_1) d\tau_1 + \int_0^\infty \int_0^\infty H_3(\tau_1, \tau_2, \tau_3) y(t-\tau_1) y(t-\tau_2) \\ &\quad y^*(t-\tau_3) d\tau_1 d\tau_2 d\tau_3 + \dots \end{aligned} \quad (9)$$

where $H_i(\tau_1, \dots, \tau_i)$ is the Volterra kernel determined by the fiber link parameters [26]. The first term is the linear intersymbol interference (ISI), and the others are nonlinear distortions. Because there are no even-order nonlinearities in optical fiber, only odd-order Volterra kernels are considered. At the receiver, an NLEE can be realized by constructing an inverse transform of (9). The equalized signal, $y_e(n)$, can thus be written in the discrete form as

$$y_e(n) = \sum_{p=-N}^N h_p y_r(n-p) + \sum_{l=-N}^N \sum_{m=l}^N \sum_{k=m}^N h_{l,m,k} y_r(n-l) y_r(n-m) y_r^*(n-k) + \dots \quad (10)$$



▲ Figure 1. Structure of the NLEE.

By solving the nonlinear Schrödinger equation with first-order perturbation theory [27], the output can be viewed as having two parts: the linear solution μ_n and the nonlinear optical-field distortion, $\Delta\mu_n$. In single-channel systems, only pulses with indices that satisfy the temporal matching condition $l + m - k = n$ induce a noticeable distortion on the pulse μ_n [28]. This is equivalent to the phase-matching of four-wave mixing (FWM) in wavelength-division multiplexing (WDM). Intrachannel self-phase modulation (ISPM) and intrachannel cross-phase modulation (IXPM) are also included by containing the items $l = m = k = n$, $l = n$, or $m = n$ (where $l \neq m$). Assuming a nonlinear fiber system and $\Delta\mu_n$, the following can be expressed according to the Volterra theory:

$$\Delta u_n = \sum_{p=-N}^N C_p u_p(n-p) + \sum_{l=-N}^N \sum_{m=l}^N \sum_{k=m}^N C_{l,m,k} u(n-l) u(n-m) u^*(n-k) + \dots \quad (11)$$

Fig. 1 shows the structure of the third-order NLEE, and the algorithm is detailed in [11]. The in-phase component of the received QPSK signals is $I(t)$, and the quadrature component of the received QPSK signals is $Q(t)$. The equalized signal for output-carrier phase estimation is $y_e(t)$. The complex conjugation of the corresponding signals is $(\cdot)^*$. The symbol duration is T , and the sampling space is qT . The discrete coefficient is h . Intrachannel nonlinear distortion is $h_{l,m,k}$, where the subscripts denote the optical pulse positions. The delay tap number, $L = 2N + 1$, is equivalent to the nonlinear ISI length. The third-order items are defined as nonlinear terms, and the equalizer coefficients are adaptively determined using the recursive least square (RLS) algorithm.

3.2 Nonlinear Electrical Equalizer for Manakov Equation

The NLEE in Fig. 1 can be extended to polarization-multiplexed systems by rewriting (11) according to the Manakov equation. We assume a transmission system has two polarizations, x and y . When compensating for polarization x nonlinearities, the distortions from polarization y should not be

neglected. For polarization x , the adjusted third-order nonlinearities with nonlinear distortions from polarization y is expressed as [29]

$$\Delta u_{x,n} = \sum_l \sum_m \sum_k C_{l,m,k} [u_x(l) u_x(m) u_x^*(k) + u_x(l) u_y(m) u_y^*(k)] \quad (12)$$

which can be expanded further as [30]

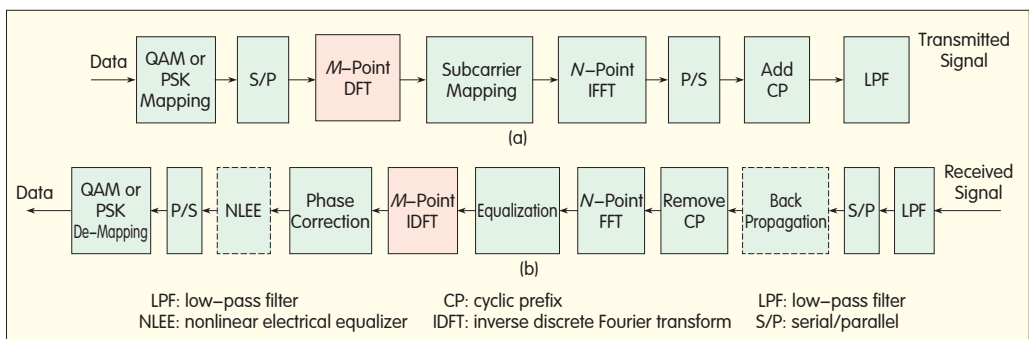
$$\Delta u_{x,n} = \sum_l C_l [u_x(l) (|u_x(l)|^2 + |u_y(l)|^2)] + \sum_l \sum_m C_{m,l} [u_x(l) (|u_x(m)|^2 + |u_y(m)|^2)] + \sum_l \sum_m C_{l,m} [u_x(m) (|u_x(l)|^2 + |u_y(l)|^2) + u_x(l) u_y(m) u_y^*(l)] + \sum_l \sum_m \sum_k C_{l,m,k} [u_x(l) u_x(m) u_x^*(k) + u_x(l) u_y(m) u_y^*(k)] \quad (13)$$

where $C_{l,m,k}$ is the coefficient determined adaptively using the RLS algorithm, and u_x and u_y are the signals from the two orthogonal polarizations. For simplicity, we do not consider the intrachannel four-wave mixing from the orthogonal polarization.

4 Coherent Optical SCFDM System

Fig. 2 shows the DSP block diagrams for the CO-SCFDM system. At the coder, the transmitted binary data is mapped into QAM or phase-shift keying (PSK) signals and then is grouped into blocks containing M symbols. The first step in the CO-SCFDM system is to perform an M -point DFT to produce a frequency-domain representation of the input symbols. Then, M -point DFT outputs are mapped to N ($N \geq M$) orthogonal subcarriers. After the N -point inverse fast Fourier transform (IFFT), which transforms the subcarriers into a time domain signal, a cyclic prefix (CP) is inserted for each block before the data sequence is transmitted. At the decoder, the N -point FFT transforms the signals into the frequency domain, and channel equalization is performed. The equalized signal is transformed into the time domain by the M -point inverse discrete Fourier transform (IDFT) for decision. CO-SCFDM is very flexible, and its parameter design can have a high degree of commonality with OFDM. Nonlinear compensation algorithms of the BP and NLEE can be implemented at different positions (Fig. 2b).

At the transmitter, the mapped quadrature phase-shift keying (QPSK) signals are first grouped into blocks of 1680



▲ Figure 2. DSP block diagram for (a) the CO-SCFDM coder and (b) the CO-SCFDM decoder.

▼ Table 1. Key CO-SCFDM design parameters

FFT/IFFT (<i>N</i> -point)	Symbol Size	Number of Pilot	Modulation	Symbol Duration
2048	2168	32	PDM QPSK	117.1 ns
DFT/IDFT (<i>M</i> -point)	Subcarrier Spacing	Net Bit Rate	FEC Ethernet Redundancy	Preamble
1712	9.04 MHz	50 Gb/s	12%	2.44%
FFT: fast Fourier transform IFFT: inverse fast Fourier transform		DFT: discrete Fourier transform IDFT: inverse discrete Fourier transform		

symbols, and 32 pilots are uniformly time-multiplexed into each block. Then, the signal is transformed into the frequency domain by 1712-point DFT. In the frequency domain, 336 guard subcarriers are added and allocated at both sides of the band. These subcarriers provide about 20% oversampling so that the aliasing products can be spectrally separated with a low-pass filter. After subcarrier mapping, the signal is converted back to the time domain by 2048-point IFFT. The cyclic prefix and cyclic suffix, each 60 symbols long, are inserted into every data block before transmission. The duration of a CO-SCFDM symbol is 117.1 ns. The preamble is 2.44% and includes synchronization and training symbols (Table 1). Taking into account 12% redundancy for Ethernet overhead and forward-error correction, PDM QPSK is capable of 50 Gb/s net.

The fiber link comprises ten spans of 80 km standard single-mode fiber, each with an average loss of 20 dB. The fiber dispersion is 17 ps/km/nm, and the fiber nonlinear coefficient is 1.32 km/W. An Erbium-doped fiber amplifier with 5 dB noise fully compensates for fiber attenuation. No in-line chromatic dispersion compensation is used. With an average launch power of 5 dBm, the signal suffers nonlinearity distortion during propagation. Nonlinearity is compensated for by either the NLEE or the BP. For NLEE, we choose NL [15]; for BP, we choose two different split-step sizes, one of which is equal to the span length. The other step is a full multistep approach determined by the maximum nonlinear phase shift in each step, which is the same 0.05 as the simulation of the transmission link.

Fig. 3 shows the results of nonlinear compensation. The error vector magnitude (EVM) is the performance indicator. For Fig. 3(a) to (d), the EVM is 15.62 dB, 18.34 dB, 18.63 dB, and 18.75 dB, respectively. Although PDM signals are transmitted and equalized, we only present the results of x polarization for the sake of simplicity. The BP with one step per span improves EVM by about 3.0 dB, similar to the full multistep approach. The NLEE provides similar performance but with asymmetric constellations.

5 Conclusion

In this paper, we review nonlinear compensation methods of digital BP propose an NLEE based on the Volterra series. In terms of computational complexity, the time-domain approach of NLEE requires one order of magnitude more than BP-SSF [11]. However, NLEE is much more convenient for real-time implementation because the pulses are processed

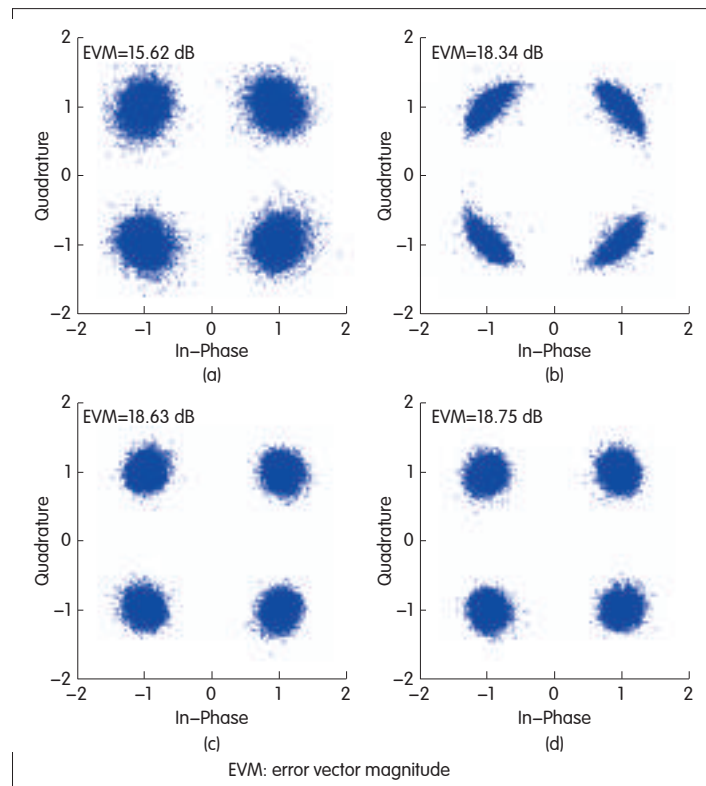
in sequence rather than in a block. BP in [8] uses split-step FIR filtering and thus supports sequential processing. By comparison, the computational complexity of NLEE is one order of magnitude lower. NLEE has an important advantage over BP in that it does not require prior knowledge of the fiber-link parameters. The equalizer coefficients are adaptively determined, and this provides flexibility when signals are routed differently in optical networks.

An NLEE based on the Volterra series can also be implemented in a frequency domain with low complexity [15], [31]. For both OFDM and SCFDM systems, Volterra series-based nonlinear equalization should be further studied for both time and frequency implementation.

This paper is mainly focused on nonlinear compensation in single-channel operation. BP in WDM systems has been well covered in [10], [13], and [32]. Besides intrachannel nonlinearities, interchannel nonlinear interactions, such as XPM and FWM, should be considered. If A_{xm} and A_{ym} are, respectively, the envelopes of x and y polarization tributaries of the received mth WDM channel field, the reconstructed total optical field is

$$A = \sum_m [A_{xm} \cdot A_{ym}]^T \exp(im\Delta\omega t) \quad (14)$$

The channel spacing is $\Delta f = \Delta\omega/2\pi$. A set of local oscillators (LOs) is used for coherent detection and reconstruction of each WDM channel. To mitigate nonlinear distortions in WDM systems, the reconstructed optical field of



▲ Figure 3. Constellations of the recovery signals after ten-span transmission (a) without nonlinear compensation, (b) with nonlinear compensator as NL, (c) with one-step-per-span BP, (d) with multistep BP.

the entire WDM band should be backward propagated using (7). In [13], nonlinear compensation for different intrachannel and interchannel effects is discussed with various channel granularities. XPM compensation significantly improves system performance, especially the fine granularity. The coherent nature of FWM requires the phase-locked LOs to preserve the relative phase between channels [13], [32].

The disadvantage of BP is that it needs the information of both the fiber link and signals of the neighboring channels. Therefore, multichannel signals must be obtained in the coherent receiver, which makes the system design more complex. As a consequence, BP is only effective in point-to-point fiber links in which all WDM channels share the same TX–RX locations [13]. For optical networks with add/drop multiplexers and signals that are routed differently, interchannel nonlinear compensation is ineffective for BP. Further study is required into blind equalization of interchannel nonlinear distortions using some kind of electrical equalization structure.

Acknowledgement

This work was supported by National Natural Science Foundation of China (No. 61077053, 60932004, and 60877045) and National Basic Research Program of China (No. 2010CB328201).

References

- [1] S. J. Savory, G. Gavioli, R. I. Killey, and P. Bayvel, "Electronic Compensation of Chromatic Dispersion Using a Digital Coherent receiver," *Opt. Express*, vol. 15, no. 5, pp. 2120–2126, Mar. 2007.
- [2] K. Kikuchi, "Phase-Diversity Homodyne Detection of Multilevel Optical Modulation with Digital Carrier Phase Estimation," *Selected Topics in Quantum Electronics*, vol. 12, no. 4, pp. 563–570, Jul. 2006.
- [3] C. Weber, J. K. Fischer, C.-A. Bunge, and K. Petermann, "Electronic Precompensation of Intrachannel Nonlinearities at 40 Gb/s," *IEEE Photon. Technol. Lett.*, vol. 18, no. 16, pp. 1759–1761, Aug. 2006.
- [4] X. Liu and D. A. Fishman, "A Fast and Reliable Algorithm for Electronic Pre-Equalization of SPM and Chromatic Dispersion," in *Proc. Opt. Fiber Commun. Conf. (OFC '06)*, Anaheim, CA, 2006, paper OThD4.
- [5] X. Li, X. Chen, G. Goldfarb, E. Mateo, I. Kim, F. Yaman, and G. Li, "Electronic Post-Compensation of WDM Transmission Impairments Using coherent Detection and Digital Signal Processing," *Opt. Express*, vol. 16, no. 2, pp. 880–888, Jan. 2008.
- [6] E. Ip and J. M. Kahn, "Compensation of Dispersion and Nonlinear Impairments Using Digital Backpropagation," *J. Lightw. Technol.*, vol. 26, no. 20, pp. 3416–3425, Oct. 2008.
- [7] Y. Gao, F. Zhang, L. Dou, Z. Chen, and A. Xu, "Digital Post-Equalization of Intrachannel Nonlinearities in Coherent DQPSK Transmission Systems," in *Proc. Coherent Opt. Tech. Appl. (COTA) 2008*, paper JMB8.
- [8] G. Goldfarb, M. G. Taylor, and G. Li, "Experimental Demonstration of Fiber Impairment Compensation Using the Split-Step Finite-Impulse Response Filtering Method," *IEEE Photon. Technol. Lett.*, vol. 20, no. 22, pp. 1887–1889, Nov. 2008.
- [9] F. Yaman and Guifang Li, "Nonlinear Impairment Compensation for Polarization-Division Multiplexed WDM Transmission Using Digital Backward Propagation," *IEEE Photonics Journal*, vol. 1, no. 2, pp. 144–152, 2009.
- [10] Ezra Ip, "Nonlinear Compensation Using Backpropagation for Polarization-Multiplexed Transmission," *IEEE J. Lightw. Technol.*, vol. 28, no. 6, pp. 939–951, 2010.
- [11] Y. Gao, F. Zhang, L. Dou, Z. Chen, and A. Xu, "Intra-Channel Nonlinearities Mitigation in Pseudo-Linear Coherent QPSK Transmission Systems Via Nonlinear Electrical Equalizer," *Opt. Commun.*, vol. 282, no. 12, pp. 2421–2425, 2009.
- [12] R. Dischler, and F. Buchali, "Transmission of 1.2 Tb/s Continuous Waveband PDM-OFDM-FDM Signal with Spectral Efficiency of 3.3 bit/s/Hz over 400 km of SSMF," in *Proc. Opt. Fiber Commun. Conf. (OFC '09)*, San Diego, CA, 2009, paper PDP2.
- [13] Mateo, E.F., X. Zhou, G. Li, "Selective Post-Compensation of Nonlinear Impairments in Polarization-Division Multiplexed WDM Systems With Different Channel Granularities," *IEEE J. Quant. Elect.*, vol. 47, no. 1, pp. 109–116, Jan. 2011.
- [14] Jie Pan, Chi-Hao Cheng, "Nonlinear Electrical Compensation for the Coherent Optical OFDM System," *Journal of Lightwave Technology*, vol. 29, no. 2 pp. 215–221, 2011.
- [15] R. Weidenfeld, M. Nazarathy, R. Noe, I. Shpanzter, "Volterra Nonlinear Compensation of 100G Coherent OFDM with Baud-Rate ADC, Tolerable Complexity and Low Intra-Channel FWM/XPM Error Propagation," in *Proc. Opt. Fiber Commun. Conf. (OFC '10)*, San Diego, CA, 2010, paper OTuE3.
- [16] M. Nazarathy, J. Khurgin, R. Weidenfeld, Y. Meiman, P. Cho, R. Noe, I. Shpanzter, and V. Karagodsky, "Phased-Array Cancellation of Non-Linear FWM in Coherent OFDM Dispersive Multi-Span Links," *Opt. Express*, vol. 16, no. 20, pp. 15777–15810, 2008.
- [17] Xiang Liu, F. Buchali, and R. W. Tkach, "Improving the Nonlinear Tolerance of Polarization-Division-Multiplexed CO-OFDM in Long-Haul Fiber transmission," *IEEE J. Lightw. Technol.* vol. 27, no. 16, pp. 3632–3640, 2009.
- [18] A. Lowery, "Fiber Nonlinearity Pre- and Post-Compensation for Long-Haul Optical Links Using OFDM," *Opt. Express*, vol. 15, no. 20, pp. 12965–12970, 2007.
- [19] Yan Tang, William Shieh, and Brian S. Krongold, "Fiber Nonlinearity Mitigation in 428-Gb/s Multiband Coherent Optical OFDM Systems," in *Proc. Opt. Fiber Commun. Conf. (OFC '10)*, San Diego, CA, 2010, paper JThA6.
- [20] Juhao Li, Su Zhang, Fan Zhang, and Zhangyuan Chen, "A Novel Coherent Optical Single-Carrier Frequency-Division-Multiplexing (CO-SCFDM) Scheme for Optical Fiber Transmission Systems," in *Proc. Photonics in Switching (PS '10)*, Monterey, CA, 2010, paper JTUB41.
- [21] 3rd Generation Partnership Project, "Physical Layer Aspects for Evolved Universal Terrestrial Radio Access (UTRA)," (2006), <http://www.3gpp.org/ftp/Specs/html-info/25814.htm>
- [22] G. P. Agrawal, *Nonlinear Fiber Optics*, 3rd ed. San Diego, CA: Academic Press, 2001.
- [23] Yan Gao, Fan Zhang, Liang Dou, Zhangyuan Chen, Anshi Xu, "Electrical Post-Compensation of Intrachannel Nonlinearities in 10GBaud Coherent QPSK Transmission Systems," *Optics Communications*, vol. 282, no. 5, pp. 992–996, 2009.
- [24] D. Marcuse, C. R. Menyuk, and P. K. A. Wai, "Application of the Manakov-PMD Equation to Studies of Signal Propagation in Optical Fibers with Randomly Varying Birefringence," *IEEE J. Lightwave Technol.*, vol. 15, no. 9, pp. 1735–1746, Sep. 1997.
- [25] M. Schetzen, *The Volterra and Wiener Theories of Non-linear Systems*. New York: John Wiley & Sons, 1980.
- [26] K. V. Peddanarappagari and M. Brandt-Pearce, "Volterra Series Transfer Function of Single-Mode Fibers," *IEEE J. Lightw. Technol.*, vol. 15, no. 12, pp. 2232–2241, Dec. 1997.
- [27] A. Mecozzi, C. B. Clausen, and M. Shtaif, "System Impact of Intra-Channel Nonlinear Effects in Highly Dispersed Optical Pulse Transmission," *IEEE Photon. Technol. Lett.*, vol. 12, pp. 1633–1635, 2000.
- [28] M. J. Ablowitz and T. Hirooka, "Resonant Intrachannel Pulse Interaction in Dispersion-Managed Transmission Systems," *IEEE J. Sel. Topics Quantum Electron.*, vol. 8, no. 3, pp. 603–614, 2002.
- [29] L. Dou, Z. Tao, L. Li, W. Yan, T. Tanimura, T. Hoshida, and J. C. Rasmussen, "A Low Complexity Pre-Distortion Method for Intra-channel Nonlinearity," in *Proc. Opt. Fiber Commun. Conf. (OFC '11)*, Los Angeles, CA, 2011, paper OTF5.
- [30] W. Yan, Z. Tao, L. Dou, L. Li, S. Oda, T. Tanimura, T. Hoshida, and J. C. Rasmussen, "Low Complexity Digital Perturbation Back-propagation," in *Proc. European Conf. Opt. Commun. (ECOC '11)*, Geneva, Switzerland, 2011, paper Tu.3.A.2.
- [31] F. P. Guiomar, J. D. Reis, A. L. Teixeira, and A. N. Pinto, "Digital Postcompensation Using Volterra Series Transfer Function," *IEEE Photon. Technol. Lett.*, vol. 23, no. 19, pp. 1412–1414, 2011.
- [32] Eduardo F. Mateo and Guifang Li, "Compensation of Interchannel Nonlinearities Using Enhanced Coupled Equations for Digital Backward Propagation," *Applied Optics*, vol. 48, no. 25, pp. 6–10, 2009.

Manuscript received: December 4, 2011

Biography

Fan Zhang (fzhang@pku.edu.cn) received his PhD degree in electromagnetic fields and microwave technology from Beijing University of Posts and Telecommunications in 2002. From 2002 to 2004, he was a senior research associate at City University, Hong Kong. From 2004 to 2006, he was a Humboldt Research Fellow at Fachgebiet Hochfrequenztechnik, Technische Universität, Berlin. Since May 2006, he has been an associate professor at the School of Electronics Engineering and Computer Science, Peking University. His current research interests include long-haul optical transmission and photonic networking technologies, especially coherent optical communication and digital signal processing. He has published more than sixty academic articles in peer-reviewed international journals. Dr. Zhang is a senior member of IEEE and a member of the Optical Society of America.

1 Tb/s Nyquist-WDM PM-RZ-QPSK Superchannel Transmission over 1000 km SMF-28 with MAP Equalization

Ze Dong, Jianjun Yu, and Hung-Chang Chien

(ZTE USA Inc., Morristown, NJ 07960, USA)

Abstract

In this paper, we evaluate transmission in a 1 Tb/s (10×112 Gb/s) Nyquist-WDM PM-RZ-QPSK superchannel over a widely-deployed SMF-28 fiber with and without maximum a-posteriori (MAP) equalization. Over 1000 km can be reached with BER below the HD FEC limit and with a spectral efficiency of 4 b/s/Hz.

Keywords

coherent detection; QPSK; maximum a-posteriori detection; Nyquist-WDM; superchannel

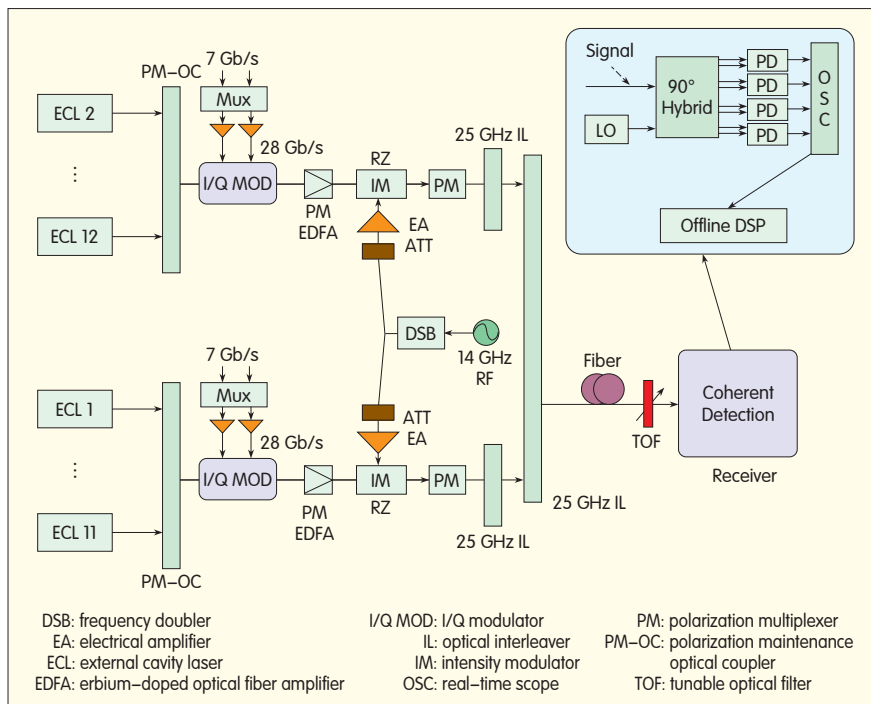
1 Introduction

Terabit superchannel technology is attracting much interest because of its unparalleled capacity, and because it can fulfil the fast-growing demand for bandwidth [1]–[8]. Coherent optical OFDM (CO-OFDM) is a candidate superchannel technology that has high spectral efficiency and superior tolerance of inter-symbol interference (ISI). However, its performance is affected by misalignment of symbol transitions, power mismatch between subcarriers, and insufficient receiver bandwidth [2]. As an alternative, Nyquist-WDM is a practical means of delivering a bundle of standardized 100G channels with partial spectral overlapping. Subcarrier crosstalk is suppressed by aggressive optical filtering, which means ISI is the dominant impairment to be tackled at the receiver [4]–[7]. Transmission of a 100 Gb/s Nyquist-WDM signal over large core fiber and short erbium-doped fiber amplifier (EDFA) span with nonlinear equalization has been realized. However, this transmission is mainly for subsea applications [4]–[7]. In this paper, we describe transmission of a 1 Tb/s Nyquist-WDM superchannel over widely deployed SMF-28 fiber within an 80 km-span EDFA system. The Nyquist-WDM superchannel comprises ten subcarriers with 25 GHz frequency spacing, and each carries a 112 Gb/s PM-RZ-QPSK signal so that the

combined bit rate is 1.12 Tb/s.

2 Testbed Setup for Terabit Nyquist-WDM Superchannel Transmission

Fig. 1 shows the experiment setup for generation and transmission of 1 Tb/s optical Nyquist-WDM PM-RZ-QPSK superchannel. The superchannel comprises 12 subchannels spaced at 25 GHz. Each subchannel is powered by an external cavity laser (ECL) with a linewidth smaller than 100 kHz. The subchannels are divided into even (ECL_{2-12}) and odd (ECL_{1-11}) groups. ECL_{2-12} and ECL_{1-11} are combined by a polarization-maintaining optical coupler (PM-OC) and are then modulated by an I/Q modulator (I/Q MOD) driven by two sets of 28 Gb/s pseudorandom binary sequences (PRBSs) with word lengths of $2^{13}-1$. The RZ carver is realized using a single-arm Mach-Zehnder intensity modulator (IM) driven by a 28 GHz RF signal multiplexed from a 14 GHz RF source. The duty cycle of the signal after the IM is about 45%. After polarization multiplexing (PM), each subchannel carries a 112 Gb/s PM-RZ-QPSK signal. The odd and even subcarriers are launched separately into two independent 25/50 GHz optical interleavers (ILs) and are then combined using a rear 25/50 GHz IL. Such cascading and aggressive optical filtering mitigates interchannel interference (ICI) between Nyquist-WDM subchannels at the cost of increasing



▲ Figure 1. Testbed setup for 1Tb/s Nyquist-WDM superchannel transmission.

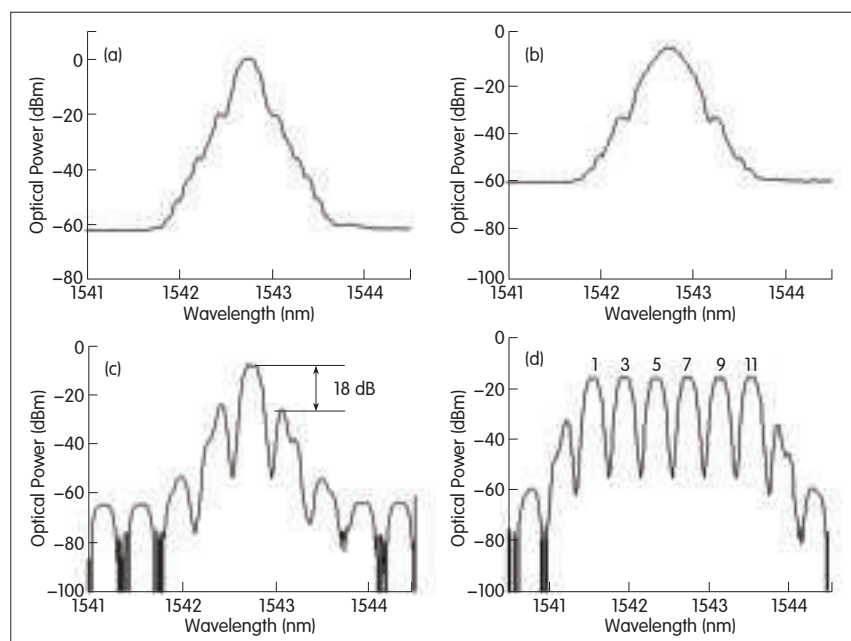
the ISI. The aggregated terabit Nyquist-WDM superchannel is then launched into a recirculating loop comprising five 80 km SMF-28 spans with an average loss of 16.7 dB and chromatic dispersion of 17 ps/km/nm at 1550 nm. The loop has no optical dispersion compensation modules. For each span, an EDFA with midstage adjustable-tilt filter is used to provide flat gain. A tunable optical bandpass filter is also used to remove amplified spontaneous emission (ASE) noise. The total launch power into the transmission fiber is 10.7 ± 4 dBm (-4 to approximately 4 dBm per subchannel) at 112 Gb/s. After that, a subcarrier is selected using a tunable optical filter (TOF) for coherent detection. At the receiver, an ECL with a linewidth less than 100 kHz is used as the fiber laser local oscillator (LO). A polarization-diverse 90 degree hybrid is used for polarization and phase-diverse coherent detection of the LO and received optical signal before balance detection is performed. Analog to digital sampling and digitization occurs in the digital scope, which has a 40 GSa/s sample rate and 16 GHz electrical bandwidth. The captured data is processed through an offline DSP. First, the clock is extracted using a square and filter method, and the digital signal is resampled at twice the baud rate of the recovery clock. Second, a $T/2$ -spaced time-domain finite impulse response (FIR) filter is used to compensate for chromatic dispersion. Third, two complex-valued, 13-tap, $T/2$ -spaced adaptive

FIR filters, based on classic constant modulus algorithm (CMA), are used to retrieve the modulus of the QPSK signal.

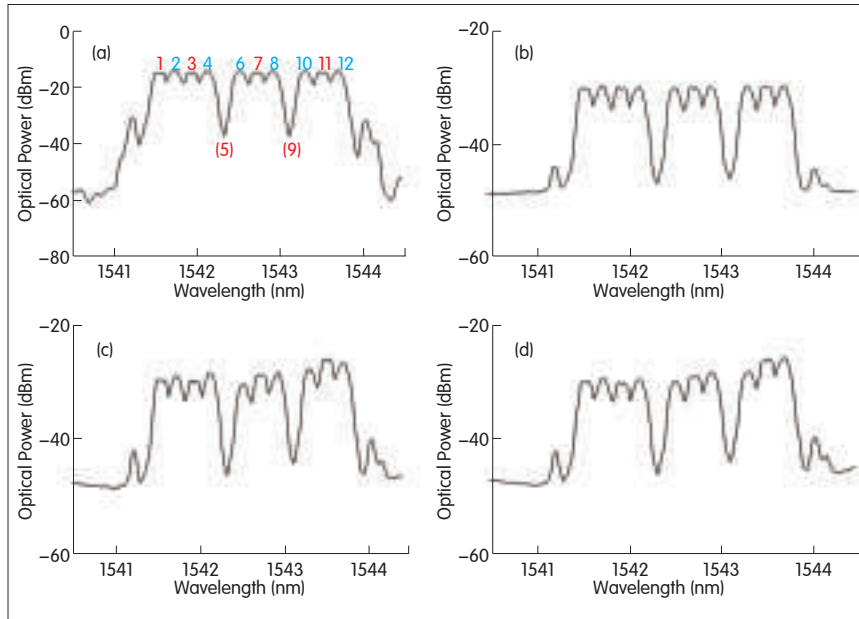
Carrier recovery is then performed. The feed-forward fourth power is used to estimate the frequency offset between the LO and received optical signal. Then, the Viterbi-Viterbi algorithm is used to estimate the carrier phase. To improve the transmission performance of a Nyquist-WDM PM-RZ-QPSK signal subject to tight optical filtering and crosstalk, we propose MAP equalization with high data-pattern dependence. First, a sequence of data symbols with BER less than 3×10^{-4} is decided before averaging so that the symbols can be arranged into a data dependence pattern (64 kinds in the case of QPSK) to be a decision reference. Then, the data received after DSP is calculated by correlating with the decision reference to the maximum extent and mapping the QPSK data dependence decisions.

3 Experiment Results

The CW light waves (ECL₁₋₁₂) range from 1541.5 nm to 1543.7 nm with wavelength spacing of 25 GHz. An IM with appropriate DC bias and electrical amplifier power control are used to create an RZ pulse with 44% duty cycle. The V_{pp} of the 28 GHz RF signal is 17 V. Fig. 2(a) shows a single-carrier 28 Gbaud QPSK signal before the RZ carver, and Fig. 2(b) shows a single-carrier 28 Gbaud QPSK signal after the RZ



▲ Figure 2. Optical spectra (0.1 nm) (a) before RZ, (b) after RZ, (c) after two ILs for ECL₇, and (d) after two ILs for ECL₁₋₁₁.



▲ Figure 3. Optical spectra (0.1 nm) of 1Tb/s signal in (a) back-to-back transmission and after (b) 1000 km, (c) 2000 km, and (d) 2400 km SMF-28 transmission.

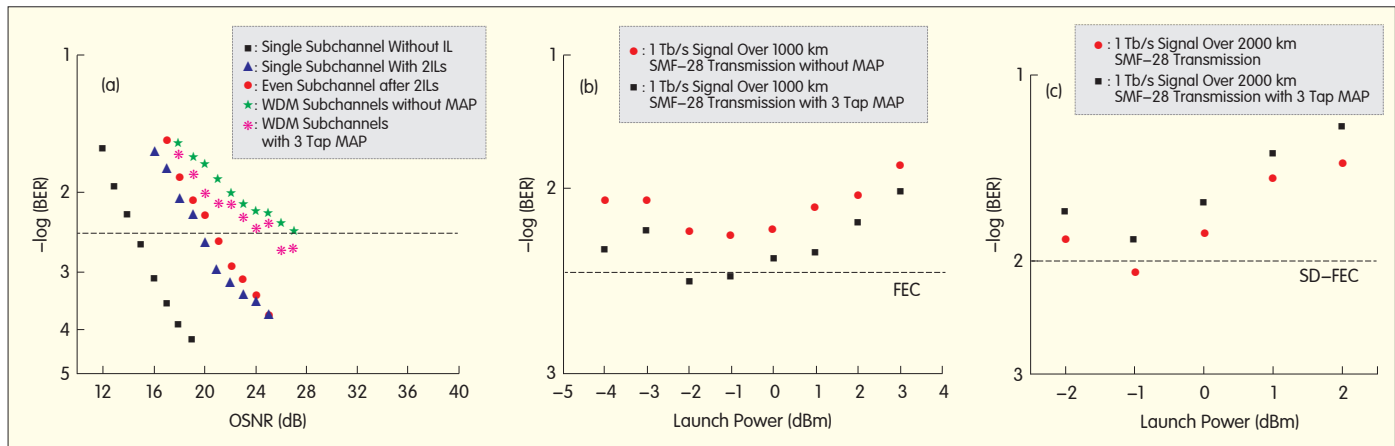
carver. Fig. 2(c) shows the optical spectrum of the subchannel (ECL₇) after two stages of 25/50 ILs. The ratio of in-band signal power to out-of-band signal leakage is about 18 dB. Such out-of-band leakage can cause ICI to spread to adjacent even channels that are 50 GHz apart. However, this is not an issue in a practical system where each subchannel is independently modulated and then combined through an arrayed waveguide grating (AWG) with the subchannel bandwidth highly confined. Fig. 2(d) shows the optical spectrum of subchannels ECL₁₋₁₁ after two stages of ILs. To simulate a practical system, we turn the fifth and ninth subchannels off to mitigate crosstalk and assess the performance of the seventh subchannel after transmission. Fig. 3 shows the optical spectra of ten subcarriers with and without transmission.

We then characterize the back-to-back performance of the seventh subchannel by aligning its subwavelength to that of the LO and turn all the other subchannels off (Fig. 4a). The required OSNR for a BER of 3.8×10^{-3} is 14.5 dB with aggressive filtering and 19.5 dB without aggressive filtering for 0.1 nm resolution. The filtering is performed by two stages of interleavers (two ILs), and 650,000 symbols are counted as BER. When all the odd subchannels are turned on, the OSNR penalty caused by ICI between 50 GHz spaced subcarriers is 0.9 dB. For a 1 Tb/s Nyquist-WDM signal, the OSNR penalty caused by 25 GHz adjacent subcarriers and tight filtering is about 13 dB. For 1000 km SMF-28 Nyquist-WDM transmission (Fig. 4b), the BER of the seventh subcarrier can barely reach the hard-decision (HD) pre-FEC limit of 3.8×10^{-3} at any launch power level unless MAP equalization is used. With MAP equalization, the BER can be brought well below the FEC limit at subchannel launch powers of -1 and -2 dBm. Similarly, for 2000

km SMF-28 Nyquist-WDM transmission (Fig. 4c), BER below soft-decision (SD) pre-FEC limit of approximately 1×10^{-2} can be obtained with MAP equalization at input power of -1 dBm. (Fig. 4c). The bit rate should be 120 Gb/s or higher if SD FEC overhead is considered.

4 Conclusion

We have described the generation, transmission, and coherent detection of a 1 Tb/s Nyquist-WDM superchannel where each subchannel carries a 112 Gb/s PM-RZ-QPSK signal on a 25 GHz grid. The robustness of MAP nonlinear equalization against tight Nyquist-WDM filtering and crosstalk has also been shown in a widely deployed SMF-28 fiber with an 80 km-span EDFA system. With subchannel launch power



▲ Figure 4. (a) BER curve of seventh subchannel (back-to-back), (b) BER curve for 1000 km SMF-28 transmission, and (c) BER curve for 2000 km SMF-28 transmission.

of approximately -1 dBm, the obtained BERs are below the HD FEC limits for Nyquist-WDM transmission over 1000 km SMF-28 with EDFA-only amplification.

References

- [1] R. Dischler, and F. Buchali, "Transmission of 1.2Tb/s Continuous Waveband PDM-OFDM-FDM Signal with Spectral Efficiency of 3.3 bit/s/Hz over 400km of SSF," in *Proc. Opt. Fiber Commun. Conf. (OFC '09)*, San Diego, CA, 2009, paper PDP2.
- [2] A. Sano, E. Yamada, H. Masuda, E. Yamazaki, T. Kobayashi, and E. Yoshida, "No-Guard-Interval Coherent Optical OFDM for 100-Gb/s Long-Haul WDM Transmission," *J. Lightw. Technol.*, vol. 27, no. 16, pp. 3705–3713, 2009.
- [3] J. Yu, "1.2 Tb/s Orthogonal PDM-RZ-QPSK DWDM Signal Transmission over 1040 km SMF-28," *Electron. Lett.*, vol. 46, no. 11, pp. 775–777, May 2010.
- [4] Y. Cai, D.G. Foursa, C.R. Davidson, J.-X. Cai, O. Sinkin, M. Nissov, and A. Pilipetskii, "Experimental Demonstration of Coherent MAP Detection for Nonlinearity Mitigation in Long-Haul Transmissions," in *Proc. Opt. Fiber Commun. Conf. (OFC '10)*, San Diego, CA, 2010, paper OTuE1.
- [5] J. X. Cai, "100G Transoceanic Length Transmission with High SE Using Bandwidth Constrained PDM-QPSK," in *Proc. Optical Fiber Commun. Conf. (OFC '11)*, Los Angeles, CA, 2011, paper OMI3.
- [6] Y. Cai, et al., "Spectral Efficiency Limits of Pre-Filtered Modulation Formats," *Optics Express*, vol. 18, no. 19, pp. 20273–20281, 2010.
- [7] J. X. Cai, et al., "Transmission of 96x100G Pre-Filtered PDM-RZ-QPSK Channels with 300% Spectral Efficiency over 10,608km and 400% Spectral Efficiency over 4,368km," in *Proc. Opt. Fiber Commun. Conf. (OFC '10)*, San Diego, CA, 2010, paper PDPB10.
- [8] Z. Dong, J. Yu, H. Chien and G.-K. Chang, "Ultra-Dense WDM-PON Delivering Carrier-Centralized Nyquist-WDM Uplink with Digital Coherent Detection," *Optics Express*, vol. 19, no. 12, pp. 11100–p11105, 2011.
- [9] G. P. Leguizamon, B. Ortega, and J. Capmany, "Advanced Subcarrier Multiplexed Label SSwapping in Optical Packet Switching Nodes for Next Generation Internet Networks," *IEEE J. Lightw. Technol.*, vol. 27, no. 6, pp. 655–669, 2009.
- [10] M. Khanal, C. J. Chae, and R. S. Tucker, "Selective Broadcasting of Digital Video Signals over a WDM Passive Optical Network," *IEEE Photon. Technol. Lett.*, vol. 17, no. 9, pp. 1992–1994, 2005.
- [11] J. Yu, M.-F. Huang, D. Qian, L. Chen, and G.-K. Chang, "Centralized Lightwave WDM-PON Employing 16-QAM Intensity Modulated OFDM Downstream and OOK Modulated Upstream Signals," *IEEE Photon. Technol. Lett.*, vol. 20, no. 18, pp. 1545–1547, 2008.
- [12] X. Liu, and F. Buchali, "Intra-Symbol Frequency-Domain Averaging Based Channel Estimation for Coherent Optical OFDM," *Opt. Express*, vol. 16, no. 26, pp. 21944–21957, 2008.
- [13] A. J. Lowery, L. Du, and J. Armstrong, "Orthogonal Frequency Division Multiplexing for Adaptive Dispersion Compensation in Long Haul WDM Systems," in *Proc. Opt. Fiber Commun. Conf. (OFC '06)*, Anaheim, CA, 2006, paper PDP39.
- [14] X. Liu, F. Buchali, and R. W. Tkach, "Improving the Nonlinear Tolerance of Polarization-Division-Multiplexed CO-OFDM in Long-Haul Fiber Transmission," *J. Lightwave Technol.*, vol. 27 no. 16, pp. 3632–3640, 2009.
- [15] D. Qian, N. Cvijetic, J. Hu, and T. Wang, "108 Gb/s OFDMA-PON with Polarization Multiplexing and Direct Detection," *J. Lightwave Technol.*, vol. 28 no. 4, pp. 484–493, 2010.
- [16] R. P. Giddings, X. Q. Jin, E. Hugues-Salas, E. Giacomidis, J. L. Wei, and J. M. Tang, "Experimental demonstration of a record high 11.25 Gb/s real-time optical OFDM transceiver supporting 25km SMF end-to-end transmission in simple IMDD systems," *Opt. Express*, vol. 18, no. 6, pp. 5541–5555, 2010.
- [17] D. Qian, N. Cvijetic, Y. Huang, J. Yu, and T. Wang, "100km Long Reach Upstream 36Gb/s-OFDMA-PON over a Single Wavelength with Source-Free ONU's," in *Proc. European Conf. Opt. Commun. (ECOC '09)*, Vienna, Austria, 2009.
- [18] C.-W. Chow, C.-H. Yeh, C.-H. Wang, F.-Y. Shih, C.-L. Pan, and S. Chi, "WDM Extended Reach Passive Optical Networks Using OFDM-QAM," *Opt. Express*, vol. 16, no. 16, pp. 12097–12101, 2008.
- [19] D. Qian, J. Hu, P. N. Ji, and T. Wang, "10 Gb/s OFDMA-PON for Delivery of Heterogeneous Services," in *Proc. Opt. Fiber Conf. (OFC '09)*, San Diego, CA, 2009, paper OWH4.
- [20] R. P. Giddings, E. Hugues-Salas, X. Q. Jin, J. L. Wei, and J. M. Tang, "Colourless Real-Time Optical OFDM End-to-End Transmission at 7.5Gb/s over 25km SSF Using 1GHz RSOAs for WDM-PONs," in *Proc. Opt. Fiber Conf. (OFC '10)*, San Diego, CA, 2010, paper OMS4.
- [21] L. A. Neto, A. Gharba, P. Chanclou, N. Genay, B. Charbonnier, M. Ouzzif, C. Aupetit-Berthelemy, and J. Le Masson, "High Bit Rate Burst Mode Optical OFDM for Next Generation Passive Optical Networks," in *European Conf. Opt. Commun. (ECOC '10)*, Torino, Italy, 2010.
- [22] J. Chen, L. Wosinska, C. Machuca, and M. Jaeger, "Cost vs. reliability performance study of fiber access network architectures," *IEEE Commun. Mag.*, vol. 48, no. 2, pp. 56–65, 2010.
- [23] M. Dueser, "Optical network architecture," in *Proc. Opt. Fiber Conf. (OFC '11)*, Los Angeles, CA, 2011, paper OMN1.
- [24] K. Grobe and J.-P. Elbers, "PON in adolescence: from TDMA to WDM-PON," *IEEE Commun. Mag.*, vol. 46, no. 1, pp. 26–34, 2008.
- [25] F. J. Effenberger, "The XG-PON System: Cost Effective 10 Gb/s Access," *J. Lightwave Technol.*, vol. 29, no. 4, pp. 403–409, 2011.
- [26] T. Kodama, N. Kataoka, N. Wada, G. Cincotti, X. Wang, T. Miyazaki, and K. Kitayama, "High-Security 2.5 Gbps, Polarization Multiplexed 256-Ary OCDM Using a Single Multi-Port Encoder/Decoder," *Opt. Express*, vol. 18, no. 20, pp. 21376–21385, 2010.
- [27] G. Manzacca, X. Wang, N. Wada, G. Cincotti, and K.-I. Kitayama, "Comparative Study of Multiencoding Schemes for OCDM Using a Single Multiport Optical Encoder/Decoder," *Photon. Technol. Lett.*, vol. 19, no. 8, pp. 559–561, 2007.
- [28] N. Cvijetic, D. Qian, and J. Hu, "100 Gb/s Optical Access Based on Optical Orthogonal Frequency Division Multiplexing," *IEEE Commun. Mag.*, vol. 48, no. 7, pp. 70–77, 2010.

Manuscript received: November 30, 2011

Biographies

Ze Dong (zdong9@mail.gatech.edu) received his BS degree in electronic information science and technology from Hunan Normal University, China, in 2006. He received his PhD degree in electrical engineering from Hunan University, China, and Georgia Institute of Technology, US, in 2011. He is currently working as a postdoctoral fellow at the School of Electrical and Computer Engineering, Georgia Institute of Technology. His research interests include broadband optical communication, and optical coherent communications. He has authored or co-authored more than 32 journal papers and conference proceedings.

Jianjun Yu (yu.jianjun@zteusa.com) received his PhD degree in electrical engineering from Beijing University of Posts and Telecommunications in January 1999. From June 1999 to January 2001, he was an assistant research professor at the Technical University of Denmark, Lyngby. From February 2001 to December 2002, he was a member of the technical staff at Lucent Technologies and Agere Systems, NJ. He became a research faculty member at Georgia Institute of Technology, Atlanta, in January 2003 and was also the director of the Optical Network Laboratory at GIT. From November 2005 to February 2010, he was a senior member of the technical staff at NEC Laboratories America. He is now the chief scientist for high-speed optical transmission and director of Optics Labs for ZTE North America. He is a chair professor at Fudan University and also an adjunct professor and PhD supervisor at Georgia Institute of Technology, BUPT, and Hunan University. He has published more than 100 journal and conference papers. He holds eight US patents and has 30 pending. Dr. Yu is a fellow of the Optical Society of America. He is editor-in-chief of the international journal *Recent Patents on Engineering*, and he is an associate editor for the *Journal of Lightwave Technology* and *Journal of Optical Communications and Networking*. Dr. Yu was a technical committee member for the IEEE LEOS from 2005 to 2007 and for OFC from 2009 to 2011.

Hung-Chang Chien is a senior member of the technical staff at Optics Lab, ZTE USA. He received his PhD degree in electro-optical engineering from National Chiao Tung University, Taiwan, in 2006. From 2007 to 2011, he was a research engineer in the School of Electrical and Computer Engineering, Georgia Institute of Technology. Dr. Chien has authored or co-authored 98 papers published in journals and conference proceedings. He holds one US patent and has nine pending in the fields of coherent DWDM optical transmission, passive optical networks, and radio-over-fiber optical-wireless communication.

From P. 44

paper OThK8.

- [3] G. P. Leguizamon, B. Ortega, and J. Capmany, "Advanced Subcarrier Multiplexed Label SSwapping in Optical Packet Switching Nodes for Next Generation Internet Networks," *IEEE J. Lightw. Technol.*, vol. 27, no. 6, pp. 655–669, 2009.
- [4] M. Khanal, C. J. Chae, and R. S. Tucker, "Selective Broadcasting of Digital Video Signals over a WDM Passive Optical Network," *IEEE Photon. Technol. Lett.*, vol. 17, no. 9, pp. 1992–1994, 2005.
- [5] J. Yu, M.-F. Huang, D. Qian, L. Chen, and G.-K. Chang, "Centralized Lightwave WDM-PON Employing 16-QAM Intensity Modulated OFDM Downstream and OOK Modulated Upstream Signals," *IEEE Photon. Technol. Lett.*, vol. 20, no. 18, pp. 1545–1547, 2008.
- [6] X. Liu, and F. Buchali, "Intra-Symbol Frequency-Domain Averaging Based Channel Estimation for Coherent Optical OFDM," *Opt. Express*, vol. 16, no. 26, pp. 21944–21957, 2008.
- [7] A. J. Lowery, L. Du, and J. Armstrong, "Orthogonal Frequency Division Multiplexing for Adaptive Dispersion Compensation in Long Haul WDM Systems," in *Proc. Opt. Fiber Commun. Conf. (OFC '06)*, Anaheim, CA, 2006, paper PDP39.
- [8] X. Liu, F. Buchali, and R. W. Tkach, "Improving the Nonlinear Tolerance of Polarization-Division-Multiplexed CO-OFDM in Long-Haul Fiber Transmission," *J. Lightwave Technol.*, vol. 27 no. 16, pp. 3632–3640, 2009.
- [9] D. Qian, N. Cvijetic, J. Hu, and T. Wang, "108 Gb/s OFDMA-PON with Polarization Multiplexing and Direct Detection," *J. Lightwave Technol.*, vol. 28 no. 4, pp. 484–493, 2010.
- [10] R. P. Giddings, X. Q. Jin, E. Hugues-Salas, E. Giacomidis, J. L. Wei, and J. M. Tang, "Experimental demonstration of a record high 11.25 Gb/s real-time optical OFDM transceiver supporting 25km SMF end-to-end transmission in simple IMDD systems," *Opt. Express*, vol. 18, no. 6, pp. 5541–5555, 2010.
- [11] D. Qian, N. Cvijetic, Y. Huang, J. Yu, and T. Wang, "100km Long Reach Upstream 36Gb/s-OFDMA-PON over a Single Wavelength with Source-Free ONU's," in *Proc. European Conf. Opt. Commun. (ECOC '09)*, Vienna, Austria, 2009.
- [12] C.-W. Chow, C.-H. Yeh, C.-H. Wang, F.-Y. Shih, C.-L. Pan, and S. Chi, "WDM Extended Reach Passive Optical Networks Using OFDM-QAM," *Opt. Express*, vol. 16, no. 16, pp. 12097–12101, 2008.
- [13] D. Qian, J. Hu, P. N. Ji, and T. Wang, "10 Gb/s OFDMA-PON for Delivery of Heterogeneous Services," in *Proc. Opt. Fiber Conf. (OFC '09)*, San Diego, CA, 2009, paper OWH4.
- [14] R. P. Giddings, E. Hugues-Salas, X. Q. Jin, J. L. Wei, and J. M. Tang, "Colourless Real-Time Optical OFDM End-to-End Transmission at 7.5Gb/s over 25km SSF Using 1GHz RSOAs for WDM-PONs," in *Proc. Opt. Fiber Conf. (OFC '10)*, San Diego, CA, 2010, paper OMS4.
- [15] L. A. Neto, A. Gharba, P. Chanclou, N. Genay, B. Charbonnier, M. Ouzzif, C. Aupetit-Berthelemy, and J. Le Masson, "High Bit Rate Burst Mode Optical OFDM for Next Generation Passive Optical Networks," in *European Conf. Opt. Commun. (ECOC '10)*, Torino, Italy, 2010.
- [16] J. Chen, L. Wosinska, C. Machuca, and M. Jaeger, "Cost vs. reliability performance study of fiber access network architectures," *IEEE Commun. Mag.*, vol. 48, no. 2, pp. 56–65, 2010.
- [17] M. Dueser, "Optical network architecture," in *Proc. Opt. Fiber Conf. (OFC '11)*, Los Angeles, CA, 2011, paper OMN1.
- [18] K. Grobe and J.-P. Elbers, "PON in adolescence: from TDMA to WDM-PON," *IEEE Commun. Mag.*, vol. 46, no. 1, pp. 26–34, 2008.
- [19] F. J. Effenberger, "The XG-PON System: Cost Effective 10 Gb/s Access," *J. Lightwave Technol.*, vol. 29, no. 4, pp. 403–409, 2011.
- [20] T. Kodama, N. Kataoka, N. Wada, G. Cincotti, X. Wang, T. Miyazaki, and K. Kitayama, "High-Security 2.5 Gbps, Polarization Multiplexed 256-Ary OCDM Using a Single Multi-Port Encoder/Decoder," *Opt. Express*, vol. 18, no. 20, pp. 21376–21385, 2010.
- [21] G. Manzacca, X. Wang, N. Wada, G. Cincotti, and K.-I. Kitayama, "Comparative Study of Multiencoding Schemes for OCDM Using a Single Multiport Optical Encoder/Decoder," *Photon. Technol. Lett.*, vol. 19, no. 8, pp. 559–561, 2007.
- [22] N. Cvijetic, D. Qian, and J. Hu, "100 Gb/s Optical Access Based on Optical Orthogonal Frequency Division Multiplexing," *IEEE Commun. Mag.*, vol. 48, no. 7, pp. 70–77, 2010.

Manuscript received: November 30, 2011

Biography

Xiangjun Xin (xjxin@bupt.edu.cn) received his BS degree from Wuhan University of Science and Technology, China, in 1993. He received his MS degree from Beijing Jiaotong University in 2000 and his PhD degree from Beijing University of Posts and Telecommunications (BUPT) in 2003. He is currently a professor at BUPT and is vice president of the School of Electronic Engineering. He oversees municipal key disciplines in optical engineering. His research interests include OFDM-PON, wavelength conversion, Raman fiber amplifier, optical switching, terabit per second optical transmission, and radio-over-fiber technologies for next-generation optical networks.

Hardware Architecture of Polyphase Filter Banks Performing Embedded Resampling for Software-Defined Radio Front-Ends

Mehmood Awan¹, Yannick Le Moullec¹, Peter Koch¹, and Fred Harris²

(1. Technology Platforms Section, Dept. of Electronic Systems, Aalborg University, Denmark;

2. Dept. of Electrical & Computer Engineering, San Diego State University, CA, USA)

Abstract

In this paper, we describe resource-efficient hardware architectures for software-defined radio (SDR) front-ends. These architectures are made efficient by using a polyphase channelizer that performs arbitrary sample rate changes, frequency selection, and bandwidth control. We discuss area, time, and power optimization for field programmable gate array (FPGA) based architectures in an M -path polyphase filter bank with modified N -path polyphase filter. Such systems allow resampling by arbitrary ratios while simultaneously performing baseband aliasing from center frequencies at Nyquist zones that are not multiples of the output sample rate. A non-maximally decimated polyphase filter bank, where the number of data loads is not equal to the number of M subfilters, processes M subfilters in a time period that is either less than or greater than the M data-load's time period. We present a load-process architecture (LPA) and a runtime architecture (RA) (based on serial polyphase structure) which have different scheduling. In LPA, N subfilters are loaded, and then M subfilters are processed at a clock rate that is a multiple of the input data rate. This is necessary to meet the output time constraint of the down-sampled data. In RA, M subfilters processes are efficiently scheduled within N data-load time while simultaneously loading N subfilters. This requires reduced clock rates compared with LPA, and potentially less power is consumed. A polyphase filter bank that uses different resampling factors for maximally decimated, under-decimated, over-decimated, and combined up- and down-sampled scenarios is used as a case study, and an analysis of area, time, and power for their FPGA architectures is given. For resource-optimized SDR front-ends, RA is superior for reducing operating clock rates and dynamic power consumption. RA is also superior for reducing area resources, except when indices are pre-stored in LUTs.

Keywords

SDR; FPGA; Digital Front-ends; Polyphase Filter Bank; Embedded Resampling

1 Introduction

Polyphase filter banks are versatile engines that perform embedded resampling uncoupled from frequency selection and bandwidth control [1], [2]. In a previous paper "Polyphase Filter Banks for Embedded Sample Rate Changes in Digital Radio Front-Ends" [3], we described the benefits of such a polyphase engine. Five embedded resampling approaches were discussed: 1) maximally decimated, 2) under-decimated, 3) over-decimated, and combined up-and down-sampling with 4) single and 5) multiple stride lengths of the commutator (which feeds input data into the

filter bank). These are efficient approaches to rational resampling in polyphase filter banks because there is no computational cost, and only a state machine is required to schedule the interactions. Polyphase engines are promising candidates for realizing software-defined radio (SDR) front-ends where embedded sample rate changes are needed. This paper describes the associated hardware architecture designed to reduce area, time, and power consumption of such a polyphase engines implemented on FPGA.

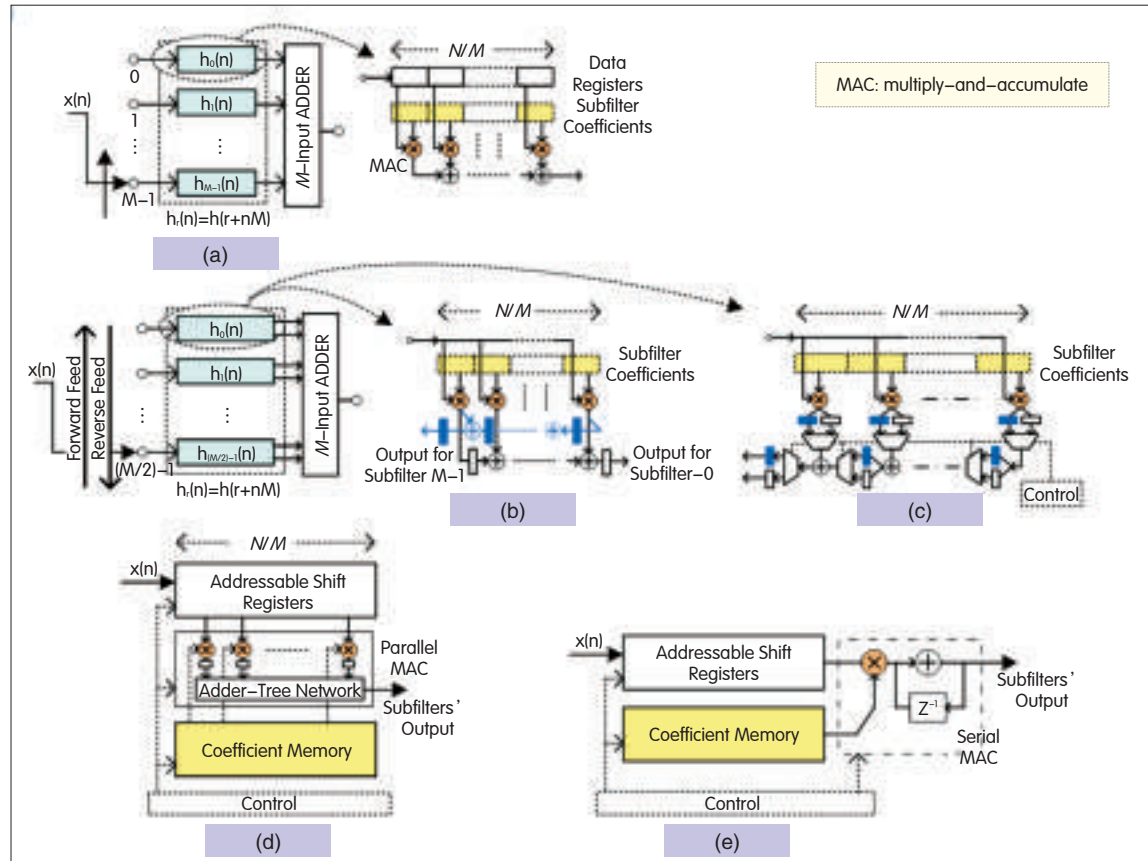
The hardware platform is the most prominent and challenging component of an SDR because it must provide massive computational power and flexibility at the same time

[4], [5]. An important semiconductor technology is the field programmable gate array (FPGA). It consists of a vast array of configurable logic blocks, multipliers, and memories, and it allows a custom data path to be tailored to the application at hand. Parallel processing capabilities in an FPGA has made them the core processing engine in SDR applications. The rich architecture of FPGA with specialized functionalities allows a large design space. In such a large design space, resource-optimized architectures are highly desirable for implementing SDR functions. In this paper, we describe an FPGA-based architecture for polyphase filter banks that is optimized in terms of area, time, and power. A filter bank performs rational sample rate changes together with frequency control and bandwidth reduction.

In section 2, we analyze five structures for the polyphase filter banks in terms of required resources (referred to as resource complexity) and operating clock rates. From these structures, we select the serial polyphase structure with parallel multiply and accumulate (MAC) and explore its implementation options. In section 3, the selected structure is mapped onto the FPGA in two different implementation architectures that are built on different scheduling. These architectures are called load-process architecture (LPA) and runtime architecture (RA). In section 4, we compare resource usages in the LPA and RA variants of the five embedded resampling cases in terms of slice registers, slice lookup tables (LUTs), and dedicated resources as well as the operating clock rates. In section 5, we analyze the dynamic power consumed in the LPA and the RA variants of the five resampling cases. Section 6 concludes the paper.

2 Architecture Design

In this section, we analyze the architectures of the FPGA



▲ Figure 1. Polyphase filter structures: (a) general, (b) symmetric, (c) adder-shared symmetric, (d) serial polyphase with parallel MAC, and (e) serial polyphase with serial MAC.

implementation of a polyphase filter performing embedded sample rate changes. We do not deal with the FFT part and simply replace it with an M -input adder, which represents the output of a channel centered at origin (channel 0). The main building blocks of a polyphase filter are an M -path polyphase lowpass filter and an M -input adder. The structural analysis of the polyphase filter includes general, symmetric, and serial polyphase structures with serial and parallel MACs.

The general M -path polyphase filter structure has M subfilters of length N/M , where N is the length of a non-partitioned lowpass filter. Each of these subfilters operates at $1/M$ times the input rate (Fig. 1a). In the symmetric structure, the symmetry property of the coefficients in the subfilters is exploited, and this reduces the number of subfilters and commutator length to $M/2$. The commutator moves in both the forward and reverse feed directions (Fig. 1b), and the multipliers are shared by the two subfilters [6]. The adders can also be shared by using multiplexers and de-multiplexers to form an adder-shared symmetric structure (Fig. 1c). In an M -path polyphase filter, only one subfilter is processed at a time, and the remaining $M-1$ subfilters are idle. The serial polyphase structure merges the subfilters' data registers to form a data-register bank and merges the subfilters' coefficients to form a coefficient bank. These data register and coefficient banks are addressed by a

▼ Table 1. Resource complexities and required process clock rates for an M -path polyphase filter with P1–P5 polyphase structures (with f_s as the input rate)

	Mults	Adds	Regs	Mux	Demux	Process Clock rate
P1	N	$\left(\frac{N}{M}-1\right)M$	N	0	0	$\left(\frac{f_s}{M}\right)$
P2	$\frac{N}{2}$	$\left(\frac{N}{M}-1\right)M$	N	0	0	$2\left(\frac{f_s}{M}\right)$
P3	$\frac{N}{2}$	$\left(\frac{N}{M}-1\right)\frac{M}{2}$	$2N$	$N-\left(\frac{M}{2}\right)$	$\frac{M}{2}$	$2\left(\frac{f_s}{M}\right)$
P4	1	1	$N+1$	$\frac{N}{M}+1$	0	$\left(\frac{N}{M}\right)f_s$
P5	$\frac{N}{M}$	$\left(\frac{N}{M}-1\right)$	$N+2\left(\frac{N}{M}\right)$	$\frac{N}{M}$	0	f_s

control sequence so that the data registers and coefficients of the desired subfilter can be selected to perform MAC operations. The MAC operations can be performed in parallel or in serial so that a serial polyphase structure with parallel MAC (Fig. 1d) or serial MAC (Fig. 1e) is formed [7].

Table 1 shows the resource complexity in an M -path polyphase filter (each path with N/M taps) for a general polyphase structure (P1), symmetric structure (P2), adder-shared symmetric structure (P3), and serial polyphase structure with serial MAC (P4) and parallel MAC (P5). It also shows the required operating clock rates for these structures (with f_s as the input rate). There is a trade-off between complexities and processing clock rates. A serial polyphase filter with serial MAC has the least complexity but demands a high clock rate. A serial polyphase filter with parallel MAC has a slightly higher complexity and operates at a clock rate that corresponds to the input clock rate. Among all the solutions which do not operate at a clock rate higher than the input clock rate, the P5 uses the least resources.

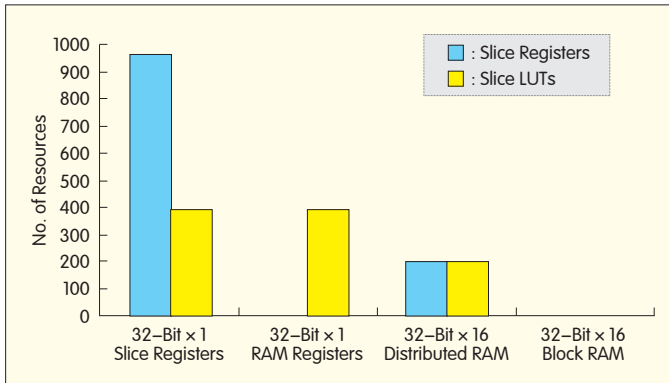
A non-maximally decimated polyphase filter bank processes M subfilters in a time period which is either less or greater than the M data-load's time period. The embedded resampling in the polyphase filter banks requires architectural changes for the structures (Fig. 1) to meet the output time constraint. These changes mainly apply to the structures which are sharing resources (P2, P3, P4 and P5). P1 is a fully parallel solution and is not operationally affected in non-maximally decimated modes because each subfilter is operating independently and M subfilters can be processed even for a single data input time period. However, it does require some changes in its state machine. Symmetric structures are limited to cases with an even number of polyphase partitions to make use of filter symmetry which is not the case for serial polyphase structures. Here, we describe the mapping of P5 onto the target platform—a Xilinx Virtex-5 FPGA (xc5vsx50t-3ff1136) [8]. A fixed-point analysis has been used to determine the word lengths that keep quantization errors below 60 dB (commonly required).

There are a number of design options that correspond to the level of FPGA resource exploitation. The targeted polyphase filter used for the embedded resampling cases [3] has five paths each with six taps. A straightforward mapping of the corresponding P5 structure onto an FPGA, where all the

filter coefficients and the subfilters' tapped delay lines are implemented as combination logic blocks (CLBs), results in relatively high usage of slice registers and LUTs. The implementation scales linearly with the filter size. Today's FPGAs have rich architectures with special memory resources such as distributed RAM and block RAM, high-performance computational resources such as DSP48E slices in addition to the basic CLBs. The DSP48E slice improves flexibility, utilization, and efficiency of applications. It also reduces overall power consumption, increases maximum frequency, and reduces setup and clock-to-out time [9]. The efficient use of these dedicated resources creates a high-performance system with high operating clock rates and reduced CLB requirements.

The filter coefficient bank can be easily replaced by FPGA block RAMs to eliminate the number of CLB resources; however, the polyphase-partitioned data bank (register bank) is a bit critical because it has to shift the new data element to the respective subfilter's tap-delay line and having access to all the taps of that subfilter at the same time. In a maximally decimated system, where the down-sampling factor is equal to the polyphase partition, a first-in first-out (FIFO) can be used as delay lines to derive the optimal architecture, as described in [9]. For non-maximally decimated systems, a two-dimensional memory solution is required in which only the targeted subfilter can be loaded with the input data. Fig. 2 shows the resource usage when mapping a 5×6 register bank (with 32-bit complex data) according to different design options available on the Virtex-5 FPGA. The 5×6 register bank based on slice registers and LUTs uses 960 slice registers and 389 LUTs. Each data register in the subfilters is replaced with a RAM-based shift register (SRL16 / SRL32 mode of the slice LUTs), and the number of slice registers and LUTs usage becomes 0 and 389, respectively. This eliminates the need for slice registers, but the LUT usage remains unchanged. In Virtex-5, each CLB has 64-bit distributed RAM [8] that is bit-addressable. For a 32-bit data register, 32 CLBs are collectively used as a single 32-bit register. The remaining 63 bits in each CLB are unused. Distributed memory is used so that each 64-bit memory contributes one bit to a 32-bit data register for 64 subfilters (only five are used). In this way, the memory that was previously used for only one data register of a subfilter is now used for one data register for all five subfilters. The resource usage for a 5×6 register bank based on distributed RAM becomes 192 slice registers and 192 LUTs. This eliminates the need for the decoder and multiplexers to select the desired subfilter's data elements in the case of a shift-register-based register bank. The same concept can be applied to block RAM, which eliminates CLB usage. Three block RAMs are used for a 5×6 register bank, which corresponds to 2% utilization of block RAM resources for a Virtex-5.

To use block RAM-based register banks, an extra clock cycle is needed for each data load and shift [10] because six block RAMs (32-bit \times 5) are cascaded to form a 5×6 register bank, and the data shift in the subfilters requires data to be available from the preceding memory. Therefore, one clock



▲ Figure 2. Resource usage for a 5×6 register bank by exploiting FPGA resources.

cycle is needed to read the (previous) data elements in the cascaded memories. The next clock cycle loads the new data element to the subfilter's data memory along with data shifting because block RAMs have synchronous read and write operations. A distributed RAM-based register bank has no extra clock cycle penalty for each data load and shift because it has asynchronous read and synchronous write operations.

3 LPA and RA Scheduling

According to the polyphase channelizer configurations for the presented embedded resampling factors [3], five polyphase subfilters need to be processed within the time period of five, three, and six samples and within the time period of zero-packed five and 15 samples. For the resampling cases, where the number of data-loads is less than M (the number of subfilters), it is not possible to process at the input sample rate of f_s in a serial polyphase structure with parallel MAC. Fig. 3 shows the time domain view of the under-decimated case where 3-to-1 down-sampling is performed in a 5-path polyphase filter. The five subfilters are to be processed within the time period of three data samples.

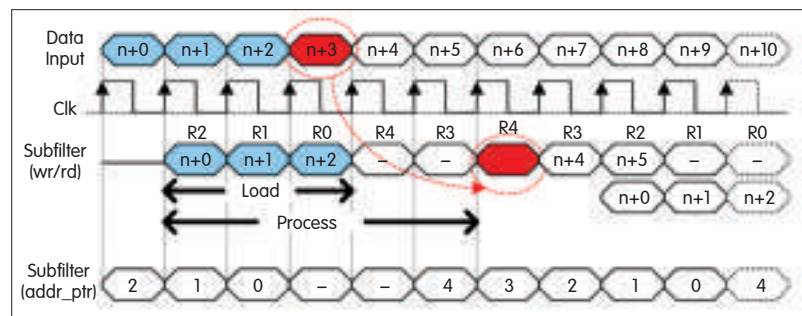
In [10], an LPA with block RAM-based register bank for a polyphase filter bank operating in under-decimated mode is described. This LPA runs at a higher clock rate and uses a FIFO to interface with the input data at lower rate. Fig. 4 shows this architecture with an output

accumulator instead of an FFT to represent the

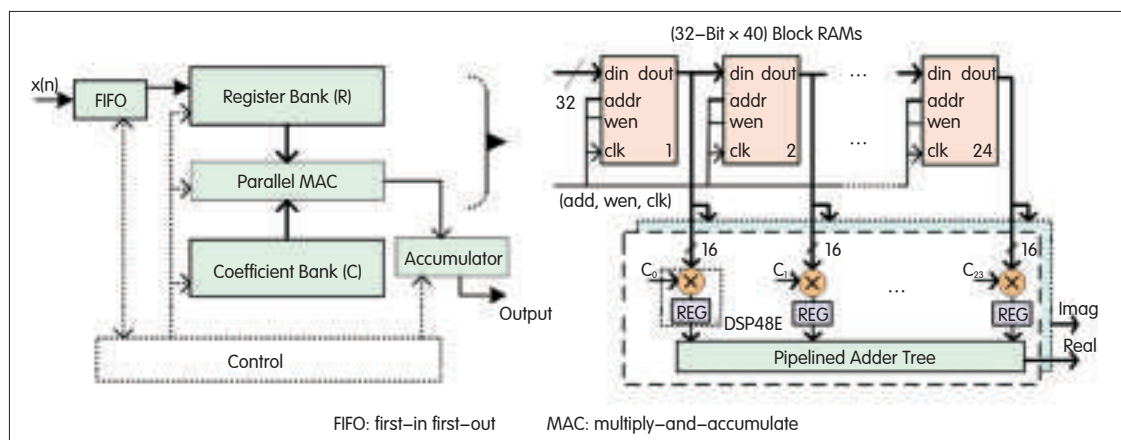
channel at baseband. In the load phase, the data elements are taken from the input FIFO and loaded into the subfilters as directed by the data pointer. In the processing phase, coefficient and data pointers with embedded shifts select the coefficient and data memory elements in order to perform MAC operations. The multipliers are based on DSP48E slices whereas the additions are performed using a CLB-based adder tree network.

The LPAs for the five embedded resampling cases [3] are based on the architecture shown in Fig. 4 according to the number of subfilters (five), number of subfilter taps (six), and corresponding data loading and filter coefficient sequences. The register and coefficient banks are based on block RAMs. Table 2 shows the operating clock rates for the designed LPAs. These clock rates meet the output time constraints of the five different cases, without overflowing the input FIFO. Cases 4 and 5 have two different load times because two different numbers of data inputs are loaded, as shown in Table 4 and Table 5 in [3].

The loading of LPA data from the input FIFO into the register bank is controlled by the FIFO empty flag, so the loading process may need to wait for the valid data sample in the FIFO. The loading time shown in Table 2 incorporates this waiting time. From Table 2, on average, approximately 60% of the loading time is used for loading the register bank. This



▲ Figure 3. Under-decimated case where 3-to-1 down sampling is performed in a 5-path polyphase filter. The five subfilters are to be processed within the time period of three data samples.



▲ Figure 4. LPA with block RAM-based register bank for a polyphase filter operating in under-decimated mode and with a clock rate higher than the input data rate.

▼ Table 2. Required operating clock rates for the five embedded resampling cases in a polyphase filter with block RAM-based register bank

Case	Output Time Constraint (ns)	Required Clock Rate		Load Time (ns)	Process Time (ns)
		Frequency (MHz)	Time Period (ns)		
1	166.6	5 ×	6.66	113.3	53.3
2	100	6 ×	5.55	55.6	44.4
3	200	4 ×	8.33	133.3	67.7
4	83.5	7 ×	4.76	57.2, 33.4	38
5	250	4 ×	8.33	199.9, 166.7	66.7

▼ Table 3. Required operating clock rates for the five embedded resampling cases in a polyphase filter with distributed RAM-based register bank

Case	Output Time Constraint (ns)	Required Clock Rate		Load Time (ns)	Process Time (ns)
		Frequency (MHz)	Time Period (ns)		
1	166.6	4 ×	8.33	100	66.6
2	100	5 ×	6.66	53.4, 40.1	53.3
3	200	3 ×	11.11	100, 122.2	88.8
4	83.5	6 ×	5.55	50, 27.9	44.4
5	250	3 ×	11.11	177.8, 144.5	88.8

eventually requires high operating clock rates in order to process the loaded data within the output time constraints. Although block RAMs do not require CLBs, the synchronous write and read operations require two clock cycles for loading and shifting the input data. Thus, the clock rates must be increased. On the other hand, the distributed RAM-based register bank has asynchronous read operation and only requires one clock cycle for loading and shifting. Therefore, the overall clock rate is reduced, but CLB resources are now required.

In the LPA with distributed RAM-based register bank, the coefficient bank is based on block RAM which requires the coefficient pointer to be one clock cycle ahead of the data pointer that drives the distributed RAM-based register bank. The operating clock rates for the LPA using distributed RAM-based register bank are listed in Table 3. These clock rates meet the output time constraints of the five different cases, without overflowing the input FIFO.

From Table 2 and Table 3, it can be seen that using distributed RAM-based register banks instead of block RAM-based register banks reduces the required operating clock rates for the LPA by approximately 20%. High clock rates for LPA may limit the polyphase filter design to a lower input sample rate because the technology platform has limited ability to achieve high operating clock rates. To overcome the high clock rate demands of the LPA, we introduce the runtime architecture (RA), which runs at a maximum of double the input data rate for the five cases. At double the input data rate, it efficiently schedules the processes of M subfilters within N data load times while simultaneously loading N subfilters. It uses a distributed RAM-based register bank and also eliminates the input FIFO for bridging the input data rate with the high processing clock rate. The RA resembles the LPA (Fig. 4) but has a different configuration of distributed RAM-based register bank, lacks

FIFO, and has a run-time scheduling instead of a load-process scheduling. Here we present the scheduling schemes for the RA for the five embedded resampling cases [3].

Case 1:

Fig. 4a [3] shows the first two loading cycles for the maximally decimated system. The timing diagram for these cycles (Fig. 5) shows the scheduling of the filter operations and input data loading at the input rate. The parallel multipliers and adder tree take four clock cycles to generate the subfilters' MAC output, which are further accumulated over five MAC outputs to get the output of the polyphase filter (channel 0).

Case 2:

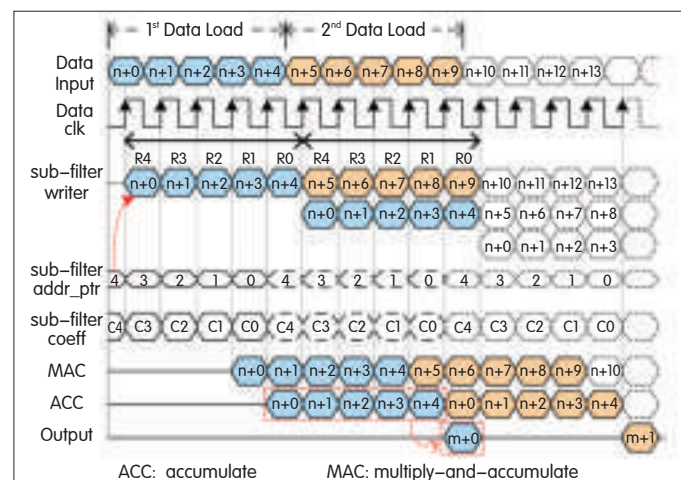
Fig. 4b [3] shows the first two loading cycles for the under-decimated system. The timing diagram for these cycles (Fig. 6) shows the scheduling of the filter operations and input data loading at double the input rate.

The first cycle of the doubled-rate ($2\times$) clock processes the targeted (data-loaded) subfilter while the second cycle of the $2\times$ clock processes the

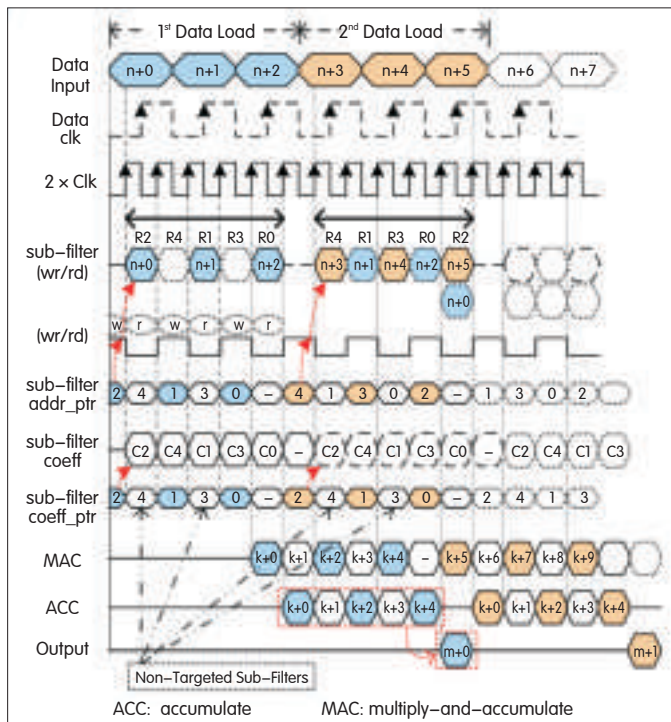
subfilter that is not targeted. The three input data periods have six periods of $2\times$ clock that (for the first load cycle) schedule the processing of the non-targeted subfilters [R4, R3] by interlacing with the processing of the targeted subfilters [R2, R1, R0]. The sixth $2\times$ clock cycle is not used because a new data sample has not yet arrived. The parallel multipliers and adder tree take four cycles of $2\times$ clock to generate the subfilters' MAC output, which is further accumulated over five MAC outputs to obtain the output of the polyphase filter.

Case 3:

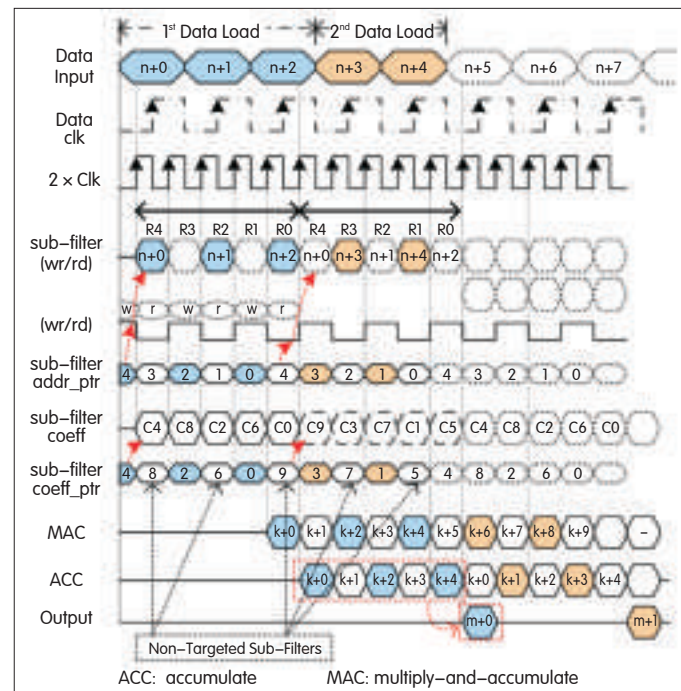
Fig. 4c [3] shows the first two loading cycles for the over-decimated system. The timing diagram for these cycles (Fig. 7) shows the scheduling of the filter operations and input data loading at the input rate. The loading and filter processing is the same as that described in case 1, but six input data samples are loaded instead of five, and the



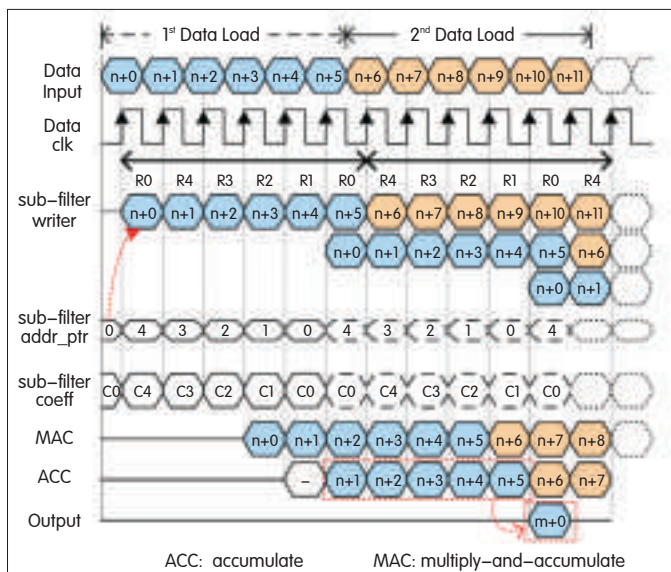
▲ Figure 5. Scheduling of the filter operations (at input clock) and input data loading in a maximally decimated system (case 1).



▲ Figure 6. Scheduling of filter operations (at $2 \times$ clock) and input data loading for an under-decimated system (case 2).



▲ Figure 8. Scheduling of filter operations (at $2 \times$ clock) and input data loading for a system up-sampled by two and down-sampled by five (case 4).



▲ Figure 7. Scheduling of the filter operations (at input clock) and input data loading for an over-decimated system (case 3).

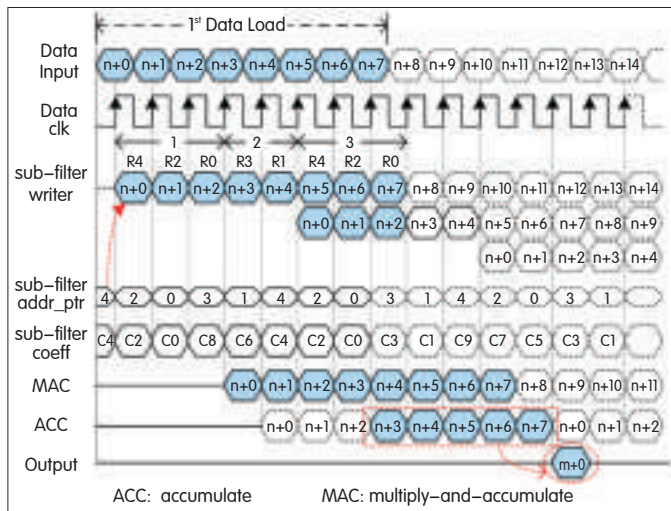
accumulation process is modified. The R0 subfilter in the first load cycle accepts two data loads and is processed separately. Only the second processed output for the subfilter (which is loaded twice) contributes to the final accumulation. This second processed output for R0 subfilter also has the contribution from the first loaded data sample, so the MAC outputs from $n+1$ to $n+5$ are accumulated for the final output.

Case 4:

Fig. 4d [3] shows the two loading cycles for the system up-sampled by two and down-sampled by five. The timing diagram for these cycles (Fig. 8) shows the scheduling of the filter operations and the input data loading at double the input rate. The data loading cycle is periodic for the two states having three and two data inputs, respectively. These two states correspond to six and four cycles of $2 \times$ clock to process five subfilters. In the first state, which has three data inputs, six cycles of the $2 \times$ clock can process five subfilters. However, the second state, which has two data inputs with four $2 \times$ clock cycles, lacks a clock cycle to process the fifth subfilter. This required processing can be achieved either by using a $3 \times$ clock to provide more clock cycles or by efficiently using the non-utilized cycle of the $2 \times$ clock in the first state. In the first state, the processing of the targeted subfilters [R4, R2, R0] is interlaced with the processing of non-targeted subfilters [R3, R1]. In the second state, processing of the non-targeted subfilters [R4, R2, R0] is interlaced with the processing of the targeted subfilters [R3, R1].

Case 5:

Fig. 4e [3] shows the two loading cycles for the system up-sampled by two and down-sampled by 15. The timing diagram for these cycles (Fig. 9) shows the scheduling of filter operations (for one loading cycle) and the input data loading at the input rate. The loading process continues for three stride lengths of the commutator, and the eight input data samples undergo filter processing. The outputs of the subfilter MACs are accumulated from outputs $n+3$ to $n+7$ because these outputs contribute to the final accumulation (which



▲ Figure 9. Scheduling of filter operations (at input clock) and input data loading for a system up-sampled by two and down-sampled by 15 (case 5).

includes outputs from the twice-loaded subfilters).

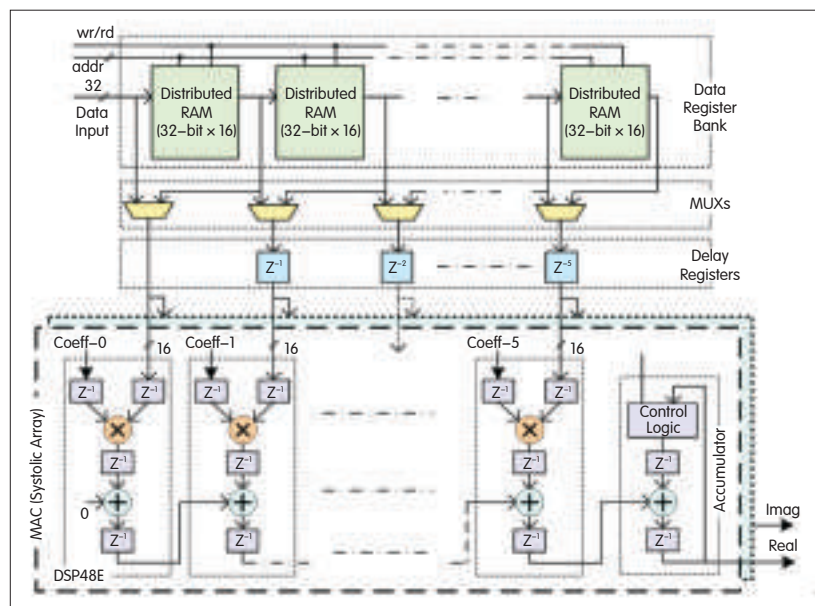
We have so far described the scheduling schemes for the subfilters' processes along with their data loading at the input data rate or double the input data rate. Their architectures have DSP48E slice-based multipliers and CLB-based adder trees that limit the overall operating clock rate to approximately 200 MHz. However, the clock rate can be improved by performing MAC operations in systolic array of DSP48E slices. To perform MAC operations in systolic arrays, the parallel data from the data register bank needs to be time-aligned. The parallel data is fed through a set of registers that delay the data, element by element, in order to align the subfilter's MAC and final accumulation process within the systolic-array-based MAC (Fig. 10). The RA with DSP48E systolic-array-based MAC has high latency because of the pipeline and delay registers, but it increases the maximum operating clock rate to 350 MHz. The multiplexer block before the delay elements switches between the processing of the targeted subfilter and non-targeted subfilter (which is used only in cases 2 and 4).

4 Resource Usage

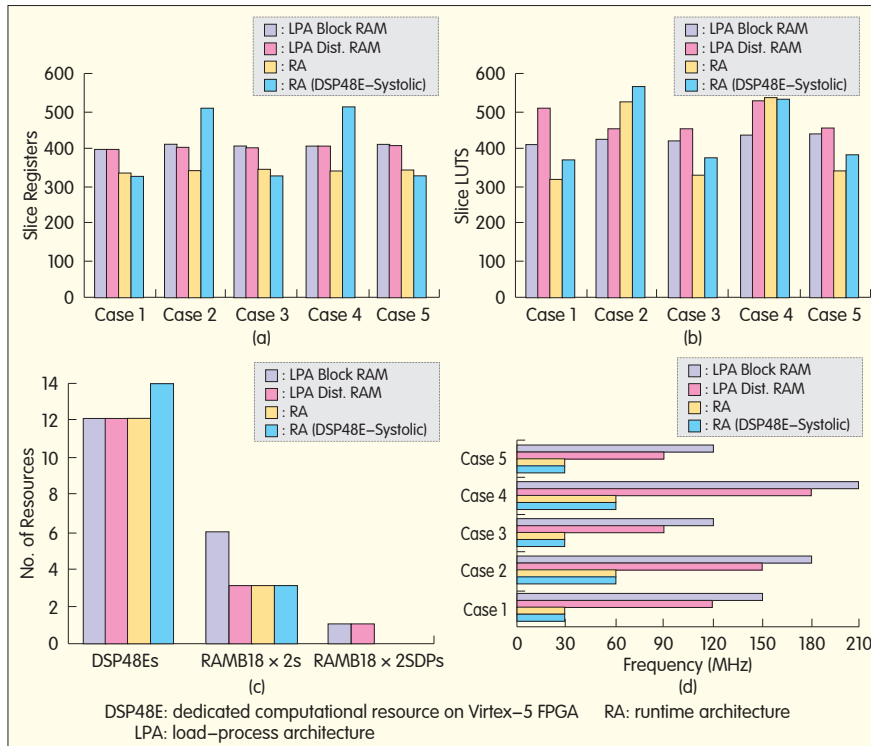
We have presented LPA with block RAM and distributed RAM-based register banks as well as RA (distributed RAM-based register bank) having DSP48E slices based multipliers and CLB-based adder tree, and RA with DSP48E slice systolic-array-based MAC. These architectures are mapped onto a Virtex-5 FPGA in the form of I/Q components. Fig. 11 shows the resource usage in the FPGA for the five embedded resampling cases. The slice registers, slice LUTs, dedicated resources, and required operating clock rates are

shown for both LPAs and RAs.

In all five cases, the LPA block RAM and LPA distributed RAM (based register banks) have almost the same slice register usage, that is, 397 to 407 slice registers. However, in all five cases, there is a difference in slice LUT usage between LPA block RAM and LPA distributed RAM. The usage in LPA block RAM ranges from 406 to 431 slice LUTs, and the usage in LPA distributed RAM ranges from 447 to 502 slice LUTs. This is due to the fact that distributed RAMs (used for the data register bank) require LUTs. The variation in slice LUT usage within LPAs block RAM and LPAs distributed RAM is due to the different sets of states and control sequences for the polyphase engines with different embedded resampling factors. The RA in all the embedded resampling cases uses almost the same number of slice registers (335–342) and almost the same number of slice LUTs (315–334). The exceptions are case 2, which has 524 slice LUTs and case 4, which has 529 slice LUTs. These two systems do not have straightforward indices for accessing their data register and filter coefficient banks. Therefore, the indices for data register and filter coefficient banks are pre-stored in LUTs instead of being generated by sets of counters. The architecture also contains the multiplexer block for switching between targeted and non-targeted subfilter processing that uses slice LUTs and slice registers. Similarly, the RA with DSP48E systolic-array-based MAC — for case 1, case 3, and case 5 — have almost the same number of slice registers (318–324) and LUTs (366–381). The RA with DSP48E systolic-array-based MAC — for case 2 and case 4 — use slightly more slice registers (510) and LUTs (528–563) because of the pre-stored indices for data register and filter coefficient banks, and multiplexer block.



▲ Figure 10. Runtime architecture with DSP48E systolic-array based MAC. The data from the register bank is fed through a set of registers that delay the parallel data, element by element, to align the timing of the subfilter MAC and final accumulation process.



▲ Figure 11. Resource usage for the five embedded resampling cases under LPA and RA: (a) slice registers, (b) slice LUTs, (c) dedicated resources, and (d) required operating clock rates.

The MAC architecture for LPA and RA has DSP48E slice-based multipliers and CLB-based adder trees. All the cases based on this MAC architecture uses 12 DSP48E slices. However, the RA with DSP48E systolic-array-based MAC uses two extra DSP48E slices for the final accumulation process. Similarly, the filter coefficient banks (which are based on block RAMs) in both LPA distributed RAM and RAs uses three dedicated RAMB18x2s [11] resources. However, the LPA block RAM uses three extra resources of RAMB18x2s for its block RAM based register bank. Furthermore, the LPAs use one RAM18x2SDPs [11] for the input FIFO (which is zero for the RAs because they do not use input FIFO).

Fig. 12 shows the number of LUTs versus (operating clock) frequency for the four design solutions for the five embedded resampling cases for the polyphase filter. The RAs for case 1, case 3, and case 5 require less area and lower processing clocks than their LPA counterparts. Similarly, the RAs for case 2 and case 4 require more area but use lower processing clocks than their LPA counterparts. This larger area is due to the pre-stored indices for addressing data register and filter coefficient banks, and also due to the use of multiplexers. Thus, RA is the preferred choice for reduced operating clock rates, and also for reduced area resources with the exception of cases 2 and 4.

5 Power Analysis

Here we analyze power consumption, focusing on dynamic power (CMOS technology is assumed) for the LPA and RA of

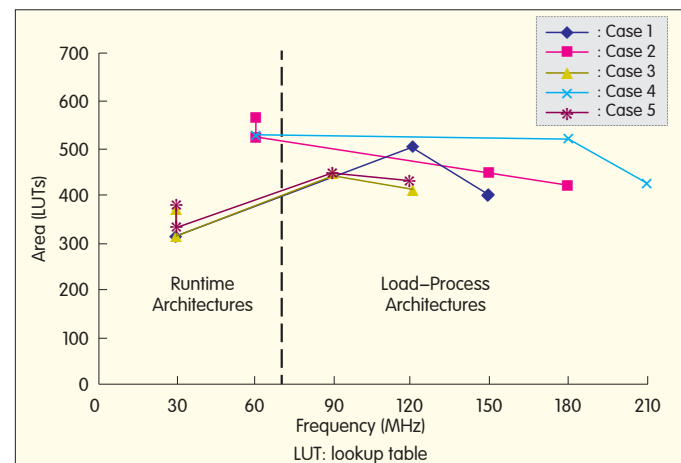
the polyphase filter with five different resampling factors. The demand for high clock rates in the LPA is often difficult to satisfy, and the architectures are power hungry because the dynamic power is proportional to the toggle frequency [12]:

$$P_{\text{dynamic}} = nCV^2f, \quad (1)$$

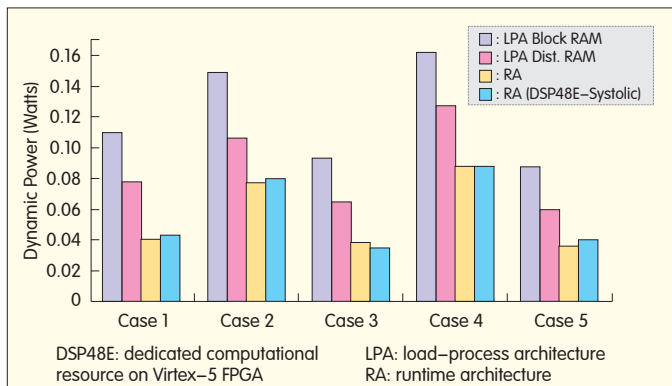
where n is the number of nodes being toggled, C is the load capacitance per node, V is the supply voltage, and f is the toggle frequency. C and V are device parameters, whereas n and f are design parameters. By keeping almost the same n and lowering f , power consumption decreases. As reduced clock operation has the same time constraint as high clock operation, energy consumption is reduced as well.

Fig. 13 shows dynamic power consumption for LPA and RA in the five embedded resampling cases. Xilinx XPA [13] tool is used. The input vector is the same for all the cases and designs, and the activity rates are calculated using ModelSim [14] post-route simulations with a run length of 500 μ s. The thermal settings for the power simulations are 25 degrees Celsius—an ambient temperature, and zero airflow.

Fig. 13 shows that the LPA with block RAM-based register bank consumes more dynamic power than LPA with distributed-RAM based register bank and also more dynamic power than RAs. The maximally decimated system (case 1) based on RAs consumes 64% less dynamic power than its LPA counterpart when block RAM-based register banks are used, and it consumes 49% less dynamic power than its LPA counterpart when distributed RAM-based register banks are used. The under-decimated system (case 2) based on RAs consumes 48% less dynamic power than its LPA counterpart when block RAM-based register banks are used, and it



▲ Figure 12. Area versus (operating clock) frequency for the four design solutions for the five embedded resampling cases.



▲ Figure 13. Dynamic power analysis for all four design solutions for the five embedded resampling cases for the polyphase filter.

consumes 27% less dynamic power than its LPA counterpart when distributed RAM-based register banks are used. The over-decimated system (case 3) based on RAs consumes 60% less dynamic power than its LPA counterpart when block RAM-based register banks are used, and it consumes 42% less dynamic power than its LPA counterpart when distributed RAM-based register banks are used. The up-sampled by two and down-sampled by five system (case 4) based on RAs consumes 46% less dynamic power than its LPA counterpart when block RAM-based register banks are used, and it consumes 31% less dynamic power than its LPA counterpart when distributed RAM-based register banks are used. The up-sampled by two and down-sampled by 15 system (case 5) based on RAs consumes 59% less dynamic power than its LPA counterpart when block RAM-based register banks are used, and it consumes 40% less dynamic power than its LPA counterpart when distributed RAM-based register banks are used. Thus, RA is superior to LPA for reducing dynamic power and clock rates. The five cases are representative for polyphase filter banks that perform embedded sample rate changes. The analysis also shows that the dynamic power for RA with DSP48E systolic-array-based MAC in cases 1, 2 and 5 is between 3% to 11% higher than their RA with DSP48E slice-based multipliers and CLB-based adder tree.

FPGAs provide high parallelism and reprogrammability but at the expense of additional signal routing resources and higher static power consumption due to transistor leakage from parasitic diodes in gate junctions [15], [16]. The static current dissipates power when the device is powered-up and no logic is being clocked. The drive toward smaller transistors in FPGA is necessary for achieving higher chip density and faster dynamic speed. This, in turn, is necessary for embedding specialized DSP functionality blocks, but it substantially increases the current leakage. As the size of transistors in FPGA drops to 70 nm, the current leakage becomes more dominant and accounts for more than 50% of power consumption [17]. The clocked (dynamic) power is added to basic static power when logic is active. Both these power contributions substantially increase as the device junction temperature increases. For the targeted Virtex-5

FPGA at 65 nm, static power consumption in all the cases of embedded resampling is around 0.660 W, significantly higher than the highest dynamic power consumption of 0.162 W. However, static power consumption is technology dependent, and only the area and clock rates can be reduced to minimize the overall power consumption in the system.

6 Conclusion

We have described the architecture and FPGA implementation of a polyphase engine that performs embedded resampling. We have analyzed the architectures for five different embedded resampling scenarios in polyphase filter banks: 1) maximally decimated, 2) under-decimated, 3) over-decimated, and combined up- and down-sampling with 4) single and 5) multiple stride lengths of the commutator that feeds the input data into the filter bank. These scenarios are applicable to any required rational sampling rate change in a polyphase channelizer-based SDR front-end. We have described the FPGA-based architectures for a serial polyphase structure with parallel MAC that has load-process and runtime scheduling. The LPA first loads the selected variable data length and then processes the subfilters that require a high clock rate. The RA, on the other hand, operates at a maximum of double the input data rate, which enables scheduling of subfilter processes along with the data loading. We have also described different design techniques for polyphase register bank mapping. A detailed analysis of area, time, and power in the two types of architectures with different resampling factors has been given. This analysis showed that RA is superior to LPA in reducing operating clock rates and dynamic power. RA is also superior in reducing area resources, except where indices are pre-stored in the LUT. Thus, RA is capable of satisfying the need for minimal area, clock frequency, and power consumption in SDR front-ends. From our FPGA implementation analysis, we have derived a set of valuable guidelines that can be used by system designers to create an SDR front-end that is optimized in terms of area, time, and power consumption given certain design specifications. Future work could include a similar analysis for FPGAs from other manufacturers. This would be valuable in generalizing the suggested hardware architectures.

References

- [1] F. Harris, C. Dick, and M. Rice, "Digital receivers and transmitters using polyphase filter banks for wireless communications", *IEEE Trans. Microw. Theory Tech.*, vol. 51, no. 4, pp. 1395–1412, 2003.
- [2] F. Harris and C. Dick, "Performing simultaneous arbitrary spectral translation and sample rate change in polyphase interpolating or decimating filters in transmitters and receivers," in *Proc. Software Defined Radio Tech. Conf. and Product Expo*, San Diego, CA, Nov. 2002.
- [3] M. Awan, Y. L. Moullec, P. Koch, and F. Harris, "Polyphase filter banks for embedded sample rate changes in digital radio front-ends," *ZTE Communications*, vol. 9, no. 4, pp. 3–9, Dec. 2011.
- [4] D. Liu, A. Nilsson, E. Tell, D. Wu, and J. Eilert, "Bridging dream and reality: programmable baseband processors for software-defined radio", *IEEE Commun. Mag.*, vol. 47, no. 9, pp. 134–140, Sept. 2009.
- [5] P. Koch and R. Prasad, "The universal handset", *IEEE Spectrum*, vol. 46, no. 4, pp. 36–41, 2009.
- [6] Raghu Rao et al., "FPGA Polyphase Filter Bank Study & Implementation",

➔ To P. 70

A Histogram-Based Static Error Correction Technique for Flash ADCs: Implementation

J Jacob Wikner¹, Armin Jalili², Sayed Masoud Sayedi², and Rasoul Dehghani²

(1. Department of Electrical Engineering, Linköping University, SE-581 83 Linköping, Sweden;

2. Department of Electrical and Computer Engineering, Isfahan University of Technology, Isfahan 84156-83111, Iran)

Abstract

In this paper, we focus on practical issues in implementing a calibration technique for medium-resolution, high-speed flash analog-to-digital converters (ADCs). In [1], we theoretically describe the calibration technique and perform a behavioral-level simulation to test its functionality [1]. In this work, we discuss some issues in transistor-level implementation. The predominant factors that contribute to static errors such as reference generator mismatch and track-and-hold (T/H) gain error can be treated as input-referred offsets of each comparator. Using the proposed calibration technique, these errors can be calibrated with minimal detriment to the dynamic performance of the converter. We simulate a transistor-level implementation of a 5-bit, 1 GHz ADC in a 1.2 V, 65 nm CMOS process. The results show that DNL can be improved from 2.5 LSB to below 0.7 LSB after calibration, and INL can be improved from 1.6 LSB to below 0.6 LSB after calibration.

Keywords

Calibration; chopping; flash ADC; PDF generator; reference generator circuit; track and hold circuit

flash ADCs and gave the results of a behavioral-level simulation. The simulation showed that the accuracy and resolution of the ADC could be significantly improved without detriment to the original analog comparator structure. In this paper, we go further by describing issues in the implementation of the ADC design and how these issues can be addressed by calibration. As we proceed in this paper, the accuracy of the calibration technique described in [1] is increased as more and more transistor-level simulations are performed. We end our work by presenting transistor-level simulation results for a 5-bit, 1 GHz flash ADC in a 1.2 V, 65 nm CMOS process.

2 Calibration Technique

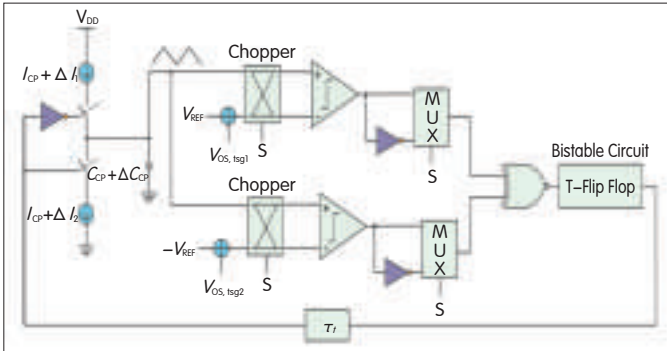
The histogram-based calibration technique for flash ADCs is introduced in [1]. The ADC operates in normal mode or calibration mode. In normal mode, the input signal is connected to the input of the ADC, which then converts as usual. In calibration mode, the output of the probability-density function (PDF) generator is connected to the ADC input. The PDF generator produces an analog signal with a known PDF, $f_{in}(x)$, which is further described in section 3. The output PDF, $f_{out}(x)$, sampled by the ADC, is a quantized version of $f_{in}(x)$. The output PDF is a discrete function of the number of bins per interval, I_i . Because of static errors, the two PDFs are not equal, and in our proposed histogram-based technique, this difference is used to extract the ADC errors.

We let the n -bit flash ADC have $2^n - 1$ reference voltage levels generated by a resistor ladder. A comparator is assigned to each reference level, and each level is compared with the input signal. At the output of all $2^n - 1$ comparators, a thermometer code is generated. Static errors are mainly caused by resistor mismatch and comparator offsets. These error components can be modeled as a voltage source, V_{os} , at the input of each comparator, which is now assumed to be ideal [1].

In the n -bit flash ADC using the histogram-based calibration technique, a multiplexer (MUX) array is used to select a set of comparators for calibration. The outputs of the

1 Introduction

Analog-to-digital converters (ADCs) are used in communications, instrumentation, video, and imaging. They are essential components in RF transceivers but also performance-limiting in many systems. The accuracy of a flash ADC is mainly limited by the offsets of the comparators and references. To increase accuracy, components are used that are well-designed and relatively large in terms of area and power. To avoid extra cost, calibration can reduce analog complexity, and analog hardware can be replaced with digital hardware. In [1], we described a calibration technique for



▲ Figure 1. Triangular signal generator (TSG) circuit with error sources indicated.

MUX are connected to the interval detector block, which determines which intervals, i ($i = 1, 2, \dots, 16$), the sampled value belongs to. The counter records the number of samples for each i . The ideal number of samples for each interval can be calculated in advance because the input PDF must be known.

The estimation block in the ADC estimates the voltage errors by comparing the wanted (ideal) number of samples, N_i , and the recorded number of samples, \tilde{N}_i (the tilde indicates the non-ideal case), for each i . The results of the comparison are then used by the trimming block to compensate for static errors. As we outlined in the behavioral-level description in [1], the trimming block can compensate for ADC errors by adjusting the voltage taps of the resistor ladder. This changes the ADC reference levels generated by the reference-selection block.

3 PDF Generator Circuit

The PDF generator is a vital component because it creates a reference signal with a known PDF, which the calibration relies on. Various analog signals might be used for test purposes, but a good candidate in terms of implementation complexity is the ramp function, which can be generated with, for example, a charge pump. Ideally, the ramp signal has a uniform distribution; that is, the PDF has a constant value because the ramp takes all analog levels with equal probability. For our ADC, we use a triangular signal generator (TSG) (Fig. 1) for uniform distribution. (We will return to the choppers and MUXs in Fig. 1.) The capacitor, C_{CP} , is charged and discharged sequentially by a pull-up or pull-down current, I_{CP} . Two comparators toggle the direction of the charge pump (up or down) with the help of a decoder and a latch. The overall circuit is a fixed-frequency oscillator.

The resulting triangular wave has amplitude of V_{REF} and a constant PDF. Ideally, the TSG range should be the same as the ADC range, that is, $V_{REF} = V_R$. The signal must be kept in the range $[-V_R, V_R]$ and should vary linearly with time. Other signal specifications do not need to be taken into account; slope variation, for example, does not affect the PDF distribution. However, in the TSG circuit (Fig. 1), some potentially dominating non-ideal effects are mismatch

between up and down currents, variation in capacitance, comparator offset, and transition delay.

Of these parameters, the current mismatch, ΔI_{CP} , and capacitor mismatch, ΔC_{CP} , only change the slopes of the generated ramps and therefore do not affect the PDF. The offset delay, $V_{OS,tsig}$, and transition delay, τ_t , change the upper and lower limits of the voltage across the capacitor. This means there is a deviation from the peak values V_{REF} and $-V_{REF}$. This variation can be determined from the resolution of the PDF circuit, and its maximum value is given by

$$V_{LSB,tsig} = V_{OS,tsig} + \tau_t (I_{CP}/C_{CP}) \quad (1)$$

where $V_{LSB,tsig}$ is the voltage of the least-significant bit (LSB) in the TSG circuit. The TSG resolution, n_{tsig} , is

$$n_{tsig} = \log_2 (2V_{REF}/V_{LSB,tsig}) \quad (2)$$

Substituting $V_{LSB,tsig}$ from (1) into (2) gives

$$n_{tsig} = \log_2 \frac{2V_{REF}}{V_{OS,tsig} + \tau_t (I_{CP}/C_{CP})} \quad (3)$$

The voltage across the capacitor forms the output of the TSG circuit and is fed to the ADC during calibration. The ratio between the TSG frequency and ADC sampling frequency should be carefully chosen to guarantee a uniform distribution [2], [3].

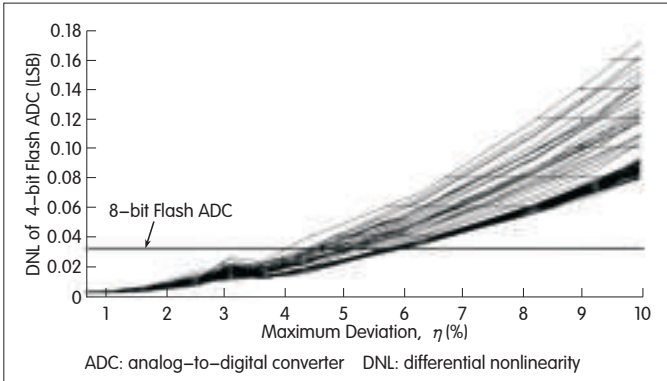
Assuming the TSG is nonlinear, we can start by looking at first-order, non-linear transfer characteristics. The linearity can be specified by the maximum deviation from a straight line between the two end points, V_{REF} and $-V_{REF}$. The deviation, η , is normalized with respect to the signal swing and is expressed as a percentage:

$$\eta = (\Delta V_{max}/2V_{REF}) \cdot 100 \quad (4)$$

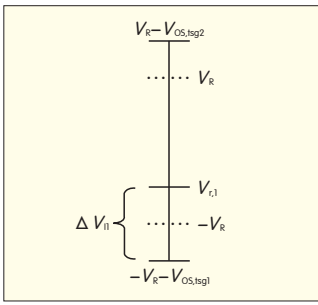
where ΔV_{max} is the maximum deviation from the straight line. Typically, this deviation is due to limited output impedance of the current sources, and a voltage-dependent capacitance, C_{CP} . To determine the effects of TSG errors on calibration, a behavioral-level model of the TSG is used for simulation. Starting with a 4-bit flash ADC and large comparator offsets (σ is approximately 60 mV for $V_R = 1$ V), we run Monte Carlo analyses and calibrate the ADC using equations (4)–(7) in [1]. The ADC differential nonlinearity (DNL) is extracted and characterized with respect to the maximum, non-ideal deviation from (4).

The simulation results are shown in Fig. 2. The DNL is expressed in LSBs, and refers to a 4-bit converter. DNL should therefore be below 0.5 LSB for full, nominal accuracy. In Fig. 2, an 8-bit resolution is indicated. In practical design, the nonlinear behavior of the TSG circuit is not significant, and the nonlinearity as high as four or five percent can be tolerated.

However, for high-resolution converters, a large n_{tsig} is required. In this case, (3) imposes stricter limitations on $V_{OS,tsig}$ and τ_t , and for each extra bit, we halve the accepted values. The design of a comparator with small offset and low delay could become quite complex, and to avoid this, we introduce a chopping technique that cancels out the effect of the offset



▲ Figure 2. DNL of the 4-bit flash ADC versus maximum deviation η for 100 Monte Carlo analyses.



▲ Figure 3. Effect of the TSG comparator offset on the reference voltage intervals.

values of the TSG comparators [4], [5].

3.1 Chopping

Fig. 3 shows the effect of an offset in the lower comparator in the TSG circuit. In this case, the number of samples belonging to the first interval, I_1 , can be estimated using

$$\tilde{N}_1 = (\Delta V_{i1} / V_{FS}) N \quad (5)$$

where ΔV_{i1} and V_{FS} , including the offset voltages, are the

spans of the first voltage interval and the full-scale voltage range, respectively. Replacing these terms with their corresponding values gives

$$\tilde{N}_1 = \frac{V_{r,1} + V_R + V_{os,tsg1}}{2V_R + \Delta V_{os,tsg}} N \quad (6)$$

where $V_{r,1}$ is the ideal reference voltage of the first ADC comparator, V_R is the reference voltage, $V_{os,tsg1}$ is the offset voltage of the bottom comparator, N is the total number of samples, and $\Delta V_{os,tsg} = V_{os,tsg1} - V_{os,tsg2}$. Assuming $\Delta V_{os,tsg}$ is small, Taylor expansion can be used to approximate (6):

$$\tilde{N}_1 = \left(\frac{\Delta V_{i1}}{2V_R} N \right) - \left(\frac{\Delta V_{i1} \Delta V_{os,tsg}}{4V_R^2} N \right) + \left(\frac{\Delta V_{os,tsg1}}{2V_R} N \right) - \left(\frac{V_{os,tsg1} \Delta V_{os,tsg}}{4V_R^2} N \right) \quad (7)$$

where ΔV_{i1} is the first voltage interval (Fig. 3). The last term in (7) is negligible as long as

$$(V_{os,tsg1} \Delta V_{os,tsg}) / 2V_R < V_{LSB} \quad (8)$$

where V_{LSB} is the LSB voltage of the ADC. Replacing the value of V_{LSB} in (8) for an n -bit converter, and considering the worst condition, $V_{os,tsg1} = -V_{os,tsg2}$, then

$$\hat{V}_{os,tsg} = V_R / (2^{n-1})^{1/2} \quad (9)$$

Even for high-resolution converters, (9) dictates that a relatively high offset is tolerable in the TSG comparators.

When the maximum offset is lower than the value estimated

in (9), the last term in the Taylor expansion (7) can be ignored. The average value, which is obtained from chopping, is simplified as

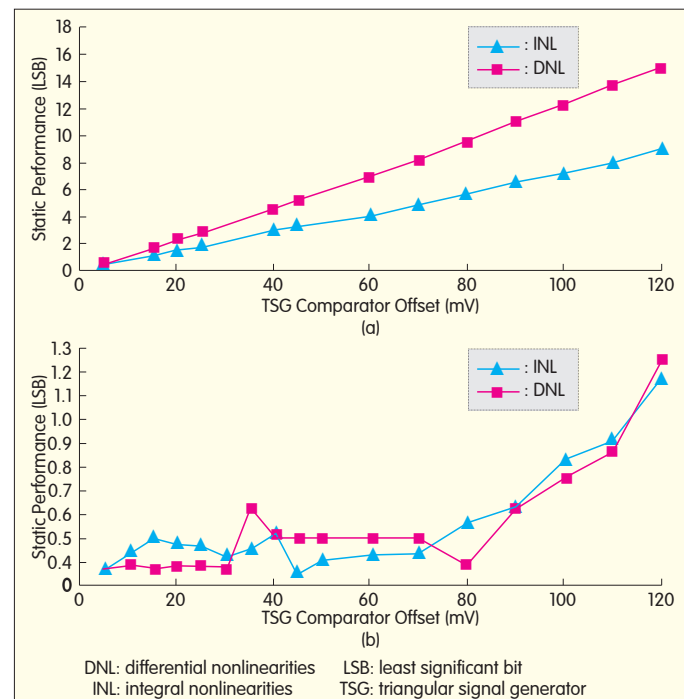
$$\tilde{N}_{1,ave} \approx (\Delta V_{i1} / 2V_R) N \quad (10)$$

where $\tilde{N}_{1,ave}$ is the average value of N_i in the two chopping states. The offsets of the TSG comparators are tolerable as long as they are less than the maximum offset defined in (9).

To determine the effects of any TSG comparator offset, a behavioral-level 8-bit flash ADC with full-scale range $V_R = 1$ V is calibrated. All the ADC error sources are set to zero so that only the offset errors of the TSG comparators are introduced. Fig. 4(a) shows simulated integral nonlinearities (INLs) and differential nonlinearities (DNLs) of the converter before chopping. Fig. 4(b) shows simulated INLs and DNLs of the converter after chopping. ADC performance degrades significantly as a function of the TSG comparator offsets (Fig. 4a). We took the DNL and INL from 100 Monte Carlo iterations and saw that by using chopping, the maximum tolerable offset was as high as 80 mV for $V_R = 1$ and $n = 8$. This is a significant improvement using very simple methods.

4 Track-and-Hold

The track-and-hold (T/H) circuit, also called sample-and-hold (S/H) circuit, is an integral part of most ADCs because it makes the converters less sensitive to jitter. In this section, we show how the proposed calibration technique also compensates for the static part of errors introduced by a typical T/H circuit. Such errors include kickback noise, gain, and nonlinearity. The proposed T/H



▲ Figure 4. INL and DNL of the 8-bit converter versus TSG comparator offset (a) before and (b) after chopping.

structure (Fig. 10) is an active, source-follower-based T/H. It contains input buffers implemented by NMOS source-followers as well as output buffers implemented by PMOS source-followers. The NMOS drives the sample-and-hold capacitor, C_H , and the PMOS drives the comparator inputs that form a potentially large capacitive load.

4.1 Kickback Noise

Kickback noise due to the capacitive coupling from comparator output to input affects both the references and signal inputs. In [1], we observed that by adding trimming switches, some of the kickback noise was suppressed onto the reference ladder. However, a T/H circuit with high driving capability (low enough output impedance) is required to diminish kickback on its own output (the comparator inputs).

Calibration relaxes design requirements by compensating for the static part of kickback noise. This can be done by assuming each comparator has zero offset error. The kickback noise on each comparator input is not detrimental unless the input signal is close to the corresponding reference voltage, that is, when the comparator makes a decision. From the point of view of static, kickback noise is deterministic and can be modeled by an equivalent offset voltage at each comparator. However, the amplitude does not depend solely on the input signal; it also depends on its derivative(s). In practice, the amount of kickback noise changes with frequency. To determine the effects of kickback noise in practice, a T/H circuit is designed in a 1.2 V, 65 nm CMOS process and used in a 4-bit flash ADC.

Fig. 5 shows deviation of kickback noise from the average for 15 reference levels. The signal frequency (full-scale sinusoid) is swept, and to isolate kickback noise from other errors—including clock feedthrough (CFT) and charge injection—the sampling switch is bypassed (its drain and source are tied together). Up to about 10 MHz, kickback noise is nearly constant and depends only on the input signal levels. For frequencies higher than 100 MHz, kickback noise amplitude increases significantly. For low frequencies, deviation from the average is nearly constant, which means that the calibration algorithm can calibrate the static part of the kickback noise.

For simplicity, we assume the kickback noise for all levels $i = 1, 2, \dots, 2^n - 1$ changes in proportion to the input signal level, given by

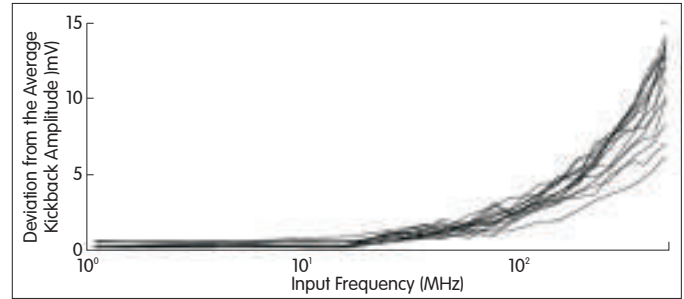
$$v_{k,i}(V_{in}) = \alpha_i V_{in} + \beta_i \quad (11)$$

where $v_{k,i}$ is the kickback amplitude, v_{in} is the input signal level and α_i and β_i are constants. In the first calibration step, the estimated comparator offset i is

$$v_{est1,i} = V_{k,i}(V_{r,i}) = \alpha_i V_{r,i} + \beta_i \quad (12)$$

where $v_{est1,i}$ is the estimated offset value and $V_{r,i}$ is the reference level, which can be used as an approximation of the input signal level. $v_{est1,i}$ is added to the reference level by the trimming circuitry [1] and compensates for the offset. The second calibration step gives

$$v_{est2,i} = V_{k,i}(V_{r,i} + v_{est1,i}) - v_{est1,i} = \alpha_i^2 V_{r,i} + \alpha_i \beta_i \quad (13)$$



▲ Figure 5. Deviation of kickback amplitude from its average versus input signal frequency.

and the m th calibration step gives

$$v_{estm,i} = \alpha_i^m V_{r,i} + \alpha_i^{m-1} \beta_i \quad (14)$$

For a nonzero comparator offset, the trip point is shifted from $V_{r,i}$ to $V_{r,i} - V_{OS,i}$ and (14) is modified as

$$v_{estm,i} = \alpha_i^m (1 - \alpha_i) V_{OS,i} + \alpha_i^m V_{r,i} + \alpha_i^{m-1} \beta_i \quad (15)$$

For a typical T/H circuit, we assume that α_i is less than 1 because it is very unlikely the kickback noise is in parity with high input signal levels. This means that the kickback amplitude of the i th comparator is less than the corresponding reference level. In this case, as m increases with calibration iterations, the estimated voltage $v_{estm,i}$ in (15) decreases. The calibration converges and compensates for the static part of the kickback noise.

To verify (15), we examine a 4-bit flash ADC implemented in a 65 nm CMOS process with the previously mentioned parameters. To focus solely on the kickback noise, the nominal condition is simulated with zero mismatch. The T/H is omitted, and source impedance is introduced into the input signal generator in order to determine kickback behavior. The ADC response to a full-scale ramp signal is shown in Fig. 6. Each ramp corresponds to one calibration step. Before calibration (the first ramp), the ADC suffers DNL errors and missing codes because of the kickback noise. After seven calibration steps, the algorithm converges and compensates for the kickback noise.

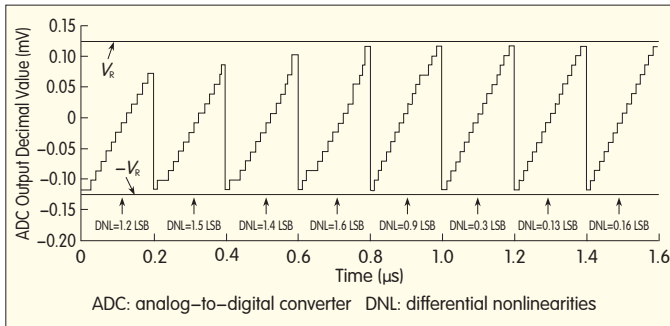
4.2 Gain Errors

Another issue with T/H circuits is gain error. Some effort is required to design a buffer with acceptable gain variations, especially in fine-line CMOS technologies where process variations can substantially affect the open-loop buffer gain. Using the proposed technique, gain error can be calibrated because the effect of the gain error can be described by a set of comparator offset voltages. The corresponding reference and trimming voltages are then rearranged to compensate for the gain error. The T/H gain error in the calibration algorithm generates equivalent offset errors given by

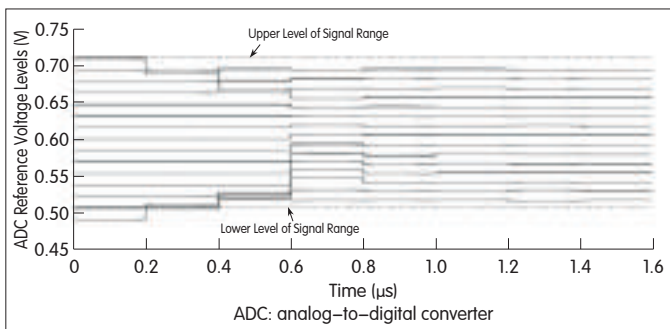
$$V_{OS,i} = -\gamma V_{r,i} \quad (16)$$

where γ is the gain error of the T/H circuit.

The T/H circuit is used in a 4-bit flash ADC, and behavioral-level models are used so that the comparators



▲ Figure 6. Transistor-level simulations showing calibration steps and compensation for T/H kickback errors.



▲ Figure 7. Calibration steps showing the compensation for T/H gain error.

can isolate the gain error. Fig. 7 shows the arrangement of the reference voltages of the ADC during calibration. At first, the reference levels are in their ideal positions. As the calibration proceeds, these reference levels are pushed towards the range of the T/H output. The original ADC range is shown by the dotted line, and the reference levels are pushed and distributed inside the signal range. Each $0.2 \mu\text{s}$ corresponds to one calibration step.

4.3 Distortion and Nonlinearity

Dominant T/H errors include distortion that are due to nonlinearity of the sample-and-hold capacitor. Switch-on resistance is another dominant T/H error. The calibration here is not intended to compensate for any dynamic nonlinear errors. For static errors, the input and output relationship can be described by a relatively well-defined polynomial:

$$V_{\text{out}} = a_0 + a_1 V_{\text{in}} + a_2 V_{\text{in}}^2 + a_3 V_{\text{in}}^3 + \dots \quad (17)$$

The T/H static nonlinearity can be calibrated as long as the a_i coefficients are small enough. To determine the effect of moderate distortion, the T/H is used in an 8-bit flash ADC. Behavioral-level comparators are used, and the sampling switch is bypassed to avoid kickback. The effect of distortion can then be analyzed in isolation. INL before calibration in Fig. 8(a) has a maximum absolute value of about 2 LSB. INL after calibration in Fig. 8(b) and is improved to about 0.15 LSB.

5 Implementation

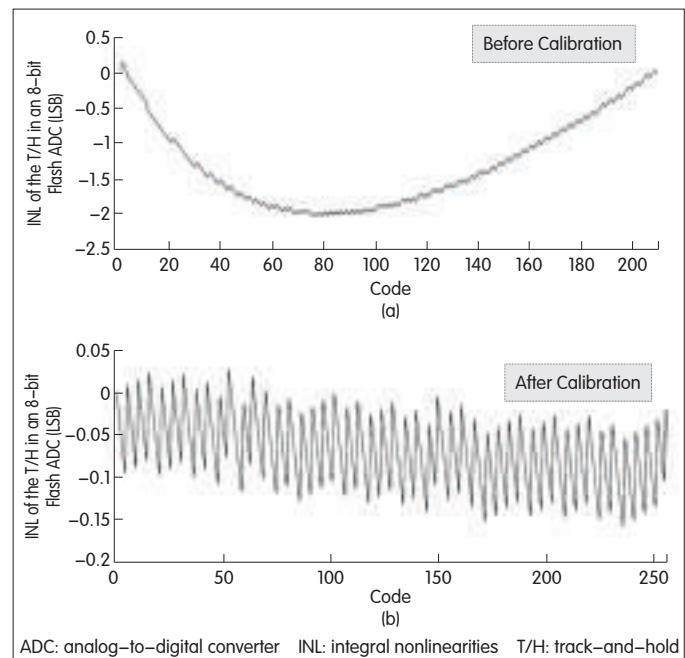
Fig. 9 shows the proposed calibration system, and an

implementation of the calibration algorithm has already been presented in [1]. The ADC input is connected to the TSG circuit (PDF generator) in calibration mode [1]. The $2^n - 1$ comparators produce a thermometer code so that an ADC level is represented by a set of r consecutive 1s at the bottom and s consecutive 0s at the top. The MUX selects a set of 16 comparators and feeds their outputs to the interval-detector block. This block then locates the input signal in the different voltage intervals and produces a 1-of-16 (walking-one) code at the block's output, which indicates the corresponding code value.

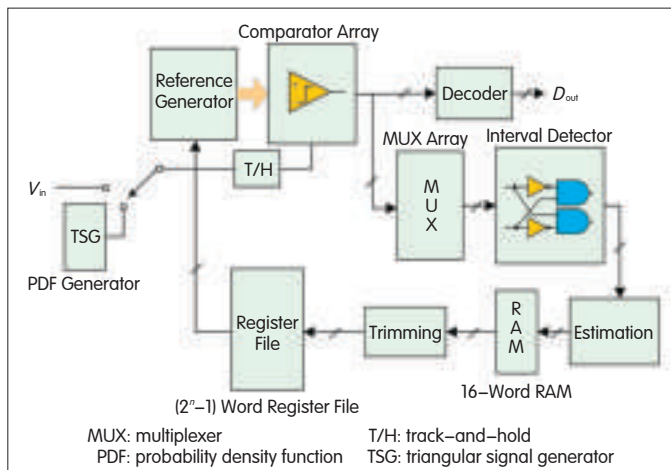
For small errors, the voltage intervals do not overlap [1], and in the thermometer code, there are normal transitions between 1 and 0, that is, no sparkle errors. However, for large offset errors, the intervals overlap, and this is detected and compensated for by the interval-detector block.

The outputs of the interval detector are applied to the estimation block, which contains an array of counters that record the number of samples belonging to each interval. All offset values are then estimated according to the procedure given in the behavioral-level description of the algorithm [1]. The estimated offset values are stored in a 16-word RAM. Each word represents the offset of a comparator in the chosen set. The trimming block in Fig. 9 reads the RAM and performs encoding to reduce the word length. It then stores the result in registers that contain $2^n - 1$ words that represent the offset for each comparator. The register word lengths typically depend on the maximum comparator offset because larger offsets result in longer word lengths.

Each register defines the select lines, which in turn control the analog multiplexers (AMUXs) in the reference generator. There is one AMUX assigned to each comparator. Each MUX



▲ Figure 8. INL of an 8-bit flash converter using a T/H circuit (a) before and (b) after calibration.



▲ Figure 9. Proposed calibration system.

can select from a batch of reference voltage taps on the resistor ladder. Each input provides a fractional LSB so that a fine voltage step can be added to or subtracted from the MUX output. This output is then used as the new reference voltage for the corresponding comparator.

5.1 Complexity

The analog switch area of the AMUX array is proportional to

$$A_{\text{ASW}} = (2^n - 1) \cdot \frac{2V_{\text{os,max}}}{V_{\text{LSB}}/M} \cdot A_{\text{ATG}} \quad (18)$$

where n is the resolution of the converter, $V_{\text{OS,max}}$ is the maximum static error amplitude covered by the calibration algorithm, V_{LSB} is the LSB voltage, M is the number of fine sub-LSB steps, and A_{TG} is the area of each TG. Inserting $V_{\text{LSB}} = 2V_{\text{R}} / 2^n$ into (18) results in

$$\frac{A_{\text{ASW}}}{A_{\text{ATG}}} = (2^n - 1) \cdot 2^n \cdot M \cdot \frac{V_{\text{os,max}}}{V_{\text{R}}} \quad (19)$$

The same equation can be used for the decoder part: the digital MUX (DMUX) array at the output of the comparators is implemented using unity TGs. In this case, the area can be approximated using

$$A_{\text{DSW}}/A_{\text{DTG}} = 2^n - 1 \quad (20)$$

where A_{DTG} is the area of the unity TG. The register file contains $2^n - 1$ words, and each represents the selected lines of the corresponding AMUX. So, similar to (19), we get

$$\frac{A_{\text{Reg}}}{A_L} = (2^n - 1) \cdot \log_2 \frac{2^n MV_{\text{OS, max}}}{V_R} \quad (21)$$

where A_L is the area of a typical latch used in the register file. According to (19)–(21), the areas of the AMUX, DMUX, and register file grow exponentially in relation to resolution n . The size of the remaining calibration blocks is proportional to the resolution because of the segmented approach [1]. With the segmented approach, a considerable amount of calibration hardware grows linearly, rather than exponentially, in relation to converter resolution.

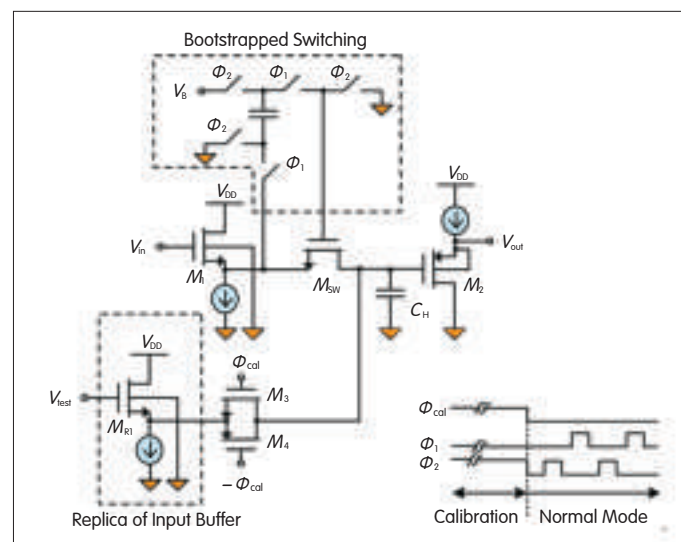
The size of the calibration blocks can be ordered according to the size of the total ADC area: all-digital estimation block, RAM, and trimming block (33%); decoder part of the AMUX array (10%); analog switches of the AMUX array (6%); TSG circuit (2%); register file (2%); and DMUX array (1%). This accounts for approximately half the total area of the ADC, which is 0.25 mm². Unlike the analog area, the calibration area does not scale exponentially as higher resolutions are attained. Using calibration, the analog comparator area can be kept fairly low and, most importantly, analog complexity can be reduced by using standard digital cells.

6 Simulation Results

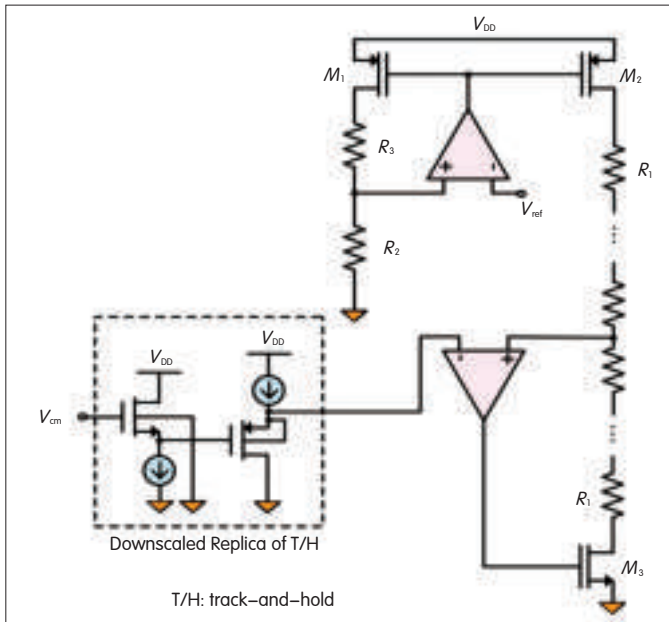
As a proof-of-concept, a single-ended, 5-bit flash ADC is designed in the same 1.2 V, 65 nm CMOS process used previously. The ADC range is from 475 to 725 mV, which allows a full range of 250 mV (related to the single-ended signal). Fig. 10 shows the T/H circuit where a boot-strapped sample switch is used to enhance performance [6]. A replica of the input buffer injects the test signal, V_{test} , during calibration. A transmission gate (M3 and M4) is used as a switch to inject the test signal. The gate can be small; in this design it is 25 times smaller than the sample switch, M_{sw} , because the test signal is typically low-frequency. Therefore, the additional parasitic capacitance is small, and the dynamic performance of the T/H remains relatively unaffected. The T/H circuit has a gain loss of approximately -1.7 dB.

Fig. 11 shows the ADC reference generator circuit adopted from [7]. A replica of the T/H circuit is used to match the common-mode level of the reference generator with the input signal. A version of the T/H, scaled down 40 times, is used. Corner and Monte Carlo analyses show that the replica matches the original T/H well within one LSB. Any residual errors due to the mismatch are, however, compensated for during calibration.

The test signal is generated using the TSG circuit in Fig. 1.



▲ Figure 10. T/H circuit and injection of the test signal.



▲ Figure 11. Reference generator circuit with downscaled replica of the T/H circuit.

The reference current, I_{CP} , is about 250 nA, and the TSG capacitor is 1 pF. A comparator with relatively small offset and very low kickback is chosen [8]. This comparator is power-hungry and slow; it is only used in calibration mode and powered down during normal operation. The TSG comparators have an offset of about 7 mV. The resulting test signal has tolerable nonlinearity of about 1% (Fig. 2).

The trimming circuit is implemented using a 32-to-1 AMUX array. A set of transmission gates are controlled by 5-bit words. Each TG is about ten times larger than the minimum-sized TG, and there are three fine LSB steps. The core flash ADC comparators have an input-referred offset of approximately 15 mV and are clocked at 1 GHz; that is, the ADC operating frequency is 1 GHz. Then, ADC is calibrated using a test signal with a ramp frequency of about 500 kHz.

To save simulation time, each step of the calibration is completed with a relatively low number of samples (approximately 2000). The simulated DNL and INL before calibration are shown in Fig. 12(a) and (b), and the results after 16 calibration steps, are shown in Fig. 12(c) and (d). The DNL is reduced from 2.5 LSB to about 0.7 LSB, and the INL is reduced from 1.6 LSB to about 0.6 LSB.

The proposed technique is effective in calibrating important errors in the structure of the flash ADC (Fig. 12). We chose a low number of samples for each calibration cycle in order to decrease the simulation time and prove the effectiveness of the calibration method. Further improvement in DNL and INL in the ADC can be achieved by using a higher number of samples in each calibration cycle. This would, however, affect the setup time of the system, and there would be a trade-off between obtainable resolution and calibration time.

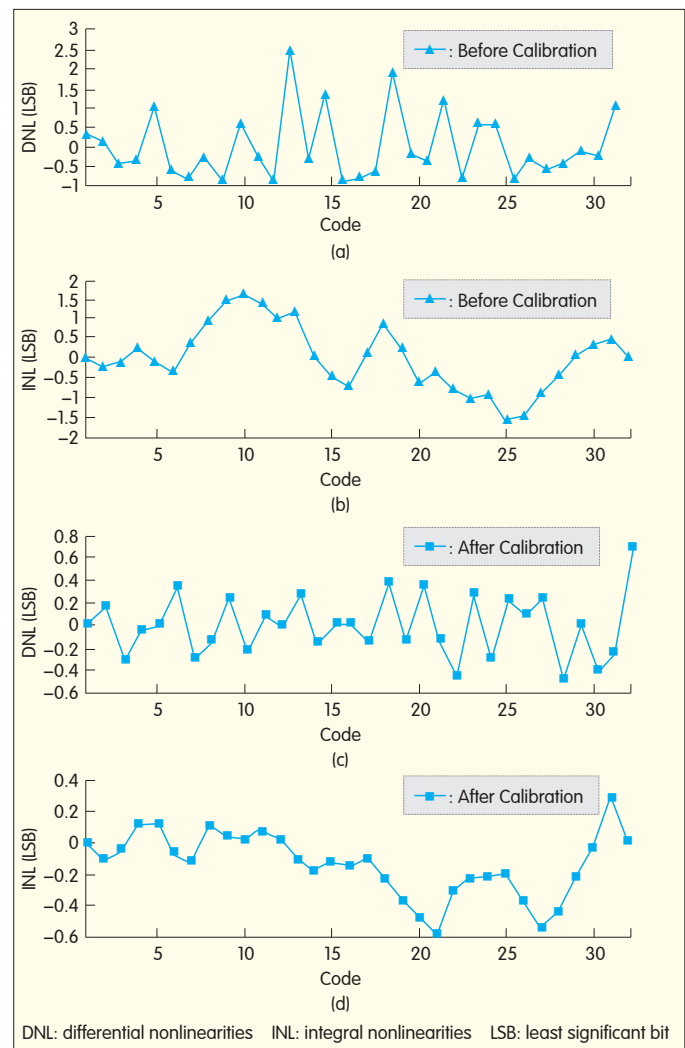
In this work, only a single-shot simulation result has been given. In the behavioral-level simulation results in [1, Fig. 8],

98% of cases were successful using an 8-bit ADC with 25 mV comparator offset. In this simulation, using a 5-bit ADC with a 15 mV comparator offset gives a higher rate of success.

7 Conclusion

The ADC architecture and calibration technique were described in [1], and this follow-up paper focuses on additional errors that arise as a result of moving towards transistor-level implementation. We show how the calibration technique handles errors that arise when different blocks of the flash ADC are implemented. The chosen implementations have a minimally detrimental effect on the ADC because they do not change the comparators. A triangular waveform is generated by a PDF circuit in which the comparator offsets could cause significant errors that affect calibration. However, using chopping, a large offset value is tolerable, and analog complexity can further be reduced.

Simulation results for different sub-blocks have also been



▲ Figure 12. (a) DNL and (b) INL of the flash ADC before calibration, and (c) DNL and (d) INL after calibration.

A Histogram-Based Static Error Correction Technique for Flash ADCs: Implementation

J Jacob Wikner, Armin Jalili, Sayed Masoud Sayedi, and Rasoul Dehghani

given. As a proof of concept, a full transistor-level simulation of a 5-bit, 0.25 mm², 1 GHz flash ADC in a 65 nm CMOS process was performed. Simulation results show that DNL improved from 2.5 LSB to about 0.7 LSB after calibration, and INL improved from 1.6 LSB to about 0.6 LSB after calibration. We have described how Analog complexity can be traded off against digital complexity and how obtainable resolution can be traded off against system setup and calibration time.

References

- [1] A. Jalili, J. J. Wikner, S. M. Sayedi, and R. Dehghani, "A Histogram-Based Static Error Correction Technique for Flash ADCs," *ZTE Communications*, vol. 9, no. 4, pp. 35–41, Dec. 2011.
- [2] P. Carbone and G. Chiorboli, "ADC sinewave histogram testing with quasi-coherent sampling," *IEEE Trans. Instrumentation and Measurement*, vol. 50, pp. 949–953, Aug. 2001.
- [3] D. Dallet, F. Valeze, P. Kadionik, M. Benkais, and P. Marchegay, "Dynamic testing of a/d converters: how many samples for a given precision?" in *Proc. IEEE Instrumentation and Measurement Technology Conf. 1996, "Quality Measurements: The Indispensable Bridge between Theory and Reality"*, Brussels, 1996, pp. 1298–1303.
- [4] Chung-Cheng Huang and Jieh-Tsorng Wu, "A background comparator calibration technique for flash analog-to-digital converters," *IEEE Trans. Circuits and Systems I*, vol. 52, pp. 1732–1740, Sep. 2005.
- [5] H. van der Ploeg, G. Hoogzaad, H.A.H. Termeer, M. Vertregt, and R.L.J. Roovers, "A 2.5–V 12-b 54–MSample/s 0.25-μm CMOS ADC in 1–mm² with mixed-signal chopping and calibration," *IEEE J. Solid State Circuits*, vol. 36, pp. 1859–1867, Dec. 2001.
- [6] H. Yu and M.-C. F. Chang, "A 1–V 1.25–GS/s 8-bit self-calibrated flash ADC in 90–nm digital CMOS," *IEEE Trans. Circuits and Systems II*, vol. 55, pp. 668–672, Jul. 2008.
- [7] V. Srinivas, S. Pavan, A. Lachhwani, and N. Sasidhar, "A distortion compensating flash analog-to-digital conversion technique," *IEEE J. Solid State Circuits*, vol. 41, pp. 1959–1969, Sep. 2006.
- [8] R. J. van de Plassche, *CMOS Integrated Analog-to-Digital and Digital-to-Analog Converters*, 2nd edition. Dordrecht, The Netherlands: Kluwer Academic Publishers, 2003.

Manuscript received: September 20, 2011

From P. 62

- Presentation, Image Communications/Reconfigurable Computing Lab. Electrical Engineering Dept.UCLA [Online]. Available: http://slaac.east.isi.edu/presentations/retreat_9909/polyphase.pdf
- [7] Patrick Murphy, "Digital Communications using FPGAs & Xilinx System Generator", Presentation, October 5–6, 2006, IIT Delhi, India. [Online]. Available: http://cmclab.rice.edu/workshops/materials/2006-10-05_DigitalComm/Rice_Comm_Workshop_Slides.pdf
 - [8] Xilinx (2009, Feb. 6). *Xilinx DS100 (v5.0) Virtex-5 Family Overview* [Online]. Available: http://www.xilinx.com/support/documentation/data_sheets/ds100.pdf
 - [9] Xilinx (2009, Jan. 12). *Xilinx UG193 Virtex-5 FPGA XtremeDSP Design Considerations User Guide* [Online]. Available: http://www.xilinx.com/support/documentation/user_guides/ug193.pdf
 - [10] M. Awan, P. Koch, C. Dick, and F. Harris, "FPGA implementation analysis of polyphase channelizer performing sample rate change required for both matched filtering and channel frequency spacing", in *Proc. 44th Asilomar Conf. on Signals, Syst., and Comput.*, CA, Nov. 7–10, 2010, pp. 414–418.
 - [11] Xilinx (2010, May 17). *UG190 (v5.3) Virtex-5 FPGA User Guide* [Online]. Available: http://www.xilinx.com/support/documentation/user_guides/ug190.pdf
 - [12] Xilinx (2008, Feb. 14). *Xilinx WP285 (V1.0) Virtex-5 FPGA System Power Design Considerations* [Online]. Available: http://www.xilinx.com/support/documentation/white_papers/wp285.pdf
 - [13] Xilinx (2008). *Xilinx ISE 10.1 Design Suite Software Manuals and Help* [Online]. Available: <http://www.xilinx.com/itp/xilinx10/books/manuals.pdf>
 - [14] ModelSim (2009, Jan. 22). *ModelSim SE User's Manual, Software Version 6.5* [Online]. Available: http://portal.model.com/d/download_request.asp
 - [15] A. D. Garcia, L. F. Gonzalez Perez, R. F. Acuna, "Power consumption management on FPGAs", *Proc. 15th International Conf. on Electronics, Communications and Computers*, Puebla, Feb. 2005, pp. 240–245.
 - [16] Thales, "Design considerations for size, weight, and power (SWAP) constrained radios", *Proc. Software Defined Radio Technical Conf. and Product Expo.*, Nov 14, 2006.
 - [17] A. Andrei, M. T. Schmitz, P. Eles, Zebo Peng, and B. M. Al Hashimi, "Quasi-static voltage scaling for energy minimization with time constraints", in *Proc. Conf. Design, Automation and Test in Europe*, Vol. 1, Mar. 2005, pp. 514–519.

Manuscript received: September 20, 2011

Biographies

J. Jacob Wikner (jacob.wikner@liu.se) received his PhD from the Department of Electrical Engineering, Linköping University, Sweden, in 2001. He has worked as research engineer at Ericsson Microelectronics, senior analog design engineer at Infineon Technologies, and senior design engineer and chip architect at Sicon Semiconductor. Dr. Wikner has been an associate professor at Linköping University since 2009. His research interests include biologically inspired architectures, high-speed A/D and D/A converters, and general analog and mixed-signal design. He holds six patents, has published 40 scientific papers, and has co-authored "CMOS Data Converters for Telecommunication." He is the co-founder of CogniCatus and AnaCatum Design.

Armin Jalili (arminj@ec.iut.ac.ir) received his BSc and MSc degrees in electrical engineering from Isfahan University of Technology (IUT) in 2004 and 2006. He is currently working towards his PhD degree in electrical engineering at IUT. His interests include ADC design.

Sayed Masoud Sayedi (m_sayedi@cc.iut.ac.ir) received his BSc and MSc degrees in electrical engineering from Isfahan University of Technology (IUT), Iran, in 1986 and 1988. He received his PhD degree in electronics from Concordia University in 1996. From 1988 to 1992, and since 1997, he has worked at IUT, where he is currently an associate professor in the Department of Electrical and Computer Engineering. His research interests include VLSI fabrication processes, low power VLSI circuits, vision sensors, and data converters.

Rasoul Dehghani (dehghani@cc.iut.ac.ir) received his BSEE, MSc, and PhD degrees in electrical engineering from Sharif University of Technology (SUT), Iran, in 1988, 1991 and 2004. From 1987 to 1991, he worked on design and implementation of different electronic circuits and systems at SUT. From 1991 to 1998, he was involved in implementing various electronic circuits focused on industrial applications. From 1998 to 2004, he worked with Emad Co. in Tehran and Jaalaa Company in Kuala Lumpur as a senior design engineer. Since 2006, he has been an assistant professor at IUT. His research interests include RF IC design for wireless communication, frequency synthesis, and low-voltage low-power circuits.

Biographies

Mehmood Awan (mura@es.aau.dk) received his MSc degree in electronic engineering with specialization in applied signal processing and implementation from Aalborg University in 2007. He was a research assistant for one year and started his PhD in resource-optimal SDR front-ends in 2008. His research interests include multirate signal processing, SDR, hardware architectures, and embedded systems.

Yannick Le Moullec (ylm@es.aau.dk) received his PhD degree in electrical engineering from Université de Bretagne Sud, Lorient, France, in 2003. From 2003 to 2005, he was a post-doctoral fellow at the Center for Embedded Software Systems, Aalborg University, Denmark. From 2005 to 2008, he was an assistant professor at the Department of Electronic Systems, Aalborg University, where he is now an associate professor. His research interests include methods and tools for HW/SW co-design, embedded systems, and reconfigurable computing.

Peter Koch (pk@es.aau.dk) received his MSc and PhD degrees in Electrical Engineering from Aalborg University, Denmark, in 1989 and 1996. Since 1997, he has been an associate professor at the Department of Electronic Systems, Aalborg University, working in the interdisciplinary field between DSP and resource-optimal real-time architectures. From 2006 to 2010, he headed the Center for Software Defined Radio, Aalborg University. His research interests include optimization between DSP algorithms and architectures, and low-energy HW/SW design.

Fred Harris (fred.harris@sdsu.edu) holds the Signal Processing Chair of the Communication Systems and Signal Processing Institute at San Diego State University where he teaches DSP and communication systems. He holds 20 patents for digital receivers, and he lectures around the world on DSP applications. He is an adjunct of the Princeton IDA-CCR Center for Communications Research and is the author of "Multirate Signal Processing for Communication systems."